Measurement of Neutrino Interactions and Three Flavor Neutrino Oscillations in the T2K Experiment

Tatsuya Kikawa

September, 2014

Department of Physics, Graduate School of Science
Kyoto University

Measurement of Neutrino Interactions and Three Flavor Neutrino Oscillations in the T2K Experiment

A dissertation
submitted in partial fulfillment of the requirements
for the Degree of Doctor of Science
in the Graduate School of Science, Kyoto University

Tatsuya Kikawa

Department of Physics, Graduate School of Science
Kyoto University
September, 2014

Abstract

T2K is a long-baseline neutrino oscillation experiment. Muon neutrinos are generated by a proton beam, and are detected by near and far neutrino detectors. For a precise measurement of the neutrino oscillation, an accurate understanding of the neutrino beam and the neutrino interaction is essential. Therefore, the measurement of the neutrino beam properties and the neutrino interaction cross sections plays an important role in T2K.

Neutrino event rate, neutrino beam direction and neutrino beam width were measured with the near neutrino detector called INGRID. They were confirmed to be stable within the physics requirements and agree well with the T2K neutrino flux predictions. In addition, this measurement reduced the neutrino flux uncertainty from the neutrino beam direction which was originally 7.0% at 1 GeV to 2.5%.

The neutrino interaction cross sections in a few GeV region were also measured with INGRID. The charged current inclusive cross sections on iron and hydrocarbon and their cross section ratio were measured to be $\sigma_{\mathrm{CC}}^{\mathrm{Fe}} = (1.444 \pm 0.002(stat.)^{+0.189}_{-0.157}(syst.)) \times 10^{-38}\mathrm{cm}^2/\mathrm{nucleon}$, $\sigma_{\mathrm{CC}}^{\mathrm{CH}} = (1.379 \pm 0.009(stat.)^{+0.178}_{-0.147}(syst.)) \times 10^{-38}\mathrm{cm}^2/\mathrm{nucleon}$, and $\sigma_{\mathrm{CC}}^{\mathrm{Fe}}/\sigma_{\mathrm{CC}}^{\mathrm{CH}} = 1.047 \pm 0.007(stat.) \pm 0.035(syst.)$, at a mean neutrino energy of 1.51 GeV. They agree well with the predicted values by the neutrino interaction models used in T2K. Since the neutrino cross section in a few GeV region is sensitive to the nuclear effect of the target material, this result demonstrates that the nuclear effect is well understood and correctly treated in the models on the 3% level. The measured charged current quasi-elastic cross sections are also consistent with the neutrino interaction models. However, the measured charged current coherent pion production cross section is significantly smaller than the prediction by the original Rein-Sehgal model that is widely used in neutrino experiments. Therefore, we reveal that the original Rein-Sehgal model breaks down in a few GeV region. Since this inconsistency is within the originally assigned uncertainty, all the cross section results from INGRID demonstrate the validity of the neutrino interaction models and their uncertainties in T2K.

Finally, a neutrino oscillation analysis was performed using the neutrino flux prediction, the neutrino interaction models and the beam data in the near and far detectors. We performed a joint three-flavor neutrino oscillation analysis of the electron neutrino appearance and the muon neutrino disappearance for the first time. As the result, $\sin^2 2\theta_{13}$ for normal (inverted) neutrino mass hierarchy was determined to be $\sin^2 2\theta_{13} = 0.165^{+0.044}_{-0.073}$ $(0.191^{+0.056}_{-0.084})$. The electron neutrino appearance in a muon neutrino beam was observed because the appearance signal corresponds to a significance of 7.3σ. We also obtained $\sin^2\theta_{23} = 0.524 \pm 0.058$ $(0.524^{+0.058}_{-0.057})$ and $\Delta m^2_{32} = (2.50 \pm 0.11) \times 10^{-3}\mathrm{eV}^2$ $(\Delta m^2_{13} = (2.48 \pm 0.11) \times 10^{-3}\mathrm{eV}^2)$ for the normal (inverted) hierarchy. The measurement of $\sin^2\theta_{23}$ is the most precise in the world. Furthermore, when the T2K result was combined with the result of θ_{13} measurements by reactor experiments, 90% confidence level allowed region for δ_{CP} was obtained to be $-3.59 < \delta_{CP} < 0.43$ $(-2.84 < \delta_{CP} < -0.32)$ for the normal (inverted) hierarchy.

Acknowledgments

My works in this thesis were achieved thanks to tremendous supports from many people. Here, I would like to acknowledge each of them.

First of all, I would like to express my sincere gratitude to my supervisor, Prof. Tsuyoshi Nakaya. When I first expressed a desire to develop a new detector five years ago, he gave me the basic idea of the INGRID Proton Module and left everything to me. It inspired my enthusiasm and it lingers to the present date. In addition, his insightful advice and warm encouragements helped me a lot. My heartfelt appreciation goes to Prof. Atsuko Ichikawa, who is also my supervisor and shared the office with me both in Kyoto and Tokai. Discussions with her have always been illuminating. But, I still don't accept a dispute with her about the strawberry seed. I learned many things not only from her advice but also from her attitude to the physics and experiments. I owe a very important debt to Dr. Akihiro Minamino, who is the convener of the INGRID detector and the neutrino cross section analysis in T2K. His tremendous support led me to the best direction to the success.

I am cordially thankful to Dr. Masashi Otani, Dr. Akira Murakami and Dr. Christophe Bronner, who helped me on the operation and analysis of the INGRID detector. Dr. Masashi Otani developed the basis of the neutrino beam measurement with INGRID and has been greatly supportive to me. Dr. Akira Murakami helped me a lot on the development of the Monte Carlo simulation of the INGRID detector. Dr. Christophe Bronner made an important contribution to the development of the INGRID Proton Module. I would never have achieved the works in INGRID without their helps. I also want to thank to Prof. Masashi Yokoyama, Prof. Kazuhiro Yamamoto, Prof. Michel Gonin, Prof. Takeshi Nakadaira and Dr. Ken Sakashita for valuable advice on the operation and the analysis of INGRID. I owe my profound gratitude to Ms. Chie Matsumura, Mr. and Mrs. Taino for helping the construction of the INGRID Proton Module.

Many experts of the neutrino interaction, especially Prof. Yoshinari Hayato, Prof. Steve Dytman, Prof. Kevin McFarland, Dr. Kendall Mahn and Dr. Teppei Katori, gave me helpful advice on the neutrino cross section measurements. Prof. Yoshinari Hayato also gave me enormous technical helps about the neutrino interaction simulation. I am deeply grateful to them.

I would like to express my cordial appreciation to Dr. Megan Friend and Dr. Motoyasu Ikeda, who worked together with me on the neutrino oscillation analysis. Dr. Megan Friend developed the basis of the fitter for the neutrino oscillation analysis. Her excellent works and shrewd advice brought me to the success in the neutrino oscillation analysis. Dr. Motoyasu Ikeda gave me many useful advice on the treatment of the systematic errors in the neutrino oscillation analysis. He also helped me on the fabrication of the components for the INGRID Proton Module. I think they are models of young scientists which I should emulate.

I want to offer my thanks to J-PARC, KEK and ICRR staffs for superb operations of the accelerator, the neutrino beamline and the Super-Kamiokande detector. I am especially thankful to Prof. Takashi Kobayashi, who is the spokesperson of the T2K experiment for his strong leadership. I wish to extend my thanks to all collaborators of the T2K and Super-Kamiokande experiments. Dr. Motoyasu Ikeda, Dr. Ryosuke Ohta, Dr. Kodai Matsuoka, Mr. Hajime Kubo, Dr. Masashi Otani, Dr. Takatomi Yano, Dr. Akira Murakami, Dr. Kei Ieki, Mr. Kento Suzuki,

Mr. Shota Takahashi, Mr. Kunxian Huang, Mr. Takahiro Hiraki and Ms. Seiko Hirota worked hard together on T2K and Super-Kamiokande. I learned many things from them. I particularly appreciate the deep friendship of my fellow students: Mr. Kento Suzuki, Mr. Shota Takahashi and Mr. Kunxian Huang. I wish our friendship will last for the rest of my life.

I want to express my gratitude also to the other members of my laboratory: Prof. Noboru Sasao, Prof. Masaya Ishino, Prof. Tadashi Nomura, Dr. Hajime Nanjo, Dr. Toshi Sumida, Dr. Hideki Morii, Dr. Yasuhiro Nakajima, Dr. Yoshinori Kurimoto, Dr. Phillip Litchfield, Dr. Koji Shiomi, Dr. Takahiko Masuda, Mr. Naoki Kawasaki, Mr. Daichi Naito, Mr. Yosuke Maeda, Mr. Daniel Orme, Dr. Kiseki Nakamura, Mr. Goh Takahashi, Mr. Takahiro Yamauchi, Mr. Kohei Goda, Mr. Shigeto Seki, Mr. Takuya Tashiro, Mr. Tokio Nagasaki, Mr. Shinichi Akiyama, Mr. Naoyuki Kamo, Mr. Keiji Tateishi, Mr. Takaaki Hineno, Mr. Yuuki Ishiyama, Mr. Ichinori Kamiji, Mr. Takuto Kunigo, Mr. Kota Nakagiri, Mr. Keigo Nakamura, Mr. Tatsuya Hayashino, Mr. Kento Yoshida, Mr. Miao Jiang, Mr. Keisuke Kondo, Mr. Satoshi Shinohara, Mr. Kento Haneda, Mr. Sei Ban, Ms. Mika Yamamoto, Mr. Ryutaro Monden, and Ms. Saori Yanagita. Having spent five years with them has given me a great deal of experience as well as pleasure. I am grateful to the secretaries of Kyoto University, KEK, J-PARC and ICRR, especially to Ms. Mayumi Hiraoka, Ms. Noriko Hirano, Ms. Yuri Nishikubo, Ms. Mari Mori, Ms. Mariko Tanizawa, Ms. Misa Iwaki, Ms. Terue Ishino, Ms. Saki Yamashita, Ms. Eriko Hayashi, Ms. Haru Houya, Ms. Makiko Sakurai, Ms. Ayako Kikuchi, and Ms. Yukari Wada, for taking care of every business.

Also, I appreciate the financial support of Japan Society for the Promotion of Science (JSPS) fellowship and the Global COE Program, "The Next Generation of Physics, Spun from Universality and Emergence".

Finally, I would like to express the deepest appreciation to my family, particularly to my parents, Satoshi and Hitomi Kikawa, for giving birth to me, bringing me up, and supporting me to this day.

Tatsuya Kikawa

Kyoto Japan

September 2014

Contents

Chapter 1

Introduction

Neutrino is one of the elementary particles with spin 1/2 and no electric charge, and interacts only through the weak interaction (and the gravitational interaction). Although half a century has passed after the discovery of the neutrino, there still remain many questions in the neutrino physics. This thesis presents studies of the neutrino in the T2K experiment to resolve the remaining questions. As an introduction to this thesis, the theories and the experimental status of the neutrino physics are described earlier in this chapter (Secs. 1.1, 1.2, 1.3 and 1.4). Later in this chapter, the introduction to the T2K experiment and the outline of this thesis are described (Secs. 1.5 and 1.6).

1.1 Neutrinos

1.1.1 Discovery of neutrinos

The neutrino was first postulated by W. Pauli in 1930 [1] in order to explain the continuum electron energy spectrum from the β decay ($n \to p + e^- + \bar{\nu_e}$). Its first observation was achieved by F. Reines and C. L. Cowan in 1956 [2] by detecting anti-electron-neutrinos ($\bar{\nu}_e$) from a nuclear reactor ($\bar{\nu_e} + p \to n + e^-$). Then in 1962, L. M. Lederman, M. Schwartz and J. Steinberger discovered the existence of more than one species of neutrinos [3] by detecting muon neutrinos (ν_μ) from pion decays at the Brookhaven's AGS (Alternating Gradient Synchrotron). The number of light neutrino species was determined to be three (2.984 ± 0.008 to be exact) by studying the decay of Z^0 produced in e^+e^-collisions at SLC (Stanford Linear Collider) and LEP (Large Electron Positron collider) [4]. The third species of neutrinos, tau neutrino (ν_τ), was directly detected by the DONUT (Direct Observation of the NU Tau) experiment at Tevatron in 2000 [5].

1.1.2 Neutrinos in the Standard Model

The Standard Model of particle physics was developed in the 1970s and has been providing an excellent description of almost all phenomena of particle physics over the past 40 years. By the discovery of the Higgs boson in 2012 [6, 7], the existence of all the elementary particles in the Standard Model was confirmed (Fig. 1.1). Neutrinos are included in the Standard Model and are assumed as follows:

- Neutrinos have exactly zero mass.
- There are exactly three neutrinos corresponding to the three charged leptons, and lepton number is conserved separately for each of the three lepton families (e, ν_e), (μ, ν_μ), (τ, ν_τ),

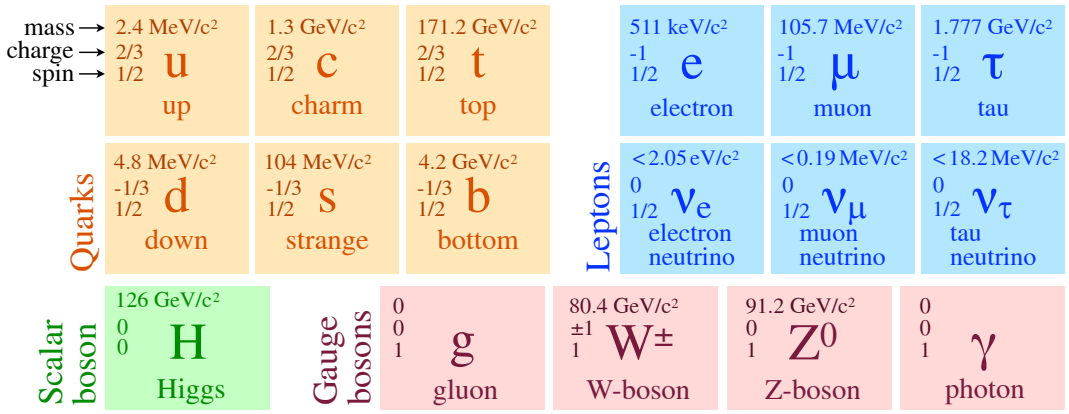

Figure 1.1: Elementary particles included in the Standard Model.

- Neutrinos and antineutrinos are distinct.
- All neutrinos are left-handed, and all antineutrinos are right-handed.

However, in 1998, the observation of the neutrino oscillation indicated a finite neutrino mass contrary to the assumption of the Standard Model. In addition, the Standard Model is unable to provide an explanation of the matter-antimatter asymmetry in the universe*. Neutrinos are believed to play an important role in the physics beyond the Standard Model.

1.2 Neutrino oscillations

1.2.1 Theory of neutrino oscillations

The idea of neutrino oscillation was first put forward in 1957 by B. Pontecorvo [9, 10], who proposed that neutrino-antineutrino transitions may occur in analogy with K^0 mixing [11]. Although such oscillation has not been observed, this idea formed the conceptual foundation of the neutrino oscillation. In 1962 (after the discovery of ν_μ), Z. Maki, M. Nakagawa, and S. Sakata proposed the neutrino flavor oscillation† [12]. The theory of the neutrino flavor oscillation is described succinctly below.

Neutrino oscillations in vacuum

When neutrinos have mass, their flavor eigenstates $|\nu_\alpha\rangle$ ($\alpha = e, \mu, \tau$) are generally expressed as superposition of the mass eigenstates $|\nu_i\rangle$ ($i = 1, 2, 3$):

$$|\nu_\alpha\rangle = \sum_i U_{\alpha i} |\nu_i\rangle, \tag{1.1}$$

where U is an element of a 3×3 unitary matrix that is referred to as the Pontecorvo-Maki-Nakagawa-Sakata (PMNS) matrix. The matrix is expressed using four independent parame-

*The Standard Model is also unable to describe the gravity, dark matter and dark energy, and has problems called the hierarchy problem and the strong CP problem [8].

†S. Tanaka, Y. Katayama, K. Matsumoto and E. Yamada also proposed the neutrino flavor oscillation around the same time [13].

ters:three mixing angles, θ_{12}, θ_{23}, θ_{13}, and one complex phase δ_{CP}:

$$\begin{aligned} U &= \begin{pmatrix} 1 & 0 & 0 \\ 0 & c_{23} & s_{23} \\ 0 & -s_{23} & c_{23} \end{pmatrix} \begin{pmatrix} c_{13} & 0 & s_{13}e^{-i\delta_{CP}} \\ 0 & 1 & 0 \\ -s_{13}e^{i\delta_{CP}} & 0 & c_{13} \end{pmatrix} \begin{pmatrix} c_{12} & s_{12} & 0 \\ -s_{12} & c_{12} & 0 \\ 0 & 0 & 1 \end{pmatrix} \\ &= \begin{pmatrix} c_{12}s_{13} & s_{12}c_{13} & s_{13}e^{-i\delta_{CP}} \\ -s_{12}c_{23} - c_{12}s_{13}s_{23}e^{i\delta_{CP}} & c_{12}c_{23} - s_{12}s_{13}s_{23}e^{i\delta_{CP}} & c_{13}s_{23} \\ s_{12}s_{23} - c_{12}s_{13}c_{23}e^{i\delta_{CP}} & c_{12}s_{23} - s_{12}s_{13}c_{23}e^{i\delta_{CP}} & c_{13}c_{23} \end{pmatrix}, \end{aligned} \tag{1.2}$$

where $c_{ij} = \cos\theta_{ij}$ and $s_{ij} = \sin\theta_{ij}$. In case of $\delta_{CP} \neq 0$, the PMNS matrix includes the imaginary parts, which causes the CP violation in the lepton sector. Hence, the δ_{CP} is called the CP phase. When a neutrino travels in vacuum, evolution of a mass eigenstate $|\nu_i\rangle$ after traveling time t is derived from Schrödinger equation:

$$i\frac{d}{dt}|\nu_i(t)\rangle = \mathcal{H}|\nu_i(t)\rangle = E_i|\nu_i(t)\rangle, \tag{1.3}$$

$$|\nu_i(t)\rangle = \exp(-iE_it)|\nu_i\rangle, \tag{1.4}$$

where $\mathcal{H}$ is the Hamiltonian, E_i is the energy of the mass eigenstate. Thus, the flavor eigenstate $|\nu_\alpha\rangle$ at time t is written as:

$$|\nu_\alpha(t)\rangle = \sum_i U_{\alpha i}\exp(-iE_it)|\nu_i\rangle. \tag{1.5}$$

Since neutrino masses are small, we can use the following approximation:

$$E_i = \sqrt{p^2 + m_i^2} \simeq p + \frac{m_i^2}{2p} \simeq p + \frac{m_i^2}{2E}, \tag{1.6}$$

where p and m_i are the momentum and mass of the mass eigenstate. With this approximation, Eq. 1.5 is written as:

$$|\nu_\alpha(t)\rangle = \sum_i U_{\alpha i}\exp(-ipt)\exp\left(-\frac{im_i^2t}{2E}\right)|\nu_i\rangle \tag{1.7}$$

$$= \sum_{i,\beta} U_{\alpha i}\exp(-ipt)\exp\left(-\frac{im_i^2t}{2E}\right)U^\dagger_{\beta i}|\nu_\beta\rangle. \tag{1.8}$$

The $\nu_\alpha \to \nu_\beta$ transition probability is calculated as:

$$\begin{aligned} P(\nu_\alpha \to \nu_\beta) &= |\langle\nu_\beta|\nu_\alpha(t)\rangle|^2 \\ &= \left|\sum_{i,\beta} U_{\alpha i}\exp(-ipt)\exp\left(-\frac{im_i^2t}{2E}\right)U^\dagger_{\beta i}\right|^2 \\ &= \sum_{i,j} U^\dagger_{\alpha i}U_{\beta i}U_{\alpha j}U^\dagger_{\beta j}\exp\left(-\frac{i(m_i^2 - m_j^2)t}{2E}\right) \\ &= \sum_{i,j} U^\dagger_{\alpha i}U_{\beta i}U_{\alpha j}U^\dagger_{\beta j}\exp\left(-\frac{i\Delta m_{ij}^2 L}{2E}\right) \\ &= \delta_{\alpha\beta} - 4\sum_{i>j}\mathrm{Re}(U^\dagger_{\alpha i}U_{\beta i}U_{\alpha j}U^\dagger_{\beta j})\sin^2\left(\frac{\Delta m_{ij}^2 L}{4E}\right) \\ &+ 2\sum_{i>j}\mathrm{Im}(U^\dagger_{\alpha i}U_{\beta i}U_{\alpha j}U^\dagger_{\beta j})\sin\left(\frac{\Delta m_{ij}^2 L}{2E}\right), \end{aligned} \tag{1.9}$$

where $\Delta m^2_{ij} \equiv m^2_i - m^2_j$ is a mass-squared difference, time t was replaced with the travel distance $L(= ct)$ since neutrinos are relativistic and the unitarity condition ($\sum_i U^\dagger_{\alpha i} U_{\beta i} = \delta_{\alpha\beta}$) was used. Equation 1.9 points that the neutrino oscillation occurs only when at least two neutrinos are not degenerate in mass ($m_i \neq m_j$) and the lepton mixing takes place ($U \neq I$). It also points that the neutrino oscillations in vacuum are parametrized by three mixing angles θ_{12}, θ_{23} and θ_{13}, two mass-squared differences Δm^2_{21} and Δm^2_{32} (since $\Delta m^2_{21} + \Delta m^2_{32} + \Delta m^2_{13} = 0$) and a CP phase δ_{CP}. From the experimental data described in Sec. 1.2.4, we know $|\Delta m^2_{32}| \simeq |\Delta m^2_{31}| \gg \Delta m^2_{21}$. Therefore, for $E/L \gg \Delta m^2_{21}$, the effect on the neutrino oscillation due to Δm^2_{21} can be disregarded and oscillation probabilities can be approximately described by two mixing angles (θ_{13}, θ_{23}):

$$P(\nu_\mu \to \nu_e) \simeq \sin^2 2\theta_{13} \sin^2 \theta_{23} \sin^2\left(\frac{\Delta m^2_{32} L}{4E}\right), \tag{1.10}$$

$$P(\nu_\mu \to \nu_\mu) \simeq 1 - \left(\cos^4 \theta_{13} \sin^2 2\theta_{23} + \sin^2 2\theta_{13} \sin^2 \theta_{23}\right) \sin^2\left(\frac{\Delta m^2_{32} L}{4E}\right), \tag{1.11}$$

The $\nu_\mu \to \nu_\mu$ survival probabilities in Eq. 1.11 for several values of Δm^2_{32} and $\sin^2 2\theta_{23}$ are shown in Fig. 1.2.

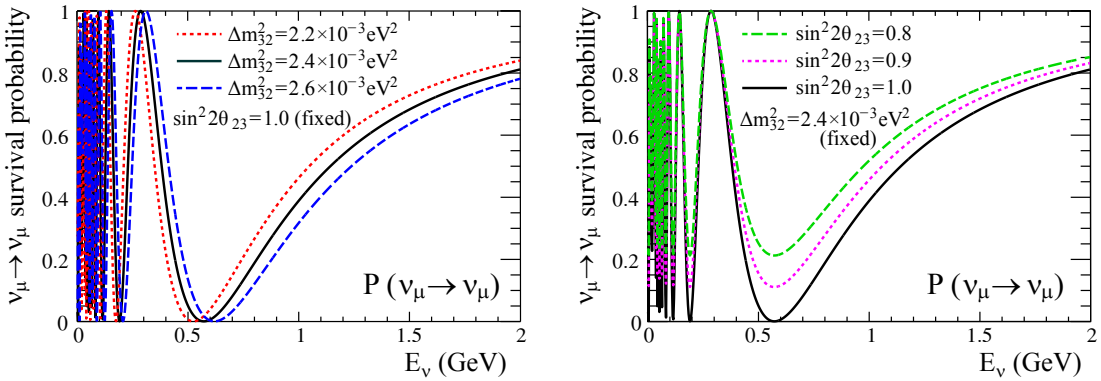

Figure 1.2: Probabilities of $\nu_\mu \to \nu_\mu$ survival for several values of Δm^2_{32} (left) and $\sin^2 2\theta_{23}$ (right) when the travel distance (L) is fixed to 295km.

Neutrino oscillations in matter

When neutrinos travel through matter (*e.g.* the sun, the earth or a supernova), their propagation can be affected by coherent forward-scatterings between the neutrinos and the matter [14]. All flavors of neutrinos have neutral current interactions with electrons and nucleons in the matter, while only electron neutrinos have charged current interactions with electrons in the matter. Therefore, electron neutrinos feel the extra potential in the matter, and the probability of neutrino oscillations in matter can be rather different from that in vacuum. This effect is known as the matter effect [15–17]. The matter effect is taken into account by adding an extra potential V in the Schrödinger equation:

$$i\frac{d}{dt}|\nu_\alpha(t)\rangle = (\mathcal{H}_{\rm vac} + V)|\nu_\alpha(t)\rangle, \tag{1.12}$$

$$V = \begin{pmatrix} \sqrt{2} G_F n_e & 0 & 0 \\ 0 & 0 & 0 \\ 0 & 0 & 0 \end{pmatrix}, \tag{1.13}$$

where $\mathcal{H}_{\rm vac}$ is the Hamiltonian in case of vacuum, G_F is the Fermi constant and n_e is the electron density in the matter. The sign of the extra potential is reversed for the antineutrino.

1.2.2 Solar neutrino problem

In the sun, electron neutrinos (ν_e) are produced by the fusion reactions in the pp chain or CNO (carbon-nitrogen-oxygen) cycle [18, 19]. These neutrinos are called solar neutrinos. The solar neutrinos are first detected by R. Davis's Homestake experiment in 1968 [20] by using the radiochemical method [21] ($\nu_e + {}^{37}\mathrm{Cl} \to e^- + {}^{37}\mathrm{Al}$). However, the Homestake experiment observed only about 1/3 of neutrinos predicted by the Standard Solar Models (SSM) [22–24]. This deficit of the solar neutrino flux was called "the solar neutrino problem". In 1989, the Kamiokande experiment confirmed that the number of observed solar neutrino events was significantly less than the prediction by the SSM in real-time measurement using a large water Cherenkov detector [25] ($\nu_e + e^- \to \nu_e + e^-$). Other experiments also observed the deficit: GALLEX [26, 27], GNO [28] and SAGE [29] utilizing another radiochemical method with Gallium ($\nu_e + {}^{71}\mathrm{Ga} \to e^- + {}^{71}\mathrm{Ge}$), and the Super-Kamiokande experiment (Super-K) with a larger water Cherenkov detector [30]. At that time, many physicists attempted to explain the deficit by proposing that the SSM were wrong and did not reach the conclusion that the deficit is caused by the neutrino oscillation.

1.2.3 Discovery of neutrino oscillations

Neutrinos are also naturally produced as decay products of hadrons generated in collisions of cosmic rays with nuclei in the atmosphere [31] ($\pi^+ \to \mu^+ + \nu_\mu$ and subsequent $\mu^+ \to e^+ + \bar{\nu}_\mu + \nu_e$). These neutrinos are called atmospheric neutrinos. In these decay processes, the ratio of $\nu_\mu + \bar{\nu}_\mu$ to $\nu_e + \bar{\nu}_e$ is expected to be two. The Kamiokande experiment observed a deficit of the atmospheric muon neutrinos and mentioned the deficit might be due to the neutrino oscillation [32]. The evidence of the neutrino oscillation was first reported in 1998 by Super-K by measuring the atmospheric muon neutrino deficit with much higher statistics [33]. Then, the solar neutrino problem was understood as due to the neutrino oscillation. The first direct evidence for the solar neutrino oscillation came in 2001 from the SNO (Sudbury Neutrino Observatory) experiment [34] combined with the Super-K solar neutrino deficit result [35]. SNO detected all flavors of neutrinos coming from the sun, and the total number of detected neutrinos agrees quite well with the prediction by the SSM. This result led physicists to the definite conclusion that the deficit of the electron neutrinos from the sun was caused by the neutrino oscillation.

1.2.4 Measurements of neutrino oscillation parameters

Not only the naturally-produced neutrinos (atmospheric and solar neutrinos) but also artificially-produced neutrinos (reactor and accelerator neutrinos) have been utilized for the measurement of neutrino oscillations. Reactor neutrinos are anti-electron neutrinos generated in the β decay of neutron-rich daughter fragments in the fission process in nuclear reactors. Accelerator neutrinos are produced as decay products of charged pions or kaons generated by slamming the accelerated protons into a fixed production target. These neutrino sources are summarized in Table 1.1 with the typical average neutrino energy ($\bar{E}$) and the typical distance between source and detector (L). The sensitivity to oscillation parameters, $\sin^2 2\theta$ and Δm^2, depends on the value of $\bar{E}/L$. Measured parameters from PDG(Particle Data Group)2013 [36] are summarized in Table 1.2.

Measurements of θ_{12} and Δm^2_{21}

θ_{12} and Δm^2_{21} have been measured by solar neutrino and long-baseline reactor neutrino experiments. The disappearance of electron neutrinos from the sun has been measured by several experiments (R. Davis*et al.* [20], Super-K [37], SNO [38], Borexino [39] and so on). These results were confirmed by KamLAND [40] via the disappearance of anti-electron neutrinos from reactors in long baseline on an assumption of the CPT invariance. Combined best fit values are $\Delta m^2_{12} = (7.50 \pm 0.20) \times 10^{-5}\mathrm{eV}^2$ and $\sin^2 2\theta_{12} = 0.857 \pm 0.024$.

Table 1.1: Characteristics of several neutrino oscillation experiments. $\bar{E}$ is the typical average neutrino energy, L is the distance between source and detector, and corresponding $\Delta m^2 \sim \bar{E}/L$ which is a sensitive Δm^2 roughly.

Source	Flavor	$\bar{E}$ (MeV)	L (km)	Δm^2 (eV^2)
Reactor (short or long baseline)	$\bar{\nu_e}$	~ 1	$\sim$1 or $\sim$100	$\sim 10^{-3}$ or $\sim 10^{-5}$
Accelerator (short or long baseline)	$\nu_{\mu,e}$, $\bar{\nu}_{\mu,e}$	$\sim 10^3$	$\sim$1 or $\sim 10^3$	~ 1 or $\sim 10^{-3}$
Atmospheric	$\nu_{\mu,e}$, $\bar{\nu}_{\mu,e}$	$\sim 10^3$	$\sim 10^4$	$\sim 10^{-4}$
Solar	ν_e	~ 1	1.5×10^8	$\sim 10^{-11}$

Table 1.2: Best fit values of the oscillation parameters from PDG2013.

Parameter	Best fit value
Δm^2_{12}	$(7.50 \pm 0.20) \times 10^{-5}\text{eV}^2$
$\lvert\Delta m^2_{32}\rvert$	$(2.32^{+0.12}_{-0.08}) \times 10^{-3}\text{eV}^2$
$\sin^2 2\theta_{12}$	0.857 ± 0.024
$\sin^2 2\theta_{23}$	> 0.95
$\sin^2 2\theta_{13}$	0.095 ± 0.010

Measurements of θ_{23} and $|\Delta m^2_{32}|$

θ_{23} and $|\Delta m^2_{32}|$ have been measured by atmospheric neutrino and long-baseline accelerator neutrino experiments. The disappearance of atmospheric muon neutrinos has been measured by Super-K [33, 41]. This result was confirmed by long-baseline accelerator neutrino experiments (K2K [42], MINOS [43]) via the disappearance of artificial muon neutrinos. Combined best fit values are $|\Delta m^2_{32}| = (2.32^{+0.12}_{-0.08}) \times 10^{-3}\text{eV}^2$ and $\sin^2 2\theta_{23} > 0.95$.

Measurements of θ_{13}

θ_{13} has been measured by short-baseline reactor neutrino and long-baseline accelerator neutrino experiments. However, only the upper limit on θ_{13} had been given until 2011 [44–46]. The non-zero θ_{13} was first reported by T2K via the appearance of electron neutrinos from muon neutrino beam in 2011 [47] and then measured by Daya Bay via the disappearance of anti-electron neutrinos from reactors in short baseline in 2012 [48]. Currently, θ_{13} was very precisely measured by reactor neutrino experiments (Daya Bay [49], RENO [50] and Double Chooz [51]) as $\sin^2 2\theta_{13} = 0.095 \pm 0.010$[‡].

1.3 Unresolved questions in neutrino physics

The last mixing angle, θ_{13}, was finally determined in 2012. However, there are still many questions in neutrino physics that have not been resolved yet.

Neutrino mixing scheme

From parameters in Table 1.2, the PMNS matrix is calculated as:

$$U = \begin{pmatrix} 0.82 \pm 0.01 & 0.55^{+0.02}_{-0.01} & 0.16 \pm 0.01 \\ -0.51^{+0.01}_{-0} & 0.57^{+0.03}_{-0.06} & 0.64^{+0.06}_{-0.02} \\ 0.26^{+0.05}_{-0.02} & -0.61^{+0.02}_{-0.04} & 0.75^{+0.02}_{-0.06} \end{pmatrix}, \tag{1.14}$$

[‡]Most recently, the Daya Bay experiment reported the latest result as $\sin^2 2\theta_{13} = 0.084 \pm 0.005$ [52]. However, it is not used in this thesis because it is a preliminary result.

The mixing in quarks is described in the same way by using a 3×3 unitary matrix, called the Cabibo-Kobayashi-Maskawa (CKM) matrix [53, 54]. The CKM matrix is measured to be

$$V = \begin{pmatrix} 0.97427 \pm 0.00015 & 0.22534 \pm 0.00065 & 0.00351^{+0.00015}_{-0.00014} \\ 0.22520 \pm 0.00065 & 0.97344 \pm 0.00016 & 0.0412^{+0.0011}_{-0.0005} \\ 0.00867^{+0.0029}_{-0.0031} & 0.0404^{+0.0011}_{-0.0005} & 0.999146^{+0.00021}_{0.000046} \end{pmatrix}, \tag{1.15}$$

The elements of the PMNS matrix are very different from those in the CKM matrix. To explain the feature of the PMNS matrix, many models have been proposed. Among them, the so-called tri-bimaximal model [55] is one of the famous approaches to explain the neutrino mixing scheme. In this model, the PMNS matrix was predicted as

$$U = \begin{pmatrix} \sqrt{\frac{2}{3}} & \sqrt{\frac{1}{3}} & 0 \\ -\sqrt{\frac{1}{6}} & \sqrt{\frac{1}{3}} & \sqrt{\frac{1}{2}} \\ \sqrt{\frac{1}{6}} & -\sqrt{\frac{1}{3}} & \sqrt{\frac{1}{2}} \end{pmatrix} = \begin{pmatrix} 0.816 & 0.577 & 0 \\ -0.408 & 0.577 & 0.707 \\ 0.408 & -0.577 & 0.707 \end{pmatrix}. \tag{1.16}$$

However, the right top element that is zero in the tri-bimaximal model was found to be non-zero by the recent θ_{13} measurement. Therefore, the exact tri-bimaximal model was already ruled out. However, there are some approaches to view the tri-bimaximal model as a leading order only, and to apply corrections to it [56]. The other famous model is called the anarchy model [57], which assumes no structure and no symmetry in the neutrino mixing scheme. This model suggests that the mixing matrix is defined as a result of a random drawing from an unbiased distribution of unitary 3×3 matrices. One of the most interesting topics of the neutrino mixing scheme is whether θ_{23} is maximal mixing. From the past measurements, θ_{23} was found to be close to $\pi/4$, *i.e.* maximal mixing. However, we don't know whether θ_{23} is smaller than, equal to or larger than $\pi/4$. The tri-bimaximal model claims θ_{23} is exactly equal to $\pi/4$, while the anarchy model claims it isn't. If θ_{23} is precisely determined, it can constrain some models of neutrino mass generation [58–63]. To proceed further discussion of the neutrino mixing scheme, more precise measurements of the mixing angles are necessary.

CP violation in the lepton sector

A solution to the matter-antimatter asymmetry in the universe requires CP violation in the early universe[§] [64]. The evidences of the CP violation have been found in the quark sector [65–67], and they are consistent with the predictions of the Kobayashi-Maskawa mechanism [54] of the Standard Model. Nevertheless, it is too small to describe the observed matter-antimatter asymmetry [68, 69]. Consequently, additional sources of the CP violation beyond the Standard Model are required. The neutrino CP phase, δ_{CP}, will be the key to understanding the origin of the matter-antimatter asymmetry[¶] because it introduces the CP violation in the lepton sector. However, the size of δ_{CP} has been totally unknown. In the three-flavor mixing including the first order of the matter effect, the probability of $\nu_\mu \to \nu_e$ oscillation is written as:

[§]In addition to the CP violation, the baryon number violation and interactions out of thermal equilibrium are required (so-called Sakharov conditions [64]).

[¶]Some physicists consider that the matter-antimatter asymmetry arises from decays of right-handed heavy neutrinos (so-called leptogenesis [70]).

$$
\begin{aligned}
P(\nu_\mu \to \nu_e) &= 4c_{13}^2 s_{13}^2 s_{23}^2 \cdot \sin^2 \Phi_{31} \\
&+ 8c_{13}^2 s_{12} s_{13} s_{23} (c_{12} c_{23} \cos\delta_{CP} - s_{12} s_{13} s_{23}) \cdot \cos\Phi_{32} \sin\Phi_{31} \sin\Phi_{21} \\
&- 8c_{13}^2 c_{12} c_{23} s_{12} s_{13} s_{23} \sin\delta_{CP} \cdot \sin\Phi_{32} \sin\Phi_{31} \sin\Phi_{21} \\
&+ 4s_{12}^2 c_{13}^2 (c_{12}^2 c_{23}^2 + s_{12}^2 s_{23}^2 s_{13}^2 - 2c_{12} c_{23} s_{12} s_{13} \cos\delta_{CP}) \cdot \sin^2 \Phi_{21} \\
&- 8c_{13}^2 c_{13}^2 s_{23}^2 \cdot \frac{aL}{4E_\nu} (1 - 2s_{13}^2) \cdot \cos\Phi_{32} \sin\Phi_{31} \\
&+ 8c_{13}^2 s_{13}^2 s_{23}^2 \frac{a}{\Delta m_{31}^2} (1 - 2s_{13}^2) \cdot \sin^2 \Phi_{31}, \qquad (1.17) \\
\Phi_{ij} &\equiv \frac{\Delta m_{ij}^2 L}{4E} \simeq 1.2669 \cdot \Delta m_{ij}^2 (\mathrm{eV}^2) \cdot \frac{L(\mathrm{km})}{E(\mathrm{GeV})}, \qquad (1.18) \\
a &\equiv 2\sqrt{2} G_F n_e E_\nu = 7.56 \times 10^{-5} \times \rho(\mathrm{g/cm}^3) \times E_\nu, \qquad (1.19)
\end{aligned}
$$

where ρ is the mass density of the Earth, and a represents the factor associated with the matter effect. $P(\bar{\nu}_\mu \to \bar{\nu}_e)$ is derived by replacing $\delta \to -\delta$ and $a \to -a$. The first term, which is equivalent to Eq. 1.10, is the probability of the $\nu_\mu \to \nu_e$ oscillation in the quasi-two-neutrino oscillation (called the leading term). The second term which contains $\cos\delta_{CP}$ is called the CP conserving term, while the third term which contains $\sin\delta_{CP}$ is called the CP violating term. The fourth term which contains s_{12}^2 is called the solar term. The last two terms represent the corrections from the matter effect. Figure 1.3 shows $P(\nu_\mu \to \nu_e)$ and $P(\bar{\nu}_\mu \to \bar{\nu}_e)$ as a function of the neutrino energy when $\delta_{CP} = \pi/2$. The CP violating term flips its sign between ν and $\bar{\nu}$, and its amplitude depends on the all mixing angles and δ_{CP}. By contrast, other terms except for the matter terms are invariant between ν and $\bar{\nu}$. Therefore, the comparison of $P(\nu_\mu \to \nu_e)$ and $P(\bar{\nu}_\mu \to \bar{\nu}_e)$ is one of the most promising methods to measure δ_{CP}.

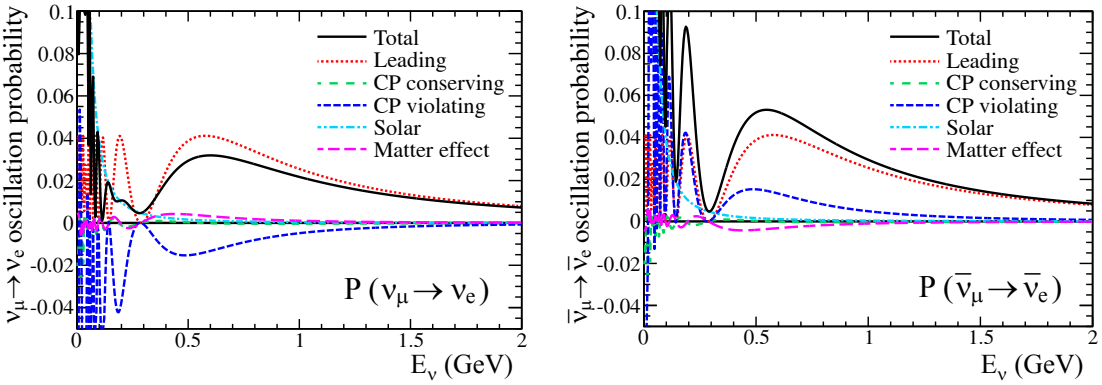

Figure 1.3: Probabilities of $\nu_\mu \to \nu_e$ oscillation (left) and $\bar{\nu}_\mu \to \bar{\nu}_e$ oscillation (right) as a function of the neutrino energy with a baseline of 295km. The CP phase δ_{CP} is set to $\pi/2$ and the other oscillation parameters are set to the best fit values shown in Table 1.2.

Mass hierarchy

In the atmospheric neutrino oscillation, the oscillation probability in the leading order does not depend on the sign of Δm_{32}^2. Therefore, there are two possible types of the neutrino mass hierarchy as illustrated in Fig. 1.4: the normal hierarchy (NH: $\Delta m_{32}^2 > 0$, $\Delta m_{31}^2 > 0$) and the inverted hierarchy (IH: $\Delta m_{32}^2 < 0$, $\Delta m_{31}^2 < 0$). The magnitude of the matter effect in Eq. 1.17 depends on the sign of Δm_{31}^2. Thus, in neutrino oscillation experiments, the matter effect may lead us to determine the hierarchy. Although the Super-K atmospheric

neutrino data slightly favors the normal hierarchy [71], it is marginal to draw a conclusion. Among the accelerator neutrino experiments, the NOνA experiment [72] (L =810km) is more sensitive to the mass hierarchy than T2K (L =295km) because the baseline is longer and the matter effect is more significant.

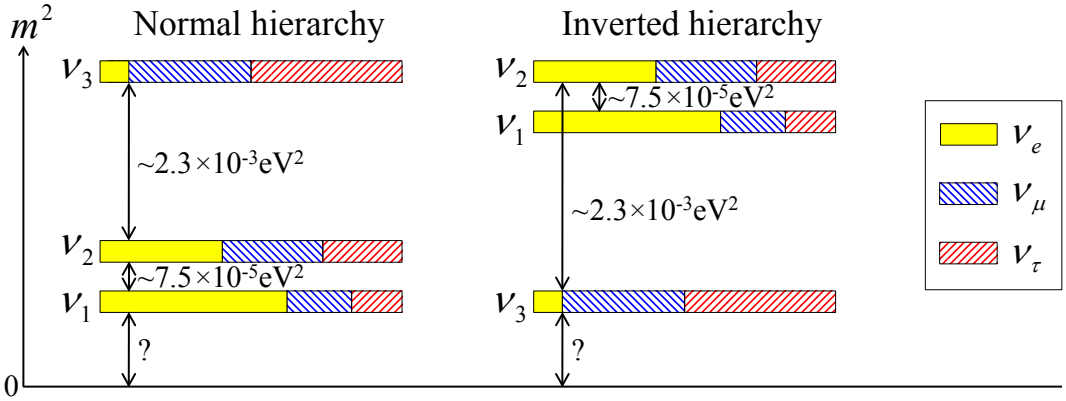

Figure 1.4: Two possible types of the neutrino mass hierarchy.

Absolute mass of neutrinos

Although the mass differences were measured in neutrino oscillation experiments, the absolute masses have never been measured yet. The upper limits for neutrino masses are summarized in Table 1.3. Precise determination of the neutrino mass is important not only for particle physics but also for cosmology because it has implications for the large-scale structure of the universe, ultra-high-energy cosmic ray and supernova dynamics. Hence, there are several experiments (KATRIN [78], MARE [79], Project8 [80] and so on) to measure the neutrino mass directly.

Table 1.3: Upper limits for neutrino masses.

Neutrino type	Mass upper limit	Measurement method	Reference
$\bar{\nu}_e$	2.05 eV	Tritium beta decay	[73, 74]
ν_μ	0.19 MeV	π decay at rest	[75]
ν_τ	18.2 MeV	τ decay	[76]
Sum of three types	0.23 eV	Cosmic microwave background	[77]

Existence of sterile neutrinos

The number of light neutrino species was determined to be three by studying the decay of Z^0 [4]. However, there could be additional neutrino species which do not interact via weak interaction [81–83]. Such hypothetical neutrinos are referred to as "sterile neutrino". The LSND experiment claimed $\bar{\nu}_\mu \to \bar{\nu}_e$ oscillations at higher Δm^2 regions than the atmospheric or solar oscillation scale [84]. Although this signal cannot be explained in the three-flavor neutrino oscillation framework, it can be interpreted as the neutrino oscillation through the sterile neutrino ($\bar{\nu}_\mu \to \bar{\nu}_s \to \bar{\nu}_e$). Some other experiments also indicated the existence of sterile neutrino [85–87], whereas there are also some experiments which showed negative indications [88–91]. However, there is no viable oscillation scheme consistent with all the experimental results [92–94]. Consequently, the existence of the sterile neutrino is still unknown. If it actually exists, it is a possible candidate of the dark matter [95, 96].

Majorana fermion or Dirac fermion

Fermions which are identical to their own antiparticles are referred to as the Majorana fermions [97], whereas those different from their own antiparticles are referred to as the Dirac fermions. Charged fermions are Dirac fermions because of the electric charge conservation. Since neutrinos do not have quantum numbers except for the lepton number, they can be either Dirac fermions or Majorana fermions. Dirac and Majorana mass effects are distinguishable in the search of the neutrinoless double-beta decay (Fig. 1.5) because this process is allowed only when neutrinos are the Majorana fermions. It is being searched for by many experiments such as CUORICINO [98], GERDA [99], EXO-200 [100], KamLAND-Zen [101] and so on.

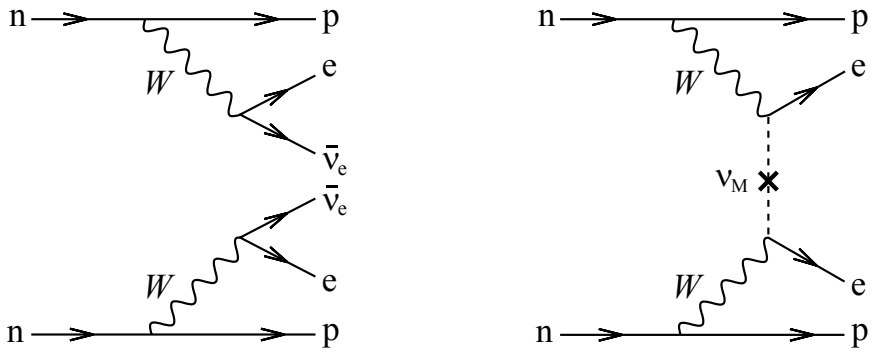

Figure 1.5: Feynman diagrams of two-neutrino double-beta decay (left) and neutrinoless double-beta decay (right). If neutrinos are the Majorana fermions, the same neutrino can be emitted and absorbed within the nucleus in the double-beta decay.

1.4 Neutrino interactions

1.4.1 Weak interactions

The weak interaction is one of the four fundamental forces of nature alongside the gravitational, electromagnetic and strong interactions. The only interactions available to neutrinos are the weak interactions (and the gravitational interactions) because the neutrinos are electrically-neutral and uncolored particles. Above the unification energy, of the order of 100 GeV, electromagnetism and the weak interaction merge in a single interaction called the electroweak interaction [102, 103], which is mediated by four massless bosons: $W^{0,\pm}$, B^0. In the Standard Model, the $W^{\pm}$, Z^0, and the photon are produced by the spontaneous symmetry breaking[‖] of the electroweak symmetry $SU(2) \times U(1)$, where W^0 and B^0 coalesce into two different bosons. The charged bosons $W^{\pm}$ mediate the charged current interaction (CC) and the neutral vector bosons Z^0 mediate the neutral current interaction (NC) as shown in Fig. 1.6. The charged and neutral currents can be expressed as:

$$j_\mu^{\pm} = \bar{u}\frac{-ig_W}{2\sqrt{2}}\gamma^\mu(1-\gamma^5)u, \tag{1.20}$$

$$j_\mu^{0} = \bar{u}\frac{-ig_Z}{2}\gamma^\mu(g_V - g_A\gamma^5)u, \tag{1.21}$$

where u and $\bar{u}$ are Dirac spinors, γ^μ are the four Dirac gamma matrices, $\gamma^5 = i\gamma^0\gamma^1\gamma^2\gamma^3$, g_W and g_Z are coupling-strengths, and g_V and g_A are vector and axial-vector coupling constants. The

[‖] In spontaneous symmetry breaking, the bosons acquire a non-vanishing mass through the absorption of Nambu-Goldstone bosons [104, 105]. This process is known as the Higgs mechanism [106].

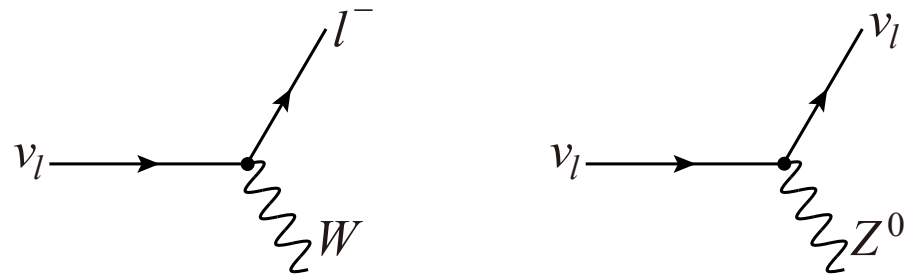

Figure 1.6: Feynman diagrams of neutrino interaction vertices in the case of charged current interactions (left) and neutral current interactions (right).

Standard Model relates the coupling strengths of the two interactions using the weak mixing angle (so-called the Weinberg angle) as:

$$\frac{g_W}{g_Z} = \cos\theta_W, \tag{1.22}$$

The weak mixing angle was empirically measured: $\theta_W = 2.87°$ [36]. It also determines the values of the vector and axial-vector couplings in the NC vertex factor, which are particle dependent, as shown in Table 1.4. The Dirac spinors are composed of both left-handed and right-handed chiral components:

$$u = u_L + u_R, \tag{1.23}$$

which can be separated out using the chiral projection operators:

$$u_L = \frac{1}{2}(1-\gamma^5)u, \quad u_R = \frac{1}{2}(1+\gamma^5)u, \tag{1.24}$$

We can re-write Eq.1.20 using some gamma-matrix algebra** as:

$$j_\mu^\pm = \frac{-ig_W}{4\sqrt{2}}\bar{u}(1+\gamma^5)\gamma^\mu(1-\gamma^5)u = \frac{-ig_W}{4\sqrt{2}}\bar{u}_L\gamma^\mu u_L, \tag{1.25}$$

In this form, CC weak interactions can be viewed as a purely vector current interacting only with the left-handed chiral component of a particle. The analogous form of NC interactions leads to the same conclusion in the case of neutrinos. Consequently, neutrinos are always created in a left-handed chiral eigenstate.

Table 1.4: Weak NC vector and axial-vector vertex factors.

Particle	g_V	g_A
Neutrinos (ν_e, ν_μ, ν_τ)	$\frac{1}{2}$	$\frac{1}{2}$
Charged leptons (e, μ, τ)	$\frac{1}{2} + 2\sin^2\theta_W$	$-\frac{1}{2}$
Up-type quarks (u, c, t)	$\frac{1}{2} + \frac{4}{3}\sin^2\theta_W$	$\frac{1}{2}$
Down-type quarks (d, s, b)	$-\frac{1}{2} + \frac{2}{3}\sin^2\theta_W$	$-\frac{1}{2}$

1.4.2 Neutrino-nucleus interactions

In the long-baseline neutrino oscillation experiments, neutrinos are detected via neutrino-nucleus interactions because these interactions are predominant in the neutrino energy region of a few GeV. In such energy range, a neutrino interacts with a nucleon in the nucleus (or entire nucleus) in the following processes via charged current (CC) and neutral current (NC).

** $(\gamma^0)^2 = 1$, $(\gamma^j)^2 = -1$ $(j \neq 0)$, $\gamma^\mu\gamma^\nu = -\gamma^\nu\gamma^\mu$ $(\mu \neq \nu)$.

Quasi-elastic scattering

The dominant neutrino interaction in the low energy region (∼1 GeV) is a two body (quasi) elastic scattering with a nucleon. There exist a charged current quasi-elastic (CCQE) scattering and a neutral current elastic scattering:

$$\nu_l + n \rightarrow l^- + p, \tag{1.26}$$
$$\nu_l + N \rightarrow \nu_l + N, \tag{1.27}$$

where l^- is the charged lepton (e^-, μ^- or τ^-) and N is the nucleon (proton or neutron).

Single resonant meson production via baryon resonances

Neutrino can excite baryon resonances via the neutrino-nucleus interaction and the resonant state is followed by its prompt decay into a nucleon and a meson in the final state:

$$\nu_l + N \rightarrow l^- + N^* \rightarrow l^- + N' + m, \tag{1.28}$$
$$\nu_l + N \rightarrow \nu_l + N^* \rightarrow \nu_l + N' + m, \tag{1.29}$$

where N^* is an intermediate baryon resonance and m is the meson. In a few GeV region, the intermediate state is dominated by the $\Delta(1232)$ resonance, which mainly decays into a nucleon and a pion:

$$\nu_l + N \rightarrow l^- + \Delta \rightarrow l^- + N' + \pi, \tag{1.30}$$
$$\nu_l + N \rightarrow \nu_l + \Delta \rightarrow \nu_l + N' + \pi. \tag{1.31}$$

They are generally referred to as CC1π and NC1π interactions. However, a variety of other final states can exist depending on the resonances and can produce multiple mesons or a radiative photon.

Coherent pion production

In addition to the resonant pion production, the neutrino can produce a pion by interacting coherently with an entire nucleus that remains unchanged in its ground state after interaction. From a microscopic perspective, the momentum transfer from the incoming neutrino virtually excites the nucleus (particle-hole and Δ-hole excitations [107–109]), and the nucleus decays back to its ground state by emitting a pion. The momentum transfer to the nucleus is kept small in this process because no nuclear breakup occurs. As a result, the outgoing lepton and pion tend to go in approximately the same direction as the incoming neutrino. Both charged current (CC) and neutral current (NC) coherent pion productions are possible:

$$\nu_l + A \rightarrow l^- + A + \pi^+, \tag{1.32}$$
$$\nu_l + A \rightarrow \nu_l + A + \pi^0, \tag{1.33}$$

where A is a nucleus.

Deep inelastic scattering

The neutrino interaction in the high energy region (>5 GeV) is dominated by the deep inelastic scattering (DIS) in which neutrinos scatters directly off the quarks inside the nucleon, including the sea quarks. It is characterized by a high momentum transfer, so the nucleon tends to break up containing the struck quark. The struck quark scatters the nucleon fragments, and the strong force between the quarks results in hadronization:

$$\nu_l + N \rightarrow l^- + N' + \text{hadrons}, \tag{1.34}$$
$$\nu_l + N \rightarrow \nu_l + N' + \text{hadrons}. \tag{1.35}$$

Figure 1.7 shows Feynman diagrams of the neutrino interaction processes of Eq. 1.26, 1.30, 1.32 and 1.34. Theoretical models describing these neutrino interaction processes will be introduced in Chapter 4. There are only a few of neutrino-nucleus cross section measurements in the few-GeV neutrino energy range, and their precision is limited by small statistics and large systematic uncertainty of the neutrino flux. Hence, the neutrino-nucleus interaction is poorly understood, and models have large uncertainties and many inconsistencies with experimental data. They cause large systematic errors on the neutrino oscillation measurement. Therefore, precise and reliable measurements of neutrino-nucleus interactions in the few-GeV neutrino energy range have been desired. It is important not only for the neutrino physics but also for the nuclear physics because the neutrino-nucleus interaction incorporates rich information on nuclear structure and interactions [110].

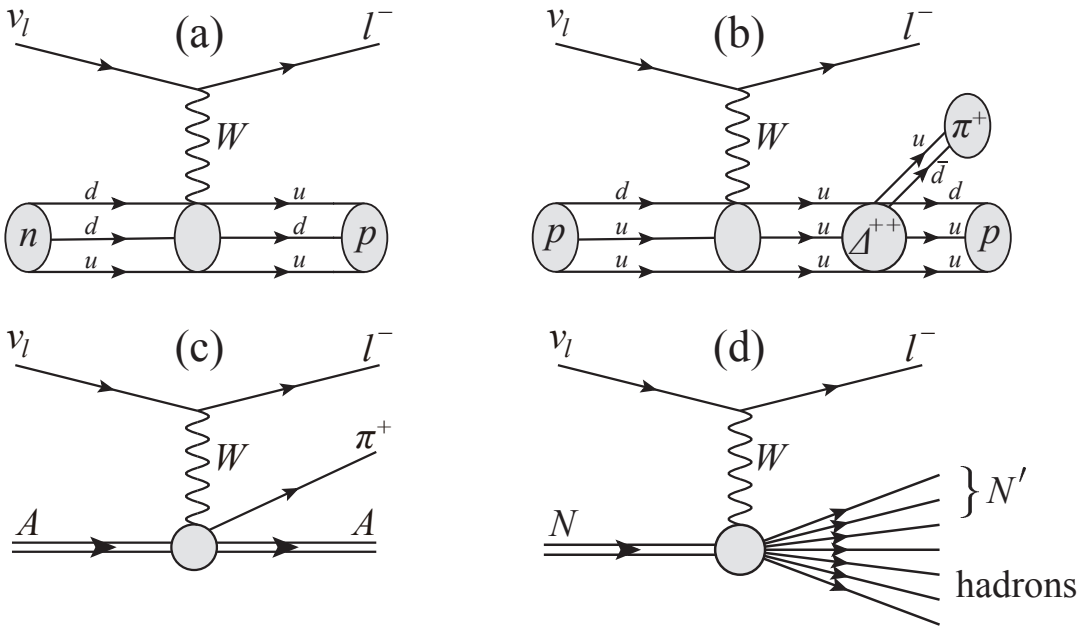

Figure 1.7: Feynman diagrams of (a) quasi-elastic scattering, (b) single resonant pion production, (c) coherent pion production and (d) deep inelastic scattering via charged current. (b) is an example of the single resonant pion production via charged current (Eq. 1.30), and there are two other varieties ($\nu_l + n \to l^- + \Delta^+ \to l^- + p + \pi^0$ and $\nu_l + n \to l^- + \Delta^+ \to l^- + n + \pi^+$).

1.5 Introduction to the T2K experiment

1.5.1 Overview

The T2K (Tokai to Kamioka) experiment is a long-baseline accelerator neutrino experiment started in 2009 [111]. The overview of T2K is illustrated in Fig. 1.8. An almost-pure intense muon neutrino beam is produced at J-PARC (Japan Proton Accelerator Research Complex) in Tokai. The neutrinos are measured by near detectors in the J-PARC site and a far detector, Super-Kamiokande (Super-K), in Kamioka located 295km away from J-PARC.

1.5.2 Physics goals

The main goal of T2K is the precise measurement of the neutrino oscillations. Following two neutrino oscillation modes are measurable in T2K.

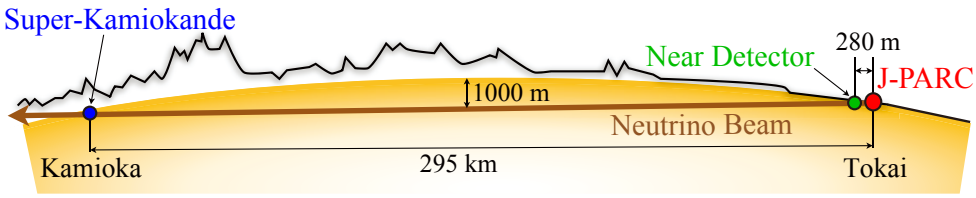

Figure 1.8: Overview of the T2K experiment.

Discovery of $\nu_\mu \to \nu_e$ oscillation

The original primary goal of T2K was the world's first finite θ_{13} measurement with a discovery of the $\nu_\mu \to \nu_e$ oscillation (Eq. 1.17). Although θ_{13} was precisely measured via the disappearance of anti-electron neutrinos from reactors, it is still important to confirm the result via the $\nu_\mu \to \nu_e$ oscillation. Furthermore, we can approach the δ_{CP} measurement by the combination of the T2K $\nu_\mu \to \nu_e$ result with the reactor θ_{13} measurement result.

Precise measurement of $\nu_\mu \to \nu_\mu$ oscillation

T2K also aims to measure θ_{23} and Δm^2_{32} precisely via the muon neutrino disappearance (Eq. 1.11). Currently, uncertainty of θ_{23} is the largest among the three mixing angles. Since θ_{23} is involved in the leading term and the CP violating term of the $\nu_\mu \to \nu_e$ oscillation probability formula (Eq. 1.17), precise measurement of θ_{23} is important not only for the understanding of the neutrino mixing scheme, but also for the measurement of δ_{CP} via the $\nu_\mu \to \nu_e$ oscillation.

So far, the analyses of these two measurements had been performed independently [47,112–116]. This thesis presents the first joint analysis of them. In addition, T2K has an accessory goal of measuring the neutrino-nucleus interactions in a few GeV region. It is important not only for the precise measurement of the neutrino oscillations but also for the resolution of the many questions in the neutrino interaction physics. This thesis also presents the measurements of the neutrino-nucleus interactions in T2K.

1.5.3 Experimental principle

Fundamental principle of the neutrino oscillation measurement in T2K is described succinctly below. More detailed overview of the measurement is explained in Chapter 5 after describing the experimental components and the Monte Carlo simulations of T2K.

Neutrino beam production

The beam protons from the J-PARC accelerator impinge the production target and the charged pions are produced. The pions decay in flight into pairs of a muon and a muon neutrino ($\pi \to \mu + \nu_\mu$). Some of the produced neutrinos fly to the near detectors and the far detector, Super-K.

Neutrino measurements

The neutrinos from J-PARC before and after oscillation are measured by the near detectors and Super-K, respectively. In Super-K, the CCQE interaction is selected as the signal mode because it is dominant in the T2K neutrino energy region, and the neutrino energy of the CCQE

interaction event can be reconstructed from the kinematics of the emitted charged lepton[††] as

$$E_{\rm rec} = \frac{m_p^2 - (m_n - E_b)^2 - m_l^2 + 2(m_n - E_b)E_l}{2(m_n - E_b - E_l + p_l \cos\theta_l)}, \tag{1.36}$$

where m_n, m_p and m_l are masses of neutron, proton and charged lepton, E_b is the neutron binding energy in oxygen (27 MeV) and E_l, p_l and θ_l are energy of charged lepton, its momentum and its emission angle relative to the beam direction, respectively. Super-K can separate CC interactions by ν_e and ν_μ with high accuracy, whereas ν_τ cannot be detected via CC interaction because almost all T2K neutrinos have energy below the τ production threshold (3.5 GeV). At the J-PARC cite, there are two near detectors (INGRID and ND280), and independent measurements are performed by each detector.

Neutrino event prediction

The expected number of neutrino events detected at Super-K assuming the neutrino oscillations is predicted as a function of reconstructed neutrino energy with Monte Carlo simulation as

$$\begin{aligned} N_{\rm SK}^{\rm exp}(E_{\rm rec}; \delta_{CP}, \theta_{13}, \theta_{23}, \Delta m^2_{32}) &= \int \Phi_{\rm SK}(E_\nu) \cdot P(E_\nu; \delta_{CP}, \theta_{13}, \theta_{23}, \Delta m^2_{32}) \cdot T_{\rm SK} \\ &\quad \cdot \sigma(E_\nu) \cdot \varepsilon_{\rm SK}(E_\nu) \cdot R_{\rm SK}(E_{\rm rec}, E_\nu) dE_\nu, \end{aligned} \tag{1.37}$$

where $\Phi_{\rm SK}$ is the neutrino flux at Super-K without neutrino oscillations, P is the neutrino oscillation probability, $T_{\rm SK}$ is the number of target nuclei in Super-K, σ is the neutrino-nucleus interaction cross-section, $\varepsilon_{\rm SK}$ is the Super-K detection efficiency and $R_{\rm SK}$ is the Super-K detector response function representing the probability of observing E_ν as $E_{\rm rec}$. $\Phi_{\rm SK}$ is predicted with the neutrino flux simulation, σ is calculated based on the neutrino-nucleus interaction models and $\varepsilon_{\rm SK}$ and $R_{\rm SK}$ are estimated with the Super-K detector simulation. The result of the neutrino measurements with the near detectors is used to reduce the uncertainties on $\Phi_{\rm SK}$ and σ.

Neutrino oscillation analysis

The neutrino oscillation parameters, θ_{13}, θ_{23}, Δm^2_{32} and δ_{CP}, are determined via the $\nu_\mu \to \nu_e$ and $\nu_\mu \to \nu_\mu$ oscillations by comparing the observed neutrino energy spectra for ν_e and ν_μ events at Super-K with the expected ones.

1.6 Outline of this thesis

This thesis reports the measurement of three-flavor neutrino oscillations in T2K by a first joint analysis of the $\nu_\mu \to \nu_e$ and $\nu_\mu \to \nu_\mu$ oscillations with precise measurements of the neutrino beam properties and the neutrino-nucleus interaction cross sections with the INGRID detector. The remainder of this thesis is organized as follows. Chapter 2 introduces the T2K experimental setup and the data set. Since the INGRID detector is especially important for this thesis, it is described in detail in Chapter 3. Chapter 4 explains how to predict the neutrino events using the Monte Carlo simulations. Then, an overview of the measurements presented in this thesis is summarized in Chapter 5. Chapter 6 describes the measurement of the neutrino beam properties and their stabilities with INGRID that is essential for all the physics results of T2K. Measurement of the neutrino-nucleus interaction cross sections (CC inclusive cross section, CCQE cross section and CC coherent pion cross section) with INGRID is presented in Chapter 7–9. And then, in light of the measurements with INGRID, the neutrino oscillation measurement is performed in Chapter 10. Finally, conclusions are given in Chapter 11.

[††]In the CCQE interaction, the neutrino energy is uniquely determined from the charged lepton kinematics using the conservation laws of energy and momentum because it is a two-body interaction.

Chapter 2

T2K Experiment

The T2K experimental setup consists of the J-PARC accelerator, a neutrino beamline, near detectors and a far detector (Super-K) as illustrated in Fig. 2.1. The T2K neutrino beamline is configured such that the far detector is 2.5° off the beamline axis. Since it is an important feature of the T2K experiment, it is described in the beginning of this chapter (Sec. 2.1). Then, details of the hardware components (Secs. 2.2, 2.3, 2.4 and 2.5) and data set acquired until May 2013 (Sec. 2.6) are explained.

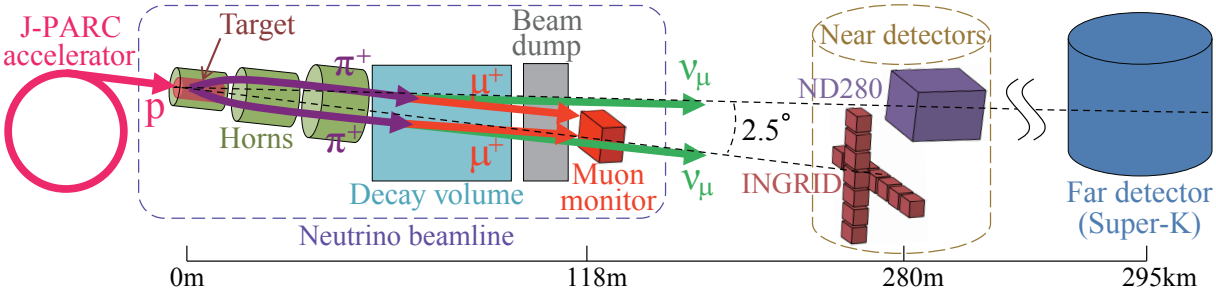

Figure 2.1: Schematic view of the T2K hardware components.

2.1 Off-axis beam configuration

When a neutrino is produced from the pion two-body decay, the neutrino energy in the laboratory system (E_ν) is described as:

$$E_\nu = \frac{m_\pi^2 - m_\mu^2}{2(E_\pi - p_\pi \cos\theta_\nu)}, \tag{2.1}$$

where, m_π and m_μ are the pion and muon masses, E_π and p_π are the pion energy and momentum and θ_ν is the angle between the pion and neutrino directions. Figure 2.2 shows the relation between p_π and E_ν in the two body decay for some θ_ν. When θ_ν is shifted from zero, the energy of a neutrino from the two-body decay weakly depends on the pion momentum [118]. In T2K, the neutrino beam is purposely directed at 2.5° with respect to the baseline connecting the production target and Super-K as shown in Fig. 2.1. This feature makes the narrow-band neutrino beam toward Super-K. The 2.5° off-axis angle was determined so that the neutrino beam has a peak energy at ∼0.6 GeV, which maximizes the neutrino oscillation probabilities at 295km as shown in Fig. 2.3. In addition, it reduces background neutrino interactions; our signal is charged current quasi-elastic (CCQE) interaction as explained in Chapter 1 and the main background is charged current pion production (CC1π) and neutral current pion production (NC1π) interaction. T2K is the first experiment that adopts the

off-axis beam configuration*. However, the off-axis neutrino beam is very sensitive to the off-axis angle, hence a deviation of neutrino beam direction causes a large uncertainty of the neutrino beam. For example, when the neutrino beam direction deviates by 1 mrad, the intensity and peak energy of the neutrino beam at Super-K are predicted to change by 5% and 3%, respectively. To achieve the target sensitivities in T2K, the neutrino beam direction is required to be controlled within 1 mrad and be measured with a much better precision.

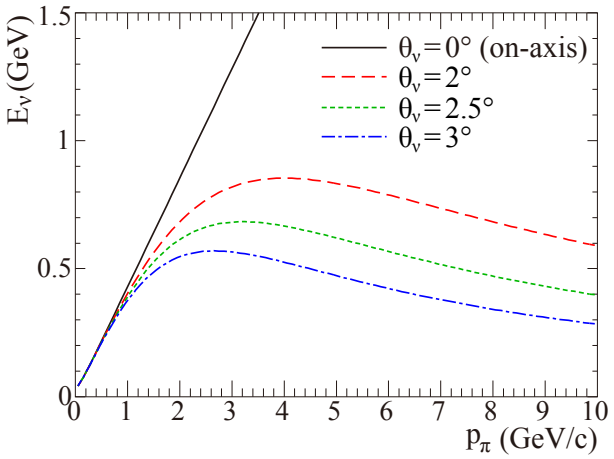

Figure 2.2: The relation between pion momentum (p_π) and neutrino energy (E_ν) in the pion two body decay.

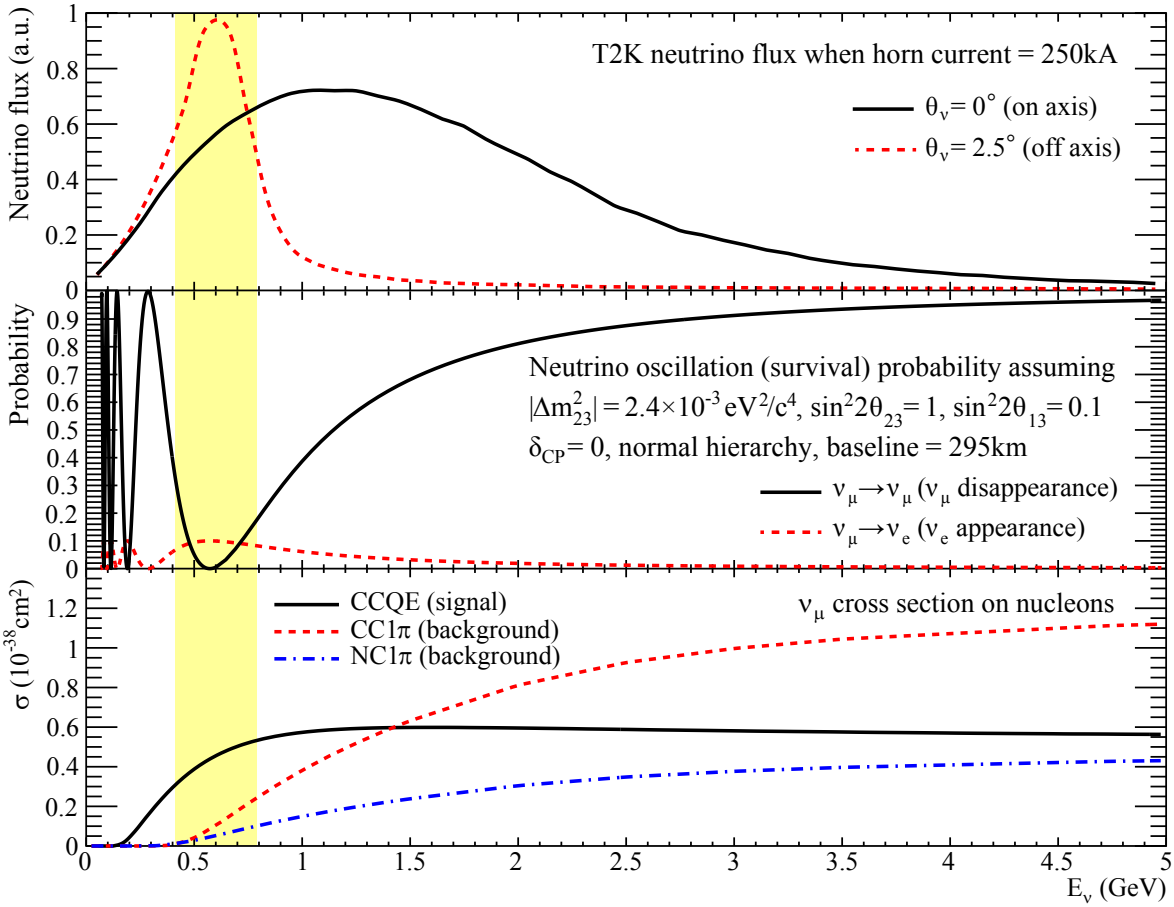

Figure 2.3: Neutrino energy spectra on axis and 2.5° off axis (top), neutrino oscillation (survival) probabilities (middle), and neutrino interaction cross sections divided by the neutrino energy (bottom) as a function of the neutrino energy.

*The NOνA experiment [72] which started in 2014 also adopts the off-axis beam configuration.

2.2 J-PARC accelerator

J-PARC [117] consists of three accelerators as shown in Fig. 2.4.

- A linear accelerator (LINAC) accelerates an H^- beam up to 400 MeV (181 MeV as of May 2013) and converts it to an H^+ beam by charge-stripping foils.
- A rapid-cycling synchrotron (RCS) accelerates the beam up to 3 GeV with a 25 Hz cycle.
- A main ring (MR) synchrotron takes about 5% of the beam[†] and accelerates it up to 30 GeV.

For each acceleration cycle, the beam is fast-extracted from the MR to the T2K neutrino beamline as a "spill". One spill contains eight bunches in 4.1 μs as illustrated in Fig. 2.5. The design values of the extracted proton beam to the T2K neutrino beamline are listed in Table 2.4 together with the present values as of May 2013. J-PARC is designed to produce the most powerful beam (design intensity is 750 kW) in the world. This feature increases the intensity of the neutrino beam.

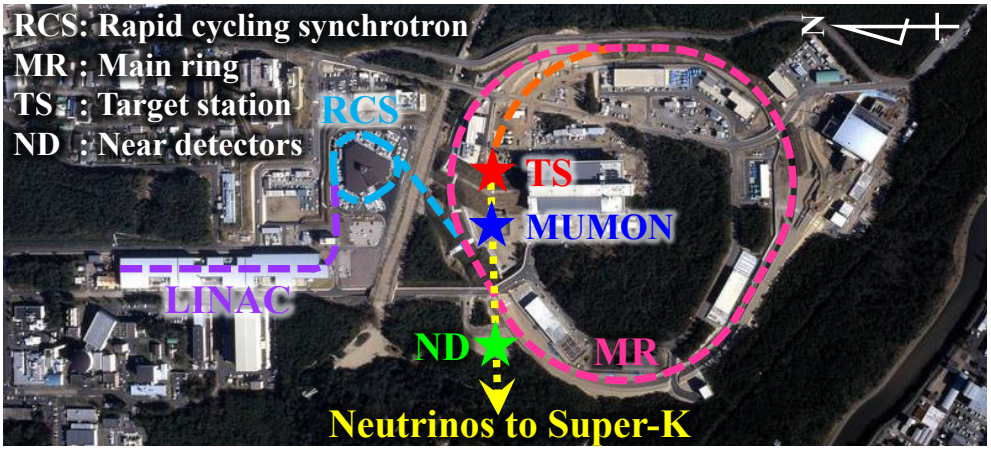

Figure 2.4: The J-PARC site viewed from above.

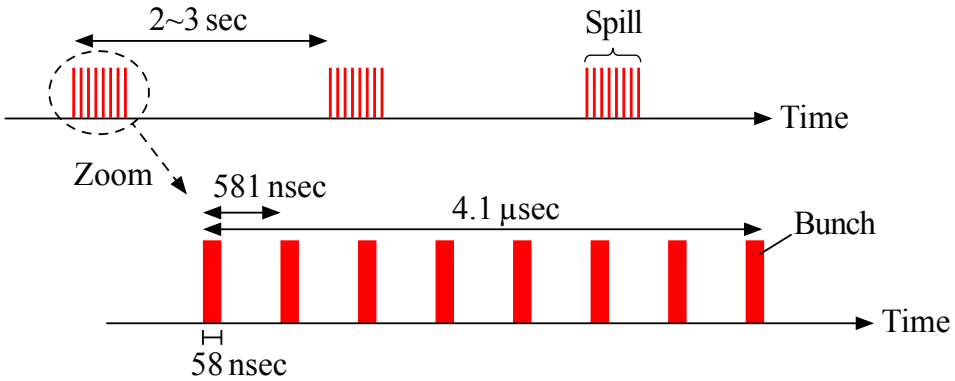

Figure 2.5: Schematic view of the beam spill.

[†]The rest of the beam is supplied to the muon and neutron beamline in the Material and Life Science Facility (MLF).

Table 2.1: Design and present values of the fast extracted proton beam to the T2K neutrino beamline.

Parameter	Design value	Present value (May, 2013)
Beam power	750 kW	220 kW
Beam kinetic energy	50 GeV	30 GeV
Number of protons	3.3×10^{14} /spill	1.2×10^{14} /spill
Number of bunches	8 bunches/spill	8 bunches/spill
Spill interval	3.3 sec	2.48 sec
Bunch interval	581 nsec	581 nsec
Bunch width	58 nsec	58 nsec
Spill width	4.1 μsec	4.1 μsec

2.3 T2K neutrino beamline

The T2K neutrino beamline is composed of two sections: the primary and secondary beamlines. In the primary beamline, the extracted protons from MR are bent toward the direction of Super-K. In the secondary beamline, they collide with graphite target, producing secondary pions and other hadrons, which are focused by magnetic horns and decay into neutrinos. An overview of the neutrino beamline is illustrated in Fig. 2.6.

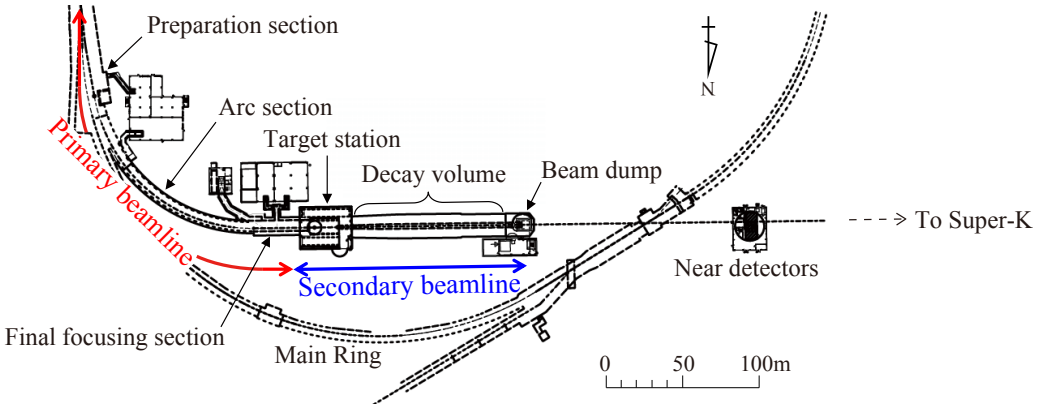

Figure 2.6: Overview of the T2K neutrino beamline.

2.3.1 Primary beamline

The primary beamline consists of the preparation (∼50 m long), arc (∼150 m) and final focusing (∼40 m) sections as shown in Fig. 2.6. In the preparation section, the extracted proton beam is tuned with a series of 11 normal conducting magnets so that the beam can be accepted by the arc section. In the arc section, the beam is bent toward the direction of Super-K by 80.7°, with 104 m radius of curvature, using 14 doublets of superconducting combined function magnets [119–121] (SCFMs). At intervals of SCFMs, three pairs of horizontal and vertical superconducting steering magnets are installed to correct the beam orbit. In the final focusing section, ten normal conducting magnets guide and focus the beam onto the production target, while directing the beam downward by 3.637°. The beam duct, inside of the primary beamline, is kept at high vacuum. A well-tuned proton beam is essential for the stable neutrino beam production, and to minimize beam loss in order to achieve high-power beam operation. Therefore, the intensity, position, profile and loss of the proton beam in the primary sections have been precisely monitored. This

is achieved by five current transformers (CTs), 21 electrostatic monitors (ESMs), 19 segmented secondary emission monitors (SSEMs) and 50 beam loss monitors (BLMs). Their location is shown in Fig. 2.7.

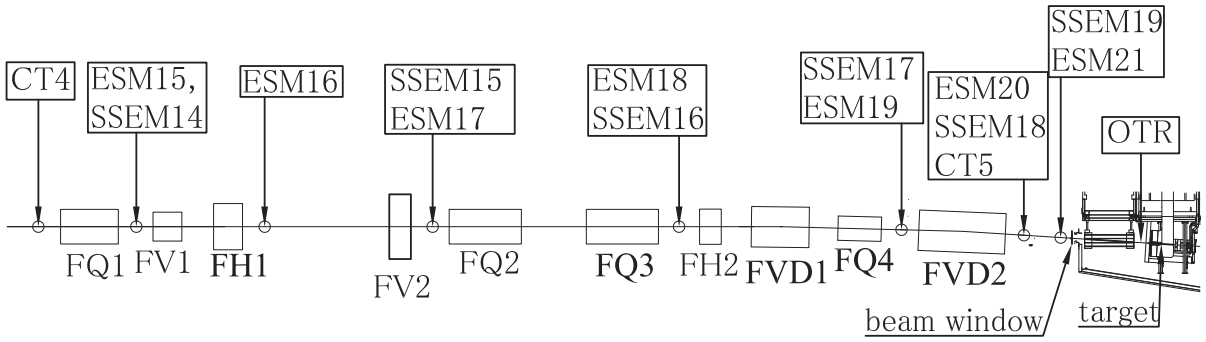

Figure 2.7: Location of the primary beamline monitors in the final focusing section.

2.3.2 Secondary beamline

The secondary beamline consists of four sections (Fig. 2.8): the target station, decay volume, beam dump and muon monitor.

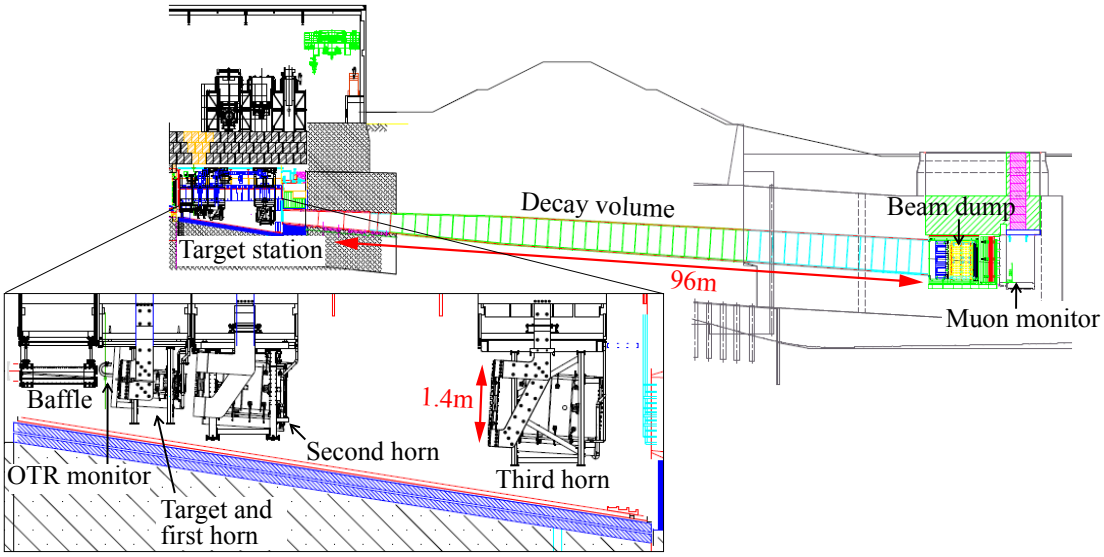

Figure 2.8: Side view of the secondary beamline.

Target station

The proton beam from the primary beamline goes through the baffle, which is a graphite block with a beam hole of 30 mm in a diameter, and impinges the production target. The optical transition radiation (OTR) monitor [122] is installed between the baffle and the target to monitor the beam profile and center. The target core is a 91.4 cm long, 2.6 cm diameter graphite [123] and is sealed inside a 0.3 mm thick titanium case as shown in Fig. 2.9. The target assembly is cantilevered inside the bore of the first horn inner conductor. In T2K, three magnetic horns are used. Each horn consists of two coaxial (inner and outer) conductors which encompass a closed volume [125, 126]. A toroidal magnetic field is generated in that volume. The field varies

in inverse proportion to the distance from the horn axis. The first horn collects the charged pions that are produced at the target installed in its inner conductor as illustrated in Fig. 2.10. The second and third horns focus the pions. In the Run 1-4 operation, positive pions had been focused to produce neutrinos[‡]. However, when the polarity of the horn current is inverted, negative pions are focused and antineutrinos are produced.

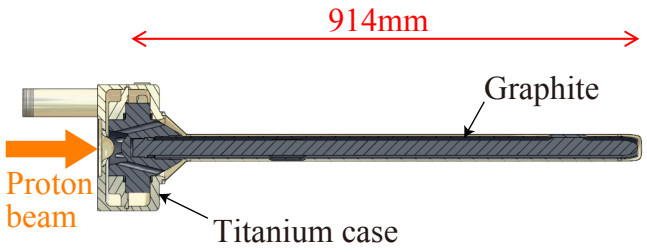

Figure 2.9: Cross section view of the target.

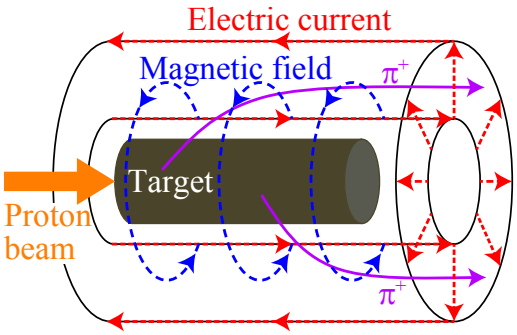

Figure 2.10: Illustration of the first horn.

Decay volume and beam dump

The pions decay to muon neutrinos and muons in the decay volume. The decay volume is a 96 m long steel tunnel. The cross section is 1.4 m wide and 1.7 m high at the entrance, and 3.0 m wide and 5.0 m high at the end. At the end of the decay volume, there is a beam dump composed of graphite blocks and concrete walls. The beam dump stops all the particles except for neutrinos and high energy muons.

Muon monitor (MUMON)

The neutrino beam intensity and direction can be indirectly monitored on a bunch-by-bunch basis by measuring the profile distribution of muons after the beam dump. Since the muons are produced from the same parent particles as the neutrinos, the measurement of their properties also provides information about the neutrino beam indirectly. This is achieved by the muon monitor (MUMON) [127, 128] which is located behind the beam dump at a distance of 118 m from the production target, as shown in Fig. 2.8. It consists of two kinds of detector arrays: ionization chambers and silicon PIN photodiodes. Each array consists of 7×7 sensors at 25 cm intervals and covers a 150×150 cm^2 area. The photograph of the muon monitor and the typical charge distribution of silicon arrays are shown in Fig. 2.11. The center of the muon profile can be measured with 2.95 cm accuracy, which corresponds to 0.25 mrad precision on the beam direction.

2.4 Near detectors

The T2K near neutrino detectors are composed of the on-axis neutrino beam monitor (INGRID) and the off-axis neutrino spectrometer (ND280) as shown in Fig. 2.12. These detectors are housed in a pit inside the detector hall whose diameter and depth are 17.5m and 37m respectively that is located 280m downstream from the production target.

[‡]Even when the positive pions are focused, antineutrinos mix in the neutrino beam by about 5%.

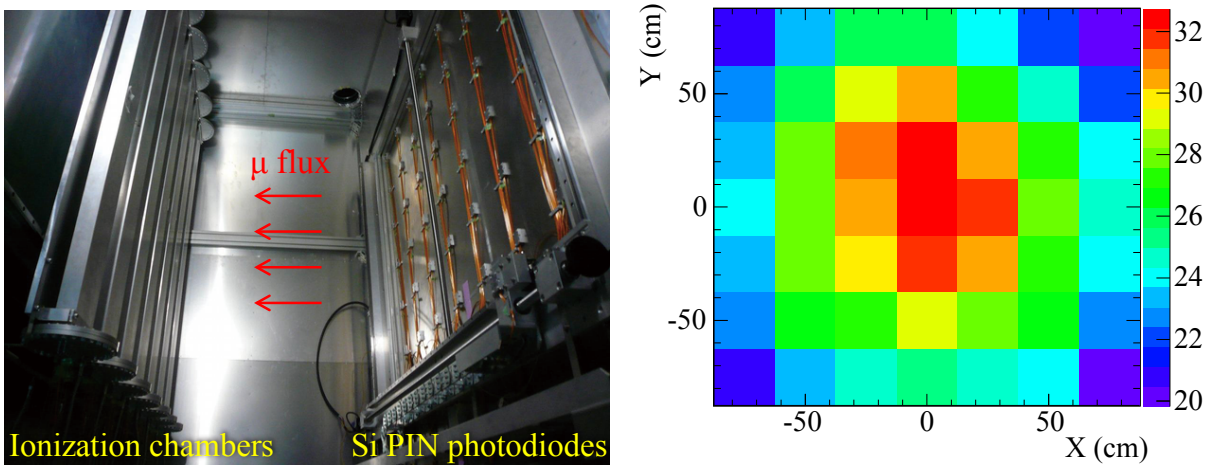

Figure 2.11: The photograph of the muon monitor (left) and the typical charge distribution of silicon arrays (right).

2.4.1 INGRID

INGRID (Interactive Neutrino GRID) [129] is a neutrino detector centered on the neutrino beam axis. Its main purpose is to measure the on-axis neutrino beam profile to monitor the neutrino beam direction. Details of INGRID are described in Chapter 3.

2.4.2 ND280

The ND280 detector is a complex of many components as shown in Fig. 2.13.

- A Pi-Zero Detector (P0D) [130] is placed at the upstream end to measure the neutral current π^0 production rate for the estimation of the background against the $\nu_\mu \to \nu_e$ signal at Super-K.
- Three Time Projection Chambers (TPC1,2,3) [131], together with two Fine Grained Detectors (FGD1,2) [132] are placed downstream of P0D to measure charged current interactions.
- An Electromagnetic Calorimeter (ECal) [133] surrounds P0D, TPCs, and FGDs.
- A magnet[§] provides a dipole magnetic field of 0.2 T to measure momenta with good resolution and determine the sign of charged particles.
- A Side Muon Range Detector (SMRD) [136] is instrumented on all sides of the magnet.

All the sub-detectors other than TPCs are based on extruded scintillators. ND280 is a totally different type of detector from Super-K because a large water Cherenkov detector in 280m location from the production target works poorly due to event pileup. In this thesis, FGDs and TPCs are used. FGDs consist of layers of finely segmented scintillating bars. They provide a target for neutrino interactions as well as tracking of charged particles coming from the neutrino interaction vertex. The outer dimensions and the total target mass of FGDs are 2.3m×2.4m×3.65m (width, height, depth in beam direction) and 1.1 tons, respectively. TPCs use a gas mixture of Ar:CF_4:C_4H_{10} (95:3:2) and MicroMEGAS [137] readout planes. They measure the momentum of charged particles from the track curvature in a magnetic field as well as the amount of ionization left by each particle to identify the types of charged particles with combination of the measured momentum.

[§]The magnet was used in the UA1 experiment [134] and the NOMAD experiment [135] at CERN and then was donated to T2K.

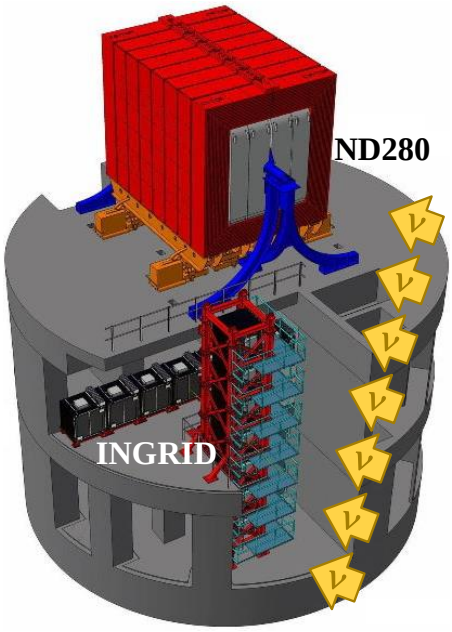

Figure 2.12: The T2K near detectors (INGRID and ND280).

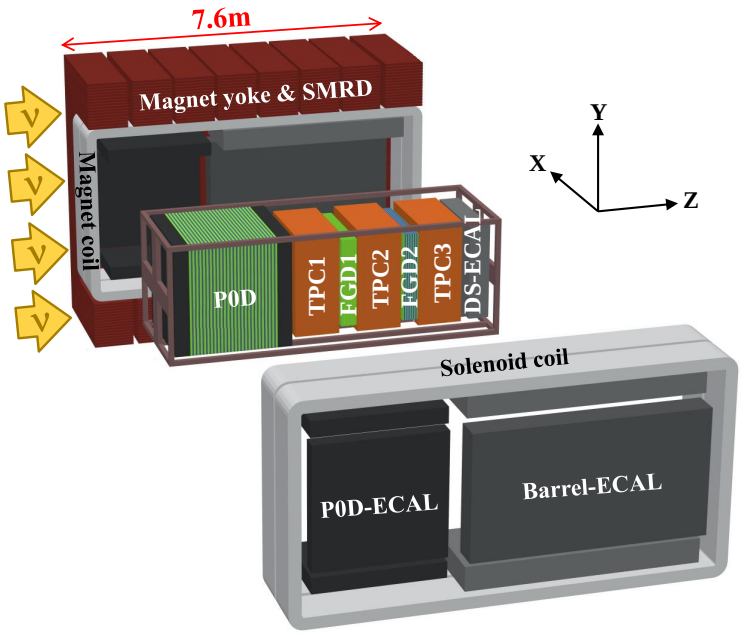

Figure 2.13: Exploded view of the ND280 detector.

2.5 Super-Kamiokande detector

2.5.1 Detector overview

The world's largest land-based water Cherenkov detector, Super-Kamiokande (Super-K) [138], serves as the far detector in the T2K experiment. The detector is located 295 km west of J-PARC, 1 km deep inside a mountain[¶]. It is a cylindrical cavern, 39.3 m in diameter and 41.4 m in height, filled with 50 kton of pure water. It is optically separated by a cylindrical stainless steel structure to make two segments as shown in Fig. 2.14.

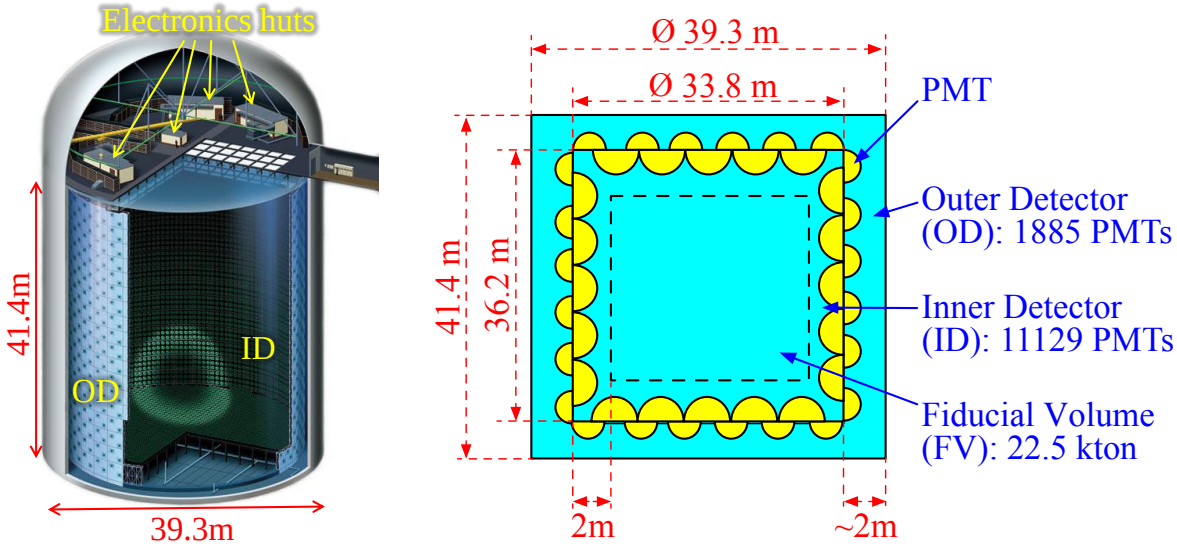

Figure 2.14: Schematic overview of Super-K (left) and cross section view of the Super-K water tank (right).

[¶]Cosmic muon rate in Super-K is 2 Hz which is 10^{-5} of that above ground.

- The inner detector (ID) is a cylindrical shell of 33.8 m in diameter and 36.2 m in height. It houses 11,129 inward-facing 50 cm diameter photomultiplier tubes (PMTs) along its inner walls, covering the 40% of the surface.
- The outer detector (OD) is a 2 m-thick space enclosing the inner detector. It contains 1,885 outward-facing 20 cm diameter PMTs along its inner walls. It is only sparsely instrumented with PMTs, but is capable of 100% rejection efficiency of cosmic ray muon backgrounds.

The fiducial volume of Super-K is defined as a virtual cylinder of 29.8 m in diameter and 32.2 m in height (>2 m from the ID wall), filled with 22.5 kton of pure water. Neutrinos are detected with the PMTs by measuring the Cherenkov lights emitted by charged particles from the neutrino interactions in the water. The particle's vertex, energies, directions are reconstructed from the timing and position of the Cherenkov lights. The particle identification (muon/electron separation) is performed based on the edge of the Cherenkov light pattern: the Cherenkov light pattern by a muon has a sharp edge, while that by an electron has a characteristic fuzzy edge due to electromagnetic showers.

2.5.2 T2K beam data

The charge and timing of each hit PMT (hit threshold is ~0.25 photoelectrons) are continuously collected, and are built as an event by an online software-trigger program. The T2K beam data is acquired by recording all hits within ±500 μsec from the beam arrival time[‖] (Fig. 2.15). The beam arrival time is determined by utilizing the GPS time synchronized between J-PARC and Super-K; the T2K beam neutrinos are expected to arrive at Super-K approximately 1 msec after the proton beam hits on the production target, where 1 msec is the neutrino TOF (Time of Flight) for 295 km. Further offline reduction of the T2K beam data is described in Chapter 10.

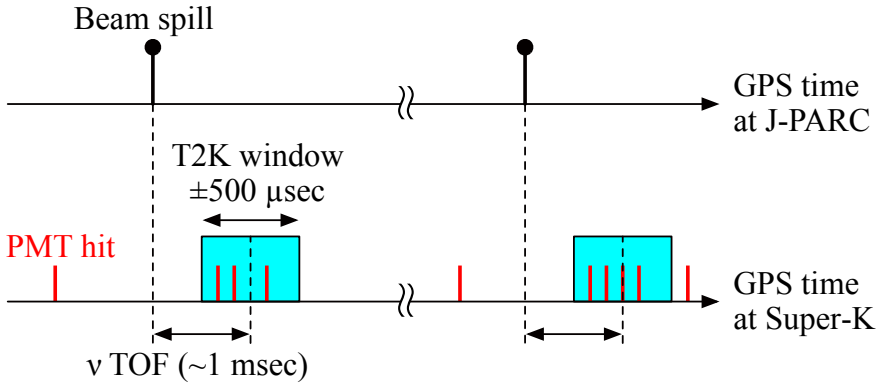

Figure 2.15: Overview of Super-K event timing.

2.6 Data set

The physics results presented in this thesis are based on four physics runs: Run 1 (January − June 2010), Run 2 (November 2010 − March 2011), Run 3 (March − June 2012) and Run 4 (October 2012 − May 2013).The Run 3 period is divided into three sub periods, Run 3a (March 2012), Run 3b (March 2012) and Run 3c (April − June 2012), according to the horn current settings (with a 0 kA setting in Run 3a and a 205 kA setting in Run 3b instead of the nominal

[‖] Probability of observing accidental atmospheric neutrinos in five-year beam operation is less than 1%.

250 kA)**. The Run 3a data is not used for the oscillation analysis because the data in this period is small (0.1% of the total) and the horn current was set to 0 kA. We select only good quality beam data for physics analysis using the following conditions.

- Each hardware component works normally.
- The deviation of all horns currents from the mean is within ±5 kA.
- The deviation of the beam angle measured by MUMON from the mean is within 1 mrad.
- The deviation of the total muon yield measured by MUMON from the mean is within ±5 %.

After the good quality cut, the fraction of beam data remained is 99.8%. Figure 2.16 shows the accumulated protons on target (POT) and protons per pulse for good quality beam data over time, and Table 2.2 summarizes the accumulated POT and horn current in each run period. The total accumulated POT in all run periods is 6.57×10^{20} POT, corresponding to 8% of T2K's exposure goal. The maximum proton beam power reached so far is 235kW.

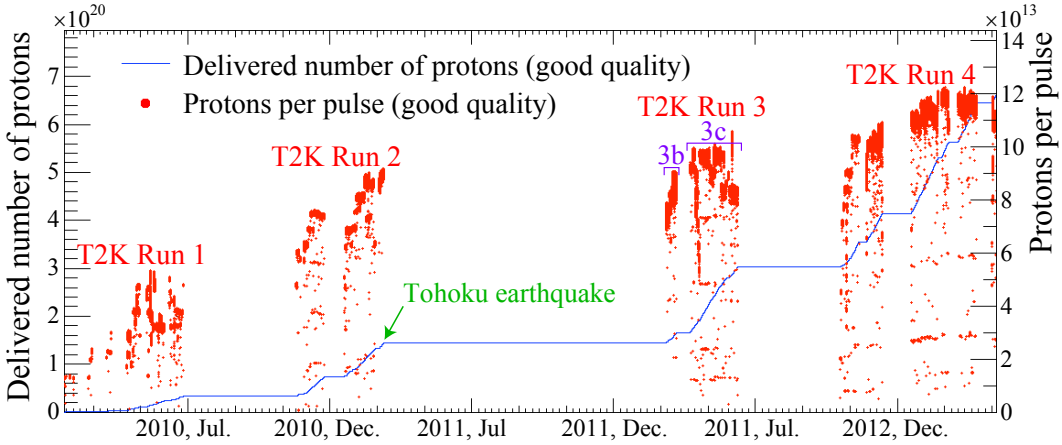

Figure 2.16: History of total accumulated protons and protons per pulse for the good quality beam data.

Table 2.2: Accumulated POT and horn current in each T2K data-taking period.

Run period	Dates	Horn current	Accumulated POT
Run 1	Jan. 2010 – Jun. 2010	250kA	0.32×10^{20}
Run 2	Nov. 2010 – Mar. 2011	250kA	1.11×10^{20}
Run 3b	Mar. 2012	205kA	0.22×10^{20}
Run 3c	Apr. 2012 – Jun. 2012	250kA	1.37×10^{20}
Run 4	Oct. 2012 – May. 2013	250kA	3.56×10^{20}
Total	Jan. 2010 – May. 2013		6.57×10^{20}

**Since the power supply of the horns were broken just before Run 3, Run 3 was started without operating horns. Then the horn operation was started with lower current settings.

Chapter 3

INGRID Detector

The INGRID (Interactive Neutrino GRID) detector is an on-axis neutrino near detector located 280m downstream of the production target. It consists of 16 identical standard modules [129] and an extra called Proton Module [139]. This chapter describes the configurations (Sec. 3.1, 3.2), the hardware components (Sec. 3.3), and the data acquisition system (Sec. 3.4) of the INGRID detector.

3.1 Standard modules

The main purpose of the INGRID standard modules is to monitor the neutrino beam profile center with a precision better than 28 cm which corresponds to 1 mrad of the beam direction at the INGRID location (280 m $\times$ 1 mrad). The spatial width (1σ) of the neutrino beam at the location of INGRID is about 5 m as shown in Fig. 3.1. In order to sufficiently cover the neutrino beam profile, INGRID is designed to sample the beam in a transverse section of 10 m $\times$ 10 m, with 14 identical modules arranged in two identical groups along the horizontal and vertical axes, as shown in Fig. 3.2. In addition, two separate modules are placed off the main cross to monitor the asymmetry of the beam. Each of the modules consists of nine iron target plates and eleven

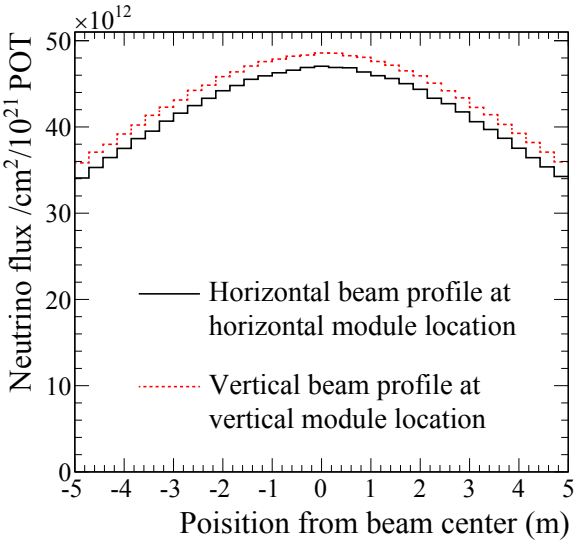

Figure 3.1: Expected neutrino beam profile at the location of INGRID. The spatial width is different in the X and Y directions because the decay volume has a rectangular cross section.

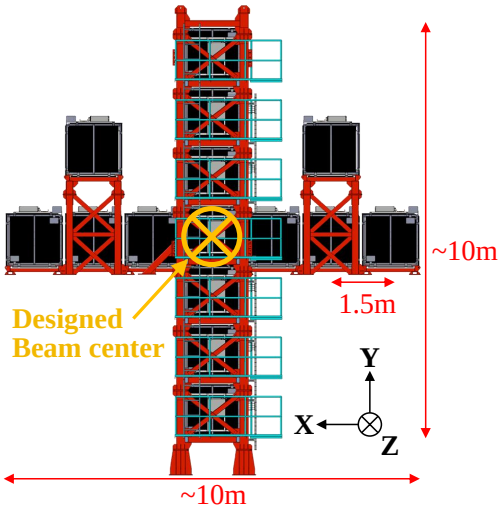

Figure 3.2: Overview of the 16 INGRID standard modules viewed from beam upstream. The horizontal center module is hidden behind the vertical center module.

tracking scintillator planes, as shown in Fig. 3.3 left. They are surrounded by veto scintillator planes (Fig. 3.3 right) to reject charged particles coming from outside of the modules. The dimensions of each iron target plate are $124\times124\text{cm}^2$ in the horizontal and vertical directions and 6.5 cm along the beam direction. The total iron mass serving as a neutrino interaction target is 7.1 tons per module. Each tracking scintillator plane consists of two scintillator layers. Each layer has 24 scintillator strips, making a plane of $120\times120\text{cm}^2$ in the horizontal and vertical directions and 1.0 cm along the beam direction (Fig. 3.4). One layer is placed perpendicular to the other layer in a tracking scintillator plane so that it is sensitive to both horizontal and vertical positions. The veto scintillator plane consists of one scintillator layer which is made up of 22 scintillator strips segmented along the beam direction, in order to identify the incoming charged particles produced by neutrino interactions in the walls of the detector hall. Scintillation light is collected and transported to a photodetector with a wavelength shifting fiber (WLS fiber) which is inserted in a hole at the center of the cross section of the scintillator strip. The light is read out by a Multi-Pixel Photon Counter (MPPC) [143, 144] attached to one end of the WLS fiber.

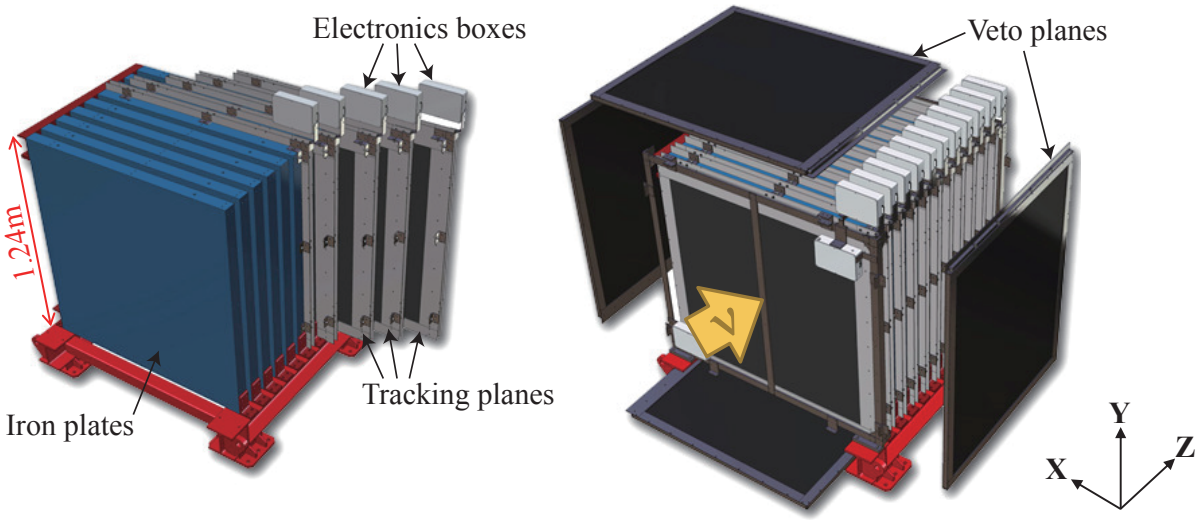

Figure 3.3: Exploded view of an INGRID standard module. It consists of iron target plates and tracking scintillator planes (left), and it is surrounded by veto scintillator planes (right).

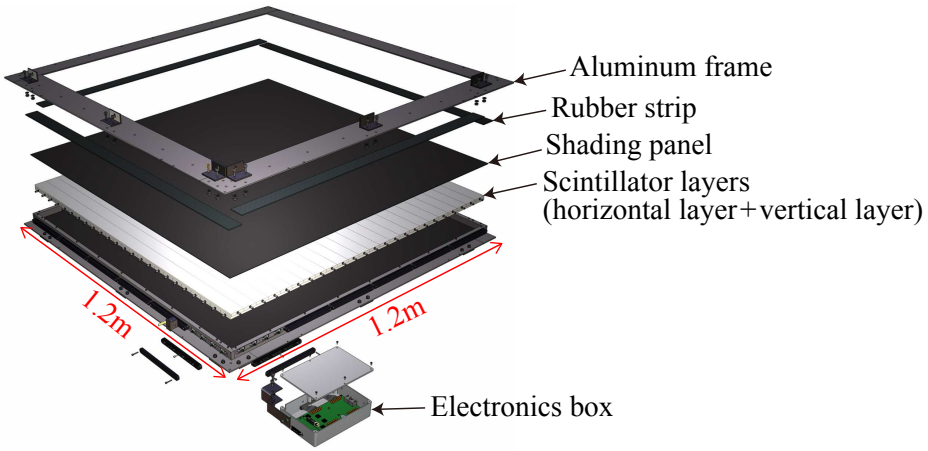

Figure 3.4: Exploded view of a tracking scintillator plane.

3.2 Proton Module

The Proton Module is an extra module located at the beam center between the horizontal and vertical standard modules (Fig. 3.5). It is a fully-active tracking detector which consists of only scintillator strips. The purpose of this Proton Module is to separate the neutrino interaction types by detecting the protons and pions together with the muons from the neutrino interactions*, and to measure the neutrino cross section for each interaction type. We started to develop the Proton Module just prior to Run 1, constructed and installed it between Run 1 and Run 2, and started the beam data acquisition from Run 2. Details of the development and the construction of the Proton Module are introduced in Appendix A. It consists of 36 tracking planes surrounded by veto planes (Fig. 3.6), where each tracking plane is an array of two types of scintillator strips. The 16 strips in the inner region have dimensions of 2.5cm×1.3cm×120cm, while the 16 strips in the outer region have dimensions of 5cm×1cm×120cm, making a plane of $120\times120\text{cm}^2$ in the horizontal and vertical directions. The former is the scintillator produced for the K2K SciBar detector [141] and the latter was produced for INGRID. The tracking planes are placed perpendicular to the beam axis at 23mm intervals. Since the strips are aligned in one direction, each tracking plane is sensitive to either the horizontal or vertical position of the tracks. The tracking planes are therefore placed alternating in the horizontal and vertical directions so that three-dimensional tracks can be reconstructed. The tracking planes also serve as the neutrino interaction target. As with the standard modules, scintillation light is read out by a WLS fiber and MPPC. The INGRID horizontal modules which lie downstream of the Proton Module are used to identify muons from the neutrino interactions in the Proton Module.

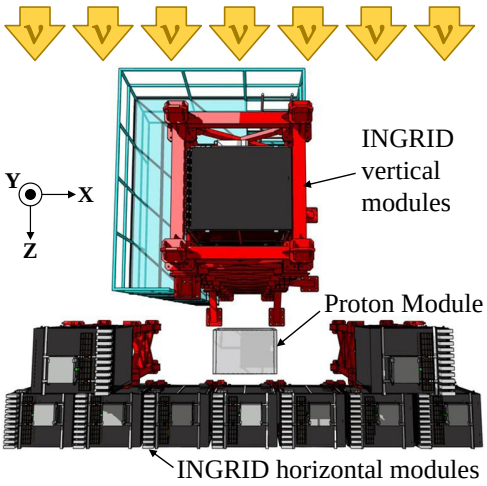

Figure 3.5: Position of the Proton Module viewed from above.

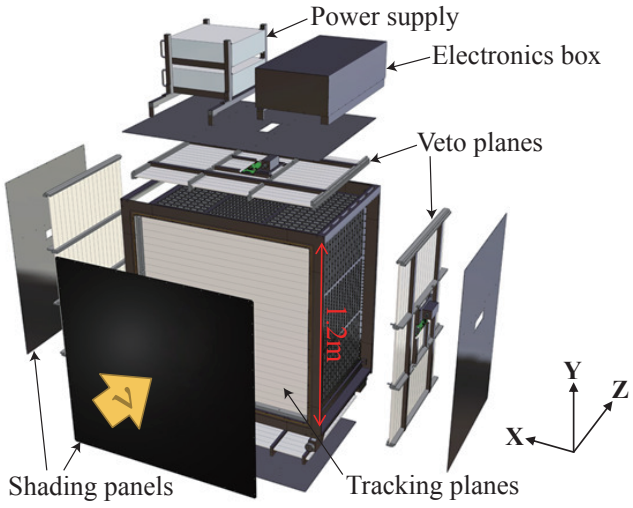

Figure 3.6: Exploded view of the Proton Module.

3.3 Hardware components

3.3.1 Iron plates

Nine iron plates are used in an INGRID standard module. Each plate has a design mass of 785kg and a design dimension of $124\times124\times6.5\text{cm}^3$. The actual mass and thickness of each plate were measured within precisions of 1kg and 1mm respectively. All the measured values are within ±2% from the design values as shown in Fig. 3.7.

*Name of the Proton Module is derived from the fact that it can efficiently detect even the short-track protons.

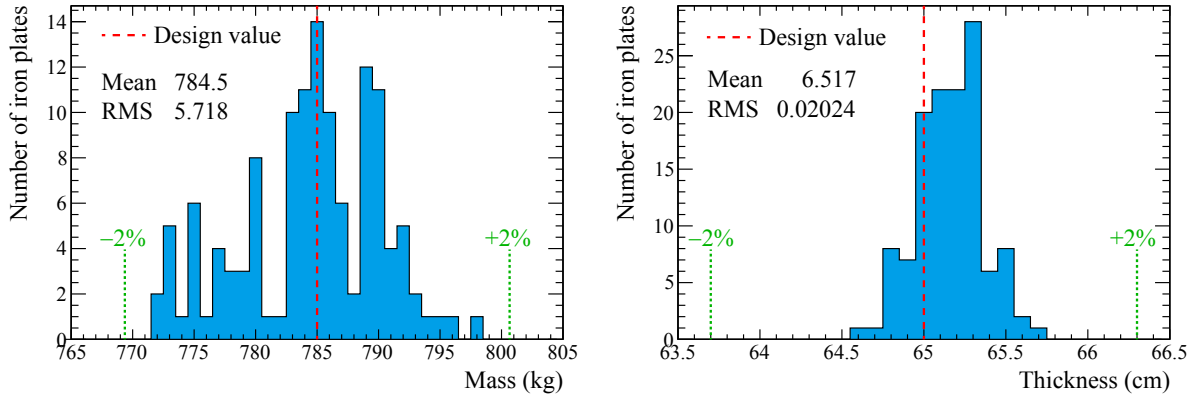

Figure 3.7: Measured mass (left) and thickness (right) of iron plates for INGRID.

3.3.2 Extruded scintillator

All the extruded scintillator strips[†] for INGRID were produced at Fermilab [140]. The scintillator strips are made of polystyrene infused with PPO and POPOP (1% and 0.03% by weight, respectively). The wavelength at the emission peak is 420nm (blue) as shown in Fig. 3.8. There is a hole in the center of the cross section to insert the WLS (wavelength shifting) fiber. The scintillator is covered with co-extruded reflective coating, composed of TiO_2 (15% by weight) infused in polystyrene, which separates each scintillator optically[‡] and increases the light yield. The specifications of the scintillator are summarized in Table 3.1. The scintillator used in the INGRID standard modules is 5.0 cm wide, 1.0 cm thick, and 120 cm long. In the Proton Module, the spare scintillator for the K2K SciBar detector [141] which is 2.5 cm wide, 1.3 cm thick, and 120 cm long is also used. Hereafter, the former is referred to as the INGRID-type scintillator and the latter as the SciBar-type scintillator. Figure 3.9 shows cross sectional dimensions of the scintillator strips.

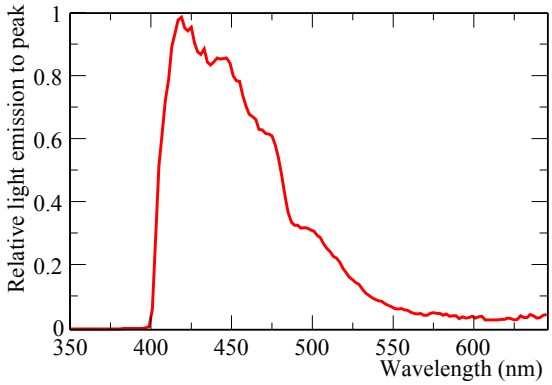

Figure 3.8: Emission light spectrum from scintillator.

Table 3.1: Specifications of scintillator.

Item	Specification
Base material	Polystyrene
Scintillator material	PPO(1%), POPOP(0.03%)
Reflector material	TiO_2(15%)
Emission wavelength	420nm (peak)
Density	1.021g/cm^3
Length	1.2 m (tracking layer)

[†]Extruded scintillators are produced by applying a pressure on the heated plastic filled in a mold form and excluding it from the mold form.

[‡]Crosstalk of the scintillation light between scintillators is less than 0.5%.

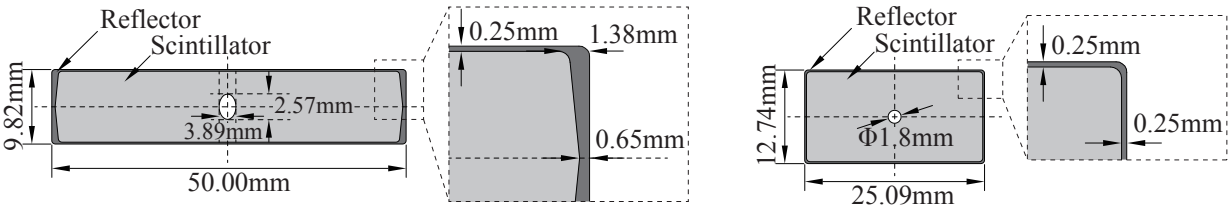

(a) INGRID-type scintillator (b) SciBar-type scintillator

Figure 3.9: Cross sectional dimensions of the scintillator strips.

3.3.3 Wavelength shifting fiber

WLS (wavelength shifting) fibers, Kuraray Y11(200)MS [142], are used to collect and transport the scintillation light. Figure 3.10 and Table 3.2 show the absorption, emission spectra and the specifications of the WLS fiber. The absorption peak wavelength of 430nm matches with the peak scintillation wavelength of 420nm. The attenuation length, 350cm, is sufficiently-long relative to the scintillator length, 120cm. Each fiber has a double clad, which enhances the reflectivity as illustrated in Fig. 3.11 and leads to the increment of the transported light.

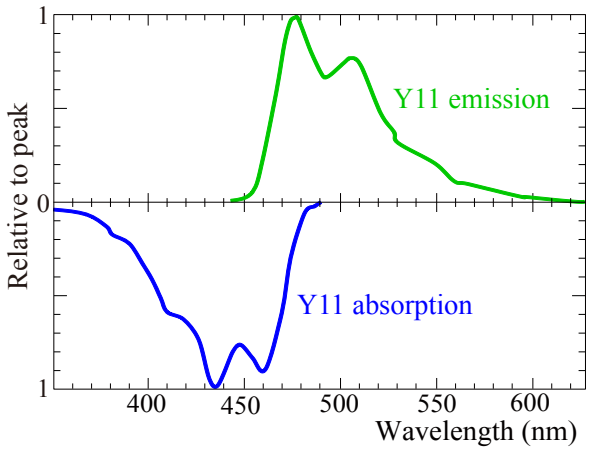

Figure 3.10: Absorption and emission spectra of the WLS fiber for INGRID (Y-11(200)MS) [142].

Table 3.2: Specifications of the WLS fiber for INGRID (Y-11(200)MS) [142].

Item	Specification
Diameter	1.0mm
Core	Polystyrene (n=1.59)
Inner clad	Acrylic (n=1.49)
Outer clad	Polyfluor (n=1.42)
Absorption wavelength	430nm (peak)
Emission wavelength	460nm (peak)
Attenuation length	350cm (typical)

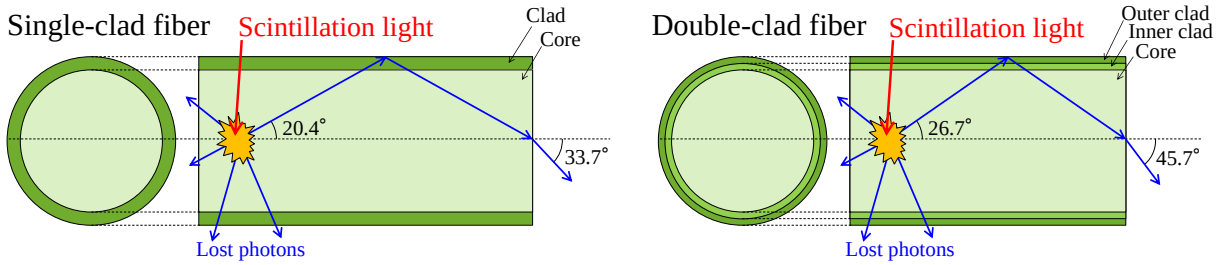

Figure 3.11: Schematic view of a single-clad fiber (left) and a double-clad fiber (right). In the double-clad fiber, the light whose angle with respect to the fiber axis is less than 26.7° is reflected and transported along the fiber.

3.3.4 Multi-pixel photon counter

Multi-Pixel Photon Counter[§] (MPPC, Hamamatsu S10362-13-050C) [143, 144] is used as the photodetector. Figure 3.12 shows the photograph and the circuit schematic of MPPC. It is an electrically parallel array of small avalanche photodiodes (APDs) which operates in Geiger-mode with an applied voltage ($V_{\rm app}$) a few volts above the breakdown voltage ($V_{\rm bd}$). When a photoelectron (P.E.) is produced, it induces a Geiger avalanche. The avalanche is passively quenched by a resistor concatenated serially to each pixel. The output charge from a single pixel (Q) is independent of the number of produced photoelectrons within the pixel, and can be written as:

$$Q = C(V_{\rm app} - V_{\rm bd}), \tag{3.1}$$

where C is the capacitance of the pixel. Since the capacitance C is on the order of 10–100 fF, it gives a gain of 10^5–10^6 when $(V_{\rm app} - V_{\rm bd})$ is a few volts. Combining the output from all the pixels, the total charge from an MPPC ($Q_{\rm tot}$) is quantized to multiples of Q and proportional to the number of pixels that underwent Geiger discharge ($N_{\rm fired}$):

$$Q_{\rm tot} = N_{\rm fired} Q. \tag{3.2}$$

The number of fired pixels is proportional to the number of injected photons if the number of photons is small compared to the total number of pixels. Thus, the MPPC has an excellent photon counting capability as shown in Fig. 3.13. Figure 3.14 shows the photon detection efficiency of MPPC as a function of the wavelength. The most sensitive wavelength of 450nm matches with the WLS fiber peak emission wavelength of 460nm. Table 3.3 shows the basic specifications of MPPC. It has a high photon detection efficiency and low operation voltage. In addition, it is very compact. However, MPPC also has a few negative characteristics. Firstly, there are three types of fake signals from MPPC.

Dark count
: Thermal carriers generate avalanches at random times independently of true signal. The typical rate of this fake signal (so-called the dark count) is 10^5 Hz.

Crosstalk
: An optical photon from an avalanche sometimes enters neighboring pixel, and triggers another avalanche. It follows the true signal with some probability (∼10%) and pads the output charge.

Afterpulse
: Electron from an avalanche is sometimes trapped in the lattice defect, is re-emitted later, and makes a second avalanche in the same pixel. When the signal charge is integrated in a time range, it also pads the output charge.

Secondly, MPPC has considerable individual differences in basic characteristics such as breakdown voltage, gain, dark rate, crosstalk and afterpulse rate, and photon detection efficiency. Thirdly, MPPC response depends significantly on temperature. Hence, the basic characteristics of all the MPPCs together with their dependences on the applied voltage and the temperature were measured before the installation (see Appendix A for details). The result of the measurement was used to determine the applied voltage to each MPPC (see Appendix B for details), and to reproduce the MPPC response in the Monte Carlo simulation. In addition, the temperature of the detector hall has been accurately controlled, and the stability of the MPPC response has been carefully monitored (see Appendix B for details). INGRID is the first large application of MPPC. Therefore, demonstration of its high availability is an important task for INGRID.

[§]Multi-Pixel Photon Counter (MPPC) is the registered trade name of Hamamatsu Photonics K.K., and this type of pixelated semiconductor photodetector is generally referred to as Pixelated Photon Detector (PPD).

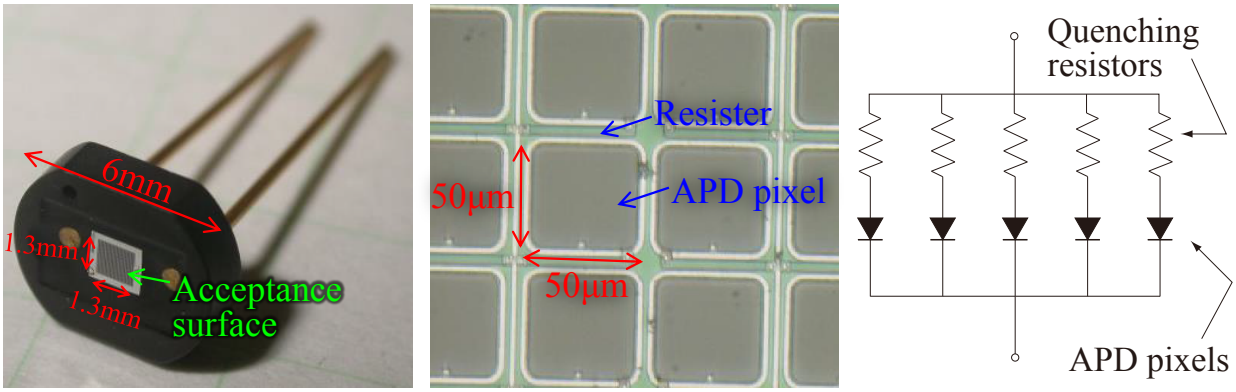

Figure 3.12: Photographs of the Multi-Pixel Photon Counter (left) and its acceptance surface (center), and its circuit schematic (right).

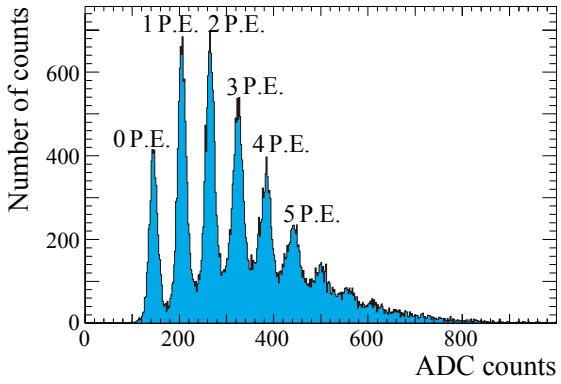

Figure 3.13: Typical charge distribution of the MPPC signal.

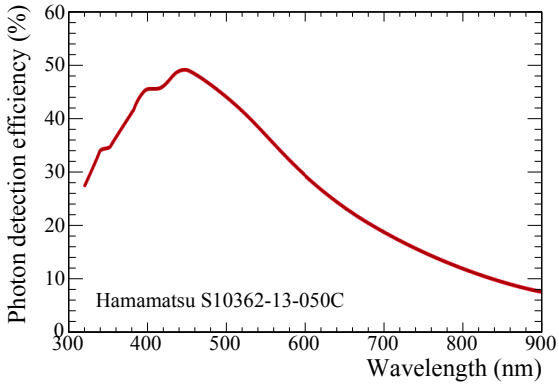

Figure 3.14: Photo detection efficiency spectrum of MPPC for INGRID [145].

Table 3.3: Specifications of MPPC for INGRID (Hamamatsu S10362-13-050C) [145].

Item	Specification
Active area	1.3×13 mm^2
Pixel size	50×50 μm^2
Number of pixels	667
Operation voltage	70 V (typical)
Photon detection efficiency	40% (500 nm)
Dark count (25C°)	<1.35 MHz (0.5 P.E.) <0.135 MHz (1.5 P.E.)

3.3.5 Connectors and cables

Figure 3.15 shows the readout components for INGRID. The WLS fiber is attached to MPPC through a specially developed optical connector [146]. Each MPPC is connected to front-end electronics via co-axial cable (Hirose U.FL-2LP-068) of 150cm [147]. The MPPC is electrically connected to the co-axial cable via a Printed Circuit Board (PCB) connector.

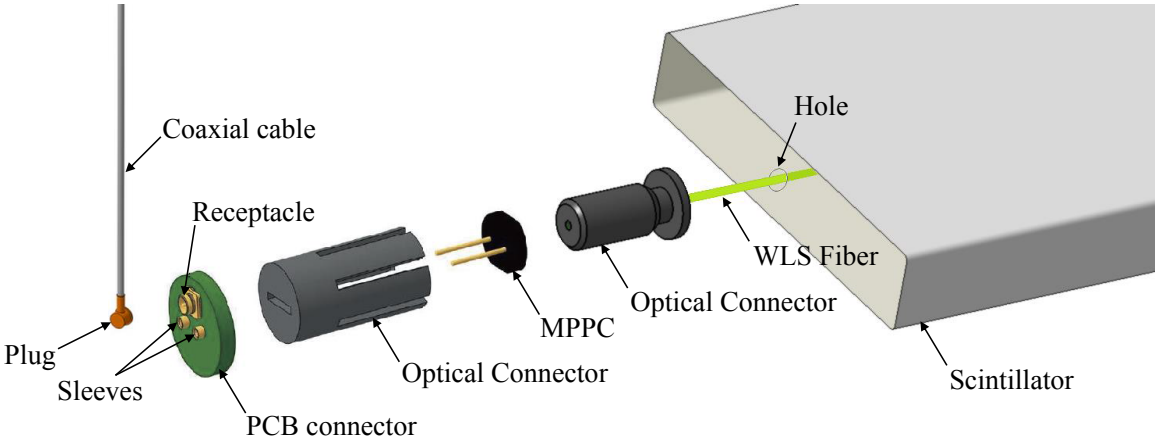

Figure 3.15: Schematic view of the readout components for INGRID and Proton Module.

3.3.6 Readout electronics

Readout electronics of INGRID consist of Trip-t front-end boards (TFBs) [148] and back-end boards (BEBs).

Front-end electronics

The electrical signal from each MPPC is digitized to charge and timing information by the TFB. The TFB is housed in the electronics box attached to the detector (Figs. 3.3, 3.4 and 3.6). A TFB has four ASIC chips (Trip-t) [149], two 10-bit dual channel ADCs (AD9201), eight 8-channel 8-bit DACs (AD5308), an FPGA (Xilinx Spartan 3 [150]) and so on (Fig. 3.16). The MPPC signals are capacitively split (low gain and high gain outputs) and routed to two separate channels of Trip-t. The DACs are used to calibrate the applied voltage to the MPPC channel-by-channel because each MPPC has different breakdown voltage. The specifications of the TFBs are summarized in Table 3.4.

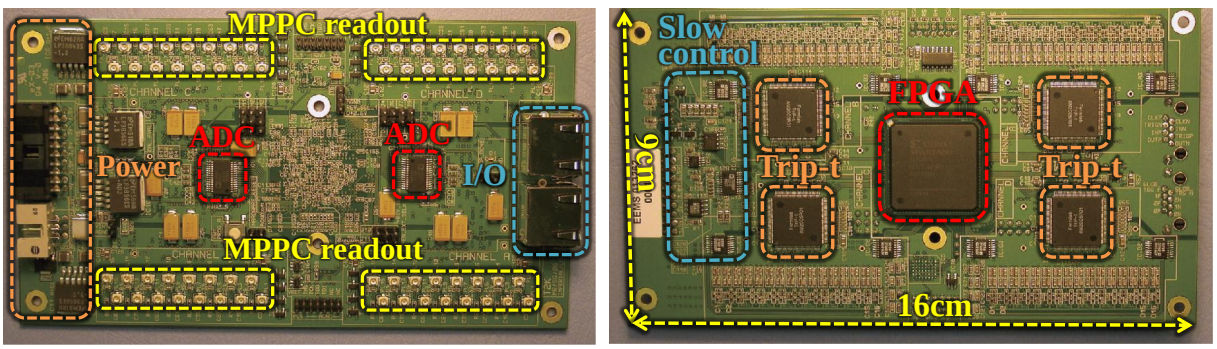

Figure 3.16: Photograph of the TFB top side (left) and bottom side (right).

Table 3.4: Specifications of Trip-t front-end boards

Item	Specification
ADC dynamic range	0∼1000 P.E.
ADC noise level	<0.21 P.E.
TDC resolution	2.5 nsec
DAC range	0∼5 V
DAC resolution	20 mV

Back-end electronics

There are three kinds of back-end boards (BEBs): readout merger module (RMM), master clock module (MCM) and cosmic-ray trigger module (CTM). All BEBs are developed on the same hardware platform with a high-end Virtex II Pro FPGA from Xilinx [151] (Fig. 3.17). Overview of the INGRID readout electronics system is shown in Fig. 3.18. RMMs are connected to TFBs via electrical cables and all BEBs are connected to each other via optical cables. RMMs transmit parameters to TFBs for the set-up and running. An MCM distributes the beam trigger to TFBs via RMMs. It also distributes the cosmic-ray trigger signal generated by a CTM. The CTM generates the cosmic-ray trigger from the primitive signal from TFBs.

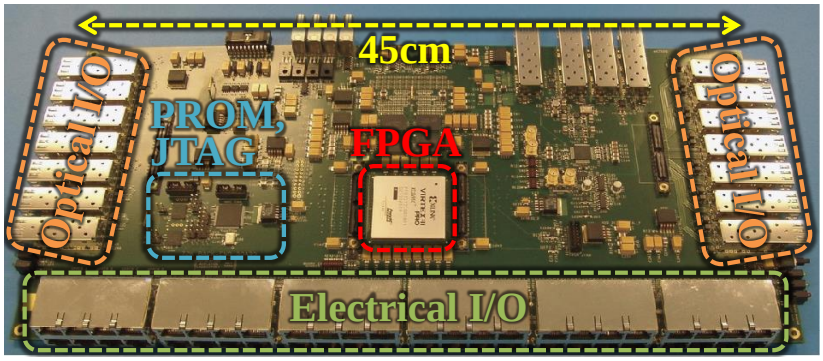

Figure 3.17: Photograph of the back-end board.

3.4 Data acquisition

Figure 3.19 illustrates the timing diagram of the INGRID data acquisition (DAQ). The beam trigger is provided from the accelerator. After getting the beam trigger, the INGRID DAQ system starts to take data of 23 integration cycles. The waiting time from the trigger receipt to the DAQ start was set to 2.5 μsec so that the beam data of the eight bunches are observed in fifth to twelfth cycles. The time window of the integration and the reset is 530 nsec and 50 nsec, respectively, whereas the beam bunch interval is 581 nsec. The beam-included events are not observed in first to fourth and thirteenth to twenty-third cycles. They are used for the studies of the accidental cosmic-ray backgrounds and the MPPC dark counts. In addition, cosmic-ray data is taken between the beam triggers. It is used for the detector performance and stability studies (see Appendix B for details). All of these DAQ systems are managed by the MIDAS framework [152].

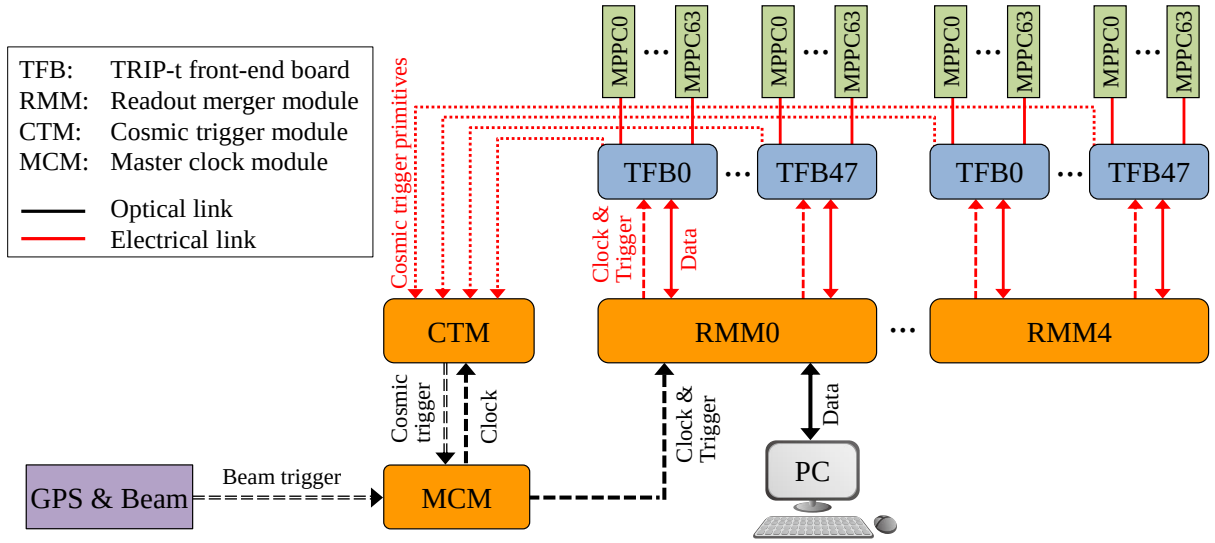

Figure 3.18: Overview of the INGRID readout electronics system.

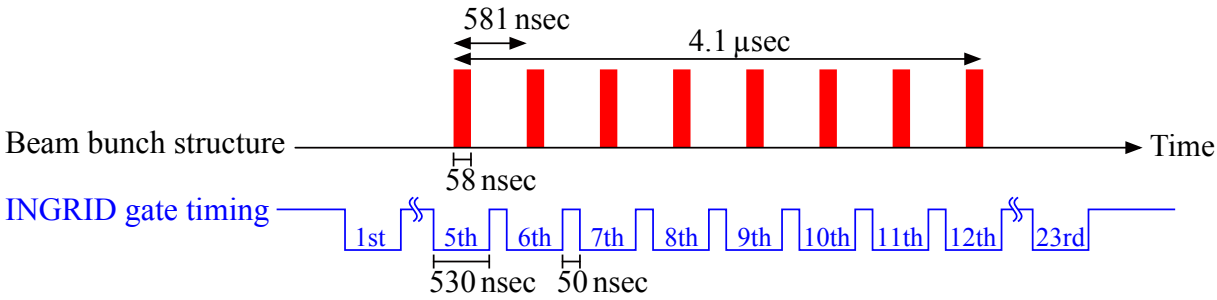

Figure 3.19: Timing diagram of the beam data acquisition.

Chapter 4

Neutrino Event Prediction

The neutrino events in INGRID, ND280 and Super-K are predicted with the Monte Carlo (MC) simulations in three steps (Fig. 4.1):

1. a neutrino beam simulation (Sec. 4.1),
2. a neutrino interaction simulation (Sec. 4.2),
3. detector simulations (Sec. 4.3).

This chapter describes details of them. The neutrino interaction models described in Sec. 4.2 are especially important for the neutrino cross section measurements presented in Chapters 7, 8 and 9.

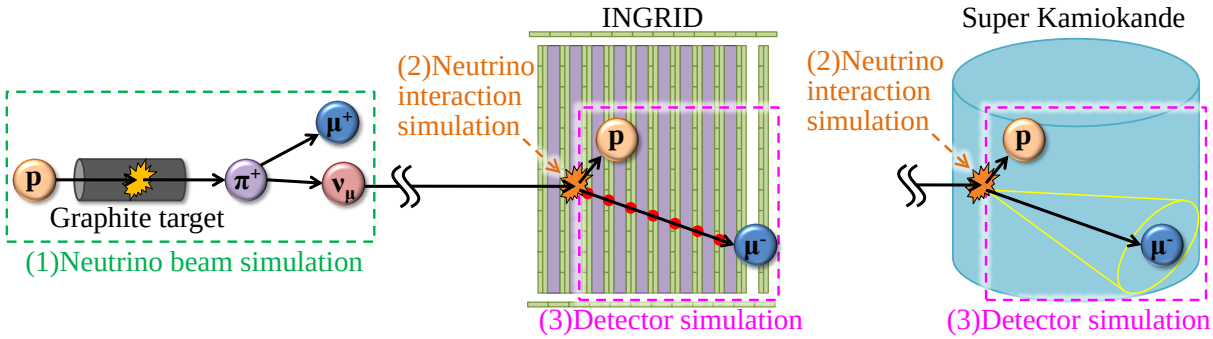

Figure 4.1: Overview of the Monte Carlo simulation.

4.1 Neutrino beam simulation

4.1.1 Method of neutrino flux prediction

The neutrino fluxes and energy spectra at Super-K, ND280 and INGRID are predicted as follows [153]. First, the 30 GeV proton interaction in the production target and its hadronic chains are simulated by FLUKA2008 [154,155] because FLUKA2008 is found to have a good agreement with external hadron production data. The proton beam properties such as spatial distribution are reproduced according to the beam monitor measurements. The particles emitted from the target in the FLUKA2008 simulation are transferred to the JNUBEAM simulation. JNUBEAM is a custom-made Monte Carlo simulation based on GEANT3 framework [156]. It replicates the geometry of the secondary beamline including the horn magnetic fields and tracks the particles

in the material until they decay into neutrinos or are absorbed in the material. Hadron interactions in JNUBEAM are simulated by the GCALOR model [157]. The tracks of neutrinos are extrapolated to Super-K, ND280 and INGRID. Their locations are positioned according to the latest surveying results. Then, the generated neutrino fluxes are tuned based on the external hadron interaction data to suppress its uncertainty. The data sets from the NA61/SHINE experiment [158,159] at CERN, Eichten *et al.* [160] and Allaby *et al.* [161] are used as the external data. Further details about the neutrino beam simulation are described in Appendix C. Figure 4.2 shows the predicted neutrino energy spectra at Super-K, ND280 and INGRID without neutrino oscillations. The neutrino energy spectrum at each INGRID module is different because each module covers different off-axis angle. The difference of the average neutrino energy between the central module and the end modules is about 0.2 GeV.

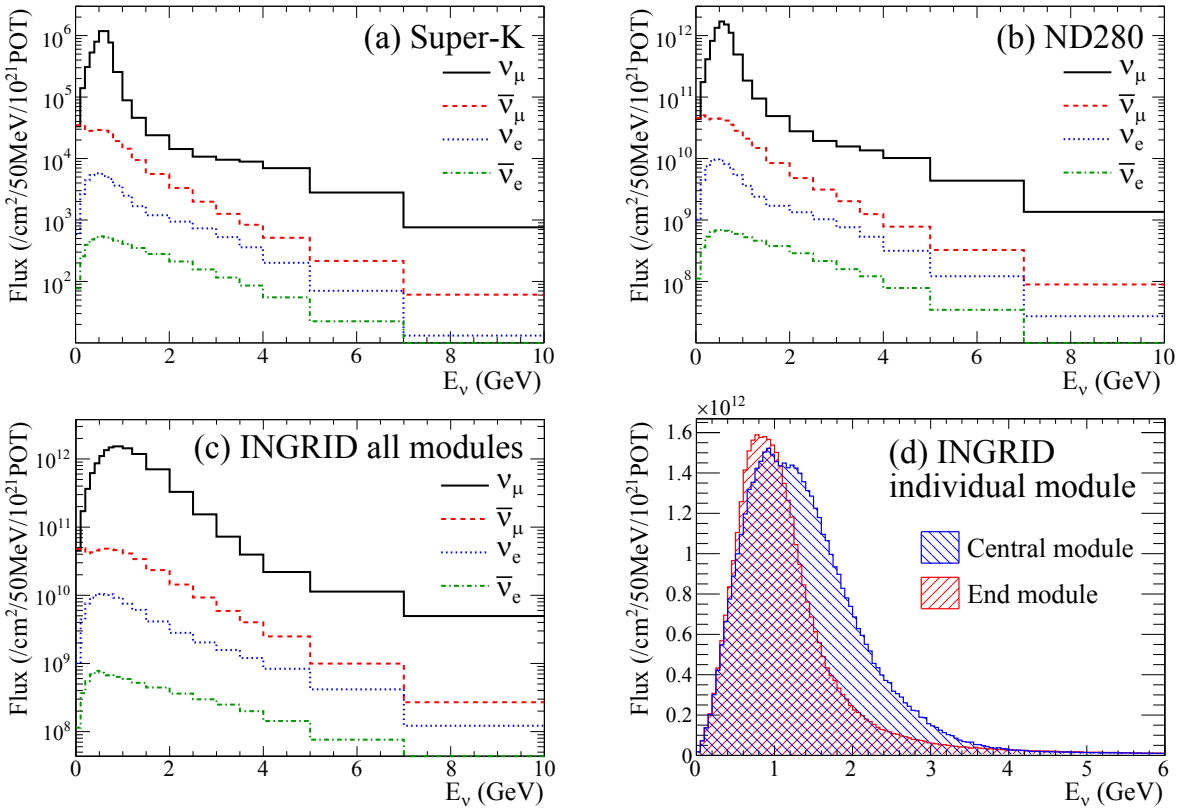

Figure 4.2: Predicted neutrino energy spectra at (a) Super-K, (b) ND280, (c) INGRID all modules and (d) INGRID individual module without neutrino oscillations.

4.1.2 Neutrino flux uncertainties

The neutrino flux uncertainty sources can be separated into two categories: hadron production uncertainties and T2K beamline uncertainties. The uncertainties on hadron production are mainly driven by the NA61/SHINE measurements [158,159] and the Eichten *et al.* and Allaby *et al.* data [160,161]. They include the uncertainties on the production cross section, the secondary nucleon production, the pion production multiplicity and the kaon production multiplicity. The second category of flux uncertainties is associated with operational variations in the beamline conditions during data taking. They include uncertainties in the proton beam position, the neutrino beam direction, the absolute horn current, the horn angular alignment, the horn field asymmetry, the target alignment, and the proton beam intensity. The neutrino beam direction

uncertainty is driven from the measurement with INGRID (described in Chapter 6). The uncertainties of the ν_μ flux at Super-K, ND280, INGRID are shown in Fig. 4.3. The total error is 15% near the peak of the flux energy spectra, and it is dominated by the uncertainties on the hadron production.

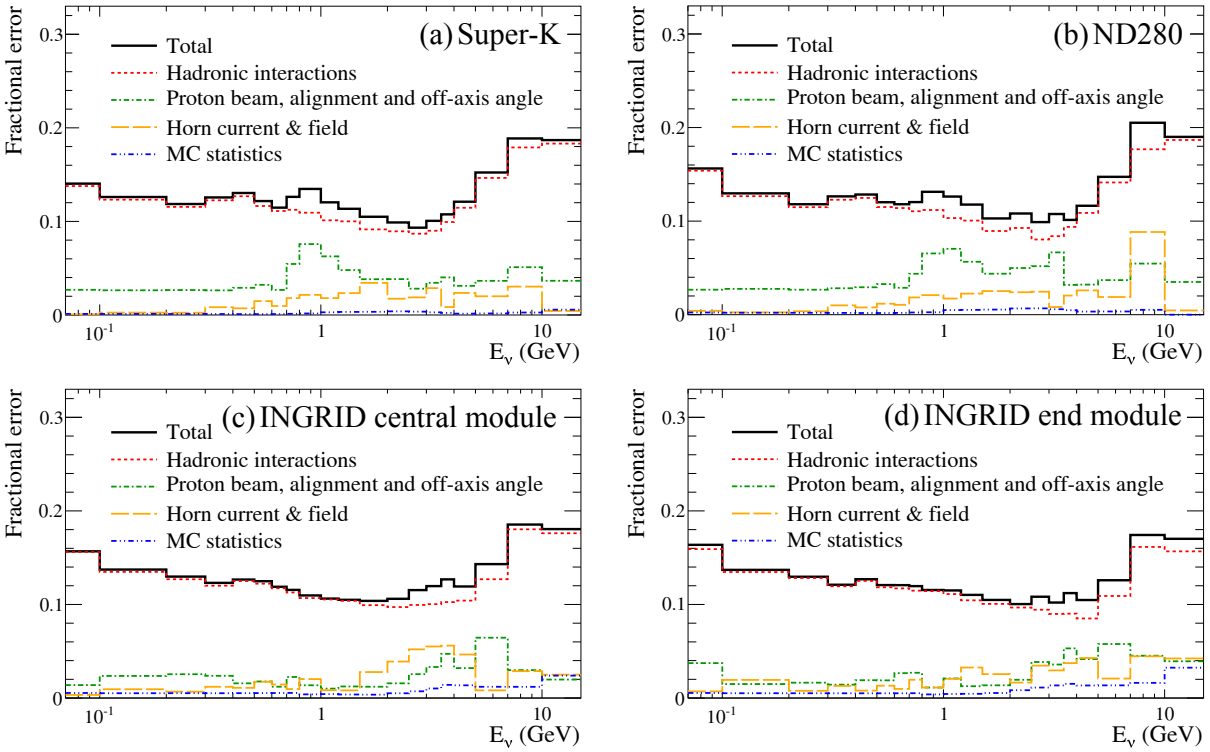

Figure 4.3: Fractional uncertainties of the ν_μ flux at (a) Super-K, (b) ND280, (c) INGRID central module and (d) INGRID end module.

4.2 Neutrino interaction simulation

The neutrino interactions with nuclear targets are simulated with the NEUT program library (version 5.1.4.2) [162–164] which has been used in the Kamiokande, Super-Kamiokande, K2K, SciBooNE, and T2K experiments*. NEUT simulates neutrino interactions with nuclear targets such as protons, oxygen, carbon, and iron, in the neutrino energy range from 100 MeV to 100 TeV. Not only primary neutrino interactions in nuclei but also the secondary interactions of the hadrons in the nuclear medium are simulated in NEUT. There are several other neutrino interaction simulators such as GENIE [165], NUANCE [166], NUGEN [167], GiBUU [168] and NuWro [169]. Because of the poor knowledge of the neutrino interaction, each simulator uses the different models or parameters for some interaction processes, hence predicts different cross section. Thus, cross section predictions by GENIE (version 2.8.0) are used for comparisons of the cross section measurement results, in addition to those by NEUT in this thesis.

*NEUT was originally developed to estimate the neutrino background for the proton decay search in Kamiokande.

4.2.1 Neutrino-nucleus interactions in NEUT

In NEUT, the following neutrino interactions in both charged current (CC) and neutral current (NC) are simulated:

- quasi-elastic scattering ($\nu + N \to \ell + N'$),
- single meson production via baryon resonances ($\nu + N \to \ell + N' + m$),
- coherent pion production ($\nu + A \to \ell + \pi + A$),
- deep inelastic scattering ($\nu + N \to \ell + N' + \text{hadrons}$),

where N and N' are nucleons (proton or neutron) which can be either free or inside nucleus, ℓ is a lepton, m is a meson and A is a nucleus. Figure 4.4 shows the neutrino-nucleus cross sections per nucleon divided by the neutrino energy modeled in NEUT.

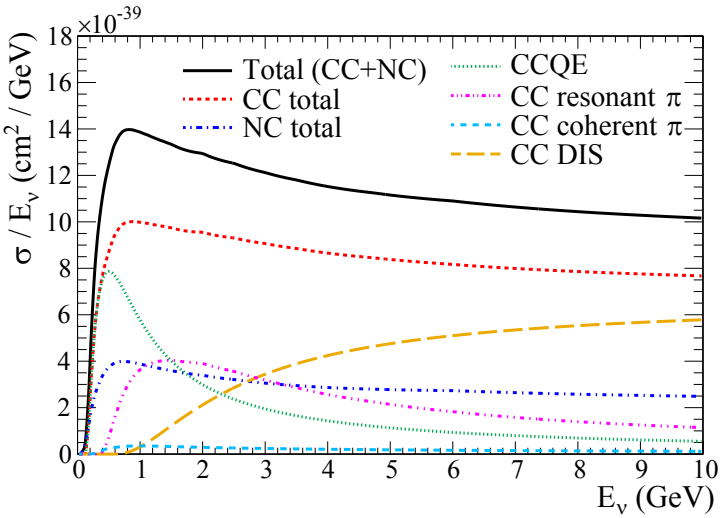

Figure 4.4: Neutrino-nucleus cross sections per nucleon divided by the neutrino energy modeled in NEUT.

Quasi-elastic Scattering

The dominant interaction in the T2K neutrino energy range is the quasi-elastic scattering. For this scattering, the formula by Llewellyn-Smith [170] is used in NEUT. The amplitude of this process is described by the product of the leptonic and hadronic weak currents:

$$\mathcal{M}_{\text{QE}} = \frac{G_F}{\sqrt{2}} \bar{u}(l)\gamma^\mu(1-\gamma^5)u(\nu)\langle N'|J_\mu^{\text{QE}}|N\rangle, \tag{4.1}$$

$$\langle N'|J_\mu^{\text{QE}}|N\rangle = \cos\theta_c \bar{u}(N')\left[\gamma_\mu F_V^1(Q^2) + \frac{i\sigma_{\mu\nu}q^\nu \xi F_V^2(Q^2)}{2m_N} + \gamma_\mu\gamma_5 F_A(Q^2)\right]u(N)\ , \tag{4.2}$$

where G_F is the Fermi coupling constant, J_μ^{QE} is the hadronic current operator for the quasi-elastic scattering, θ_c is the Cabbibo angle, $\xi \equiv \mu_p - \mu_n = 3.71$ is the difference of anomalous dipole moments between a proton and a neutron, m_N is the nucleon mass, and Q is a four-momentum

transfer. The vector form factors, F_V^1 and F_V^2, are represented as

$$F_V^1(Q^2) = \left(1+\frac{Q^2}{4m_N^2}\right)^{-1}\left[G_E^V(Q^2)+\frac{Q^2}{4m_N^2}G_M^V(Q^2)\right] , \tag{4.3}$$

$$\xi F_V^2(Q^2) = \left(1+\frac{Q^2}{4m_N^2}\right)^{-1}\left[G_M^V(Q^2)-G_E^V(Q^2)\right] , \tag{4.4}$$

where G_E^V and G_M^V are the electric and magnetic Sachs form factors [171], given by

$$G_E^V(Q^2) = \frac{1}{\left(1+\frac{Q^2}{M_V^{\mathrm{QE}2}}\right)^2} \quad , \quad G_M^V(Q^2) = \frac{1+\xi}{\left(1+\frac{Q^2}{M_V^{\mathrm{QE}2}}\right)^2} \quad . \tag{4.5}$$

The axial-vector form factor, F_A, is given by

$$F_A(Q^2) = \frac{g_A}{\left(1+\frac{Q^2}{M_A^{\mathrm{QE}2}}\right)^2} , \tag{4.6}$$

where $g_A = -1.23$ is determined from neutron decay measurements [172–174]. Both the vector and axial-vector form factors are assumed to be dipole. The vector mass (M_V^{QE}) and the axial-vector mass (M_A^{QE}) for the quasi elastic scattering are set to be 0.84 GeV/c^2 and 1.21 GeV/c^2, respectively, as suggested by recent results [175, 176].

The differential cross section is expressed as

$$\frac{d\sigma}{dQ^2} = \frac{m_N^2 G_F^2 \cos^2\theta_c}{8\pi E_\nu^2}\left[A(Q^2) \mp B(Q^2)\frac{s-u}{m_N^2} + C(Q^2)\frac{(s-u)^2}{m_N^4}\right] , \tag{4.7}$$

where E_ν is the incident neutrino energy, $s-u \equiv 4m_N E_\nu - Q^2 - m_\ell^2$, m_ℓ is the mass of the outgoing lepton, and

$$\begin{aligned} A(Q^2) = {} & \frac{m_\ell^2+Q^2}{4m_N^2}\left[\left(4+\frac{Q^2}{m_N^2}\right)|F_A|^2 - \left(4-\frac{Q^2}{m_N^2}\right)|F_V^1|^2\right. \\ & + \frac{Q^2}{m_N^2}|\xi F_V^2|^2\left(1-\frac{Q^2}{4m_N^2}\right) + \frac{4Q^2 F_V^1 \xi F_V^2}{m_N^2} \\ & \left. - \frac{m_\ell^2}{m_N^2}\left(|F_V^1+\xi F_V^2|^2 + |F_A|^2\right)\right] , \end{aligned} \tag{4.8}$$

$$B(Q^2) = -\frac{Q^2}{m_N^2}F_A\left(F_V^1+\xi F_V^2\right) , \tag{4.9}$$

$$C(Q^2) = \frac{1}{4}\left(|F_A|^2 + |F_V^1|^2 + \frac{Q^2}{m_N^2}\left|\frac{\xi F_V^2}{2}\right|^2\right) . \tag{4.10}$$

To obtain the cross sections for neutral current elastic scattering, the following relations are used [177, 178]:

$$\sigma(\nu+p\to\nu+p) = 0.153\times\sigma(\nu+n\to l^-+p) , \tag{4.11}$$

$$\sigma(\bar\nu+p\to\bar\nu+p) = 0.218\times\sigma(\bar\nu+p\to l^++n) , \tag{4.12}$$

$$\sigma(\nu+n\to\nu+n) = 1.5\times\sigma(\nu+p\to\nu+p) , \tag{4.13}$$

$$\sigma(\bar\nu+n\to\bar\nu+n) = 1.0\times\sigma(\bar\nu+n\to\bar\nu+n) . \tag{4.14}$$

For scattering off nucleons in the nucleus, we use the relativistic Fermi gas model[†] of Smith and Moniz [179]. The nucleons are treated as quasi-free particles and the Fermi motion of nucleons along with the Pauli exclusion principle is taken into account. The momentum distribution of the target nucleon is assumed to be flat up to a fixed Fermi surface momentum of 217 MeV/c for carbon and 250 MeV/c for iron. The same Fermi momentum distribution is also used for all of the other nuclear interactions. The nuclear potential is set to 27 MeV for carbon and 32 MeV for iron.

Single meson production via baryon resonances

The second most probable interaction in T2K is the resonant single meson production of π, K, and η via baryon resonances. It is described by the model of Rein and Sehgal [180]. The model assumes following processes:

$$\nu + N \rightarrow \ell + N^*, \tag{4.15}$$

$$N^* \rightarrow N' + m \quad (m = \pi,\ \eta,\ K)\ . \tag{4.16}$$

where N^* denotes an intermediate baryon resonance. The amplitudes of the resonant productions for CC and NC interactions are given by:

$$\mathcal{M}_{\mathrm{CCRES}} = \frac{G_F \cos\theta_C}{\sqrt{2}} \bar{u}(l)\gamma^\mu(1-\gamma^5)u(\nu)\langle N'|J_\mu^{\mathrm{RES}}|N\rangle, \tag{4.17}$$

$$\mathcal{M}_{\mathrm{NCRES}} = \frac{G_F}{\sqrt{2}} \bar{u}(\nu)\gamma^\mu(1-\gamma^5)u(\nu)\langle N'|J_\mu^{\mathrm{RES}}|N\rangle, \tag{4.18}$$

J_μ^{RES} is the hadronic current operator for the resonant single meson production containing a vector and an axial-vector part. Along with the quasi-elastic scattering, both the vector and axial-vector form factors are assumed to be dipole, and the vector mass (M_V^{RES}) and axial-vector mass (M_A^{RES}) for the single resonant meson production are set to be 0.84 GeV/c^2 and 1.21 GeV/c^2, respectively. The double differential cross section of single meson production depends on the amplitude for the production of a given resonance and the probability of the baryon resonance decay to the meson:

$$\frac{d^2\sigma}{dQ^2 d\nu} = \frac{1}{32\pi m_N E_\nu^2} \cdot \frac{1}{2} \sum_{\mathrm{spins}} |\mathcal{M}|^2 \cdot \delta(W^2 - M_{N^*}^2)\ , \tag{4.19}$$

where W is the hadronic invariant mass, M_{N^*} is the resonance mass and a negligible decay width is assumed. For resonances with a finite decay width, the double differential cross sections can be derived by replacing the δ-function in Eq. 4.19 with a Breit-Wigner formula [181]:

$$\delta(W^2 - M^2) \rightarrow \frac{1}{2\pi} \frac{\Gamma}{(W-M)^2 + \Gamma^2/4}\ . \tag{4.20}$$

where Γ is the decay width of N^*. The Rein and Sehgal's model is based on the FKR (Feynman-Kislinger-Ravndal) baryon model [182] to express the baryon state. In this model, for the baryon of three quarks, we have the $SU(6)$ spin and flavor multiplet (**56**, **70** and **20**) and spatial excitations of two independent three-dimensional modes of internal harmonic oscillation among the three particles. All intermediate baryon resonances with mass less than 2 GeV/c^2 are included in this model. Those baryon resonances with mass greater than 2 GeV/c^2 are simulated as deep inelastic scattering. Lepton mass effects from the non-conservation of lepton current and

[†]The Fermi gas model treats the nucleus as an ideal gas composed of weakly interacting fermions. See Appendix D for details.

the pion-pole term in the hadronic axial-vector current are included in the simulation [183, 184]. To determine the angular distribution of a pion in the final state, Rein's method [185] is used for the $P_{33}(1232)$ resonance. For other resonances, the directional distribution of the generated pion is set to be isotropic in the resonance rest frame. The angular distribution of π^+ has been measured for $\nu_\mu + p \to \mu^- + p + \pi^+$ [186] and the results agree well with NEUT's prediction. Pauli blocking is accounted for in the decay of the baryon resonance by requiring the momentum of the nucleon to be larger than the Fermi surface momentum. Pion-less Δ decay is also taken into account, where the baryon resonances interact with other nucleons and disappear without pion emissions, resulting in a CCQE-like event having only a lepton and a nucleon in the final state. The probability of this interaction is estimated to be 20% from a theoretical calculation [187].

Coherent pion production

The model of Rein and Sehgal [188, 189] is used to simulate the coherent pion production in NEUT. In the coherent pion production, the outgoing lepton tends to be nearly parallel to the incoming neutrino as described in Chapter 1. In the limit of small-angle scattering, the cross section for neutrino-nucleus scattering depends only on the divergence of the axial-vector part of the weak current. It can be calculated by use of Adler's partially conserved axial-vector current (PCAC) theorem [190], which allows the cross section for neutrino-nucleus scattering to be described in terms of the analogous pion-nucleus interaction. Based on the PCAC theorem, the differential coherent pion production cross section for $Q^2 = 0$ is expressed as

$$\left.\frac{d^3\sigma(\nu + A \to \ell + A + \pi)}{dxdyd|t|}\right|_{Q^2=0} = \frac{G_F^2}{\pi^2} f_\pi^2 m_N E_\nu (1-y) \left.\frac{\sigma(\pi + A \to \pi + A)}{d|t|}\right|_{E_\nu y = E_\pi}, \quad (4.21)$$

where $x = Q^2/2m_N\nu$ and $y = \nu/E_\nu$ are the Bjorken kinematic variables, ν is the energy transfer, $|t|$ is the square of the four-momentum transferred to the nucleus, G_F is the weak coupling constant, f_π is the pion decay constant, and m_N is the mass of nucleon. The relation expresses the forward neutrino cross section at the nucleus A in terms of the cross section for the process $\pi + A \to \pi + A$.

The extrapolation of the cross section to $Q^2 \neq 0$ is done based on the method of hadron dominance, which is an extension of the model used in electromagnetic interactions, the vector meson dominance (VMD) model [191]. The VMD model treats the electromagnetic current as a superposition of the contribution from the lightest vector mesons. Following the calculation of the VMD model, the cross section is then obtained by attaching a propagator term:

$$\frac{d^3\sigma(\nu + A \to \ell + A + \pi)}{dxdyd|t|} = \frac{G_F^2}{\pi^2} f_\pi^2 m_N E_\nu (1-y) \frac{1}{\left(1 + \frac{Q^2}{M_A^{\mathrm{COH}\,2}}\right)^2} \left.\frac{\sigma(\pi + A \to \pi + A)}{d|t|}\right|_{E_\nu y = E_\pi} \quad (4.22)$$

where M_A^{COH} is the axial-vector mass, introduced practically in the propagator.

The pion-nucleus differential cross section is expressed as

$$\frac{d\sigma(\pi + A \to \pi + A)}{d|t|} = A^2 |F_A(|t|)|^2 \left.\frac{d\sigma(\pi + N \to \pi + N)}{d|t|}\right|_{t=0} \quad (4.23)$$

where A is the atomic number of the nucleus, $F_A(|t|)$ is the nuclear form factor (including the effect of pion absorption). With the aid of the optical theorem, the pion-nucleon differential cross section in the forward direction is given by

$$\left.\frac{d\sigma(\pi + N \to \pi + N)}{d|t|}\right|_{t=0} = \frac{1}{16\pi} \left[\sigma_{\mathrm{tot}}^{\pi N}\right]^2 (1 + r^2), \qquad r = \frac{\mathrm{Re}\ f_{\pi N}(0)}{\mathrm{Im}\ f_{\pi N}(0)}\ . \quad (4.24)$$

An average cross section from measurements of pion-deuteron scattering is used to obtain $\sigma_{\rm tot}^{\pi N}$ in this model. For the nuclear form factor,

$$|F_A(|t|)|^2 = \exp(-b|t|)F_{\rm abs} \tag{4.25}$$

is used, where b denotes the width of the nuclear charge distribution related to the nuclear radius R:

$$b = \frac{1}{3}R^2 \qquad (R = R_0 A^{1/3}) \ . \tag{4.26}$$

$F_{\rm abs}$ is a $|t|$-independent attenuation factor representing the effect of pion absorption in the nucleus, expressed as

$$F_{\rm abs} = \exp(-\langle x\rangle/\lambda) \ , \tag{4.27}$$

where $\langle x\rangle$ and λ are the average path length traversed by the pion produced in the nucleus, and the absorption length, respectively. By assuming the nucleus is a homogeneous sphere with a uniform density, $\langle x\rangle$ and λ are calculated as

$$\langle x\rangle = \frac{3}{4}R \ , \qquad \lambda = A\left(\frac{4\pi R^3}{3}\right)^{-1}\sigma_{\rm inel}^{\pi N} \ , \tag{4.28}$$

where $\sigma_{\rm inel}^{\pi N}$ is the pion-nucleon inelastic cross section. As a result of this,

$$F_{\rm abs} = \exp\left(-\frac{9A^{1/3}}{16\pi R_0^2}\sigma_{\rm inel}^{\pi N}\right) \tag{4.29}$$

is obtained. Hence, the differential cross section for coherent pion production in the model of Rein and Sehgal is expressed as

$$\begin{aligned}\frac{d^3\sigma(\nu + A \to \ell + A + \pi)}{dxdyd|t|} &= \frac{G_F^2}{\pi^2} f_\pi^2 m_N E_\nu (1-y) \frac{1}{\left(1+\frac{Q^2}{M_A^{\rm COH\,2}}\right)^2} \frac{A^2}{16\pi}\left[\sigma_{\rm tot}^{\pi N}\right]^2 (1+r^2) \\ &\times \exp\left(-\frac{R_0^2 A^{2/3}|t|}{3}\right)\exp\left(-\frac{9A^{1/3}}{16\pi R_0^2}\sigma_{\rm inel}^{\pi N}\right) \ . \end{aligned} \tag{4.30}$$

The Rein and Sehgal model predicts three features of coherent pion production as follows

1. Since the axial parts of the neutral and charged currents form a triplet in isospace, we are led to

$$f_{\pi^0}^2 = \left(\sqrt{\frac{1}{2}} f_{\pi^+}\right)^2 = \frac{1}{2} f_{\pi^+}^2 . \tag{4.31}$$

   Therefore, the model predicts the relation between the neutral and charged current coherent pion production cross sections as $\sigma({\rm CC}) = 2 \times \sigma({\rm NC})$. The relation is slightly modified due to the lepton mass correction applied to the charged current coherent pion production. [189].

2. The A dependence of the coherent pion production cross section is approximately $A^{1/3}$ as the result of integrations of Eq. 4.30 over x, y and $|t|$.

3. The model predicts the same cross section for coherent pion production by neutrinos and antineutrinos.

In our MC simulation, the axial-vector mass, $M_A^{\rm COH}$, is set to 1.0 GeV/c^2, and the nuclear radius parameter, R_0, is set to 1.0 fm. The total and inelastic pion-nucleon cross sections in Eq. 4.30, $\sigma_{\rm tot}^{\pi N}$ and $\sigma_{\rm inel}^{\pi N}$, are taken from Rein and Sehgal's paper [188] in which they are parameterized by making line-fits to data from CERN-HERA [192].

Deep inelastic scattering (DIS)

The double differential cross section for the charged current deep inelastic scattering (DIS) is calculated as:

$$\frac{d^2\sigma}{dxdy} = \frac{G_F^2 m_N E_\nu}{\pi}\left[\left(1-y+\frac{1}{2}y^2+C_1\right)F_2(x) \pm y\left(1-\frac{1}{2}y+C_2\right)xF_3(x)\right], \quad (4.32)$$

$$C_1 = \frac{m_\ell^2(y-2)}{4m_N E_\nu x} - \frac{m_N xy}{2E_\nu} - \frac{m_\ell^2}{4E_\nu^2}, \quad (4.33)$$

$$C_2 = -\frac{m_\ell^2}{4m_N E_\nu x}, \quad (4.34)$$

where $x \equiv Q^2/(2m_N(E_\nu - E_\ell) + m_N^2)$ and $y \equiv (E_\nu - E_\ell)/E_\nu$ are the Bjorken scaling parameters, and E_ℓ is the energy of the final state lepton. The nucleon structure functions, F_2 and xF_3, are calculated using the GRV98 (Glück-Reya-Vogt-1998) parton distribution functions [193]. In addition, we have included the corrections in the small Q^2 region developed by Bodek and Yang [194,195]. In the calculation, the hadronic invariant mass, W, is required to be larger than 1.3 GeV/c^2.

The multi-hadron final states are simulated with two models. In the range of $1.3 < W < 2.0$ GeV/c^2, a custom-made program [196] is employed where the mean multiplicity of pions is estimated from the experimental result [197] and the number of pions for each event is determined using KNO (Koba-Nielsen-Olesen) scaling [198]. For the events with $W > 2$ GeV/c^2, PYTHIA/JETSET [199] is used to calculate the kinematics of hadronic final states.

To obtain the cross sections for neutral current deep inelastic scattering, we use the following relations:

$$\frac{\sigma(\nu \text{ NC-DIS})}{\sigma(\nu \text{ CC-DIS})} = \begin{cases} 0.26 & (E_\nu \le 3 \text{ GeV}) \\ 0.26 + 0.04 \times (E_\nu/3 - 1) & (3 < E_\nu < 6 \text{ GeV}) \\ 0.30 & (E_\nu \ge 6 \text{ GeV}) \end{cases}, \quad (4.35)$$

$$\frac{\sigma(\bar{\nu} \text{ NC-DIS})}{\sigma(\bar{\nu} \text{ CC-DIS})} = \begin{cases} 0.39 & (E_\nu \le 3 \text{ GeV}) \\ 0.39 - 0.02 \times (E_\nu/3 - 1) & (3 < E_\nu < 6 \text{ GeV}) \\ 0.37 & (E_\nu \ge 6 \text{ GeV}) \end{cases}. \quad (4.36)$$

These relations are estimated from the experimental results [200, 201].

4.2.2 Neutrino-nucleus interactions in GENIE

GENIE uses the Llewellyn Smith formalism with the relativistic Fermi gas model for the quasi-elastic scattering, the Rein-Sehgal model for the single resonant meson production and the coherent pion production and GRV98 parton distribution functions with Bodek-Yang modifications for the deep inelastic scattering in common with NEUT. However, GENIE uses some different approaches from NEUT as follows.

- Some default values of model parameters used in GENIE are different from NEUT as shown in Table 4.1.
- In the treatment of nuclear effects, GENIE incorporates short range nucleon-nucleon correlations in the relativistic Fermi gas model and handles kinematics for off-shell scattering according to the model of Bodek and Ritchie [202] while NEUT uses the Smith-Moniz model [179].

Table 4.1: Default values of model parameters used for neutrino interaction simulation.

Model parameter	NEUT	GENIE
Axial-vector mass for quasi elastic scattering (M_A^{QE})	1.21 GeV/c^2	0.99 GeV/c^2
Axial-vector mass for resonant meson production (M_A^{RES})	1.21 GeV/c^2	1.12 GeV/c^2
Axial-vector mass for coherent pion production (M_A^{COH})	1.0 GeV/c^2	1.0 GeV/c^2
Hadronic invariant mass cut off for resonant meson production	2.0 GeV/c^2	1.7 GeV/c^2

- For the non-resonant process at low W, GENIE uses the Andreopoulos-Gallagher-Kehayias-Yang (AGKY) hadronization model [203] to decompose the Bodek and Yang model into single pion and two pion production contributions while NEUT uses W-dependent function to determine the pion multiplicity.
- For the coherent pion production, GENIE uses a recent revision of the Rein-Sehgal model [189] while NEUT uses the original Rein-Sehgal model [188]. In the revised Rein-Sehgal model, the PCAC formula was updated to take into account lepton mass terms. In addition, the revised Rein-Sehgal model uses more modern pion-nucleon cross section data taken from PDG2008 [204] for the cross section calculation in Eq. 4.30.

4.2.3 Intra-nuclear interactions in NEUT

NEUT also simulates intra-nuclear interactions of mesons and nucleons which are produced in neutrino interactions [‡]. These interactions are treated using a cascade model [205], and each of the particles is traced until it escapes from the nucleus. The probability distribution of the neutrino interaction position in the nucleus is calculated using the Wood-Saxon type nucleon density distribution [206]:

$$\rho(r) = \frac{Z}{A}\rho_0 \left[1 + \exp\left(\frac{r-c}{a}\right)\right]^{-1} , \tag{4.37}$$

where $\rho_0 = 0.48 m_\pi^3$, A and Z are the mass number and atomic number of the nucleus, respectively. For carbon nucleus, $a = 0.52$ fm and $c = 2.36$ fm [207]. Fermi motion of nucleons in the nucleus and Pauli blocking effect are taken into account in the simulation. The Fermi surface momentum at the interaction point is defined as

$$p_F(r) = \left(\frac{3}{2}\pi^2 \rho(r)\right)^{\frac{1}{3}} . \tag{4.38}$$

Pion interactions

The inelastic scattering, charge exchange and absorption of pions in the nuclei are simulated. The interaction cross sections of pions in the nuclei are calculated using the model by Salcedo *et al.* [208], which agrees well with past experimental data [209]. If inelastic scattering or charge exchange occurs, the direction and momentum of outgoing pions are determined by using results from a phase shift analysis of pion-nucleus scattering experiments [210]. Figure 4.5 shows the results on the pion scattering simulations compared to experimental data.

[‡]Such intra-nuclear interactions are often referred to as the final state interactions (FSI) in the neutrino interaction community.

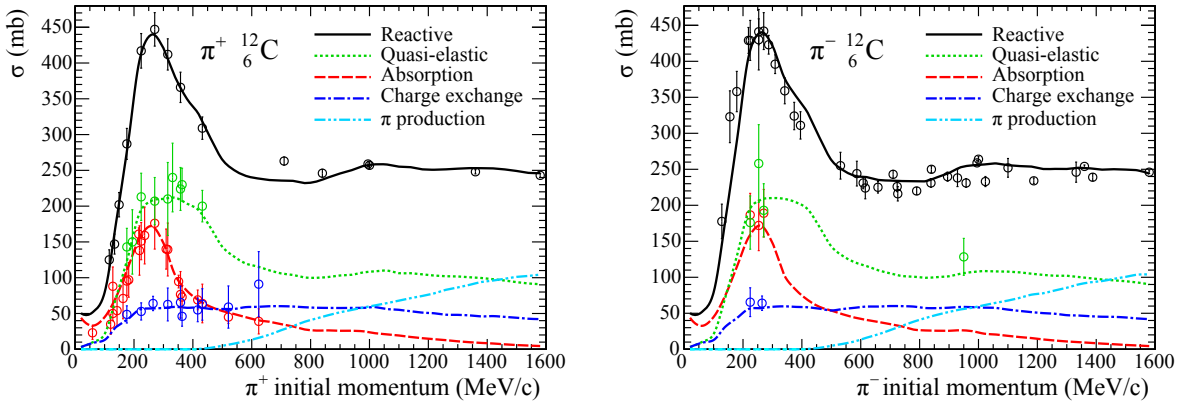

Figure 4.5: NEUT simulations of π^+-^{12}C scattering (left) and π^--^{12}C scattering (right) compared to experimental data.

Nucleon interactions

Re-interactions of the recoil protons and neutrons produced in neutrino interactions are also simulated. Nucleon-nucleon interactions modify the outgoing nucleon's momentum and direction. Both elastic scattering and pion production are considered. The differential cross sections were obtained from nucleon-nucleon scattering experiments [211]. For pion production, the isobaric nucleon model [212] is used.

4.2.4 Neutrino interaction model uncertainties

We used a data-driven method to calculate the neutrino interaction model uncertainties, where NEUT predictions are compared to external neutrino-nucleus interaction data in the energy region relevant for T2K. We fit the free parameters of the models implemented in NEUT, and introduce ad hoc parameters, often with large uncertainties, to take into account remaining discrepancies between NEUT and the data. The model parameters and the ad hoc parameters are as follows.

Axial-vector masses
: Axial-vector masses for quasi-elastic scatterings and resonant meson productions, M_A^{QE} and M_A^{RES}, are included in the model. The uncertainties on them are evaluated from the fits of the MiniBooNE CCQE data [213] and CC single pion production data [214–216].

π-less Δ decay parameter
: This parameter changes the probability of the π-less Δ decay process. An absolute error of 20% is assigned.

Fermi gas model parameters
: The Fermi momentum (p_F) and the binding energy (E_B) are included in the Fermi gas model. The uncertainties on them are determined from electron-nucleus scattering data [217].

Spectral function parameter
: Spectral function [218] is known as a more sophisticated nuclear model than the relativistic Fermi gas model. It is made up of a part for single particles and that from correlated pairs of nucleons. The former part is obtained from mean-field calculations and electron-nucleus scattering experiments, and the latter part is evaluated in local-density approximation. As a result, the momentum distribution of a nucleon in a nucleus given by the spectral

function is uneven and extends out to very high momentum while it is assumed to be flat up to a fixed Fermi surface momentum in the relativistic Fermi gas model as shown in Fig. 4.6. Electron-nucleus scattering data demonstrate that the spectral function is the better representation of the nuclear model [219, 220] (Fig. 4.7). Thus, the spectral function parameter is introduced to take in the difference in the two nuclear models. When this parameter is set to one (zero), the nuclear model represents the spectral function (the relativistic Fermi gas model). Hence, it is truncated between zero and one. The intermediate state between zero and one is implemented by means of interpolation. More details of the spectral function and the Fermi gas model are described in Appendix D.

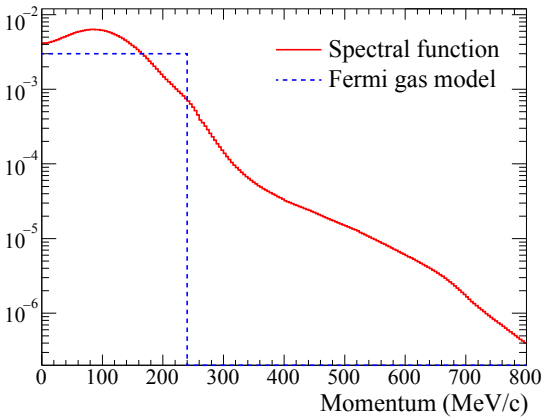

Figure 4.6: Nucleon momentum distributions from the relativistic Fermi gas model and the spectral function for ^{16}O.

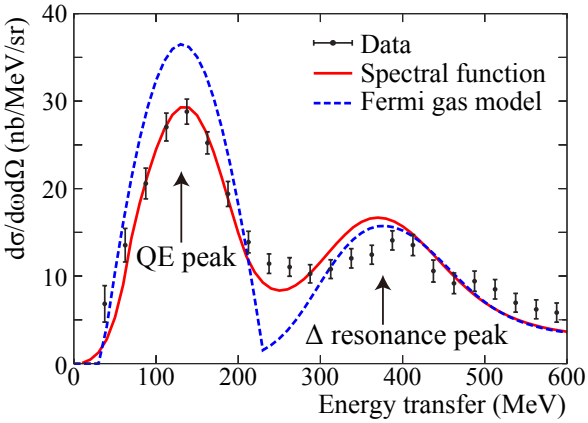

Figure 4.7: Differential cross section of electron scattering on ^{16}O at electron beam energy of 880 MeV. This figure was taken from Ref. [220].

Normalization parameters for interaction types

These parameters scale the size of the cross section for each interaction type. They are introduced to take account of discrepancies between the model and external data [213–216, 221–226]. There are overall normalizations for CC coherent pion, NC1π^0, NC1$\pi^\pm$, NC coherent pion, and NC other interactions. On the other hand, the normalization for CCQE (CC1π) interactions is defined separately for three (two) neutrino energy regions, and that for other CC interactions (mainly CC deep inelastic scatterings) is defined as a function of the neutrino energy.

***W*-shape parameter**

This parameter changes the width of the hadronic resonance. It is introduced to modify the shape of the pion momentum distributions in resonance interactions, which shows poor agreement with MiniBooNE NCπ^0 data [216].

Normalization parameters for ν_e and $\bar{\nu}$

Foregoing parameters and uncertainties on the neutrino interaction are determined from the experimental results of ν_μ interactions. Thus, additional overall 3% and 20% uncertainties are assigned to the cross sections of ν_e and $\bar{\nu}$, respectively, based on calculations over the T2K energy range [227].

Intra-nuclear interactions

Uncertainties of the pion intra-nuclear interactions are estimated from the external pion-nuclei scattering data [228–239]. Uncertainties of the nucleon intra-nuclear interactions are estimated from the measured yield of scattered protons in electron scattering data on ^{12}C nucleus [240].

The nominal values and uncertainties of these parameters are summarized in Table 4.2. Details of the derivations of the uncertainties are described in Appendix D.

Table 4.2: The nominal values and the uncertainties of the interaction parameters. 0 and 1 in the nominal value mean that the effect or the normalization is not implemented and is implemented by default, respectively.

Parameter	Nominal value	Uncertainty
M_A^{QE}	1.21 GeV/c^2	16.53%
M_A^{RES}	1.21 GeV/c^2	16.53%
CCQE normalization (E_ν <1.5 GeV)	1	11%
CCQE normalization (1.5< E_ν <3.5 GeV)	1	30%
CCQE normalization (E_ν >3.5 GeV)	1	30%
CC1π normalization (E_ν <2.5 GeV)	1	21%
CC1π normalization (E_ν >2.5 GeV)	1	21%
CC coherent π normalization	1	100%
CC other E_ν shape	0	40%
NC1π^0 normalization	1	31%
NC1$\pi^\pm$ normalization	1	30%
NC coherent π normalization	1	30%
NC other normalization	1	30%
ν_e normalization	1	3%
$\bar{\nu}$ normalization	1	20%
W-shape parameter	87.7 MeV/c^2	52%
π-less Δ decay parameter	0.2	20%
Spectral function parameter	0	100%
Fermi momentum for Fe	250 MeV/c	12%
Fermi momentum for CH	217 MeV/c	13.83%
Binding energy for Fe	33 MeV	27.27%
Binding energy for CH	25 MeV	36%
Pion absorption	1	50%
Pion charge exchange (low energy)	1	50%
Pion charge exchange (high energy)	1	30%
Pion QE scattering (low energy)	1	50%
Pion QE scattering (high energy)	1	30%
Pion inelastic scattering	1	50%
Nucleon interaction	1	10%

4.3 Detector simulation

4.3.1 INGRID

Detector structure and passage of particles

The INGRID detector simulation was developed using the GEANT4 (version 9.2.01.00) framework [241]. It models the real detector structures. The geometries of the scintillator strips with the reflector coating and the iron plates are reproduced based on the measured dimensions (Figs. 3.7 and 3.9). The particles' motion and physics interactions with the materials are simulated, and the energy deposit of each particle inside the scintillator is stored. Simulations of

hadronic interactions are performed with the QGSP BERT (Quark-Gluon String Precompound with Bertini cascade) physics list [242].

Response of detector components

The energy deposit inside the scintillator is converted into the number of photons. Quenching effects of the scintillation are modeled based on the Birks' law [243, 244] and the result of a proton beam irradiation test (Fig. 4.8). The effects of collection and attenuation of the light in the scintillator and the WLS fiber are modeled based on the results of electron beam irradiation tests (Fig. 4.9). The non-linearity of the MPPC response is also taken into account because the number of detectable photons is limited by the number of MPPC pixels. The light yield is smeared according to statistical fluctuations and electrical noise. The dark counts of MPPCs are added with a probability calculated from the measured dark rate. Since the response of ADCs on TFBs is not linear, it is modeled based on the results of a charge injection test to the ADCs (Fig. 4.10).

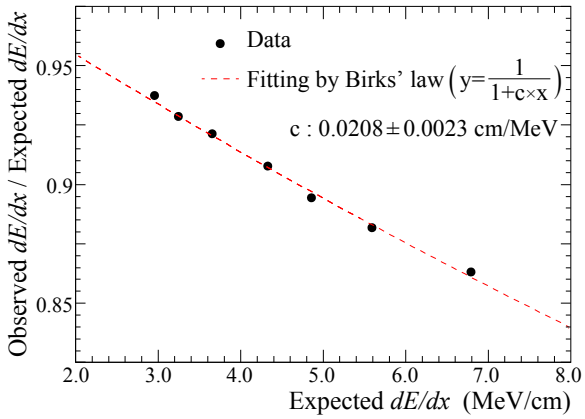

Figure 4.8: Ratio of the observed dE/dx to the expected dE/dx as a function of the expected dE/dx measured by the proton beam irradiation test. The attenuation is attributed to the scintillator quenching.

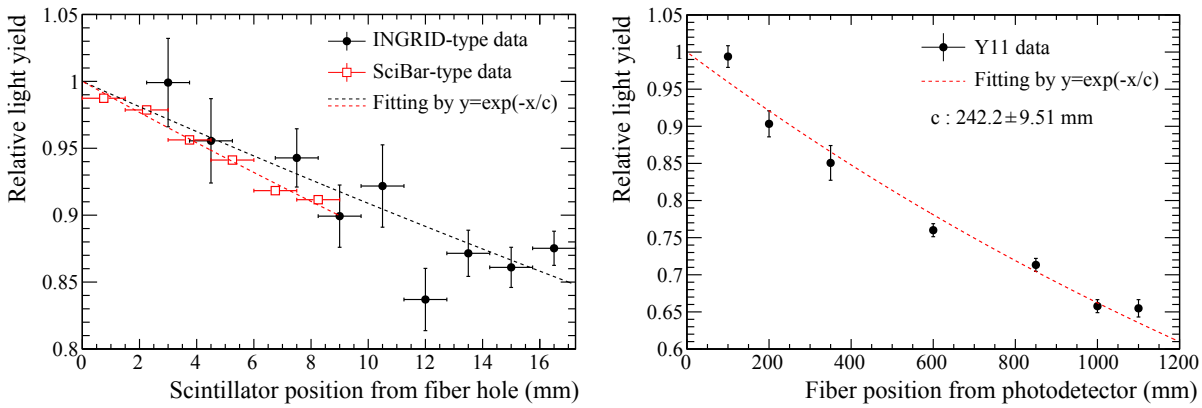

Figure 4.9: Light attenuation effect in scintillator (left) and that in fiber (right) measured by the electron beam irradiation tests.

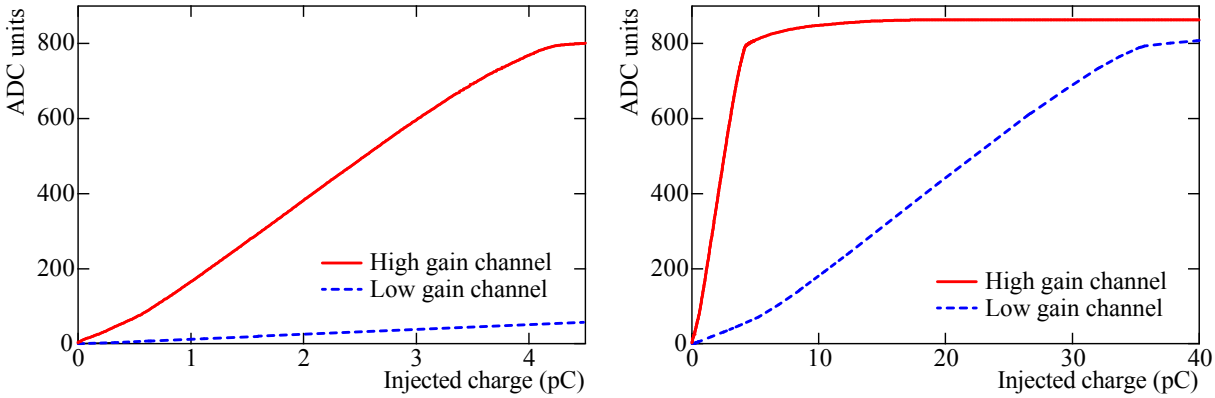

Figure 4.10: Response of ADCs on TFBs as a function of the injected charge in the region of $0 \sim 5$ pC (left) and $0 \sim 40$ pC (right).

Simulation of external backgrounds

The particles produced from the neutrino interactions in the walls of the ND280 hall are considered as the background source. In the background MC simulation, the neutrino flux at the upstream plane from INGRID is generated and the neutrino interaction is uniformly generated in the upstream wall region shown in Fig. 4.11. Muons produced from the neutrino interactions in the walls are used as the control sample to evaluate the detector simulation. The light yield and hit detection efficiency[§] for the muons in the MC simulation agree well with the data as shown in Figs. 4.12 and 4.13.

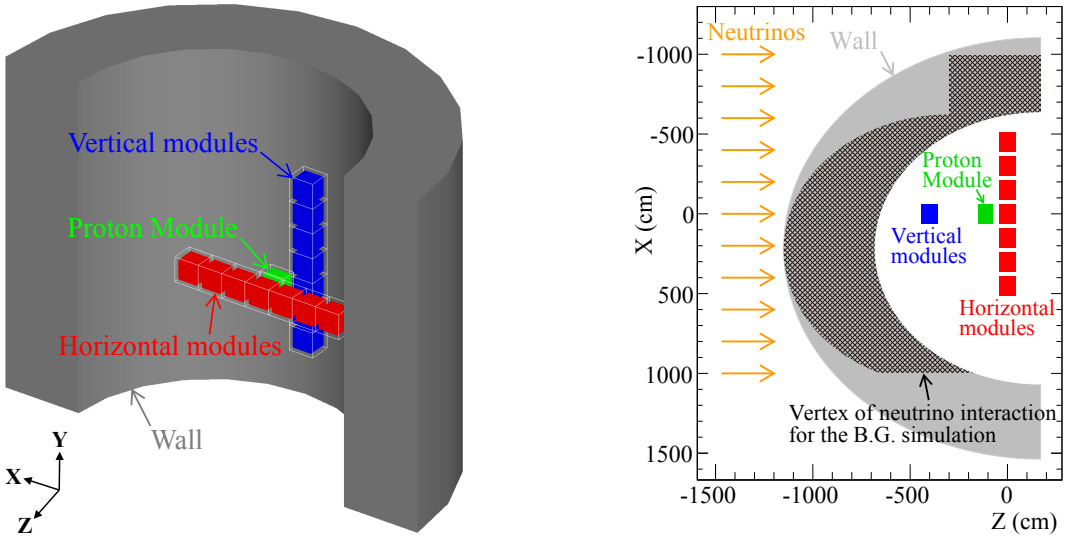

Figure 4.11: The walls of the ND280 hall reproduced in the GEANT4 simulation (left) and the vertex of the neutrino interaction for the background MC simulation (right).

[§]The methods of estimating the light yield and hit detection efficiency are described in Appendix B.

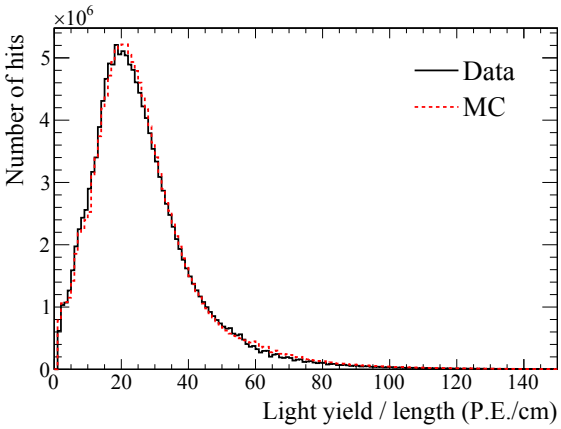

Figure 4.12: The light yield distribution for muons produced from the neutrino interactions in the walls.

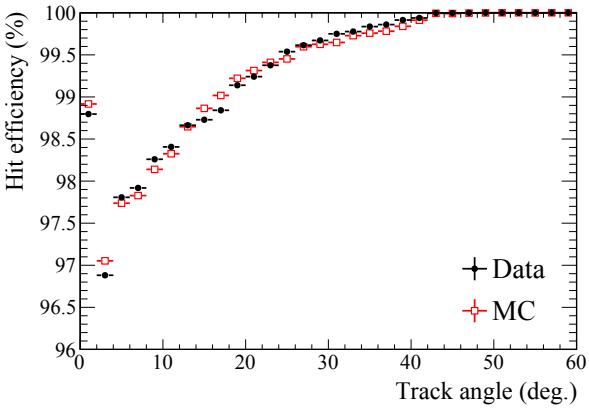

Figure 4.13: Hit detection efficiency for muons produced from the neutrino interactions in the walls as a function of the track angle.

4.3.2 ND280

GEANT4 is also used to simulate the response of the ND280 detectors[¶]. The geometry of the detectors is constructed in GEANT4 code and the energy deposits from the final state particles that pass through the detector is simulated. The response of the active detectors (scintillator strips, WLS fibers, MPPCs and electronics, and TPC electron drift and electronics) is simulated through custom-written code [111, 245].

4.3.3 Super-Kamiokande

The Super-Kamiokande detector response to the particle generated in the neutrino interaction is simulated by SKDETSIM [111], a program library based on GEANT3 [156]. SKDETSIM simulates the particle propagation across the detector, Cherenkov photon propagation, photo-electron production at PMT and response of the electronics. For the propagation of the Cherenkov photons in water, the absorption, Raleigh scattering and Mie scattering are considered. The parameters of the scatterings are tuned based on measurements with calibration sources. The refractive index of water is set at a value from the experimental data [246]. In addition to the propagation in water, the reflection, refraction and absorption at the detector components such as the PMT surface are also implemented. The absolute quantum efficiency for the photo-electron production at PMT refers to the measurement by Hamamatsu Photonics K.K. The relative efficiency of the PMTs is calibrated by the measurement with the Ni calibration source [247]. The energy scale for SKDETSIM is checked by using cosmic data. For all samples, the agreement of the energy scale between data and SKDETSIM is within a few percent as shown in Fig. 4.14.

[¶]The ND280 detector simulation was developed independently of INGRID.

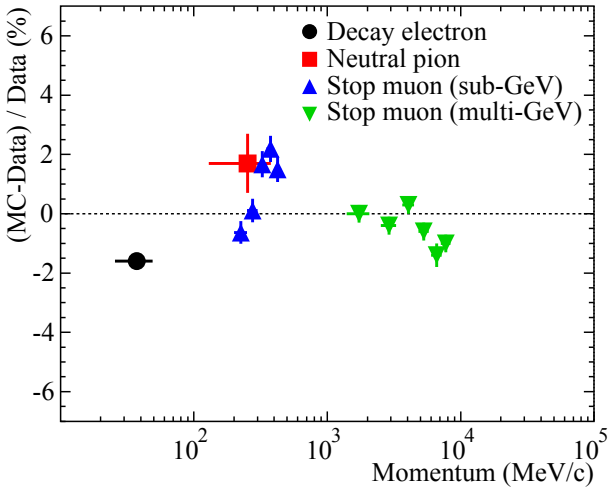

Figure 4.14: Comparison between data and the SKDETSIM prediction of the reconstructed momentum of different event samples derived from cosmic ray events observed in Super-Kamiokande.

Chapter 5

Overview of Measurements

This chapter describes the overview of the measurements of neutrino beam properties, neutrino interaction cross sections and neutrino oscillations in the T2K experiment which are presented from the next chapter.

5.1 Overall flow of measurements

Figure 5.1 illustrates the overall flow of the T2K neutrino oscillation measurement. The MC simulations for the neutrino beam, neutrino interaction, and detector response were constructed as described in Chapter 4. They are used to predict the energy spectra at Super-K. Uncertainties on the neutrino flux and neutrino interaction are evaluated with the external data and are further constrained by the ND280 measurement. The neutrino oscillation analysis is performed by comparing the measured energy spectra of ν_e and ν_μ at Super-K with the expected ones.

The precise neutrino oscillation measurement requires good knowledge of the neutrino flux and the neutrino interaction. Therefore, the measurement of the neutrino beam properties and the neutrino interaction cross sections plays an important role in the T2K experiment. They will gain further importance in the future because the statistical error that is currently dominant will be reduced, and the systematic errors from the uncertainties of the neutrino beam and neutrino interaction will be dominant in the future.

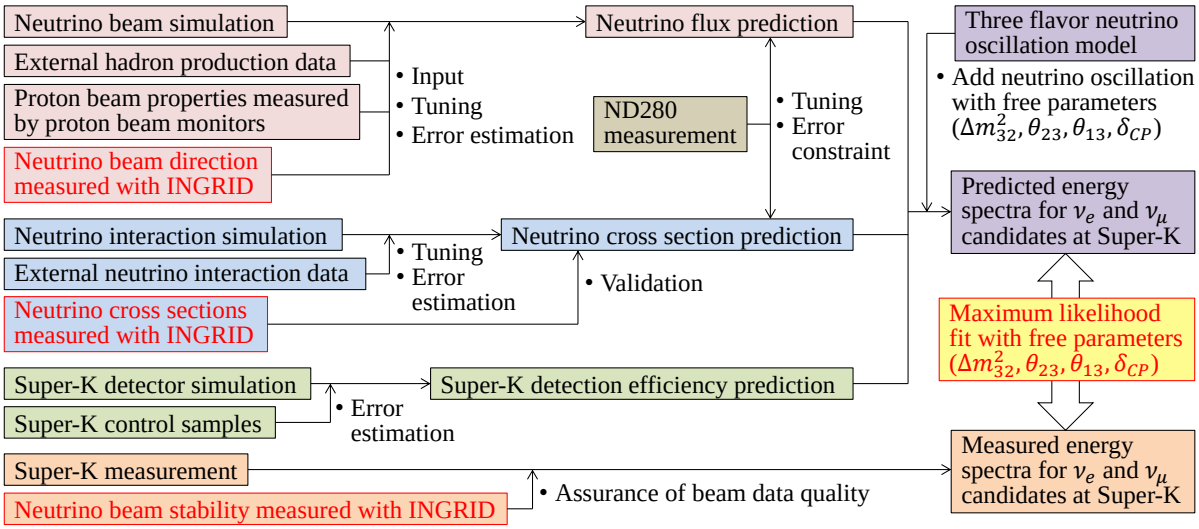

Figure 5.1: Overview of the neutrino oscillation measurement flow. The main topics of this thesis are written in red letters.

5.2 Measurement of neutrino beam properties

The off-axis neutrino beam is very sensitive to the neutrino beam direction. Thus, for the accurate prediction of the neutrino flux, the neutrino beam direction is required to be controlled within 1 mrad and be measured with a much better precision. In addition, measurement of other neutrino beam properties such as the neutrino event rate and the neutrino beam width are also important to check the validity of the neutrino flux prediction. Moreover, the monitoring of the stability of these neutrino beam properties is essential to assure the beam data quality because T2K is a long-term experiment. The stability of the neutrino event rate is especially important to check the damage of the neutrino production target. The damage of the target is a matter of concern for T2K because graphite which constitutes the target is fragile and the T2K proton beam is intense. It can be checked by the neutrino event rate stability because a serious damage of the target causes a decrease in the neutrino event rate. They are achieved by the neutrino beam property measurement with INGRID. Details of the measurement are described in Chapter 6.

5.3 Measurement of neutrino-nucleus cross sections

The neutrino interaction models used in T2K were evaluated by the external neutrino-nucleus interaction data as described in Chapter 4. However, the reliability and precision of the neutrino interaction models are not sufficiently high because there are only a few external neutrino-nucleus interaction data in a few GeV region. Therefore, the neutrino interaction models should be further validated and improved by the T2K internal neutrino-nucleus interaction data. In addition, since there are many unsolved problems in the neutrino-nucleus interaction in a few GeV region, an accurate understanding of the neutrino-nucleus interaction may reveal something we are missing. Thus, the neutrino-nucleus interaction in a few GeV region is a physics topic of great interest as well as the neutrino oscillation. For these reasons, we measured the CC inclusive cross section, the CCQE cross section and the CC coherent pion production cross section in a few GeV region using INGRID (mainly the Proton Module), and details of each cross section measurement are presented in Chapters 7, 8 and 9, respectively. The results of the cross section measurements are discussed from a broad perspective of the neutrino interaction physics in the final section of each chapter. In this thesis, the results were used to check the validity of the neutrino interaction models used in T2K. In the future, they will be used to improve the neutrino interaction models and to reduce the uncertainties on the models.

5.4 Measurement of neutrino oscillations

Finally, a neutrino oscillation analysis is performed using the neutrino flux prediction, the neutrino interaction models, and the Run 1-4 ND280 and Super-K data. To date, analysis for the measurement of $\sin^2 2\theta_{13}$ and δ_{CP} via the $\nu_\mu \to \nu_e$ oscillation and that of $\sin^2 \theta_{23}$ and $|\Delta m^2_{32}|$ via $\nu_\mu \to \nu_\mu$ oscillation had been performed separately [47, 112–116]. In these analyses, other oscillation parameters were fixed or constrained from the other experimental results. We performed a joint three-flavor neutrino oscillation analysis of the $\nu_\mu \to \nu_e$ and $\nu_\mu \to \nu_\mu$ oscillations for the first time. The motivation for the joint oscillation analysis is to avoid fixing any of $\sin^2 2\theta_{13}$, $\sin^2 \theta_{23}$, $|\Delta m^2_{32}|$ and δ_{CP} and to perform a joint determination of all four oscillation parameters with a simultaneous fit for the energy spectra of the ν_e and ν_μ candidate events at Super-K. Furthermore, the allowed region for δ_{CP} is determined by combining the T2K joint oscillation analysis with the result of the θ_{13} measurements by the reactor neutrino experiments. Details of the neutrino oscillation measurement are described in Chapter 10.

Chapter 6

Measurement of Neutrino Beam Properties

Measurement of the T2K neutrino beam properties is essential for all the physics results of the T2K experiment. This chapter describes the methods (Secs. 6.1, 6.2 and 6.3) and results (Secs. 6.4 and 6.5) of the T2K neutrino beam property measurement with the INGRID standard modules.

6.1 Analysis overview

Fourteen standard modules (seven horizontal and seven vertical modules) are used for the beam property measurement. The basic analysis procedure is as follows.

1. Neutrino events in each module are reconstructed and selected.
2. Neutrino event rate is calculated from the number of selected neutrino events in all modules normalized by POT.
3. Neutrino beam profile is reconstructed from the number of selected neutrino events in each module.
4. Neutrino beam direction and width are obtained from the reconstructed neutrino beam profile.
5. Neutrino flux uncertainty from the beam direction uncertainty is estimated from the measured beam direction.

The original analysis method for the beam property measurement with INGRID was established in 2010. In 2012, we developed a new analysis method which enabled many improvements as follows.

- Effects of the MPPC dark count and event pileup were suppressed.
- Neutrino detection efficiency was increased.
- Systematic errors from the event pileup and the veto plane efficiency were properly evaluated.
- Total systematic error was significantly reduced.

The new analysis method and the results of the beam measurement with that method are presented in this chapter.

6.2 Event reconstruction and event selection

6.2.1 Data set

During the Run 1-4 period, INGRID recorded more than 99.5% of the delivered beam data. The results of the beam measurement with all the recorded data are presented in this chapter. The main reason of the missing beam data is the trouble of the DAQ system.

6.2.2 Event reconstruction

A neutrino interaction event is identified by long tracks of charged particles generated by the neutrino interaction. First, hits are clustered by timing. A pre-selection is applied to reject accidental MPPC dark count events. Then, tracks are reconstructed using the hit information. If tracks are reconstructed, vertexing is performed. In this process, each module is treated separately. These event reconstruction criteria are described below.

Time clustering

When there are four or more hits in a 100 nsec time window, all hits within ±50 nsec of the average time make up a timing cluster.

Pre-selection

A tracking plane with at least one hit in both the horizontal and vertical layers is defined as an active plane. The timing clusters with three or more active planes are selected as shown in Fig. 6.1. Although the procedures so far are the same as the original analysis method, subsequent procedures were newly developed.

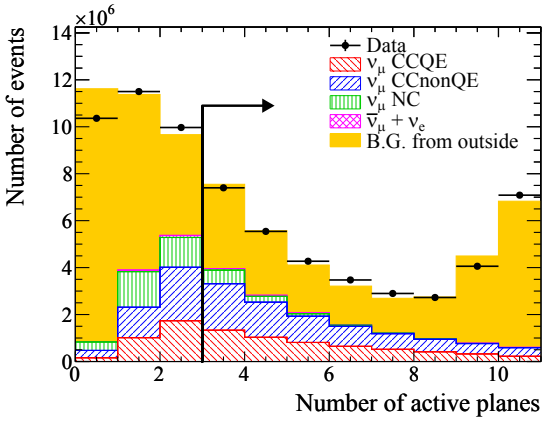

Figure 6.1: The number of active planes. Events with more than two active planes are selected.

Two-dimensional track reconstruction

The next step is the reconstruction of the tracks. First, two-dimensional XZ tracks and YZ tracks are reconstructed independently from the hit information. We developed our own track reconstruction algorithm based on the cellular automaton* [248, 249]. The cellular automaton is a dynamical system that evolves in discrete time steps. It consists of a finite number of "cells", each in one of a finite number of "states". For each cell, a set of cells called its "neighborhood" is defined relative to the specified cell. An initial state (time step $t = 0$) is selected by assigning

*The cellular automaton was used for the track reconstruction for the K2K SciBar detector [250], and our track reconstruction algorithm is analogous with it.

a state for each cell. A new generation is created (incrementing t by one), according to some fixed "rule" that determines the new state of each cell in terms of the current state of the cell and the states of the cells in its neighborhood. Our track reconstruction algorithm based on the cellular automaton is described below.

1. Before applying the cellular automaton algorithm, adjacent hits are organized as a hit cluster in each layer as shown in Fig. 6.2(a) because a slanting track may hit more than one channel in a layer.

2. Two clusters in adjacent layers are connected with a straight line segment as shown in Fig. 6.2(b). This line segment is defined as the cell for the cellular automaton. To take into account detector inefficiency and geometrical acceptance due to the reflective coating, the line segment is allowed to skip over one layer. Each cell has a state value. At this stage, all cells are initialized with state values equal to zero.

3. Only pair of cells with a common cluster that satisfies the following χ^2 limit is defined as the neighborhood for the cellular automaton. The χ^2 value is computed from a linear least square fit to the center position of three clusters which belong to the pair of cells, where the scintillator size is considered as the error of the position. If the χ^2 value for the pair of cells is less than 1.5, it is defined as the neighborhood. The upper limit on χ^2 is determined in consideration of the multiple scattering and the detector segmentation.

4. At each time step, if the upstream neighborhoods of cells have the same state value as the cells, the state value of the cells is incremented by one unit. This is the rule of the

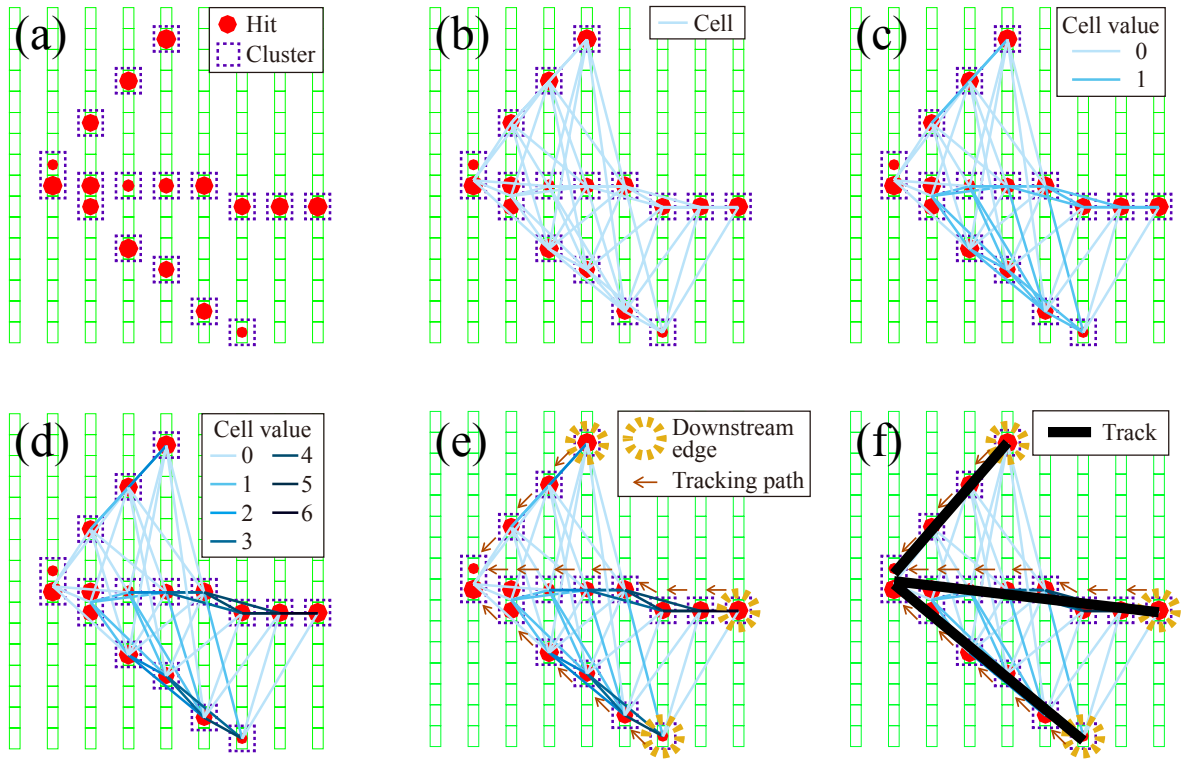

Figure 6.2: Process flow of the cellular automaton track reconstruction. Formations of (a) clusters and (b) cells, evolutions of the cells in (c) the first step and (d) the final step, (e) process of the tracking and (f) the reconstructed tracks. The area of the hit circle is proportional to the light yield. The left hand of the figure corresponds to the beam upstream.

evolution for the cellular automaton. Figure 6.2(c) shows the state values after the first evolution. The evolution stops when there are no more neighborhoods with the same state value as shown in Fig. 6.2(d).

5. After the cell evolution stops, cells which have state value more than zero and no neighborhoods with larger state value are defined as the downstream edges of the tracks (Fig. 6.2(e)). From these cells, the upstream neighborhoods are tracked back layer by layer to the cells with state value equal to zero. Finally, two-dimensional track is reconstructed from a linear least square fit to the clusters which belong to the tracked cells (Fig. 6.2(f)).

The track reconstruction efficiency of this algorithm is 15% higher than that of the original analysis method. In addition, it can reconstruct not only one track but also more tracks in a module.

Three-dimensional tracking

Three-dimensional tracks are searched for among pairs of two-dimensional XZ tracks and YZ tracks according to the following rules. If the difference in the upstream Z point between an XZ track and a YZ track is smaller than three layers, they are combined into a three-dimensional track. If an XZ or YZ track meets the above condition with more than one YZ or XZ track, the pair of tracks with the smallest difference in upstream Z point is combined.

Vertexing

After the reconstruction of a three-dimensional track, the upstream edge of the three-dimensional track is identified as a reconstructed vertex. If a pair of three-dimensional tracks meet the following conditions, they are identified as tracks coming from a common vertex:

1. The sum of the Z position differences between the upstream edges of the two tracks in XZ and YZ planes is less than two planes.
2. The distance between the upstream edges of the two tracks on the XY plane is less than 150mm.

This vertexing is performed for all combinations of three-dimensional tracks, allowing more than two tracks to be associated with the same reconstructed vertex. Each reconstructed vertex is expected to correspond to a single neutrino interaction. In the current beam intensity, more than one neutrino interaction event often occurs in a module in a cycle. Even when such an event pileup occurs, events are handled correctly in this analysis method as long as the vertices are distinguishable.

Summary of event reconstruction

Figure 6.3 shows the reconstruction resolutions of the vertex and track. Standard deviations of the differences between true and reconstructed vertex positions in the X and Y directions are 1.9cm and 1.8cm, respectively, which are much smaller than the width of the scintillator, 5cm. Probability of mis-reconstructing vertex Z plane is 17%. The three-dimensional angle between true and reconstructed muon tracks is less than 5° for almost all events. All these reconstruction resolutions are better than those with the original analysis method.

6.2.3 Event selection

After the event reconstruction, events caused by charged particles from outside of the module make up 62.3% of the reconstructed MC events. They are rejected with the timing cut, veto cut, and fiducial volume cut. These event selection criteria are described below.

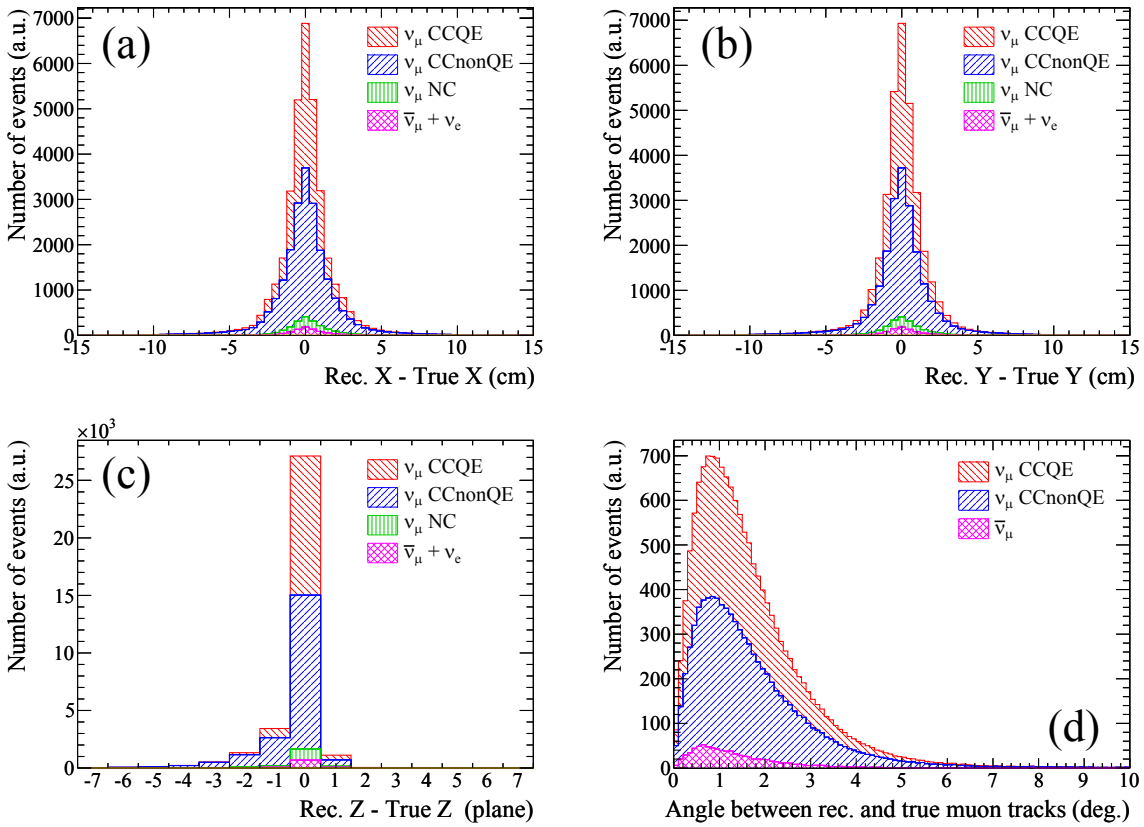

Figure 6.3: Differences between true and reconstructed vertex position in the X, Y and Z directions (a, b and c) and angle between true and reconstructed muon tracks (d).

Timing cut

To reject off-timing events, such as cosmic-ray events, only events within ±100 nsec from the expected timing are selected (Fig. 6.4). The expected timing is calculated from the primary proton beam timing, the time of flight of the particles from the target to INGRID, and the delay of the electronics and cables. The event time is defined by the time of the hit at the start point of the track.

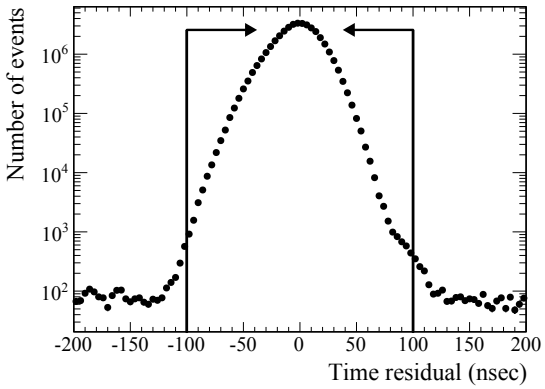

Figure 6.4: Time difference between the measured event timing and the expected neutrino event timing. Events within ±100 nsec are selected.

Veto cut

The upstream veto cut is applied to reject incoming particles produced by neutrino interactions in upstream materials, such as the walls of the detector hall. The first tracker plane is used as the front veto plane, and events which have a vertex in that plane are rejected as shown in Fig. 6.5. Since the events rejected by this front veto cut are dominated by muons created by the neutrino interactions in the walls of the detector hall, they are hereinafter referred to as the beam-induced external muon events. In addition, events which have a hit in a side veto plane at the upstream position extrapolated from the reconstructed track are rejected. An event display of an event rejected by the side veto cut is shown in Fig. 6.6.

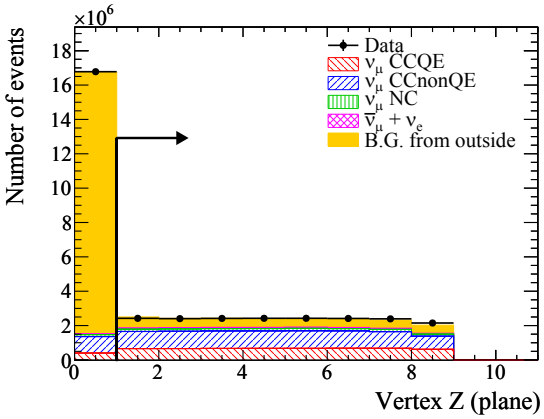

Figure 6.5: Vertex Z distribution before applying the veto and FV cuts.

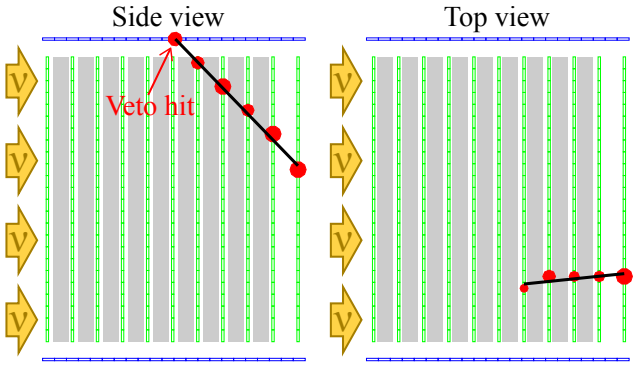

Figure 6.6: Event display of a rejected event by the side veto cut.

Fiducial volume (FV) cut

After the veto cut, a fiducial volume (FV) cut is applied. The FV of each module is defined as a volume within ±50 cm from the module center in the X and Y directions, and from the second to the ninth tracker plane in the Z direction. The ratio of the FV to the total target volume is 61.7%. Events having a vertex inside the FV are selected as shown in Fig. 6.7.

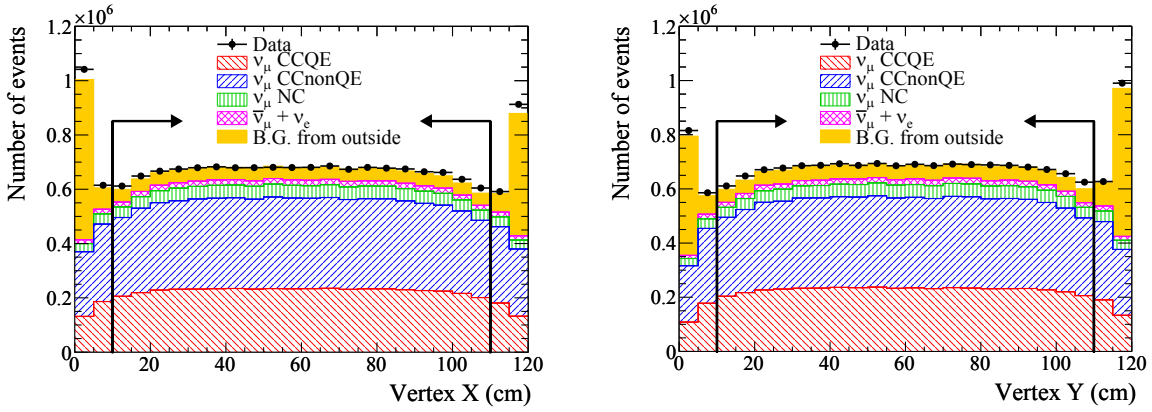

Figure 6.7: Vertex X and Y distributions after applying the veto cut. A volume within ±50 cm in the X and Y directions from the module center is defined as the fiducial volume (FV). Most of the background events which pass the FV cut in one direction (X or Y) are actually rejected by the FV cut in the other direction (Y or X).

Summary of event selection

The results of the event selection are summarized in Table 6.1. Finally, 4.81×10^6 events are selected as candidates of the neutrino events in INGRID. The expected purity of the neutrino events in INGRID is 99.58%. Figure 6.8 shows the vertex distributions and neutrino event selection efficiency as a function of true neutrino energy after all cuts.

Table 6.1: Summary of the event selection for the INGRID beam measurement. The efficiency is defined as the number of selected neutrino events divided by the number of neutrino interactions in the FV. The purity is defined as the ratio of the selected neutrino events in INGRID to the total selected events.

Selection	Data	MC	Efficiency	Purity
Event reconstruction	1.75×10^7	1.74×10^7	80.65%	37.70%
Timing cut	1.75×10^7	1.74×10^7	80.65%	37.70%
Veto cut	7.47×10^6	7.39×10^6	76.23%	83.90%
Fiducial volume cut	4.81×10^6	4.79×10^6	58.64%	99.58%

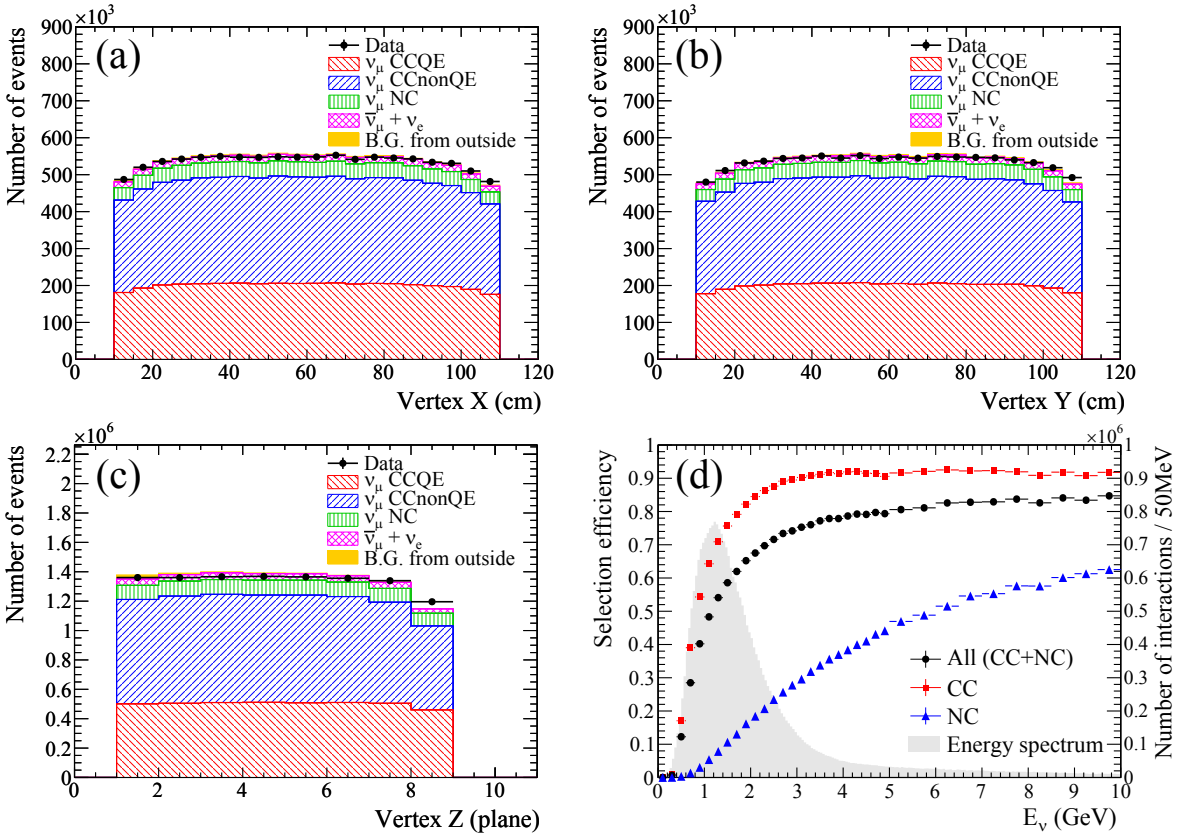

Figure 6.8: Distributions of vertex X, Y and Z (a, b and c) and neutrino event selection efficiency as a function of true neutrino energy (d) following the event selection. The energy spectrum of the neutrino interactions in the standard modules is overlaid in (d).

6.2.4 Corrections

Individual differences of the modules cause systematic errors on the reconstructed beam profile. Thus, some corrections are applied to the number of selected events for the real data to compensate the known individual differences of the modules.

Target mass

Difference of the individual iron target mass (Fig. 6.9) causes the different number of neutrino interactions in each module. Thus, a correction is applied module-by-module based on the measured mass of the iron target of the module: $-1\% \sim +1\%$ for each module.

Dead channels

There are 18 dead channels out of 8360 channels in the 14 standard modules. Since they affect the detection efficiency, this effect needs to be corrected. The correction factor is estimated module-by-module from the difference in the detection efficiencies for MC samples with and without the dead channels. The number of dead channels in each module and the variation of the detection efficiency due to the dead channels estimated by the MC simulation are shown in Fig. 6.10[†].

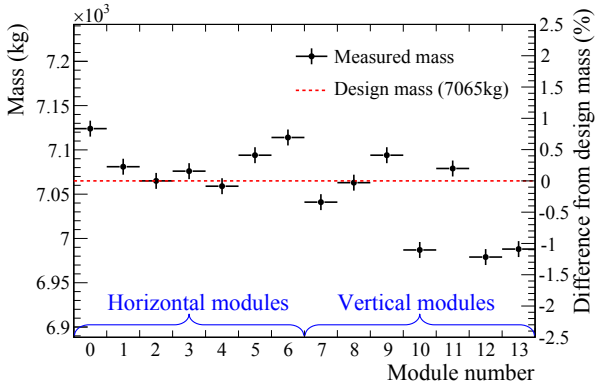

Figure 6.9: Measured mass of iron plates for each module. The design value is 7065 kg (785 kg × 9 plates). Vertical error bars represent measurement errors.

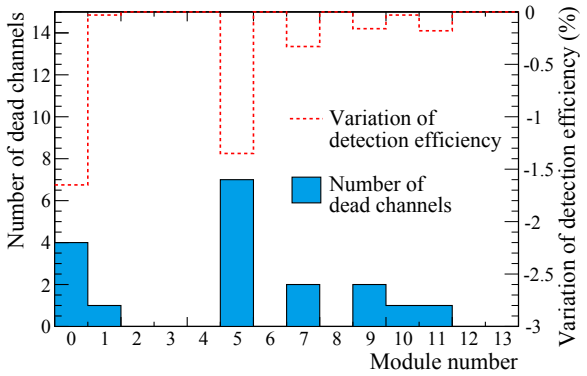

Figure 6.10: The number of dead channels in each module and the variation of the detection efficiency due to the dead channels estimated by the MC simulation.

Backgrounds

The number of the beam-induced external background events is estimated by the MC simulation and is subtracted from the number of selected events. Almost all the background events are induced by neutrons or photons[‡] generated by neutrino interactions in the upstream walls as shown in Fig. 6.11.

[†]Variation of the detection efficiency due to the dead channels is not always proportional to the number of dead channels because it also depends on the position of the dead channels.

[‡]Most of the photons from outside are produced by π^0 decays.

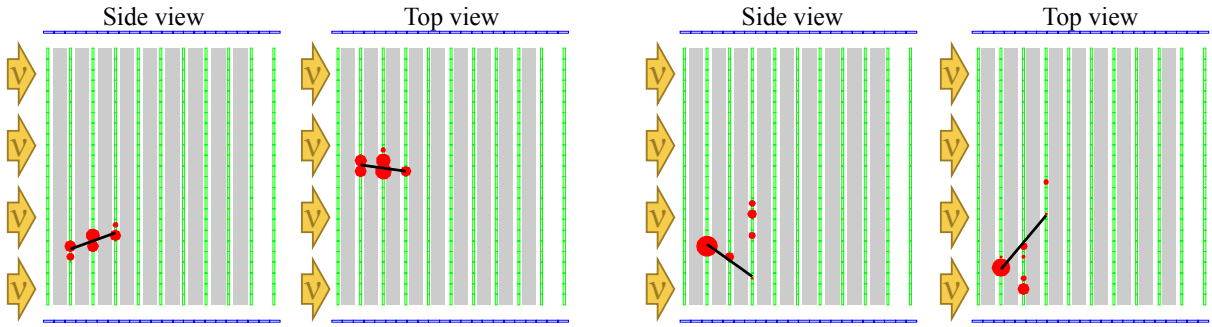

(a) Background event by neutron from outside (b) Background event by γ-ray from outside

Figure 6.11: Event displays of MC background events induced by neutral particles from outside.

Event pileup

Even when two or more neutrino events occur in a cycle in a module, mostly they can be separately reconstructed as shown in Fig. 6.12 (a). However, when a track from a neutrino event piles up with a track from another neutrino event, vertices may fail to be reconstructed as shown in Fig. 6.12 (b). Since this results in the loss of events, this event-pileup effect needs to be corrected. The event-pileup effect is proportional to the beam intensity (*i.e.* POT per bunch). Thus, the event loss caused by the event pileup can be corrected as follows:

$$N_{\mathrm{corr}} = \frac{N_{\mathrm{sel}}}{1 - C_{\mathrm{loss}} n_{\mathrm{ppb}}}, \tag{6.1}$$

where N_{corr} and N_{sel} are the number of selected events with and without the correction, n_{ppb} is the POT per bunch and C_{loss} is a constant which is hereafter referred to as "event-loss constant". The event-loss constant is estimated as follows. First, the beam data are categorized into eleven sub-samples according to the POT per bunch as shown in Fig. 6.13. For each sub-sample, average POT per bunch, $n_{\mathrm{ppb}}^{\mathrm{AV}}$, is calculated. Then, the pseudo event pileups are generated in each sample as follows. All INGRID hits in two beam cycle are summed together to make one new pseudo beam data which is hereafter referred to as pseudo data 1. This procedure effectively doubles the beam intensity and MPPC dark counts observed by INGRID. On the other hand, all INGRID hits in a beam bunch cycle and a dummy cycle are summed together to make another pseudo beam data which is hereafter referred to as pseudo data 2. This procedure effectively doubles only the MPPC dark counts observed by INGRID. The track reconstruction and event selection are applied to both pseudo data, and the number of selected events per POT, N_1 and

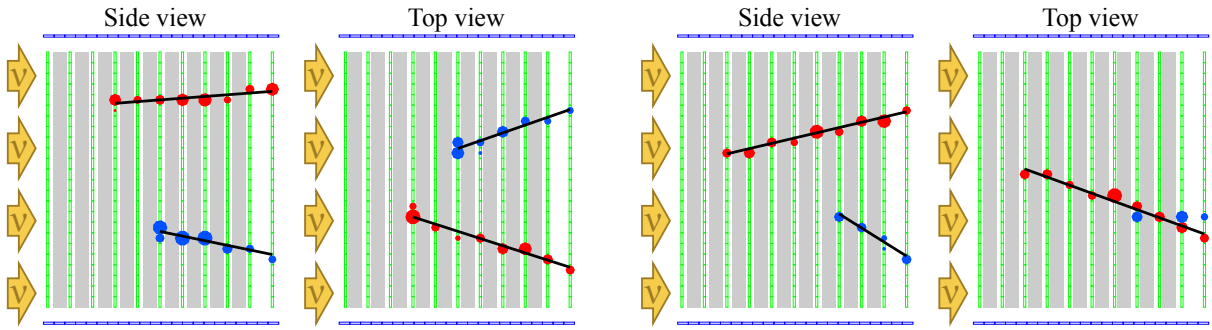

(a) Separately reconstructed events (b) Overlapped events

Figure 6.12: Event displays of the event pileups in the MC simulation. Red and blue circles represent hits caused by different neutrino interactions.

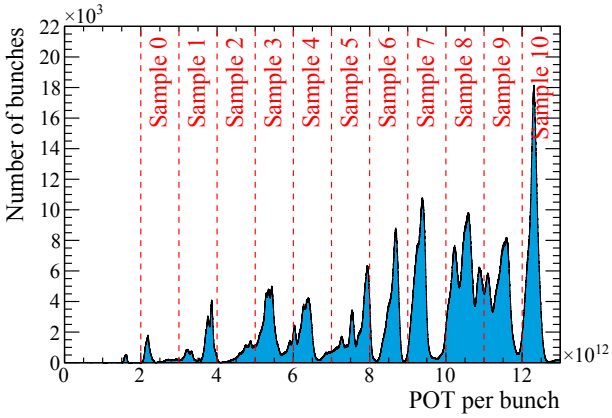

Figure 6.13: Categorization of beam data by POT per bunch.

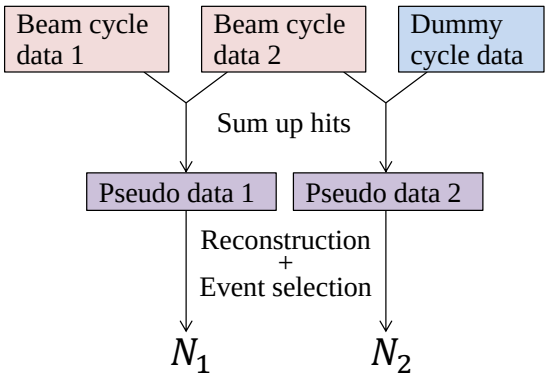

Figure 6.14: Procedure of making the pseudo data for the event-pileup estimation.

N_2 for pseudo data 1 and 2, are estimated. This procedure is summarized in Fig. 6.14. Finally, the event-loss constant is calculated from N_1, N_2 and $n_{\mathrm{ppb}}^{\mathrm{AV}}$. Since the corresponding average POT per bunch for the pseudo data 1 and 2 are $2n_{\mathrm{ppb}}^{\mathrm{AV}}$ and $n_{\mathrm{ppb}}^{\mathrm{AV}}$, respectively, N_1 and N_2 should satisfy Eq. 6.1 as follows:

$$N_{\mathrm{corr}} = \frac{N_1}{1 - C_{\mathrm{loss}} 2 n_{\mathrm{ppb}}^{\mathrm{AV}}}, \quad N_{\mathrm{corr}} = \frac{N_2}{1 - C_{\mathrm{loss}} n_{\mathrm{ppb}}^{\mathrm{AV}}}. \tag{6.2}$$

Therefore, the event-loss constant is calculated as follows:

$$C_{\mathrm{loss}} = \frac{N_2 - N_1}{n_{\mathrm{ppb}}^{\mathrm{AV}}(2N_2 - N_1)}. \tag{6.3}$$

The event-loss constant is estimated in this way in each sample for each module. Finally, the average of the event-loss constants in eleven samples, calculated for each module as shown in Fig. 6.15, is used for the event-pileup correction. The average event-loss constant for each module is shown in Fig. 6.16.

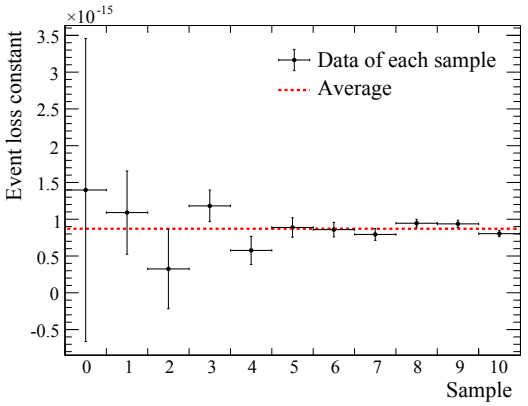

Figure 6.15: Event-loss constants in eleven samples for module 0 and the average of them. Vertical error bars represent statistical errors.

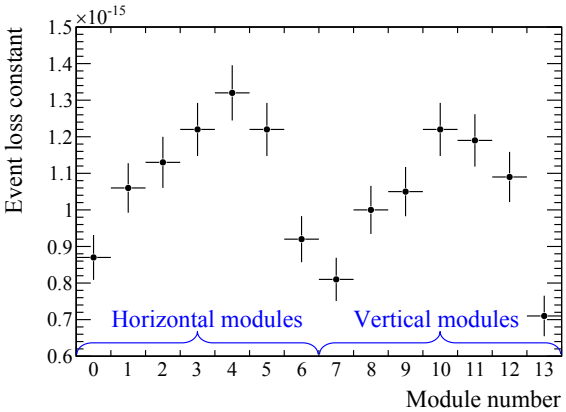

Figure 6.16: Average event-loss constant for each module. Vertical error bars represent statistical errors.

6.3 Systematic errors

Table 6.2 shows the summary of the systematic errors on the number of selected events in INGRID. The total systematic error, calculated from the quadrature sum of all the systematic errors, is 0.91%. It corresponds to about a quarter of the 3.73% error from the original analysis method. The reduction of the systematic error results from the insusceptibility to the MPPC dark count and the event pileup, the high track reconstruction efficiency, and the realistic estimation of systematic errors which have been conservatively estimated in the original analysis. Detailed comparisons between the original and new analysis methods are given in Appendix G. Each systematic error is evaluated as follows.

Table 6.2: Summary of the systematic errors on the neutrino beam measurement.

Item	Error
Target mass	0.13%
MPPC dark count	0.27%
Hit efficiency	0.39%
Event pileup	0.14%
Beam-induced external background	0.27%
Cosmic-ray background	0.01%
2D track reconstruction	0.49%
3D tracking	0.19%
Vertexing	0.43%
Timing selection	0.01%
Veto cut	0.13%
Fiducial volume cut	0.09%
Total	0.91%

Target mass

The uncertainty of the iron mass measurement, 1kg, corresponds to 0.13% relative to the total mass. It is directly taken as the systematic error because the number of neutrino events is proportional to the target mass.

MPPC dark count

The largest variation of the measured MPPC dark rate during the Run 1-4 period is 5.84 hits/module/cycle. It is taken as the uncertainty of the dark rate. The relation between the dark rate and the neutrino detection efficiency is estimated by the MC simulation as shown in Fig. 6.17. The variation of the neutrino detection efficiency corresponding to the variation of the dark rate by 5.84 hits/module/cycle is assigned as a systematic error.

Hit efficiency

Hit efficiency is defined as the probability of observing hits when a minimum ionizing particle goes through a scintillator layer. The discrepancy between the hit efficiency measured with beam-induced external muon events and that of the MC simulation is calculated to be 0.17% from Fig. 4.13. It is assigned as the uncertainty in the hit efficiency. The relation between the hit efficiency and the neutrino detection efficiency is estimated by the MC simulation as shown in Fig. 6.18. The variation of the neutrino detection efficiency corresponding to the variation of hit efficiency by 0.17% is assigned as a systematic error.

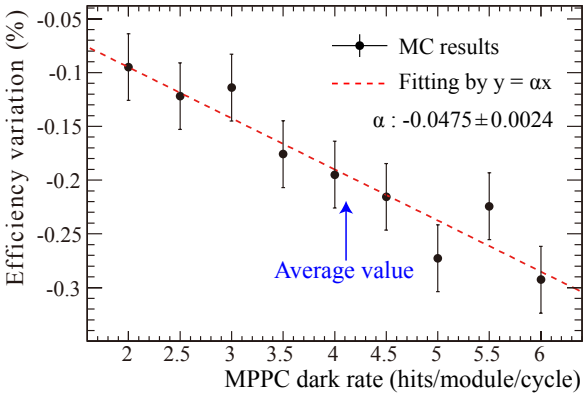

Figure 6.17: Variation of the detection efficiency due to the MPPC dark count.

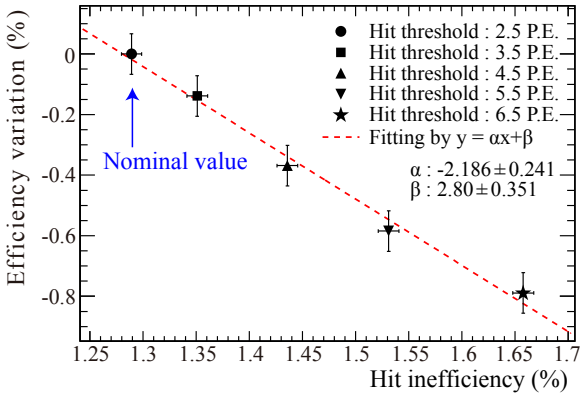

Figure 6.18: Variation of the detection efficiency due to the hit inefficiency.

Event pileup

Two sources are considered for the errors on the event-loss constant. The first one is the statistical error on the estimation of the event-loss constant. The largest statistical error among all modules is 7.8% at module 13. The second one is the effect of the MPPC dark counts because the event-loss constant is estimated using the pseudo data in which the MPPC dark rate is doubled. This effect is evaluated with the MC simulation to be 2.2%. The quadrature sum of the two errors, 8.1%, is taken as the total error on the event-loss constant. The systematic error on the number of selected events from the error on the event-loss constant is calculated from the product of the error on the event-loss constant, the largest event-loss constant among all modules, and highest POT per bunch during the Run 1-4 period, $8.1\% \times (1.32 \times 10^{-15}) \times (1.28 \times 10^{13}) = 0.14\%$.

Beam-induced external background

There is a 30% discrepancy between the beam-induced external muon event rate estimated by the MC simulation and that measured from the data. Hence, all the MC evens induced by the neutrino interactions in the walls of the detector hall are normalized by the beam-induced external muon event rate. The change in the beam-induced external background contamination fraction from this 30% discrepancy is taken as the systematic error on the beam-induced external background.

Cosmic-ray background

The number of cosmic-ray background events is estimated from the out-of-beam data. It was found to be very small relative to the number of neutrino events (0.01%).

Event selection

The systematic error on the track reconstruction efficiency is estimated by comparing the efficiency between the data and the MC simulation for several sub-samples divided by the number of active planes as shown in Fig. 6.19. The standard deviation of the data − MC of the track reconstruction efficiency for the sub-samples is taken as the systematic error. The systematic errors from the all event selections are evaluated by varying the selection threshold. The maximum differences of the data − MC for several selection thresholds are taken as the systematic errors. For example, the systematic error from the fiducial volume cut is evaluated as 0.09% from the data − MC for the number of selected events in several tentative fiducial volumes as shown in Table 6.3.

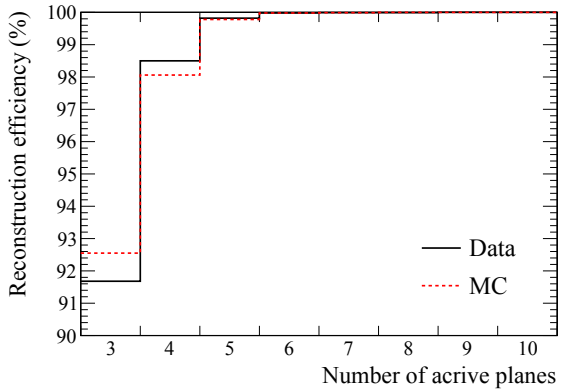

Figure 6.19: Track reconstruction efficiency for several sub-samples divided by the number of active planes.

Table 6.3: Number of selected events in several tentative fiducial volumes relative to that in the nominal fiducial volume. Tentative fiducial volumes are defined in XY dimensions from the module center.

Tentative FV	Data	MC	|Data−MC|
<50 cm (nominal)	100%	100%	0%
<25 cm	26.14%	26.05%	0.09%
25∼40 cm	39.96%	40.04%	0.08%
40∼50 cm	33.90%	33.91%	0.01%
Maximum difference			0.09%

6.4 Results

6.4.1 Event rate

Figure 6.20 shows the daily rates of the neutrino events normalized by POT. When the horn current is turned down to 205kA, the on-axis neutrino flux decreases because the forward focusing of the charged pions by the horns becomes weaker. An increase by 2% and a decrease by 1% of event rate were observed between Run 1 and Run 2, and during Run 4, respectively. However, a continuous or drastic decrease was not observed. It demonstrates that the target was not seriously damaged in Run 1-4. For all run periods with the horns operated at 250kA, the neutrino event rate is stable within the bound of 2%, and the standard deviation of the event rate is 0.7%. Since they are much smaller than the 10% neutrino flux uncertainty considered in T2K, we concluded that the beam neutrino production rate is stable enough.

The data to MC ratios of the neutrino event rate with the horns operated at 250kA and 205kA are calculated to be

$$\frac{N^{\mathrm{data}}_{250\mathrm{kA}}}{N^{\mathrm{MC}}_{250\mathrm{kA}}} = 1.014 \pm 0.001(stat.) \pm 0.009(syst.), \tag{6.4}$$

$$\frac{N^{\mathrm{data}}_{205\mathrm{kA}}}{N^{\mathrm{MC}}_{205\mathrm{kA}}} = 1.026 \pm 0.002(stat.) \pm 0.009(syst.), \tag{6.5}$$

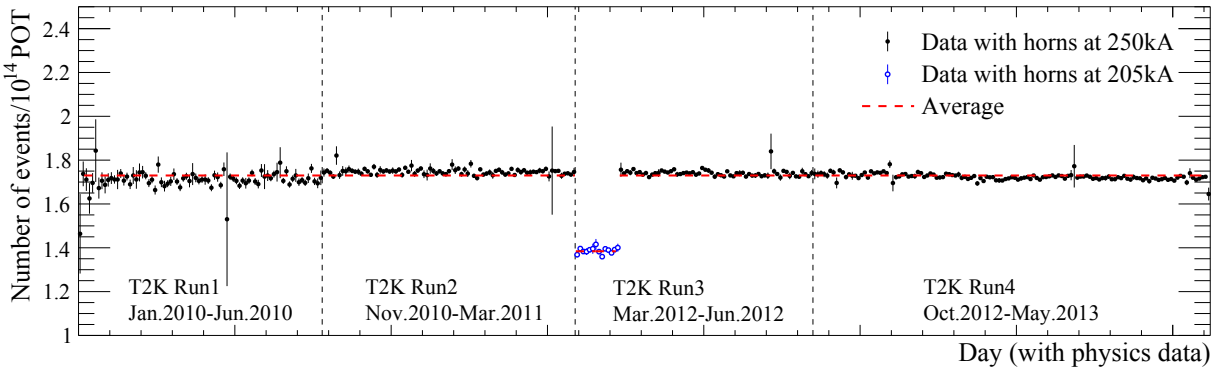

Figure 6.20: Daily event rate of the neutrino events normalized by POT. The error bars show the statistical errors.

respectively, where the uncertainties from the neutrino flux prediction and the neutrino interaction models are not included in the systematic error. The event rates for data agree well with the MC predictions.

6.4.2 Beam direction

The profiles of the neutrino beam in the horizontal and vertical directions are reconstructed with the number of neutrino events in the seven horizontal and seven vertical modules, respectively. The observed profiles are fitted with a Gaussian function as shown in Fig. 6.21. The peak position of the fit is defined as the profile center. Finally, the neutrino beam direction is reconstructed as the direction from the proton beam target position to the measured profile center at INGRID using the result of accurate surveys of the proton beam target and the INGRID detectors[§]. Figure 6.22 shows the history of the horizontal and vertical neutrino beam directions relative to the nominal directions. The measured neutrino beam directions are stable within the physics requirement of 1 mrad. The neutrino beam directions measured with INGRID agree well with the muon beam directions measured by the muon monitor[¶]. In Run 1, the neutrino beam direction as well as the muon beam direction is directed downward by 0.2 mrad. Since a misalignment in the proton beamline was adjusted after the end of Run 1, the subsequent beam direction is shifted toward the nominal direction. In addition, the neutrino beam direction is directed to upward by 0.2 mrad from the middle of Run 3 to the beginning of Run 4. It was gotten back to the nominal direction by tuning the proton beam condition during Run 4. The systematic error of the profile center measurement was estimated by a toy MC simulation. In the simulation, the number of events at each module is independently changed within the range of the total detector systematic error of 0.91% and standard deviations of reconstructed direction values are taken as the systematic errors. The average horizontal and vertical beam directions relative to the nominal directions are measured as

$$\bar{\theta}_X^{\text{beam}} = 0.030 \pm 0.011(stat.) \pm 0.095(syst.) \text{ mrad}, \quad (6.6)$$

$$\bar{\theta}_Y^{\text{beam}} = 0.011 \pm 0.012(stat.) \pm 0.105(syst.) \text{ mrad}, \quad (6.7)$$

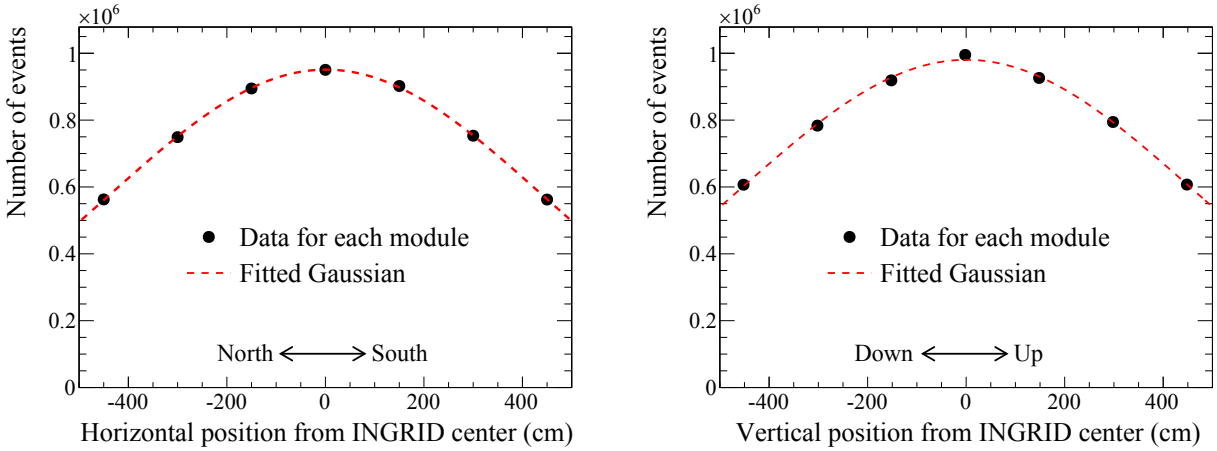

Figure 6.21: Reconstructed neutrino beam profiles for horizontal (left) and vertical (right) directions. Each point represents the number of selected events in each module.

[§]The uncertainty of the survey (2 mm) is negligibly small.

[¶]The muon beam directions are reconstructed by performing a 2D Gaussian fitting to the charge distribution of silicon arrays of the muon monitor.

respectively. We achieved the target precision of being much better than 1 mrad. The neutrino flux uncertainty due to the beam direction uncertainty described in Chapter 4 was evaluated from this result. The variation of the neutrino flux when the detector position (Super-K, ND280 or INGRID) is moved by the angle which corresponds to the error size of the beam direction measured with INGRID is taken as the neutrino flux uncertainty due to the beam direction uncertainty. The new INGRID beam analysis dramatically reduced the neutrino flux uncertainty as shown in Fig. 6.23.

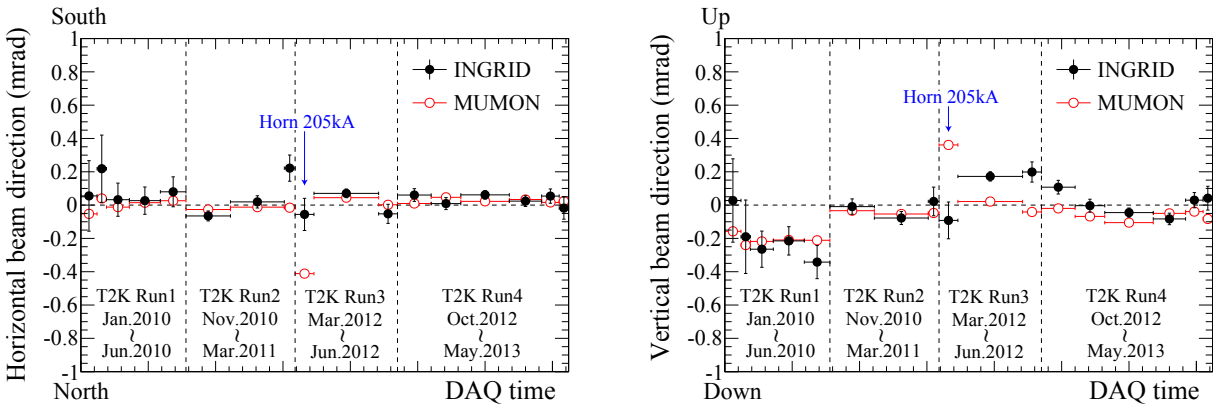

Figure 6.22: History of neutrino beam directions for horizontal (left) and vertical (right) directions. The muon beam directions measured by the muon monitor (MUMON) are overlaid. The zero points of the vertical axis correspond to the nominal directions. Each point includes sequential data grouped in a period of fixed beam conditions. The error bars show the statistical errors.

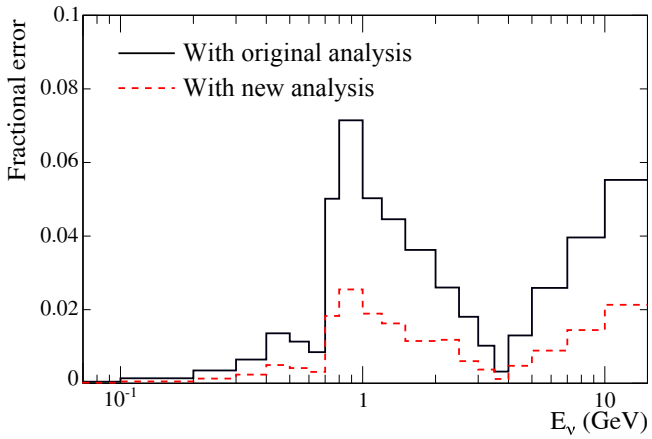

Figure 6.23: Fractional uncertainties of the ν_μ flux at Super-K due to the beam direction uncertainty evaluated from the original and new INGRID beam analyses.

6.4.3 Beam width

The standard deviation of the Gaussian fit of the observed profile is defined as the neutrino beam width. Figure 6.24 shows the history of the neutrino beam width in the horizontal and vertical directions with the horns operated at 250kA. The measured beam width is stable within the statistical error. The stability of the neutrino beam direction and width confirms that the neutrino energy spectrum in Super-K is stable. The data to MC ratio of the beam width with

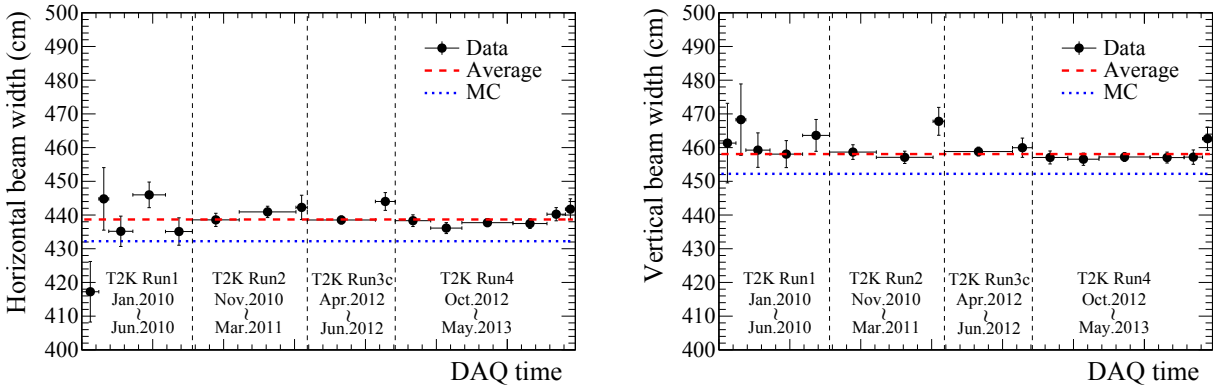

Figure 6.24: History of neutrino beam width for horizontal (left) and vertical (right) directions for the horn 250kA operation. The error bars show the statistical errors.

the horns operated at 250kA is calculated to be

$$\frac{W_X^{\rm data}}{W_X^{\rm MC}} = 1.015 \pm 0.001(stat.) \pm 0.010(syst.), \tag{6.8}$$

$$\frac{W_Y^{\rm data}}{W_Y^{\rm MC}} = 1.013 \pm 0.001(stat.) \pm 0.011(syst.), \tag{6.9}$$

for the horizontal and vertical direction, respectively. Agreement between the data and the MC simulation is very good.

6.4.4 Summary

The neutrino beam direction measurement using the new analysis method reduced the neutrino flux uncertainty from the neutrino beam direction which was originally 7.0% at 1 GeV to 2.5%. In addition, the measured neutrino event rate and neutrino beam width agree with the predictions based on the T2K neutrino flux simulation. Moreover, all the beam properties are confirmed to be stable within the physics requirements. They assure the T2K beam data quality for Run 1-4 and the consistency of the neutrino flux prediction. These results enable the measurements of the neutrino cross sections and the neutrino oscillations which will be presented from the next chapter because the precise neutrino flux prediction and the assured beam data are essential for these measurements.

This beam property measurement played an especially important role after the Tohoku earthquake in 2011 (the end of Run 2). The T2K beamline was seriously damaged by the earthquake, and then was restored over a half year. We confirm that the neutrino beam properties measured with INGRID after the beamline restoration are not changed from those before the earthquake. This result demonstrated that the T2K neutrino beamline was restored to the original condition and the T2K experiment can continue the beam operation.

6.5 Considerations

6.5.1 Future prospects of the beam property measurement

We have to go on this beam property measurement with keeping the precision as long as the T2K experiment continues. The new analysis method for the beam property measurement is insusceptible to the MPPC dark count and the event pileup. Thus, even if the MPPC dark rate or the beam intensity increases in the future, their effects on the beam property measurement

are small enough. For example, if the MPPC dark rate becomes double (8 hits/module/cycle) and the beam intensity comes up to the design value (750 kW), the total systematic error on the neutrino event rate that is currently 0.91% will be 1.05%, and that on the neutrino beam direction which is currently 0.095 mrad will be 0.111 mrad. In addition, this analysis method is directly applicable to the measurement of the antineutrino beam (see Appendix G for details) which is produced by inverting the horn current polarity as described in Chapter 2. Therefore, we established a strong analysis method which is permanently usable without any changes.

6.5.2 Slight variations

Although the stabilities of all the neutrino beam properties are sufficient in the physically required levels, there exist slight variations in the neutrino event rate and the vertical neutrino beam direction as shown in Fig. 6.25. They both have jumps between Run 1 and Run 2. Since there are some known differences in hardware conditions between Run 1 and Run 2, their effects on the neutrino event rate and the vertical neutrino beam direction were estimated with the MC simulation. However, the expected jumps from the known differences are smaller than the observed ones as shown in Table 6.4. It means that there may exist unknown sources of the variations. Both variations may stem from the same sources since they appear to be correlated as shown in Fig. 6.25. We need to pin down the sources to get a better understanding of the neutrino beam properties in the future although their effects on the physics results are currently negligible.

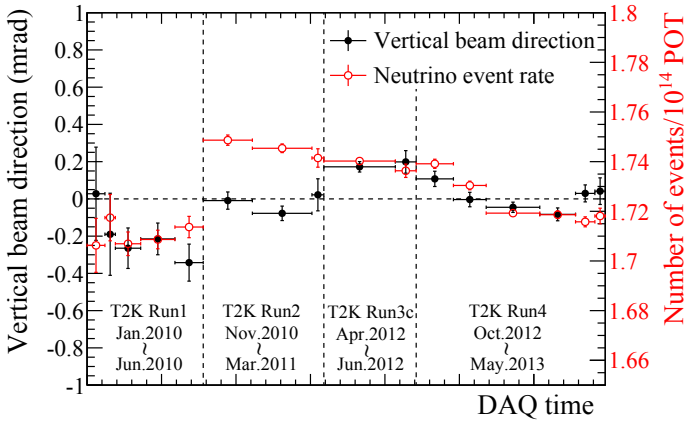

Figure 6.25: History of the vertical beam direction and the neutrino event rate for the horn 250kA operation. The error bars show the statistical errors.

Table 6.4: Observed and expected differences in the neutrino event rate and the vertical beam direction between Run 1 and Run 2. Errors in the observed differences represent statistical errors.

Source	Neutrino event rate	Vertical beam direction
Effect of the proton beam condition (MC)	+0.32%	+0.065 mrad
Effect of the horn condition (MC)	+0.32%	−0.007 mrad
Effect of the INGRID condition (MC)	+0.22%	+0.006 mrad
Total difference (MC)	+0.86%	+0.064 mrad
Observed difference	+2.11±0.14%	+0.204±0.078 mrad

Chapter 7

Measurement of Charged Current Inclusive Cross Section

The neutrino charged current (CC) interaction is especially important for neutrino oscillation measurements because the neutrino flavor is identifiable only via the CC interaction. This chapter describes the measurement of the ν_μ charged current inclusive cross section on iron and hydrocarbon with the INGRID standard module and the Proton Module.

7.1 Introduction to the measurement of the charged current inclusive cross section

Figure 7.1 shows the summary of existing ν_μ CC inclusive cross section measurements. In a few GeV region, where the recent oscillation experiments are conducted, the CC interactions have been studied in the past predominantly on deuterium targets [251, 253]. The T2K and other modern neutrino oscillation experiments* use heavier targets such as carbon, oxygen and iron. The SciBooNE experiment measured the CC inclusive cross section on carbon in a few GeV region, and the result at a neutrino energy of $\sim$1 GeV is about 30% higher than the model predictions, which corresponds to 2σ deviation [279]. The nuclear effects of the neutrino target material are significant for the heavy targets in a few GeV region. However, it could not be directly tested by the neutrino cross section measurement because the systematic error from the neutrino flux uncertainty ($\sim$10%) is larger than the nuclear effect ($\sim$3%). Consequently, the CC interactions in a few GeV region and the nuclear effects of the neutrino target material are not well known. It is a grave concern for T2K because the target material for Super-K (H_2O) is different from that for ND280 (CH). Therefore, a better sense of the nuclear effects of the target material is required.

Iron (Fe) makes up 96.23% of the target mass in the standard module, and hydrocarbon (CH) makes up 98.57% of the target mass in the Proton Module as shown in Table 7.1. Thus, we measured the ν_μ CC inclusive cross sections on Fe and CH from the number of selected CC events in the standard module and the Proton Module respectively. We also determined the ν_μ CC inclusive cross section ratio on Fe to CH using these two modules. The central standard module and the Proton Module are on the central axis of the beam and are exposed to the same neutrino beam. Thus, this cross section ratio is expected to be measured very precisely since many of the large systematic errors from the neutrino flux uncertainties will be cancelled between the two detectors. The CC inclusive cross section ratio on different target nuclei is expected to be different from unity due to the difference in the ratio of neutrons and protons in the nuclei. In addition, it will be affected by the nuclear effect, especially in the low energy

*T2K, MINOS, NOνA and OPERA use oxygen, iron, carbon and lead as the neutrino target, respectively.

region. Therefore, this measurement can provide a good test of the nuclear effect in the neutrino interaction model.

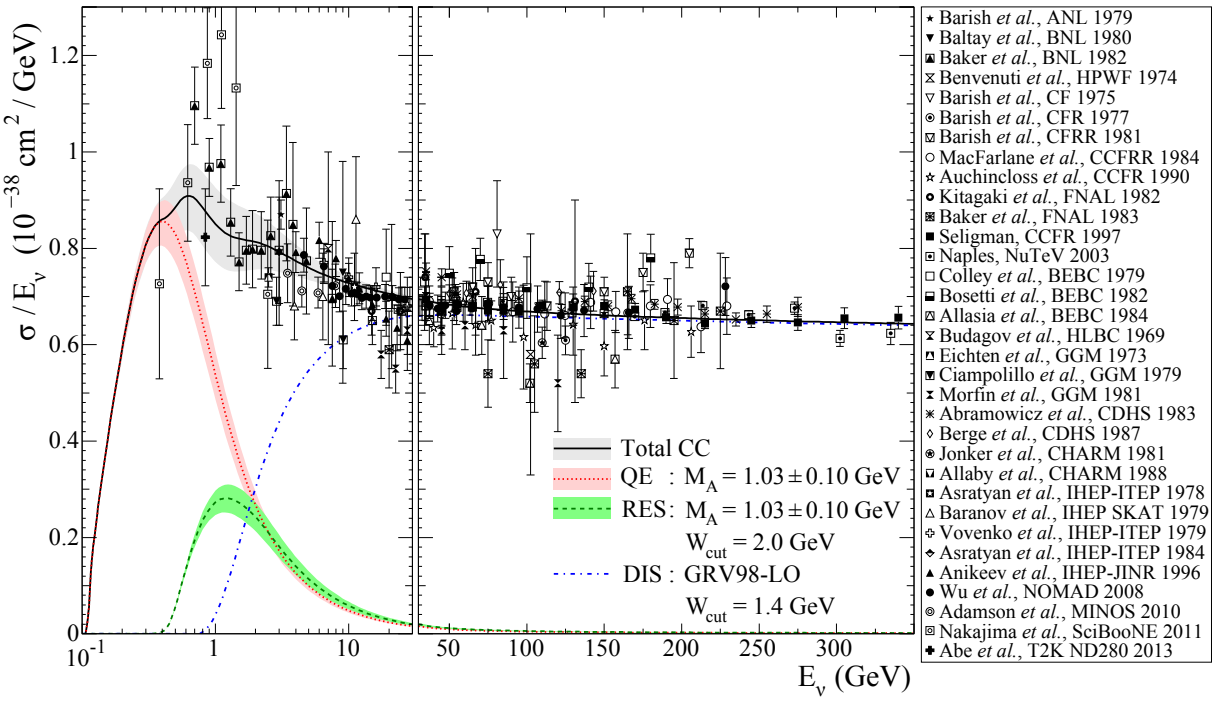

Figure 7.1: Total ν_μ charged current inclusive cross section divided by the neutrino energy [226, 251–280]. The low energy region is dominated by the quasi-elastic (QE) contribution, the high energy region by the deep inelastic (DIS) contribution and the intermediate region is dominated by the resonance (RES) contribution. This figure was taken from Ref. [278] and some data points from recent experiments [226, 279, 280] were added.

Table 7.1: The elemental composition of the target material by weight. Details of the elemental composition are described in Appendix F.

	H	C	N	O	Ti	Fe
Standard module	0.29%	3.42%	0.003%	0.03%	0.03%	96.23%
Proton Module	7.61%	90.96%	0.07%	0.59%	0.76%	0%

7.2 Event selection

7.2.1 Data set

For this cross section measurement, data from Run 2, 3c, 4 are used. Data from Run 1, in which the Proton Module was not installed, and that from Run 3b, in which the horns were operated with lower current settings, are not used. The data set corresponds to 6.04×10^{20} POT. For a good cancellation of the neutrino flux error in the measurement of the CC inclusive cross section ratio on Fe to CH, only the central standard module and the Proton Module are used.

7.2.2 Event selection for the Proton Module

For the beam measurement with the standard modules, we reconstruct tracks and vertices, and select the events whose vertices are in the fiducial volume as described in Chapter 6. If the same event reconstruction and event selection are applied to the Proton Module, the beam-induced external backgrounds make up 50% of the selected events. These backgrounds mainly arise from neutral particles (neutrons and photons) created by neutrino interactions in the walls of the detector hall. They enter the Proton Module without being detected by the veto planes, interact in the fiducial volume, and produce charged particles. The Proton Module is also sensitive to such particles because it is a fully-active tracking detector, whereas the standard module is sensitive to only muons. To reduce such background events, the horizontal standard modules located downstream of the Proton Module are used to identify muons generated by the ν_μ CC interaction in the Proton Module. The total flow of the event selection is as follows. First, time clustering, pre-selection (Fig. 7.2) and two-dimensional track reconstruction are applied to the Proton Module and the horizontal standard modules as with Chapter 6. Next, tracks starting from the Proton Module and reaching to the horizontal standard module are searched for. When a two-dimensional track reconstructed in the Proton Module is matched with that in the horizontal standard module in the same integration cycle, they are merged. Requirements for the track matching are as follows.

1. The upstream edge of the standard module track is in either of the most upstream two layers.
2. The downstream edge of the Proton Module track is in either of the most downstream two layers.
3. The difference between the reconstructed angles of the standard module and Proton Module tracks is less than 35°.
4. At the halfway point between the standard module and the Proton Module, the distance between the extrapolated standard module and Proton Module tracks is less than 85mm.

Figure 7.3 shows an example of a merged track. This track matching is applied to select long muon tracks from ν_μ CC interactions and to reject short tracks caused by neutral particles from outside, like neutrons and photons, or NC interactions. Then, the three-dimensional tracking, vertexing, timing cut (Fig. 7.4), and veto and fiducial volume cuts (Figs. 7.5 and 7.6) are applied to the merged tracks as with Chapter 6. The ratio of the FV to the total target volume is 58.1%. The results of the event selection for the Proton Module are summarized in Table 7.2.

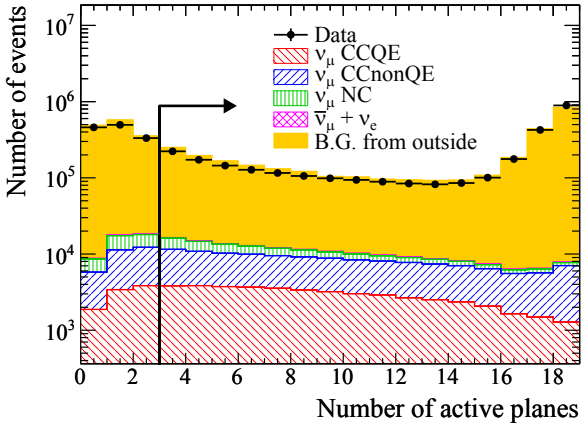

Figure 7.2: The number of active planes. Events with more than two active planes are selected.

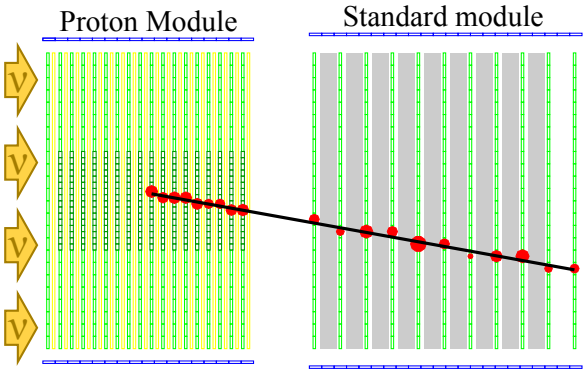

Figure 7.3: Event display of a merged track.

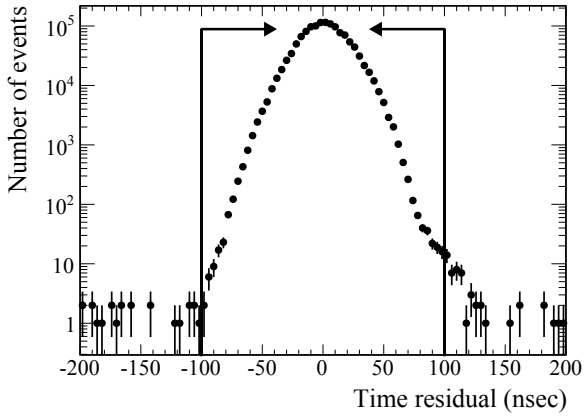

Figure 7.4: Time difference between measured event timing and expected neutrino event timing. Events within ±100 nsec are selected.

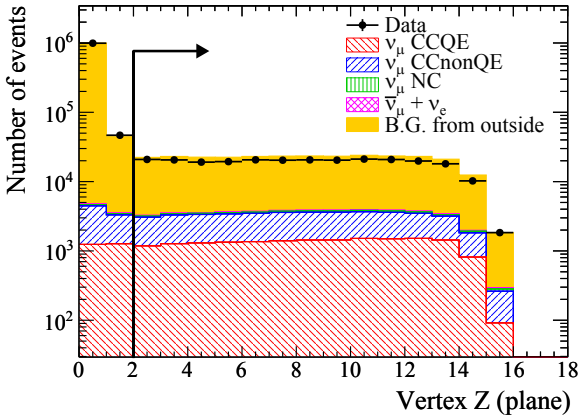

Figure 7.5: Vertex Z distribution before applying the veto and FV cuts.

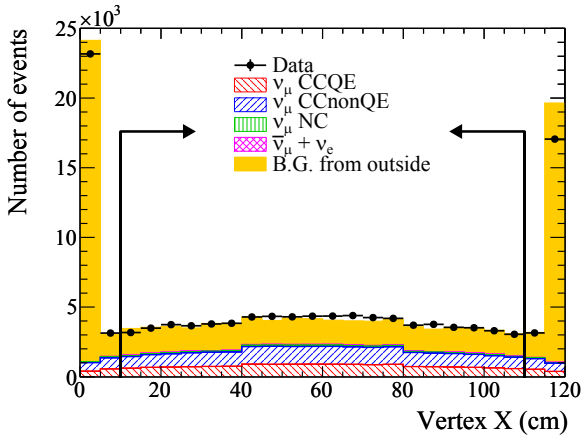

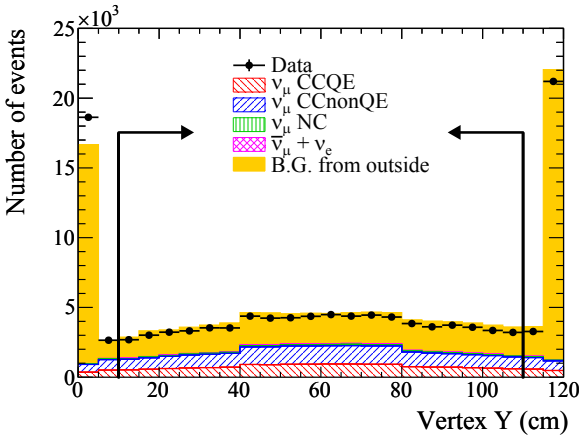

Figure 7.6: Vertex X and Y distributions after applying the veto cut. A volume within ±50 cm in the X and Y directions from the module center is defined as the fiducial volume (FV). Most of the background events which pass the FV cut in one direction (X or Y) are actually rejected by the FV cut in the other direction (Y or X).

Table 7.2: The number of events passing each selection step for the Proton Module. The efficiency is defined as the number of selected ν_μ CC events divided by the number of ν_μ CC interactions in the FV. The purity is defined as the ratio of the selected ν_μ CC events on CH to the total selected events.

Selection	Data	MC	Efficiency	Purity
Event reconstruction	1.296×10^6	1.317×10^6	65.6%	3.88%
Timing cut	1.294×10^6	1.317×10^6	65.6%	3.88%
Veto cut	1.281×10^5	1.380×10^5	53.0%	29.86%
Fiducial volume cut	3.618×10^4	3.585×10^4	41.2%	89.40%

7.2.3 Event selection for the standard module

The ν_μ CC interactions in the standard module can be selected with sufficiently high purity by the event selection for the beam measurement described in Chapter 6. However, if the same event selection is used for the standard module, there are large differences in the selection efficiency between the standard module and the Proton Module, as shown in Fig. 7.7. It is because the acceptance of the Proton Module is limited by the required track matching with the standard module. This difference enlarges the systematic error on the measurement of the CC inclusive cross section ratio on Fe to CH because it causes non-cancelable systematic errors between the measurements with the standard module and the Proton Module. To minimize this difference, the following acceptance cut is added to the event selection for the standard module. First, an imaginary standard module is defined directly behind the standard module. The distance between the standard module and the imaginary module is the same as that between the Proton Module and the standard module. The reconstructed tracks are then extended further downstream, even if the track has stopped in the module. If any of extended tracks from the vertex do not reach the imaginary module, the event is rejected as illustrated in Fig. 7.8. After applying this acceptance cut, the difference in the selection efficiencies between the standard module and the Proton Module is greatly reduced, as shown in Fig. 7.7. The results of the event selection are summarized in Table 7.3.

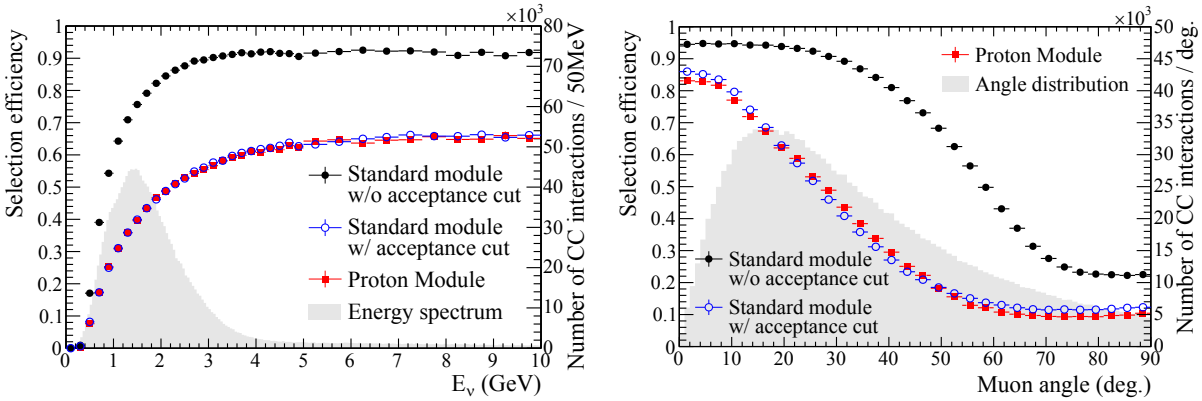

Figure 7.7: Event selection efficiency of CC interactions for the standard module and the Proton Module as a function of true neutrino energy (left) and true muon scattering angle (right). The energy spectrum and the angular distribution of the CC interactions in the standard module are overlaid.

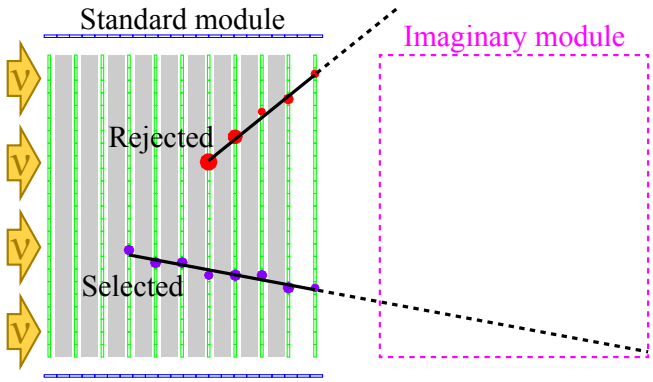

Figure 7.8: Event display of a selected event and a rejected event by the acceptance cut.

Table 7.3: The number of events passing each selection step for the standard module. The efficiency is defined as the number of selected ν_μ CC events divided by the number of ν_μ CC interactions in the FV. The purity is defined as the ratio of selected the ν_μ CC events on Fe to the total selected events.

Selection	Data	MC	Efficiency	Purity
Event reconstruction	3.179×10^6	3.194×10^6	96.7%	35.88%
Timing cut	3.179×10^6	3.194×10^6	96.7%	35.88%
Veto cut	1.369×10^6	1.418×10^6	88.8%	74.19%
Fiducial volume cut	8.875×10^5	9.169×10^5	74.4%	86.59%
Acceptance cut	5.185×10^5	5.130×10^5	42.7%	88.75%

7.2.4 Event-pileup correction

The numbers of finally-selected ν_μ CC candidate events in the standard module and the Proton Module are 518512 and 36182, respectively. The event-pileup effect is estimated and corrected in the same method as the Chapter 6. After the event-pileup correction, the numbers of selected events in the standard module and the Proton Module become 523045 and 36330, respectively.

7.3 Analysis strategy

The flux-averaged ν_μ CC inclusive cross section is calculated from the number of selected events using the background subtraction and efficiency correction:

$$\sigma_{\mathrm{CC}} = \frac{N_{\mathrm{sel}} - N_{\mathrm{BG}}}{\phi T \varepsilon}, \tag{7.1}$$

where N_{sel} is the number of selected events from real data, N_{BG} is the expected number of selected background events, ϕ is the integrated ν_μ flux, T is the number of target nucleons, and ε is the detection efficiency for CC events. N_{BG}, ϕ, and ε are estimated by using the MC simulation, and T is calculated from the target mass measured prior to the detector assembly (see Appendix F for details). These quantities for the measurements on Fe and CH targets are summarized in Table 7.4. The background events for this analysis consist of NC events, $\bar{\nu}_\mu$ events, ν_e events, interactions on elements other than the measuring elements in the detector, and external background events created by neutrino interactions in the material surrounding the detector. The breakdowns of the background events are summarized in Table 7.5. Difference in ϕ for the measurements on Fe and CH targets is very small because two detectors are located close to each other on the same neutrino beam axis. Difference in ε is also very small owing to the acceptance cut. In order to avoid a subjective bias, a blind analysis technique was employed, and the number of selected events from real data had been masked until the event selection criteria and the systematic error estimation method were established. This technique was used in all the cross section analyses in this thesis.

Table 7.4: Summary of the inputs for the calculation of the CC inclusive cross section on Fe and CH.

	N_{sel}	N_{BG}	ϕ	T	ε
Fe target (standard module)	523045	67838	$2.999\times10^{13}\mathrm{cm}^{-2}$	2.461×10^{30}	0.4270
CH target (Proton Module)	36330	5385.5	$3.025\times10^{13}\mathrm{cm}^{-2}$	1.799×10^{29}	0.4122

Table 7.5: The expected breakdown of the background events for the CC inclusive cross section analysis. Ratio to the total number of selected events is shown in parenthesis.

Category	Fe target	CH target
NC events	33705 (6.44%)	1548.5 (4.19%)
$\bar{\nu}_\mu$ events	10686 (2.04%)	884.4 (2.39%)
ν_e events	5160 (0.99%)	269.2 (0.73%)
Other target elements	13995 (2.67%)	515.4 (1.39%)
Background events from outside	4292 (0.82%)	2168.0 (5.87%)

7.4 Systematic errors

Uncertainties on N_{BG}, ϕ, T, and ε cause systematic errors on the cross section results. The sources of the uncertainties can be categorized into three groups: those from the neutrino flux prediction, the neutrino interaction model including intra-nuclear interactions, and the detector response.

7.4.1 Systematic errors from the neutrino flux prediction

To evaluate the systematic error from the neutrino flux uncertainties, we need to take account not only of the fractional uncertainties of the neutrino flux in bins of neutrino energy, but also of their correlations among the bins. Thus, the flux uncertainties and correlations are evaluated in the form of the covariance matrix [281,282]. There are many sources of the flux uncertainties as described in Chapter 4. The neutrino fluxes are re-simulated with $\pm 1\sigma$ variations of each error source parameter, and the covariance matrix element is calculated as:

$$V_{ij} = \frac{1}{2}\frac{(\phi^i_{\mathrm{nom}} - \phi^i_+)(\phi^j_{\mathrm{nom}} - \phi^j_+)}{\phi^i_{\mathrm{nom}}\phi^j_{\mathrm{nom}}} + \frac{1}{2}\frac{(\phi^i_{\mathrm{nom}} - \phi^i_-)(\phi^j_{\mathrm{nom}} - \phi^j_-)}{\phi^i_{\mathrm{nom}}\phi^j_{\mathrm{nom}}}, \tag{7.2}$$

where ϕ^i_{nom} is the nominal flux, ϕ^i_+ and ϕ^i_- are the re-simulated fluxes for $+1\sigma$ and -1σ variations of an error source parameter, and i specifies the neutrino energy bin. The combined uncertainty on the flux prediction, represented by the sum of the covariances from each independent error source, is shown in Fig. 7.9.

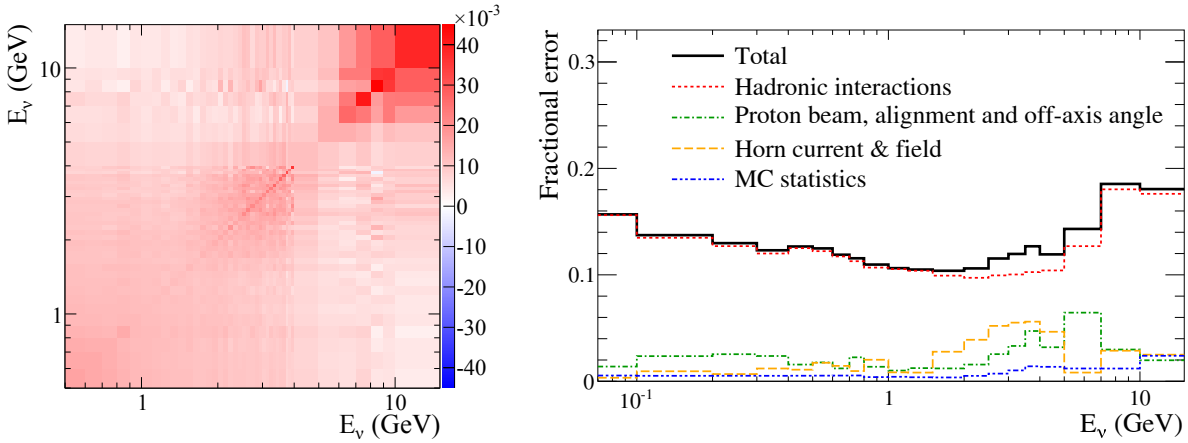

Figure 7.9: Covariance matrix (left) and the fractional error (right) of the T2K on-axis neutrino flux uncertainty. The fractional error corresponds to the square root of the diagonal element of the covariance matrix.

Then, the neutrino flux is fluctuated using the covariance matrix. This is repeated for many toy MC data sets, and the $\pm 1\sigma$ of the change in the cross section result is taken as the systematic error associated with the neutrino flux. There is a strong correlation between the variations of the cross section result on Fe and CH, hence the systematic error on their ratio is much smaller as shown in Fig. 7.10.

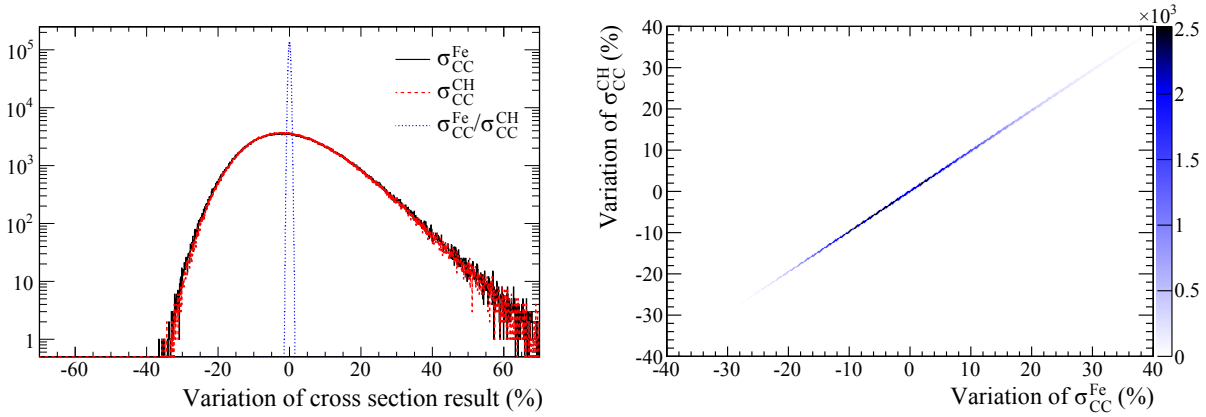

Figure 7.10: The variations of the CC inclusive cross section results for 10^6 toy MC sets generated according to the flux covariance matrix (left) and the correlation between the cross section results on Fe and CH (right).

7.4.2 Systematic errors from the neutrino interaction model

Systematic errors from the neutrino interaction model are estimated from variations of the cross section results when the interaction parameters introduced in Chapter 4 are varied within their uncertainties as shown in Fig. 7.11. For the measurement of the CC inclusive cross section ratio on Fe to CH, we assume that the uncertainties of M_A^{RES}, CC1π normalizations, NC normalizations, Fermi gas parameters and pion secondary interactions are fully correlated between the Fe target and the CH target cases because these uncertainties are understood as independent of the target nucleus. By contrast, the uncertainties of M_A^{QE}, CCQE normalizations, CC coherent pion normalization and spectral function parameter are assumed to be uncorrelated because nuclear dependences of these uncertainties are not well understood. In addition, the uncertainty of the CC other shape parameter which scales the number of the other CC interaction events (mainly CC deep inelastic scattering events) as a function of the neutrino energy is left out of the cross section ratio measurement because there is no evidence for a large nuclear modification in the deep inelastic scattering regime.

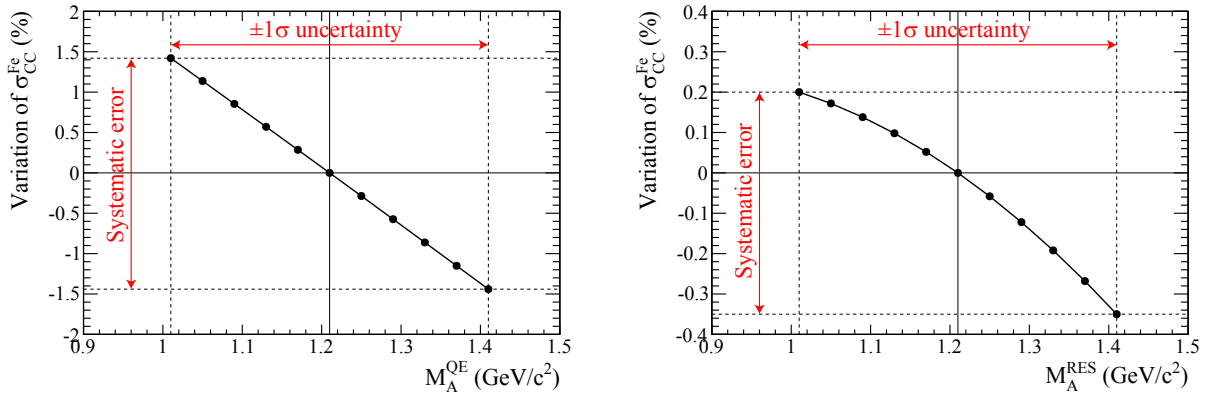

Figure 7.11: The variations of the CC inclusive cross section result on Fe when M_A^{QE} (left) and M_A^{RES} (right) are varied within their uncertainties.

7.4.3 Systematic errors from the detector response

The methods of estimating systematic errors from the detector response are the same as those for the neutrino beam measurement described in Chapter 6. The track matching for the Proton Module and the acceptance cut for the standard module are newly introduced in this cross section analysis. Thus, systematic errors from them are evaluated from the maximum difference of the data − MC for several selection thresholds as with other event selections.

7.4.4 Summary of the systematic errors

Table 7.6 summarizes the systematic errors. The total systematic errors on the CC inclusive

Table 7.6: Summary of the systematic errors on the CC inclusive cross section measurement.

Item	Fe target	CH target	Fe/CH ratio
Neutrino flux	−10.34%+12.74%	−10.12%+12.48%	−0.31%+0.31%
M_A^{QE}	−1.44%+1.42%	−0.60%+0.72%	−1.61%+1.55%
M_A^{RES}	−0.35%+0.20%	−0.61%+0.45%	−0.25%+0.27%
CCQE normalization (E_ν <1.5 GeV)	−0.82%+0.79%	−0.52%+0.50%	−0.95%+0.94%
CCQE normalization (1.5< E_ν <3.5 GeV)	−0.45%+0.50%	−0.67%+0.76%	−0.88%+0.83%
CCQE normalization (E_ν >3.5 GeV)	−0.11%+0.11%	−0.10%+0.11%	−0.15%+0.15%
CC1π normalization (E_ν <2.5 GeV)	−1.50%+1.37%	−1.72%+1.66%	−0.28%+0.22%
CC1π normalization (E_ν >2.5 GeV)	−0.50%+0.52%	−0.54%+0.56%	−0.04%+0.04%
CC coherent π normalization	−0.48%+0.49%	−1.03%+1.10%	−1.20%+1.14%
CC other shape	−0.82%+0.77%	−1.07%+1.02%	–
NC1π^0 normalization	−0.30%+0.31%	−0.18%+0.18%	−0.13%+0.13%
NC1$\pi^\pm$ normalization	−0.31%+0.31%	−0.23%+0.23%	−0.07%+0.07%
NC coherent π normalization	−0.02%+0.02%	−0.01%+0.01%	−0.01%+0.01%
NC other normalization	−1.21%+1.23%	−0.71%+0.72%	−0.51%+0.51%
π-less Δ decay	−0.50%+0.54%	−0.35%+0.39%	−0.15%+0.15%
Spectral function	−0.76%+0.00%	−0.98%+0.00%	−0.76%+0.98%
Fermi momentum	−0.43%+0.49%	−0.39%+0.41%	−0.04%+0.08%
Binding energy	−0.31%+0.32%	−0.22%+0.25%	−0.09%+0.07%
Pion absorption	−0.15%+0.13%	−0.09%+0.08%	−0.05%+0.04%
Pion charge exchange (low energy)	−0.06%+0.09%	−0.07%+0.10%	−0.16%+0.17%
Pion charge exchange (high energy)	−0.09%+0.08%	−0.08%+0.08%	−0.02%+0.00%
Pion QE scattering (low energy)	−0.14%+0.15%	−0.18%+0.13%	−0.00%+0.06%
Pion QE scattering (high energy)	−0.16%+0.11%	−0.23%+0.21%	−0.10%+0.08%
Pion inelastic scattering	−0.24%+0.20%	−0.26%+0.23%	−0.03%+0.02%
Target mass	±0.14%	±0.27%	±0.30%
MPPC dark count	±0.23%	±0.12%	±0.26%
Hit efficiency	±0.44%	±0.44%	±0.62%
Event pileup	±0.05%	±0.03%	±0.06%
Beam-induced external background	±0.10%	±0.93%	±0.94%
Cosmic-ray background	±0.01%	±0.02%	±0.02%
2D track reconstruction	±0.50%	±0.58%	±0.77%
Track matching	–	±0.31%	±0.31%
3D tracking	±0.15%	±0.97%	±0.98%
Vertexing	±0.31%	±0.12%	±0.33%
Timing cut	±0.01%	±0.01%	±0.01%
Veto cut	±0.53%	±0.58%	±0.79%
Fiducial volume cut	±0.40%	±0.18%	±0.44%
Acceptance cut	±0.36%	–	±0.36%
Total	−10.84%+13.11%	−10.69%+12.91%	−3.33%+3.32%

cross sections on Fe and CH, and their ratio are $^{+13.11\%}_{-10.84\%}$, $^{+12.91\%}_{-10.69\%}$, and $^{+3.32\%}_{-3.33\%}$, respectively. They are calculated from the quadrature sum of all the systematic errors. The neutrino flux error is the dominant systematic error for the measurement of the CC inclusive cross section on Fe and CH. However, it is small for the measurement of the cross section ratio on Fe to CH because this error mostly cancels between two detectors, as expected. On the other hand, systematic errors from M_A^{QE}, CCQE normalizations, CC coherent pion normalization and spectral function parameter are large for the measurement of the cross section ratio because the nuclear dependences of these parameters are conservatively treated.

7.5 Results

The measured flux-averaged CC inclusive cross sections on Fe and CH and their ratio are

$$\sigma_{\mathrm{CC}}^{\mathrm{Fe}} = (1.444 \pm 0.002(stat.)^{+0.189}_{-0.157}(syst.)) \times 10^{-38}\mathrm{cm}^2/\mathrm{nucleon}, \quad (7.3)$$

$$\sigma_{\mathrm{CC}}^{\mathrm{CH}} = (1.379 \pm 0.009(stat.)^{+0.178}_{-0.147}(syst.)) \times 10^{-38}\mathrm{cm}^2/\mathrm{nucleon}, \quad (7.4)$$

$$\frac{\sigma_{\mathrm{CC}}^{\mathrm{Fe}}}{\sigma_{\mathrm{CC}}^{\mathrm{CH}}} = 1.047 \pm 0.007(stat.) \pm 0.035(syst.), \quad (7.5)$$

at a mean neutrino energy of 1.51 GeV [283]. They agree well with the predicted values by NEUT and GENIE shown in Table 7.7. The cross section results are shown in Figs. 7.12, 7.13, and 7.14 together with the predictions and measurements from other experiments. Our CC inclusive cross section result on Fe is the first cross section measurement on Fe in a few GeV region while that in higher energy region (5–50 GeV) was measured by MINOS [226]. Although the CC inclusive cross section on CH at a neutrino energy of ∼1 GeV measured by SciBooNE is about 30% higher than the model predictions at the 2σ level [279], such an inconsistency is not observed in our cross section result on CH at a comparable neutrino energy. The CC inclusive cross sections on CH in higher and lower energy regions were measured by the T2K ND280 detector [280] and the NOMAD experiment [278] respectively. To be exact, the result from MINOS (T2K ND280, SciBooNE and NOMAD) is the CC inclusive cross section on mixture target whose dominant element is Fe (CH). By contrast, we measured the CC inclusive cross section purely on Fe (CH) target because the CC interactions on elements other than Fe (CH) are treated as the background events in our analysis. Our result of the cross section ratio on Fe to CH is accurate to the level of 3%. Hence, its consistency with the neutrino interaction models demonstrates that the target dependence of the nuclear effect is well understood and correctly treated in the models on the 3% level. Although the nuclear effect on the neutrino interaction has been modeled using the results of the electron-nucleus scattering as described in Chapter 4, we checked the validity directly from the result of the neutrino interaction for the first time. Although the MINERνA experiment recently measured the CC inclusive cross section ratio at higher neutrino energies with 6∼9% precision in the similar method [284], our measurement is much more precise (Fig. 7.14). It is in large part because the selection efficiencies for Fe and CH targets are uniformed in our analysis method.

Table 7.7: Flux-averaged CC inclusive cross sections on Fe and CH and their ratio predicted by NEUT and GENIE.

	$\sigma_{\mathrm{CC}}^{\mathrm{Fe}}$	$\sigma_{\mathrm{CC}}^{\mathrm{CH}}$	$\sigma_{\mathrm{CC}}^{\mathrm{Fe}}/\sigma_{\mathrm{CC}}^{\mathrm{CH}}$
NEUT	$1.398\times10^{-38}\mathrm{cm}^2$	$1.348\times10^{-38}\mathrm{cm}^2$	1.037
GENIE	$1.241\times10^{-38}\mathrm{cm}^2$	$1.188\times10^{-38}\mathrm{cm}^2$	1.044

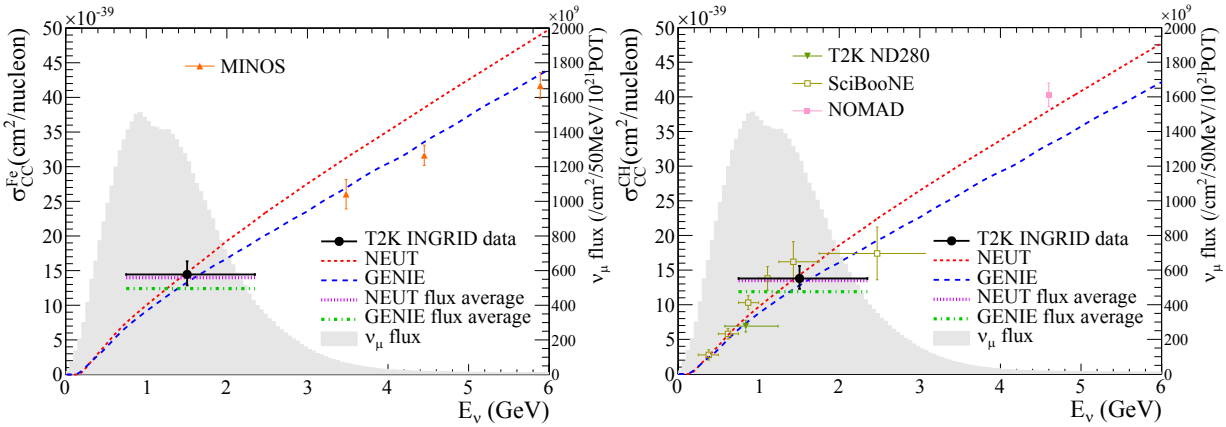

Figure 7.12: The inclusive ν_μ charged current cross section on Fe (left) and that on CH (right) with predictions by NEUT and GENIE. Our data point is placed at the flux mean energy. The vertical error bar represents the total (statistical and systematic) uncertainty, and the horizontal bar represents 68% of the flux at each side of the mean energy. The MINOS, T2K ND280, SciBooNE and NOMAD results are also plotted [226, 278–280].

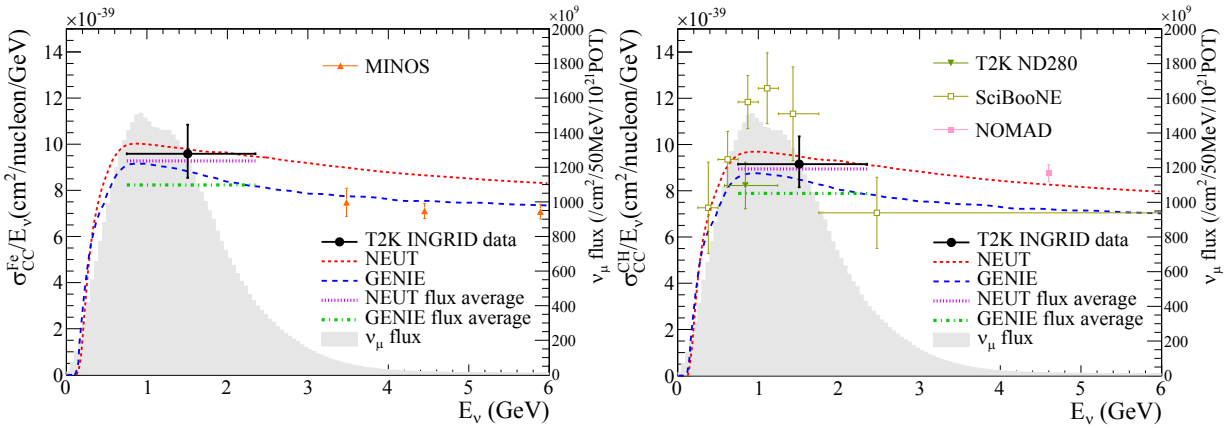

Figure 7.13: The inclusive ν_μ charged current cross section on Fe (left) and that on CH (right) divided by the neutrino energy with predictions by NEUT and GENIE.

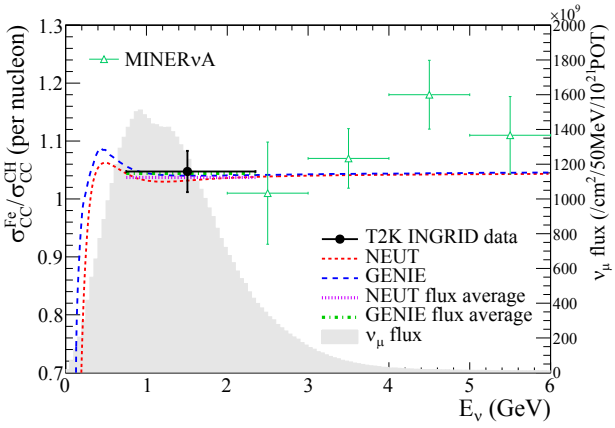

Figure 7.14: The ratio of the inclusive ν_μ charged current cross section on Fe to CH with predictions by NEUT and GENIE. The MINERνA result is also plotted [284].

7.6 Considerations

7.6.1 Impact of our absolute CC inclusive cross section results

Our CC inclusive cross section measurement is nearly free from the uncertainty of the intra-nuclear hadronic interactions because systematic errors from the uncertainty is only 0.35%. It is because only the muon candidate tracks are used for the measurement. On the other hand, exclusive cross section measurements such as the CCQE and CC coherent pion cross section measurements presented from the next chapter are generally sensitive to the hadronic interactions because hadronic tracks are also used for the measurement. Hence, the CC inclusive cross section measurement is complementary to the exclusive cross section measurements. Our CC inclusive cross section result is useful to tune the neutrino interaction model with limited influence of the intra-nuclear interactions, and thus will be helpful not only for T2K but also for many other neutrino experiments.

7.6.2 Future prospects of absolute CC inclusive cross section measurement

We achieved about 12% precisions in the measurement of the CC inclusive cross section on Fe and CH, which are equal to the best in the world in a few GeV region. However, better precisions are required in order to gain a better understanding of the neutrino interaction. Currently, the systematic error is dominated by the 10% neutrino flux error. This error will be reduced by using more data from the NA61/SHINE experiment for the hadron production tuning. Thus, more precise cross section measurements will be possible in the future. Ultimately, the neutrino flux error is expected to be reduced to the 5% level. If the 5% precision is achieved in the CC inclusive cross section measurement, we will be able to indicate our data prefers NEUT or GENIE at the 3σ level.

7.6.3 Impact of our CC inclusive cross section ratio result on different targets

In the current T2K neutrino oscillation analysis, many of the neutrino interaction uncertainties are treated independently between ND280 and Super-K due to the difference in the target material. As a result, they are not constrained by the ND280 measurement and thus cause large systematic errors on the T2K neutrino oscillation measurement. For example, about 5% out of the total 7% systematic error on the number of neutrino events in Super-K comes from the neutrino interaction uncertainties which are treated independently between ND280 and Super-K. Although this treatment is considered to be too conservative, there had been no experimental evidence to justify the dependent treatment. Our result of the CC inclusive cross section ratio on CH to Fe demonstrated that the dependence between carbon nucleus and iron nucleus is correctly treated in the neutrino interaction model. The difference in the nuclear effect between the carbon nucleus ($A = 6$) and oxygen nucleus ($A = 8$) is expected to be much smaller than that between the carbon nucleus and iron nucleus ($A = 26$). Thus, our result will be a good experimental evidence although it is not enough to justify the dependent treatment of all the neutrino interaction uncertainties. In order to justify the dependent treatment of all the uncertainties, similar measurements on various combinations of targets at various neutrino energies are required.

7.6.4 Future prospects of CC inclusive cross section ratio result measurement on different targets

The measurement of the neutrino cross section ratio on different targets using two detectors on the same beamline was conducted for the first time in the world. This measurement demonstrates that a major part of the systematic errors is cancelled between the two detectors and the total

systematic error becomes very small (∼3%), as expected. Thus, similar measurements will follow in the future, which will bring a better understanding of the nuclear effects of the target material. For example, a measurement of the CC inclusive cross section ratio on H_2O to CH using the ND280 detector is going on. If it is precisely measured and agrees with the model prediction, it will be a stronger evidence to justify the dependent treatment of the neutrino interaction uncertainties between ND280 and Super-K.

7.6.5 Establishment of the method of neutrino cross section measurements using INGRID

This is the first neutrino cross section result using INGRID. Although INGRID was originally developed for the measurement of the neutrino beam properties, we demonstrated its ability to measure the neutrino cross section. In addition, we have established a strong basis of the neutrino cross section measurement in T2K (*i.e.* the neutrino detector, the Monte Carlo simulation, and the analysis tools for the event selection and the systematic error evaluation). They are applicable not only to the CCQE and CC coherent pion cross section measurements presented from the next chapter, but also to various other neutrino cross section measurements. Thus, many neutrino cross section analyses using INGRID are going on or projected, and they will bring many interesting results in the near future.

Chapter 8

Measurement of Charged Current Quasi-Elastic Cross Section

The charged current quasi-elastic (CCQE) scattering is a two-body scattering between a neutrino and a nucleon ($\nu_l + n \rightarrow l^- + p$), which is the signal mode for the T2K neutrino oscillation measurement. This chapter describes the measurement of the ν_μ CCQE cross section on carbon with the Proton Module.

8.1 Introduction to the measurement of the charged current quasi-elastic cross section

The ν_μ CCQE cross section on carbon was measured by MiniBooNE [221], SciBooNE [285], NOMAD [222] and LSND [286] and the results are summarized in Fig. 8.1. The cross section predictions in this figure are calculated by the Llewellyn-Smith's formula [170] using the relativistic Fermi gas model with a free axial-vector mass parameter, M_A^{QE}. However, this approach cannot fully describe all the data sets. It is the largest problem facing neutrino interaction physics. Although there are some approaches to explain the discrepancy [287–298], none of them has definitive evidence. Among them, an introduction of neutrino interactions with two or more nucleons into the neutrino interaction model is one of the promising approaches [287–293].

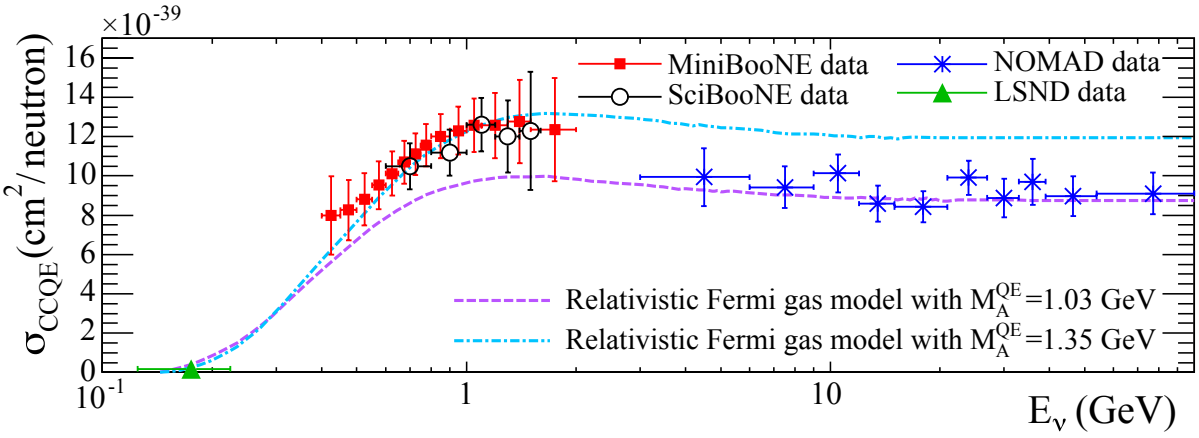

Figure 8.1: The ν_μ CCQE cross section as a function of the neutrino energy measured by MiniBooNE [221], SciBooNE [285], NOMAD [222] and LSND [286]. Predictions using the relativistic Fermi gas model with different parameter variations are superimposed.

This process emits one lepton and two or more nucleons via so-called meson exchange current (MEC)* as shown Fig. 8.2. Since a Cherenkov detector such as the MiniBooNE detector essentially cannot detect the nucleons, it cannot discriminate this multi-nucleon interaction from the CCQE interaction. Therefore, if the multi-nucleon interaction actually exists, MiniBooNE overestimates the CCQE cross section [288]. On the other hand, the uncertainty of the nuclear model is also regarded as a possible cause of the discrepancy [297] because the effect of the nuclear model is significant in a few GeV region. To obtain helpful information to solve the puzzle, following things are desired in the CCQE cross section measurement.

- A proton track from the CCQE interaction should be reconstructed in addition to a muon track.
- The CCQE cross section should be measured at various energy regions.
- Cross section results assuming various neutrino interaction models should be compared to each other.

We measure the ν_μ CCQE cross section on carbon using the T2K on-axis neutrino beam and the INGRID detector. In this measurement, the Proton Module is used as the neutrino interaction target. The reconstruction efficiency of the proton track in the Proton Module is relatively high (47% for the protons from CCQE) because it is a fully-active tracking detector. The T2K on-axis neutrino energy spectrum is widely distributed up to around 3 GeV. Thus, we measure the CCQE cross sections in the MiniBooNE energy region (∼1 GeV) and the higher energy region (∼2 GeV), separately. It is expected to bridge the energy gap between the measurements by MiniBooNE and NOMAD. In addition, we estimate the CCQE cross section using neutrino interaction models other than the T2K default model. Note that the T2K default neutrino interaction model is used in the MC simulation unless otherwise noted.

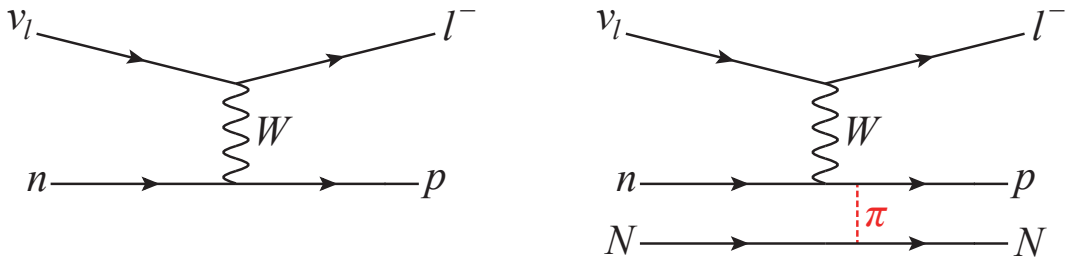

Figure 8.2: Feynman diagrams of the CCQE scattering (left) and the multi-nucleon interaction via the meson exchange current (right). The right diagram is an example of the multi-nucleon interaction, and there are many other varieties.

8.2 Event selection

8.2.1 Overview of event selection

As the first step, the same event selection as the one in Chapter 7 is applied to enrich the CC interaction events in the Proton Module and to reduce NC interaction events and background events from outside. After this selection, CCQE events make up 37.67% of the MC sample. To increase the selection purity for CCQE events, additional cuts are applied as illustrated in Fig. 8.3. First, CCQE events are enriched based on the number of reconstructed tracks, the

*The meson exchange current was originally conceived to be responsible for the dip region in the electron-nucleus scattering cross section as a function of the electron energy loss [299, 300].

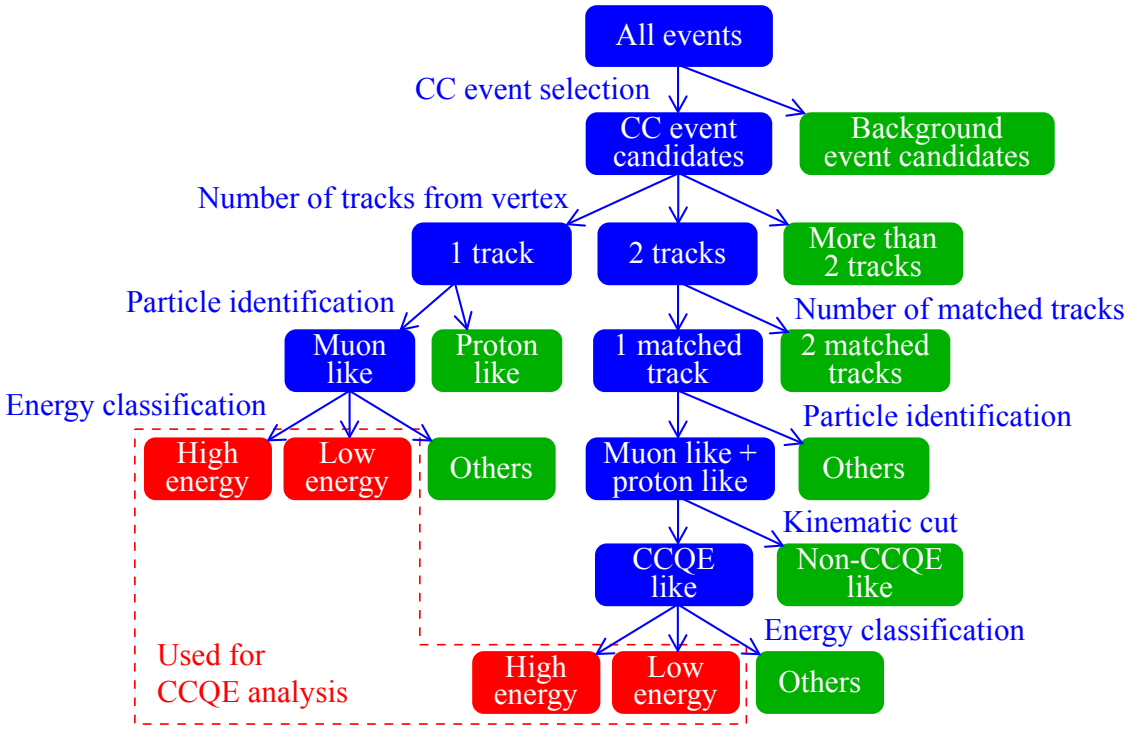

Figure 8.3: The flow chart of the CCQE event selections. Red, green and blue groups represent finally-selected samples, rejected samples and intermediary samples, respectively.

dE/dx particle identification variable and the reconstructed event kinematics [301]. Then the selected CCQE candidate events are classified according to the neutrino energy.

8.2.2 The number of tracks

The number of tracks from the vertex

The CCQE interaction produces two particles inside the target nucleus, a muon and a proton. However, the proton undergoes the intra-nuclear interactions and doesn't always escape from the nucleus. In addition, the proton may not be reconstructed in the detector due to its short range as shown in Fig. 8.4. Thus, events with one or two reconstructed tracks coming from the vertex are selected (Fig. 8.5). Hereafter, the events with one and two reconstructed tracks are referred to as the one-track sample and the two-track sample, respectively.

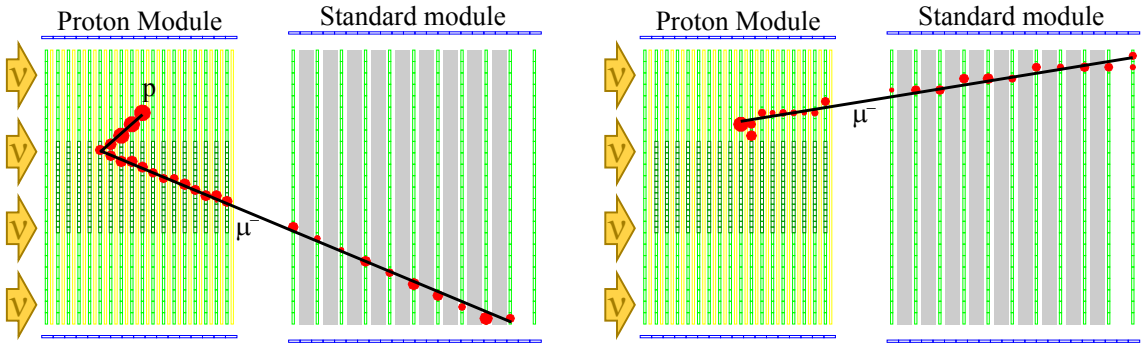

Figure 8.4: Event displays of MC CCQE events in the Proton Module when the proton track is reconstructed (left) and not reconstructed (right).

The number of matched tracks

At the step of the CC event selection, events with at least one matched track between the Proton Module and the standard module are selected in order to select long muon tracks as described in Chapter 7. About 7% of the selected events in the two-track sample have two matched tracks, which are mainly due to pions from CC-nonQE interactions. On the other hand, almost all the protons from CCQE interactions are not reconstructed in the standard module. Thus, events with only one matched track are selected for the two-track sample (Fig. 8.6). Hereafter, the matched track is referred to as the first track and the remaining track as the second track.

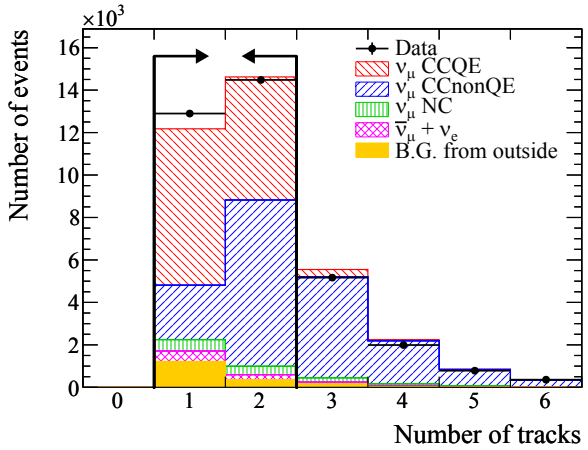

Figure 8.5: The number of reconstructed tracks from a vertex in the Proton Module.

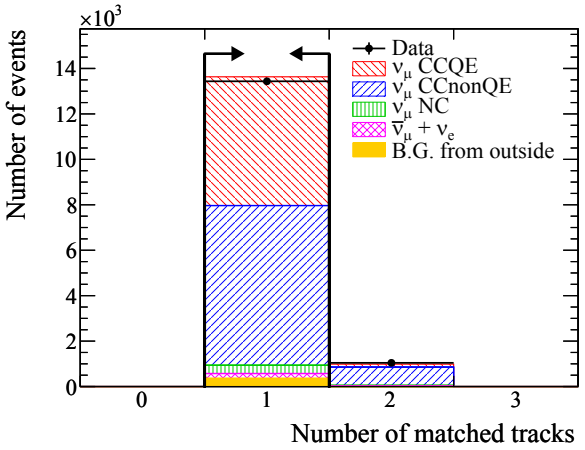

Figure 8.6: The number of matched tracks between the Proton Module and the standard module for the two track sample.

8.2.3 Particle identification

Definition of the muon confidence level (MuCL) variable

Particle identification (PID) based on dE/dx information is applied on both the one-track sample and the two-track sample in order to separate muon and pion tracks from proton tracks. The dE/dx for each scintillator plane is calculated from the light yield and the path length of the track in the scintillator in consideration of the light attenuation in the WLS fiber. The first step of the particle identification is to estimate a confidence level that a particle is a muon on a plane-by-plane basis. The confidence level at each plane is defined as the fraction of events in the expected dE/dx distribution of muons above the observed dE/dx value. The expected dE/dx distribution of muons is obtained from the beam-induced external muon events. The cumulative distribution function of the muon dE/dx distribution corresponds to the confidence level (Fig. 8.7). The calculated confidence level at the i-th plane as a function of dE/dx is referred to as CL_i. The next step is to combine the confidence levels (CL_i) obtained from all the planes penetrated by the track to form a total confidence level. In the case where the track penetrates only two planes, the procedure to combine the two confidence levels, CL_1 and CL_2, is as follows. Assuming the confidence levels to be independent of one another, the product, $P = CL_1 \times CL_2$ is the combined probability. In the (CL_1, CL_2) plane, the hyperbola $P = CL_1 \times CL_2$ gives such a combined probability and the unified muon confidence level, MuCL, is the fraction of possible CL_1, CL_2 values that gives $P < CL_1 \times CL_2$. Therefore, the shaded area indicated in Fig. 8.8

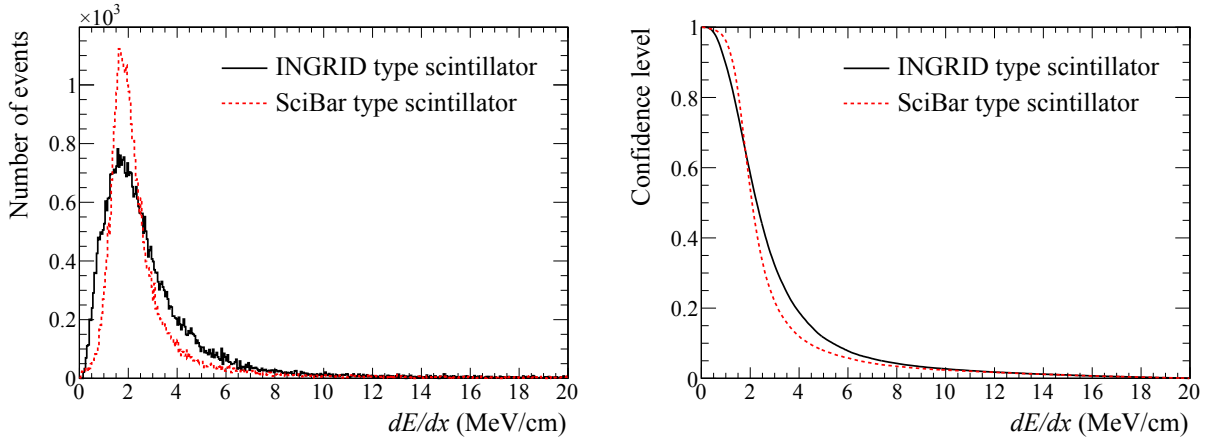

Figure 8.7: The dE/dx distribution of muons obtained by the beam-induced external muon events (left) and the confidence level of muon as a function of dE/dx (right).

can be considered as the unified muon confidence level, MuCL, which is expressed as

$$\begin{aligned} \text{MuCL} &= 1 - \int_P^1 d(CL_2) \int_{P/CL_2}^1 d(CL_1) \\ &= P(1 - \ln P). \end{aligned} \tag{8.1}$$

In analogy with the two plane case, the muon confidence level combined from n planes is expressed as

$$\text{MuCL} = P \times \sum_{i=0}^{n-1} \frac{(-\ln P)^i}{i!}, \; P = \prod_{i=1}^{n} CL_i. \tag{8.2}$$

When a Proton Module track is matched with a standard module track, the standard module track is also used to make the MuCL.

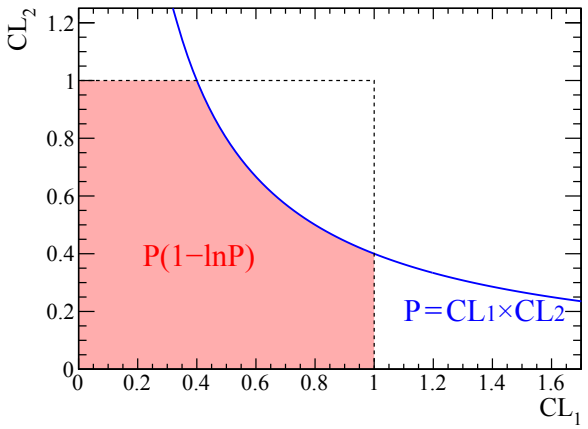

Figure 8.8: The hyperbola obtained from two independent confidence level, CL_1 and CL_2. The red area corresponds to the confidence level combined together from the two.

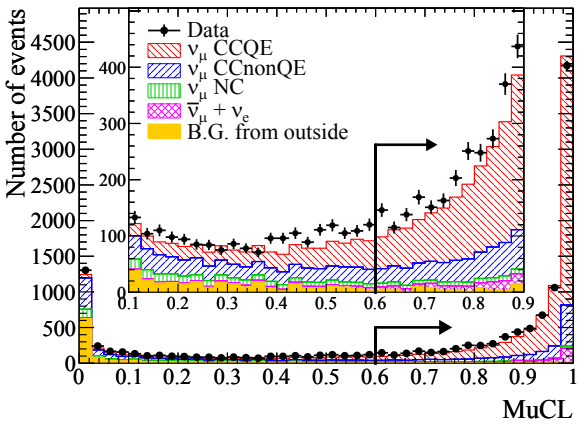

Figure 8.9: MuCL distributions for the one-track sample.

Separation of muon-like tracks and proton-like tracks

The last step of the particle identification is to distinguish the tracks using the MuCL. In this analysis, tracks whose MuCL are more than 0.6 are identified as muon-like and those less than 0.6 are identified as proton-like. The probability of misidentifying a muon track (a proton track) as proton-like (muon-like) in the MC simulation is 12.5% (10.9%). Most pion tracks are identified as muon-like since both muons and pions are minimally ionizing particles at the energies seen by INGRID. For the one-track sample, that track is required to be muon-like (Fig. 8.9) and the selected events are taken as the CCQE enhanced sample of the one-track sample. For the two-track sample, the first track is required to be muon-like and the second track to be proton-like (Fig. 8.10).

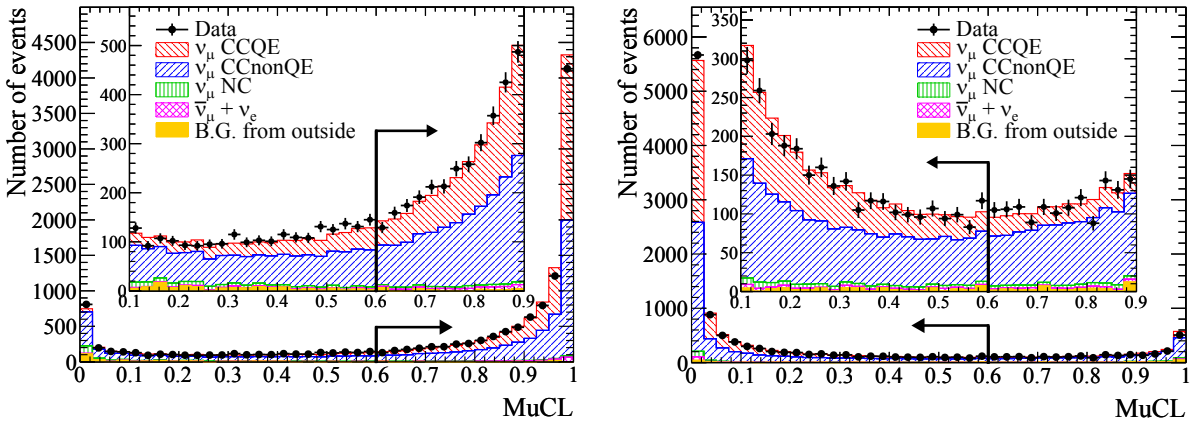

Figure 8.10: MuCL distributions of the first track (left) and the second track (right) for the two-track sample.

8.2.4 Kinematic cut

In addition, two kinematic cuts are applied to the two-track sample. These cuts use two angles called the coplanarity angle and the opening angle defined as shown in Fig. 8.11.

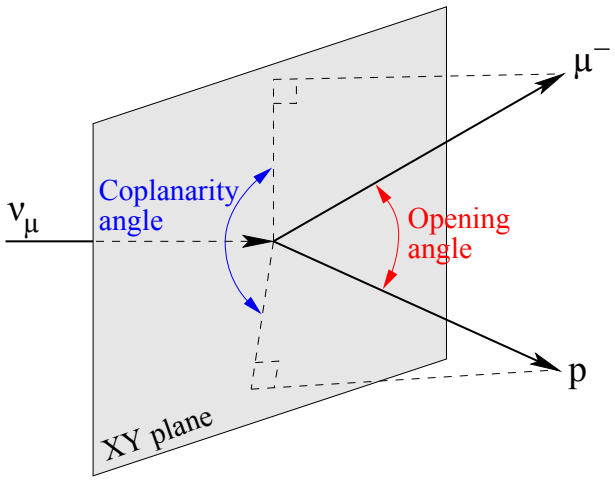

Figure 8.11: Definition of the coplanarity angle and the opening angle.

Coplanarity angle cut

Since CCQE events are (quasi) two-body scattering interactions, all the tracks in a CCQE event (an incident neutrino track and scattered muon and proton tracks) are expected to lie in the same plane if the effects of the proton re-scatterings and the Fermi momentum are neglected. To evaluate such a coplanarity, the coplanarity angle is defined as the angle between the two reconstructed tracks projected to the XY plane, where the XY plane is perpendicular to the neutrino beam axis (Fig. 8.11). When the three tracks are coplanar, the coplanarity angle becomes 180°. Thus, events with a coplanarity angle above 150° are selected (Fig. 8.12).

Opening angle cut

The opening angle is defined as the three-dimensional angle between the two reconstructed tracks (Fig. 8.11). The opening angle of the CCQE interaction tends to be large because the two particles from the CCQE interaction are produced back to back in the center-of-mass frame. Thus, events with an opening angle above 60° are selected (Fig. 8.13).

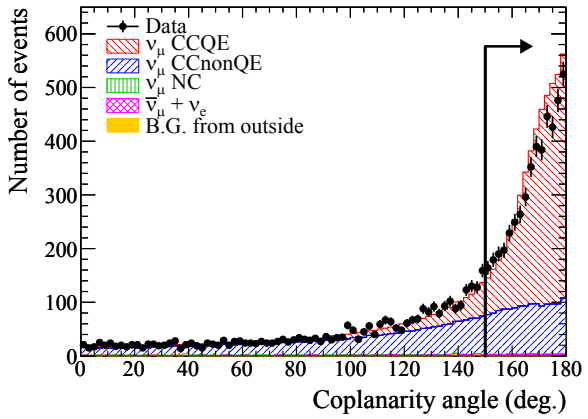

Figure 8.12: Coplanarity angle distribution following the PID cut for the two track sample.

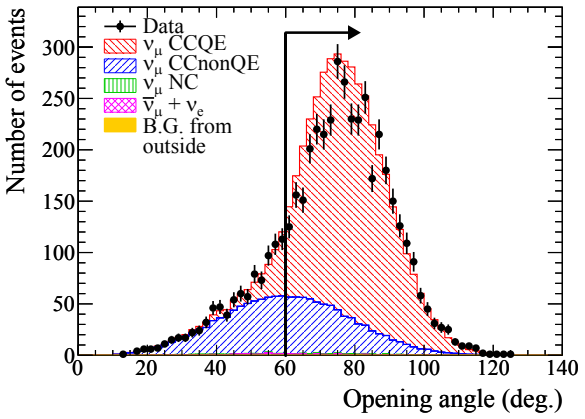

Figure 8.13: Opening angle distribution following the PID and coplanarity angle cuts for the two track sample.

8.2.5 Energy classification

We aim to measure the CCQE cross section in the low energy region (∼1 GeV) and the high energy region (∼2 GeV) separately. Thus, an energy classification is applied to the CCQE enhanced samples to enhance the high energy events and the low energy events separately. The classification criterion is shown in Fig. 8.14. Events with a muon candidate track which penetrates all the standard module iron layers are selected as the high energy sample. Events with a muon candidate track which stops in the standard module are selected as the low energy sample. Other events with a muon candidate track which escapes from the side of the standard module are not used in this analysis. Figure 8.15 shows the neutrino energy spectra of the CCQE enhanced samples before and after applying the energy classification. Most of the CCQE events at neutrino energies below 1.0 GeV (above 1.5 GeV) are rejected by the high energy selection (the low energy selection).

8.2.6 Summary of event selection

The results of the CCQE event selection are summarized in Table 8.1. The numbers of finally-selected CCQE candidate events after the energy classification are summarized in Table 8.2.

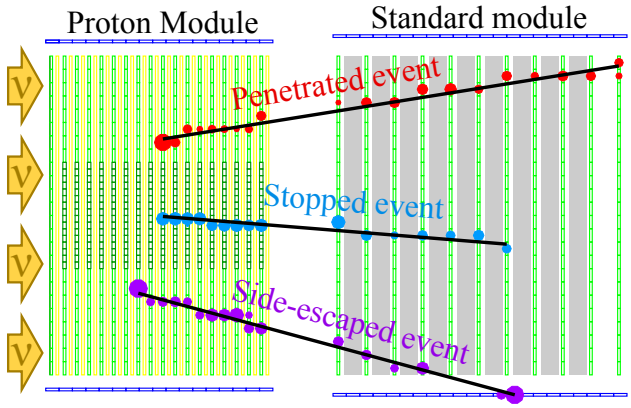

Figure 8.14: Event display of the penetrated, stopped and side-escaped events. All events are examples of the one-track sample.

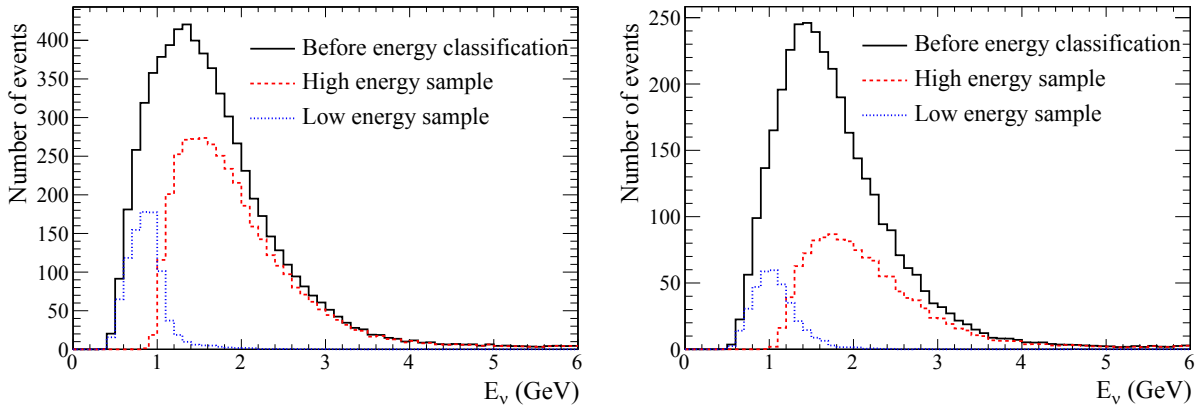

Figure 8.15: True neutrino energy spectra of the CCQE enhanced sample before and after applying the energy classification for the one-track sample (left) and the two-track sample (right).

Table 8.1: The number of events passing each CCQE selection step. The efficiency is defined as the number of selected ν_μ CCQE events divided by the number of ν_μ CCQE interactions in the FV. The purity is defined as the ratio of the selected ν_μ CCQE events to the total selected events.

Selection	Data	MC	Efficiency	Purity
Number of tracks = 1	12896	1.225×10^4	25.50%	60.13%
Particle identification	9059	8.749×10^3	23.04%	76.05%
Number of tracks = 2	14479	1.473×10^4	20.07%	39.36%
Number of matched tracks = 1	13436	1.374×10^4	19.62%	38.48%
Particle identification	7981	8.316×10^3	15.81%	54.91%
Kinematic cut	3832	4.234×10^3	12.24%	83.51%

Table 8.2: The numbers of finally-selected CCQE candidate events after the CCQE event selection and energy classification.

	High energy region		Low energy region	
	One-track	Two-track	One-track	Two-track
Without event-pileup correction	5000	1441	1448	406
With event-pileup correction	5018.06	1445.49	1456.85	408.93

8.3 Analysis strategy

We estimate the CCQE cross section in high and low energy regions which are defined as above 1.0 GeV and below 1.5 GeV from the high and low energy samples. The average energies of the neutrino flux in the high and low energy regions are 1.94 GeV and 0.93 GeV, respectively. As with the CC inclusive cross section analysis, the CCQE cross section is also calculated from the number of selected CCQE candidate events using the background subtraction and efficiency correction:

$$\sigma_{\mathrm{CCQE}} = \frac{N_{\mathrm{sel}} - N_{\mathrm{BG}}}{\phi T \varepsilon}, \tag{8.3}$$

where N_{sel} is the number of selected CCQE candidate events from real data, N_{BG} is the number of selected background events predicted by the MC simulation, ϕ is the integrated ν_μ flux, T is the number of target neutrons, and ε is the detection efficiency for CCQE events predicted by the MC simulation. The ϕ is integrated in each energy region and the ε is calculated for CCQE events in each energy region. CCQE events out of each energy region are taken as the background events. Furthermore, the CCQE cross section in each energy region is estimated from the one-track sample, two-track sample, and combined sample, separately. The one-track sample (the two-track sample) has an enhanced content of low (high) energy protons from CCQE interactions as shown in Fig. 8.16. However, the kinematics of the protons from CCQE is not well understood because it has never been measured. If it is not correctly predicted by the neutrino interaction model, it will give rise to a difference in the cross section result from each sample. Therefore, comparisons between the results from the different samples will provide a good test of the neutrino interaction model.

The quantities of N_{sel}, N_{BG}, ϕ, T and ε for each sample are summarized in Table 8.3. The background events for this analysis consist of CC-nonQE events, NC events, $\bar{\nu}_\mu$ events, ν_e events, external background events created by neutrino interactions in the material surrounding the detector, and CCQE events out of the energy region. They are dominated by the CC resonant pion events as shown in Table 8.4.

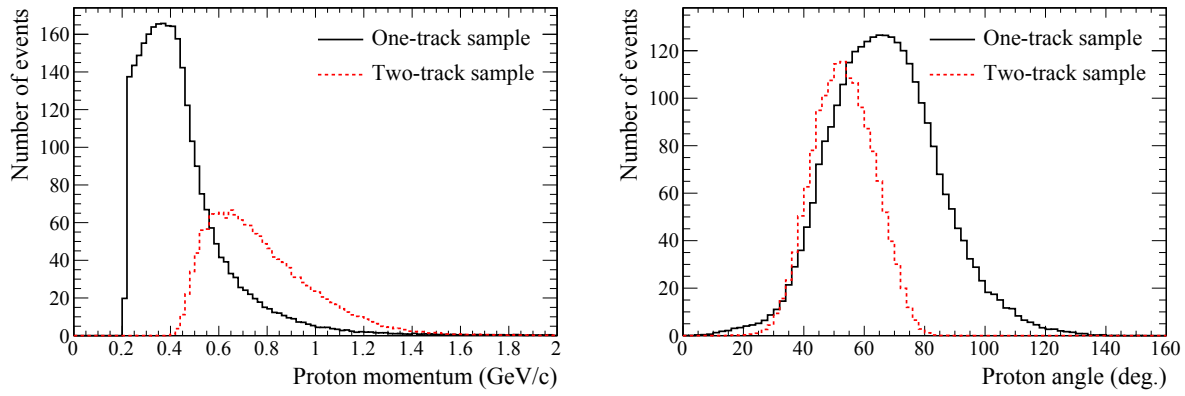

Figure 8.16: Distributions of the true momentum (left) and angle (right) of protons from the CCQE events in the one-track sample and the two-track sample. The cutoff around 0.2 GeV/c in the proton momentum distribution stems from the effect of the Pauli blocking.

Table 8.3: Summary of the inputs for the CCQE cross section calculation.

	N_{sel}	N_{BG}	ϕ	T	ε
High energy one-track sample	5018.06	1073.73	$2.025\times10^{13}\mathrm{cm}^{-2}$	8.453×10^{28}	0.1875
High energy two-track sample	1445.49	244.78	$2.025\times10^{13}\mathrm{cm}^{-2}$	8.453×10^{28}	0.0639
High energy combined sample	6463.54	1318.51	$2.025\times10^{13}\mathrm{cm}^{-2}$	8.453×10^{28}	0.2514
Low energy one-track sample	1456.85	479.22	$1.885\times10^{13}\mathrm{cm}^{-2}$	8.453×10^{28}	0.0528
Low energy two-track sample	408.93	155.24	$1.885\times10^{13}\mathrm{cm}^{-2}$	8.453×10^{28}	0.0199
Low energy combined sample	1865.78	634.46	$1.885\times10^{13}\mathrm{cm}^{-2}$	8.453×10^{28}	0.0727

Table 8.4: The expected breakdown of the background events for the CCQE cross section analysis.

Category	High energy region		Low energy region	
	One-track	Two-track	One-track	Two-track
CCQE events out of the energy region	20.11	0.19	25.28	25.34
CC resonant pion events	558.65	186.96	217.97	91.33
CC other events	172.35	49.34	61.63	29.47
NC events	6.61	0.68	87.93	6.32
$\bar{\nu}_\mu$ events	279.80	7.55	37.78	1.71
ν_e events	0.11	0.01	4.58	1.09
Background events from outside	36.07	0.02	44.01	0.01

8.4 Systematic errors

The methods of estimating systematic errors are the same as those for the CC inclusive cross section measurement described in Chapter 7 except for an additional systematic error from the uncertainty of the light yield. This error is added because this analysis uses the light yield for the particle identification based on dE/dx. First, the uncertainty of the light yield is evaluated by using beam-induced external muon events as the control sample. Figure 8.17 shows the average light yield per hit as a function of reconstructed track angle for the beam-induced external muon events. Differences in average light yield between the data and the MC simulation are taken as the uncertainties of the light yield. Then, light yields of hits included in the reconstructed tracks are varied by the light yield uncertainty as a function of the track angle. Differences in the cross section results with the nominal and varied light yield are taken as the systematic errors. Moreover, the systematic error from the scintillator quenching is additionally taken into account because it depends heavily on the kind of particles though the muon enhanced sample is used for the evaluation of the systematic error from the light yield. It is estimated from the variations of the cross section results when a constant in the Birks' law (so-called the Birks' constant) was varied within its uncertainty (0.0208±0.0023 cm/MeV, Fig. 4.8) in the MC simulation. The quadrature sum of the two errors is taken as the systematic error due to the light yield uncertainty. The total systematic errors on the CCQE cross section results from the one-track sample, the two-track sample and the combined sample for the high energy region are $^{+15.95\%}_{-12.97\%}$, $^{+16.97\%}_{-14.04\%}$ and $^{+15.19\%}_{-12.28\%}$, respectively, and those for the low energy region are $^{+20.35\%}_{-17.04\%}$, $^{+24.20\%}_{-18.86\%}$ and $^{+19.04\%}_{-15.49\%}$, respectively. The breakdown of the errors on the results from the combined sample is summarized in Table 8.5. As with the CC inclusive cross section measurement, the flux error is the dominant systematic error.

Table 8.5: Summary of the systematic errors on the CCQE cross section measurement from the combined sample.

Item	High energy region	Low energy region
Neutrino flux	$-11.01\% + 13.61\%$	$-13.57\% + 17.04\%$
M_A^{QE}	$-0.89\% + 2.25\%$	$-0.08\% + 0.39\%$
M_A^{RES}	$-0.92\% + 1.31\%$	$-0.82\% + 1.10\%$
CC1π normalization (E_ν <2.5 GeV)	$-0.55\% + 0.50\%$	$-3.71\% + 3.59\%$
CC1π normalization (E_ν >2.5 GeV)	$-0.33\% + 0.31\%$	$-0.75\% + 0.74\%$
CC coherent π normalization	$-1.40\% + 1.38\%$	$-1.73\% + 1.71\%$
CC other E_ν shape	$-0.86\% + 0.85\%$	$-0.11\% + 0.09\%$
NC1π^0 normalization	$-0.65\% + 0.65\%$	$-0.40\% + 0.40\%$
NC1$\pi^\pm$ normalization	$-0.47\% + 0.47\%$	$-0.46\% + 0.45\%$
NC coherent π normalization	$-0.10\% + 0.10\%$	$-0.09\% + 0.09\%$
NC other normalization	$-2.69\% + 2.69\%$	$-1.88\% + 1.83\%$
π-less Δ decay	$-0.54\% + 2.10\%$	$-1.60\% + 3.34\%$
Spectral function	$-0.00\% + 2.01\%$	$-0.00\% + 1.21\%$
Fermi momentum	$-1.67\% + 2.22\%$	$-3.71\% + 4.43\%$
Binding energy	$-0.44\% + 0.65\%$	$-1.24\% + 1.42\%$
Pion absorption	$-0.20\% + 0.81\%$	$-0.80\% + 1.20\%$
Pion charge exchange (low energy)	$-0.15\% + 0.18\%$	$-0.22\% + 0.28\%$
Pion charge exchange (high energy)	$-0.11\% + 0.13\%$	$-0.11\% + 0.11\%$
Pion QE scattering (low energy)	$-0.66\% + 0.71\%$	$-0.84\% + 0.79\%$
Pion QE scattering (high energy)	$-0.04\% + 0.03\%$	$-0.09\% + 0.09\%$
Pion inelastic scattering	$-0.05\% + 0.04\%$	$-0.29\% + 0.25\%$
Nucleon elastic scattering	$-0.25\% + 0.21\%$	$-0.29\% + 0.21\%$
Nucleon single π production	$-0.15\% + 0.11\%$	$-0.60\% + 0.51\%$
Nucleon two π production	$-0.57\% + 0.42\%$	$-0.01\% + 0.01\%$
Target mass	$\pm 0.31\%$	$\pm 0.38\%$
MPPC dark noise	$\pm 0.03\%$	$\pm 0.08\%$
Hit efficiency	$\pm 0.84\%$	$\pm 0.41\%$
Light yield	$\pm 1.47\%$	$\pm 2.22\%$
Event pileup	$\pm 0.02\%$	$\pm 0.06\%$
Beam-induced external background	$\pm 0.00\%$	$\pm 0.00\%$
Cosmic-ray background	$\pm 0.00\%$	$\pm 0.01\%$
2D track reconstruction	$\pm 0.67\%$	$\pm 0.81\%$
Track matching	$\pm 0.45\%$	$\pm 1.13\%$
3D tracking	$\pm 0.21\%$	$\pm 0.15\%$
Vertexing	$\pm 0.30\%$	$\pm 0.43\%$
Timing cut	$\pm 0.00\%$	$\pm 0.00\%$
Veto cut	$\pm 0.82\%$	$\pm 0.64\%$
Fiducial volume cut	$\pm 1.55\%$	$\pm 0.84\%$
Secondary interaction	$\pm 2.45\%$	$\pm 2.37\%$
Total	$-12.28\% + 15.19\%$	$-15.49\% + 19.04\%$

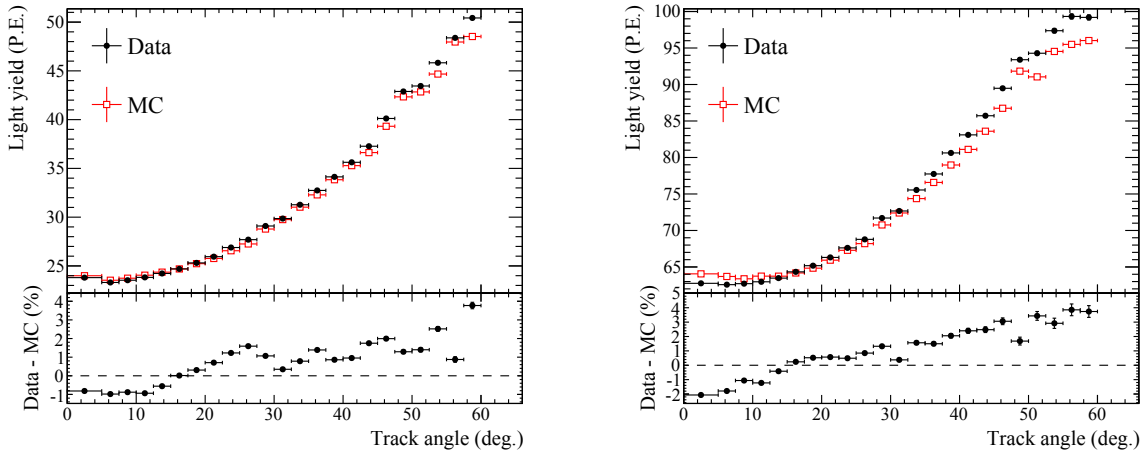

Figure 8.17: Average light yield per hit as a function of reconstructed track angle for the beam-induced external muon events for the INGRID-type scintillator (left) and the SciBar-type scintillator (right).

8.5 Results

8.5.1 Results with the T2K default interaction model

The result of the CCQE cross section measurement from the each sample is summarized in Table 8.6. The measured CCQE cross sections from the combined sample are

$$\sigma_{\mathrm{CCQE}}(1.94\mathrm{GeV}) = (11.95 \pm 0.19(stat.)^{+1.82}_{-1.47}(syst.)) \times 10^{-39}\mathrm{cm}^2/\mathrm{neutron}, \quad (8.4)$$

$$\sigma_{\mathrm{CCQE}}(0.93\mathrm{GeV}) = (10.64 \pm 0.37(stat.)^{+2.03}_{-1.65}(syst.)) \times 10^{-39}\mathrm{cm}^2/\mathrm{neutron}, \quad (8.5)$$

at mean neutrino energies of 1.94 GeV and 0.93 GeV (for the high and low energy regions), respectively. The NEUT and GENIE predictions of the CCQE cross sections on carbon for the high and low energy regions are shown in Table 8.7. The difference in the predictions by NEUT and GENIE is mainly attributed to the difference in the nominal M_A^{QE} value, 1.21 GeV/c^2 for NEUT and 0.99 GeV/c^2 for GENIE. The cross section results are shown in Fig. 8.18 together with the predictions and the measurements of other experiments. The results of the measurements agree within 2σ with predictions by NEUT and GENIE. However, the cross section result from the one-track sample differs from that from the two-track sample in the low energy region.

Table 8.6: The CCQE cross section measured from each sample ($\times 10^{-39}\mathrm{cm}^2$). Mean neutrino energies of the high and low energy regions are 1.94 GeV and 0.93 GeV, respectively.

Used sample	High energy region	Low energy region
One-track sample	$12.29 \pm 0.22(stat.)^{+1.96}_{-1.59}(syst.)$	$11.63 \pm 0.45(stat.)^{+2.37}_{-1.98}(syst.)$
Two-track sample	$10.98 \pm 0.35(stat.)^{+1.86}_{-1.54}(syst.)$	$8.01 \pm 0.64(stat.)^{+1.94}_{-1.51}(syst.)$
Combined sample	$11.95 \pm 0.19(stat.)^{+1.82}_{-1.47}(syst.)$	$10.64 \pm 0.37(stat.)^{+2.03}_{-1.65}(syst.)$

Table 8.7: The NEUT and GENIE predictions of the flux averaged CCQE cross sections on carbon for the high energy region and the low energy region.

	High energy region	Low energy region
NEUT	$11.88\times10^{-39}\mathrm{cm}^2$	$10.34\times10^{-39}\mathrm{cm}^2$
GENIE	$9.46\times10^{-39}\mathrm{cm}^2$	$8.49\times10^{-39}\mathrm{cm}^2$

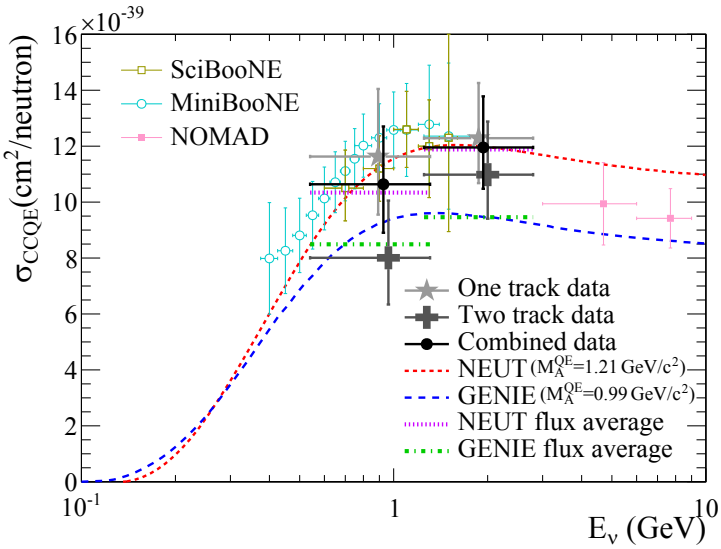

Figure 8.18: The CCQE cross section result with predictions by NEUT and GENIE. Our data point is placed at the flux mean energy. The vertical error bar represents the total (statistical and systematic) uncertainty, and the horizontal bar represents 68% of the flux at each side of the mean energy. The SciBooNE, MiniBooNE and NOMAD results are also plotted [221, 222, 285].

8.5.2 Results with the spectral function model

The T2K default interaction model uses the relativistic Fermi gas model as the default nuclear model, whereas the spectral function is more sophisticated nuclear model as described in Chapter 4. When the spectral function is used in the MC simulation for the efficiency correction instead of the relativistic Fermi gas model, the CCQE cross section results are slightly changed as shown in Table 8.8. The cross section results with the spectral function are shown in Fig. 8.19 together with the model predictions. With the spectral function, the difference in the cross section results from the one-track sample and the two-track sample in the low energy region becomes smaller as shown in Table 8.9. This change mainly comes from the differences in the final state proton kinematics between the relativistic Fermi gas model and the spectral function (Fig. 8.20) because they cause event migrations between the one-track sample and the two-track sample. Therefore, this result may indicate that the spectral function is a better representation of the nuclear model than the relativistic Fermi gas model.

Table 8.8: The CCQE cross section ($\times 10^{-39}$cm^2) measured from each sample when the spectral function is used as the nuclear model in the MC simulation.

Used sample	High energy region	Low energy region
One-track sample	$12.46 \pm 0.22(stat.)^{+1.98}_{-1.62}(syst.)$	$11.04 \pm 0.43(stat.)^{+2.26}_{-1.84}(syst.)$
Two-track sample	$11.43 \pm 0.36(stat.)^{+1.85}_{-1.60}(syst.)$	$8.84 \pm 0.70(stat.)^{+1.94}_{-1.70}(syst.)$
Combined sample	$12.19 \pm 0.19(stat.)^{+1.84}_{-1.50}(syst.)$	$10.77 \pm 0.38(stat.)^{+2.05}_{-1.71}(syst.)$

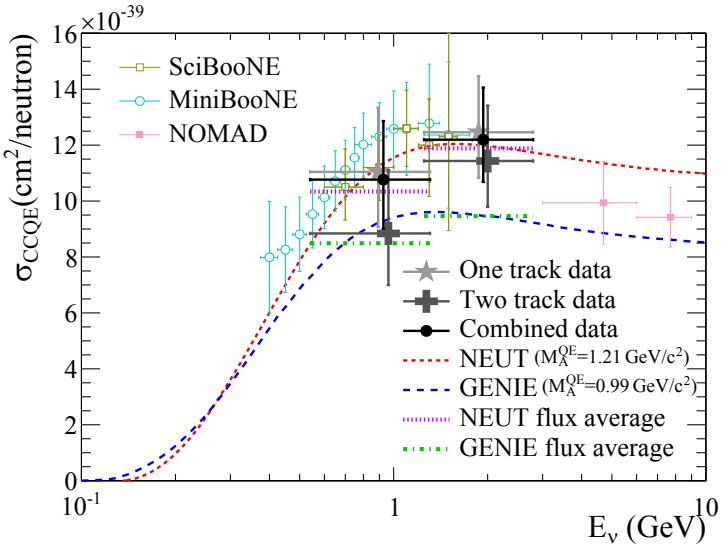

Figure 8.19: The CCQE cross section result when the spectral function is used as the nuclear model in the MC simulation.

Table 8.9: Ratio of the CCQE cross section result from the one-track sample to that from the two-track in the low energy region when the relativistic Fermi gas model or the spectral function is used in the MC simulation.

Nuclear model in MC	Ratio of cross section results
Relativistic Fermi gas model	$1.45 \pm 0.09(stat.)^{+0.24}_{-0.29}(syst.)$
Spectral function	$1.25 \pm 0.08(stat.)^{+0.22}_{-0.26}(syst.)$

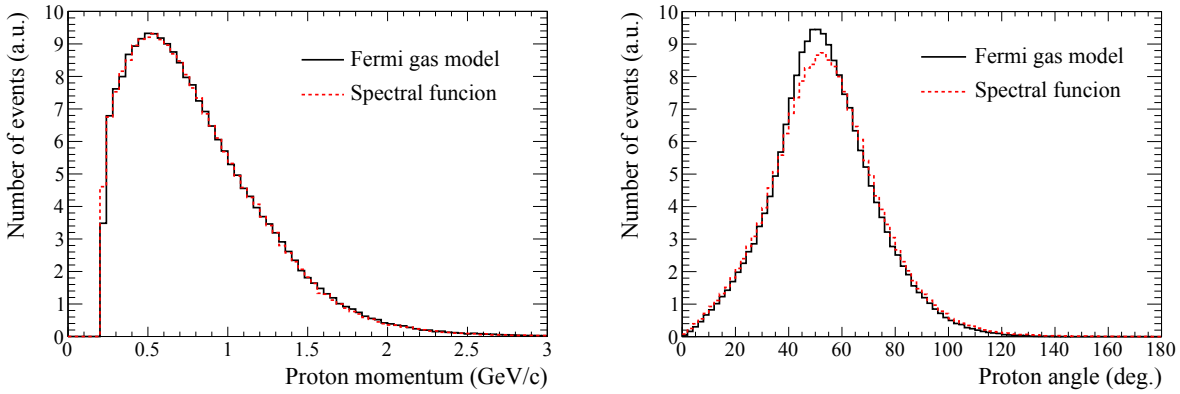

Figure 8.20: Distributions of true angle (left) and true momentum (right) of protons from CCQE for the MC simulation with the relativistic Fermi gas model and that with the spectral function.

8.5.3 Results assuming the existence of the multi-nucleon interaction

The T2K default interaction model does not assume the existence of the multi-nucleon interaction via the meson exchange current. However, the CCQE cross section measurement is expected to be sensitive to the effect of the multi-nucleon interaction, if it actually exists. Therefore, we also estimate the CCQE cross section assuming the existence of the multi-nucleon interaction. Although there are many multi-nucleon interaction models [287–293], we used a model proposed

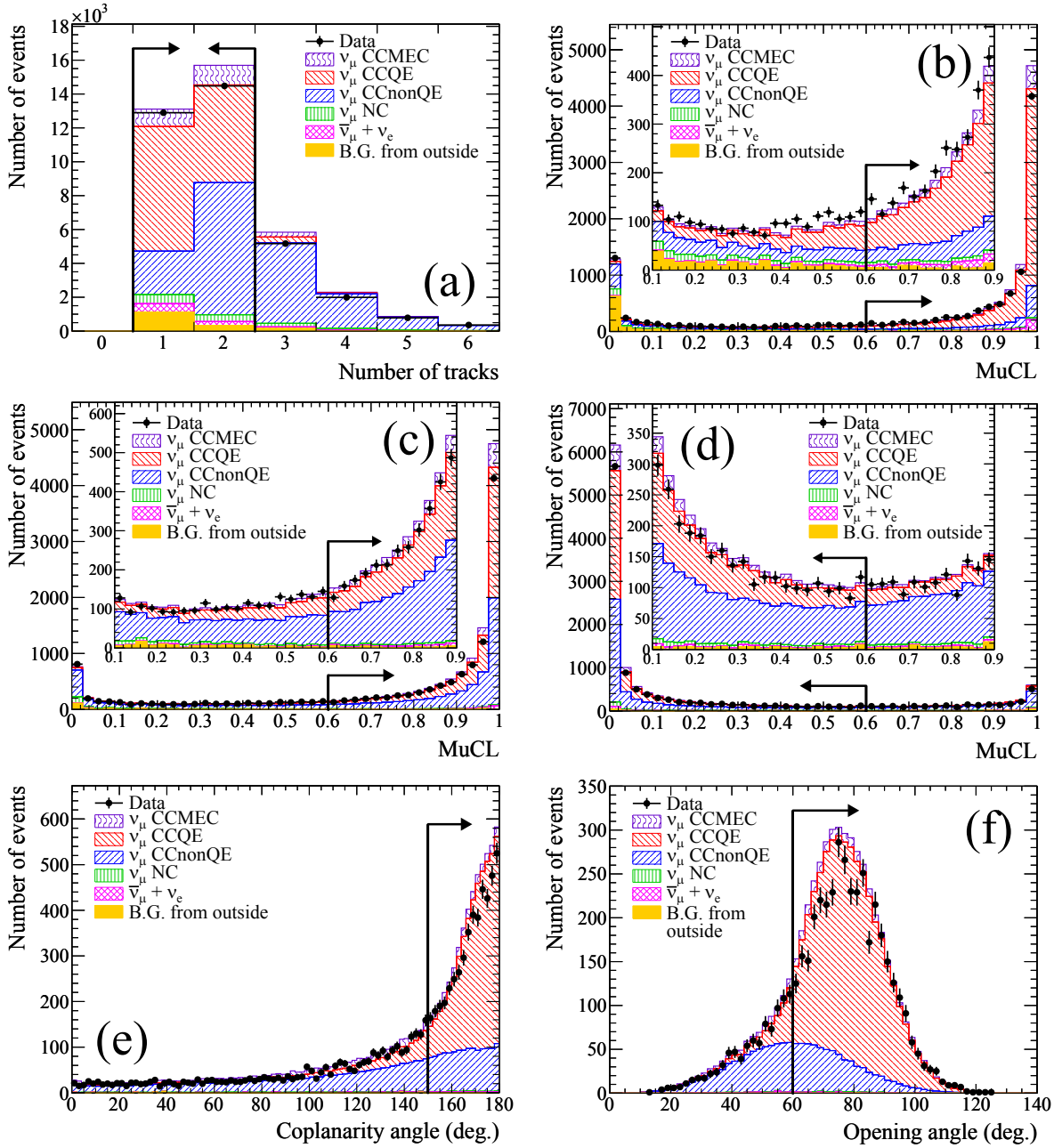

Figure 8.21: CCQE event selection with the MC simulation assuming the existence of the multi-nucleon interaction. (a) The number of tracks, particle identifications for (b) the one-track sample and (c), (d) the two-track sample, (e) the coplanarity angle, and (f) the opening angle. CCMEC represents the charged current multi-nucleon interaction via the meson exchange current.

by J. Nieves [289, 290] which describes the multi-nucleon interaction in a consistent theoretical scheme with the CCQE interaction. Then, the CCQE event selection is applied to the MC events including the multi-nucleon interaction events as shown in Fig. 8.21. The numbers of finally-selected multi-nucleon interaction events are summarized in Table 8.10. In this CCQE cross section analysis, the CCQE signal is defined as the conventional two-body interaction with a single nucleon. Therefore, the multi-nucleon interaction events are taken as the background events and are subtracted from the selected events. The CCQE cross section results assuming the existence of the multi-nucleon interaction are shown in Table 8.11 and Fig. 8.22. Although the measured CCQE cross sections become 6–13% smaller by assuming the existence of the multi-nucleon interaction, they are still compatible with the predictions.

Table 8.10: The numbers and the fractions of the multi-nucleon interaction events in the finally-selected samples of the MC simulation.

	High energy region		Low energy region	
	One-track	Two-track	One-track	Two-track
Number of multi-nucleon interaction events	480.39	75.83	127.19	27.29
Fraction of multi-nucleon interaction events	8.83%	4.61%	8.55%	5.30%

Table 8.11: The CCQE cross section ($\times 10^{-39}$cm^2) measured from each sample when the existence of the multi-nucleon interaction is assumed in the MC simulation for the background subtraction.

Used sample	High energy region	Low energy region
One-track sample	$10.79 \pm 0.22(stat.)^{+2.01}_{-1.63}(syst.)$	$10.11 \pm 0.45(stat.)^{+2.41}_{-2.03}(syst.)$
Two-track sample	$10.28 \pm 0.35(stat.)^{+1.85}_{-1.52}(syst.)$	$7.14 \pm 0.64(stat.)^{+1.96}_{-1.56}(syst.)$
Combined sample	$10.66 \pm 0.19(stat.)^{+1.88}_{-1.52}(syst.)$	$9.30 \pm 0.37(stat.)^{+2.13}_{-1.75}(syst.)$

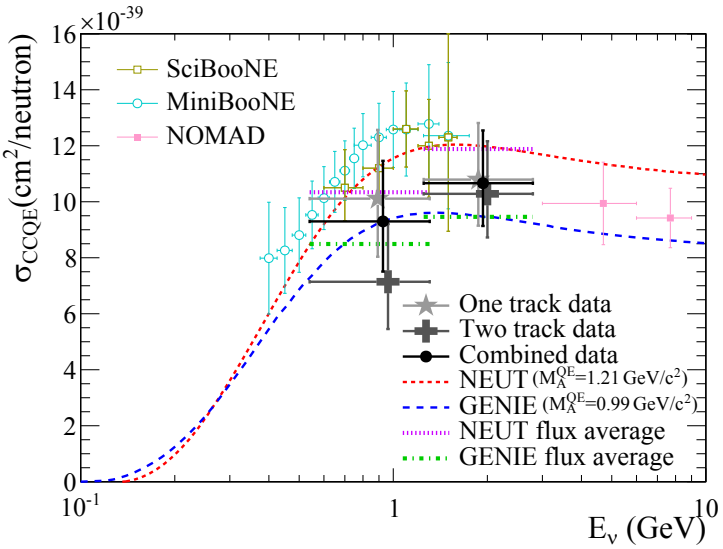

Figure 8.22: The CCQE cross section result when the existence of the multi-nucleon interaction is assumed in the MC simulation for the background subtraction.

8.5.4 Cross section ratio of CCQE to total CC interaction

We also estimate the cross section ratio of CCQE to total CC interaction. This cross section ratio is expected to be measured precisely because a major part of the systematic errors from neutrino flux uncertainties will be cancelled as with the measurement of the CC inclusive cross section ratio on Fe to CH presented in Chapter 7. Events selected by the CC event selection for the Proton Module described in Chapter 7 are used as the CC inclusive sample. We estimate the flux averaged cross section ratio of CCQE to total CC interaction because the CC inclusive sample cannot be classified by the neutrino energy. Thus, events selected by the CCQE event selection without energy classification are used as the CCQE sample. The cross section ratio is estimated by applying the background subtraction and efficiency correction to each sample as before. There is a strong correlation between the variations of the CC inclusive cross section result and the CCQE cross section result due to the neutrino flux uncertainty as shown in Fig. 8.23. Hence, the systematic error from the neutrino flux becomes tiny, and total systematic error on this cross section ratio measurement consequently becomes about half of that for the absolute CCQE cross section measurement. The measured cross section ratio of CCQE to total CC interaction is

$$\frac{\sigma_{\mathrm{CCQE}}}{\sigma_{\mathrm{CC}}} = 0.3835 \pm 0.0049(stat.)^{+0.0272}_{-0.0242}(syst.) \tag{8.6}$$

at a mean neutrino energy of 1.51 GeV when the combined CCQE sample is used. Results with the one-track or two-track CCQE sample are shown in Table 8.12. The NEUT and GENIE predictions of the cross section ratio of CCQE to total CC interaction is 0.3744 and 0.3433, respectively. Our results are shown in Fig. 8.24 together with the predictions. They also agree with the predictions and thus demonstrate the consistency with the models with better precision.

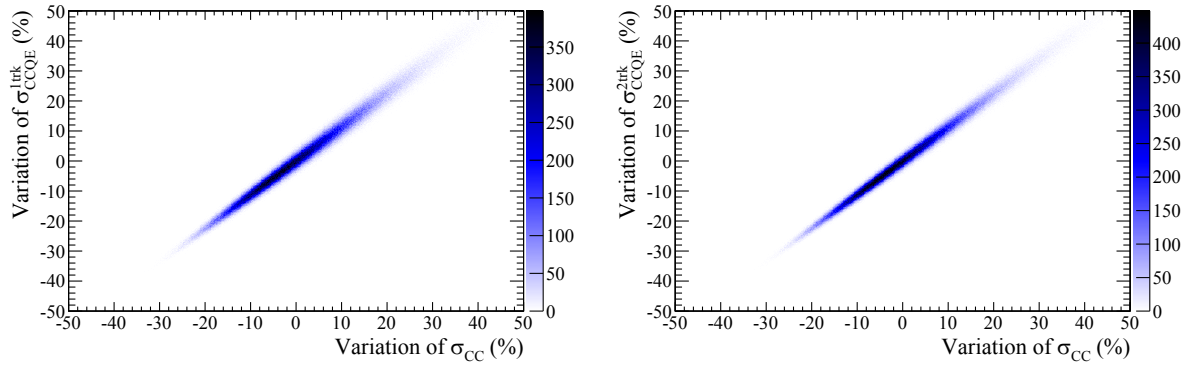

Figure 8.23: Correlation between the CCQE cross section result and CC inclusive cross section result for 10^6 toy MC sets generated according to the flux covariance matrix.

Table 8.12: The cross section ratio of CCQE to total CC interaction measured from each CCQE sample.

Used sample	Cross section ratio of CCQE to total CC interaction
One-track sample	$0.4048 \pm 0.0061(stat.)^{+0.0314}_{-0.0279}(syst.)$
Two-track sample	$0.3433 \pm 0.0071(stat.)^{+0.0322}_{-0.0315}(syst.)$
Combined sample	$0.3835 \pm 0.0049(stat.)^{+0.0272}_{-0.0242}(syst.)$

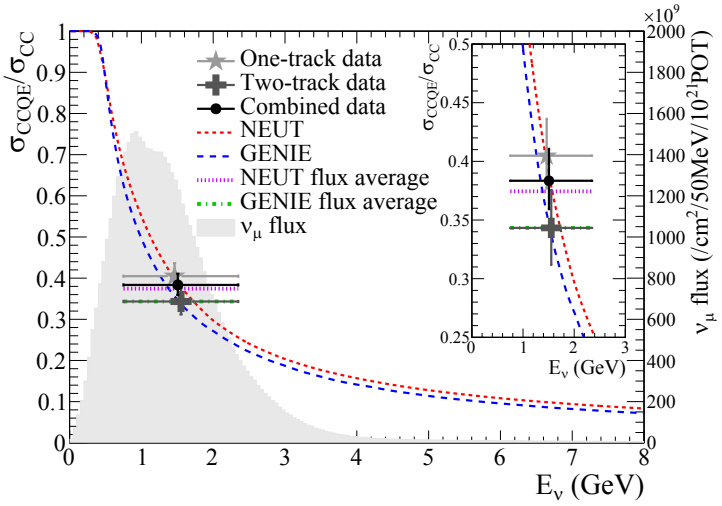

Figure 8.24: The cross section ratio of CCQE to total CC interaction.

8.6 Considerations

8.6.1 Impact of our CCQE cross section results on T2K

This CCQE cross section result is especially useful for the T2K experiment because the CCQE interaction is used as the signal mode for the neutrino oscillation measurement. In the current T2K analysis, large uncertainty of 30% is assigned for the CCQE cross section normalization at 1.5∼3.5 GeV as described in Chapter 4 because the CCQE cross section on heavy target in this energy region had never been measured. We first measured the CCQE cross section on carbon in this energy region with an accuracy of 15% and demonstrated a consistency with the neutrino interaction model. In addition, the MINERνA experiment recently measured the flux averaged differential CCQE cross section, $d\sigma/dQ^2$, at a mean neutrino energy of 3.5 GeV and showed a consistent result with the model [302]. Thus, this uncertainty will be reduced to 15% from the next year's analysis. Moreover, T2K intends to use the spectral function instead of the relativistic Fermi gas model from the next year's analysis. Although the validity of the spectral function had been supported only by the results of the electron-nucleus scattering, we checked the validity directly from the neutrino interaction result for the first time.

8.6.2 Inconsistency between the MiniBooNE and NOMAD results

Our measurement result cannot bring a definitive solution of the inconsistency between the MiniBooNE and NOMAD results. However, it provides important clues to the solution.

First, we demonstrate that the result of the CCQE cross section measurement depends on the assumed neutrino interaction model on the 10% level. In our CCQE event selection, 19% of the multi-nucleon interaction events in the Proton Module are expected to be misidentified as the CCQE event candidates. As a result, if the multi-nucleon interaction actually exists, the CCQE cross section is overestimated by 6–13% in our measurement. The NOMAD detector is the same type of the scintillator tracking detector as the Proton Module. In addition, event selection criteria of NOMAD are analogous to ours. Thus, if the multi-nucleon interaction actually exists, not only MiniBooNE but also NOMAD is expected to overestimate the CCQE cross section. It indicates that the introduction of the multi-nucleon interactions into the neutrino interaction model may not result in a consistency between the results from MiniBooNE and NOMAD. In order to conclude whether the multi-nucleon interaction actually can describe the inconsistency, NOMAD should perform the CCQE analysis assuming the existence of the

multi-nucleon interaction like MiniBooNE and we did.

Second, our CCQE cross section results from the one-track and the two-track sample will be helpful in the construction of the solution. NOMAD also measured the CCQE cross section separately from the one-track sample and the two-track sample [222]. In the NOMAD result, the CCQE cross section from the one-track sample is smaller than that from the two-track sample contrary to our measurement although the systematic errors are large and the energy region is different from our measurement. NOMAD tuned a parameter called "formation time" which migrates events between the one-track sample and the two-track sample to get better data-MC agreement. However, the validity of this tuning has been questioned [303,304]. We don't use such a tuning, thus comparisons between our result and the NOMAD result may indicate something we are missing.

8.6.3 Future prospects of CCQE cross section measurement

In the future, more precise cross section measurements are required in order to solve the puzzle in the CCQE cross section. As with the CC inclusive cross section measurement, systematic error of this CCQE cross section measurement is also dominated by the neutrino flux error, and it will be reduced by using more data from the NA61/SHINE experiment for the hadron production tuning.

Meanwhile, specialized measurements to search for the multi-nucleon interactions are also needed in order to conclude the existence of the multi-nucleon interaction. For this search, two protons from the multi-nucleon interaction are required to be separately reconstructed in addition to a muon track. The path length of the proton tracks from the multi-nucleon interaction in scintillator is 11 cm on average. The Proton Module whose position resolution is 2.5 or 5 cm is scarcely able to reconstruct the proton tracks separately. In order to achieve the separate reconstruction, position resolution better than 3 mm is required. Thus, finely segmented scintillation fiber tracking detector, liquid argon TPC (Time Projection Chamber) and emulsion detector will be the optimal detectors to search for the multi-nucleon interaction.

Chapter 9

Measurement of Charged Current Coherent Pion Production Cross Section

The coherent pion production is the neutrino interaction with an entire nucleus involving a pion production ($\nu_l + A \to l^- + A + \pi^+$) as described in Chapter 1. It is one of the background interactions for the T2K neutrino oscillation measurement and has 100% uncertainty because it is poorly understood. This chapter describes the measurement of the ν_μ charged current coherent pion production cross section on carbon with the Proton Module.

9.1 Introduction to the coherent pion production measurement

The measurement of the coherent pion production has already been the subject of several experiments. Table 9.1 summarizes the past measurements of the coherent pion production and Fig. 9.1 summarizes the results below 20 GeV. Although there exist positive coherent pion production results at high neutrino energies (3–300 GeV) via charged and neutral current interactions [306–313], K2K and SciBooNE reported null observations of charged current coherent pion production at low neutrino energies ($\sim$ 1 GeV) [223, 224]. On the other hand, MiniBooNE and SciBooNE observed the neutral current coherent pion production at the low neutrino energies [225, 314]. The Rein-Sehgal model for the coherent pion production [188] described in Chapter 4 has been commonly used in neutrino experiments. It well explains these experimental results except for the CC coherent pion results from the K2K and SciBooNE experiments. In addition, several other models* were proposed [316–324]. However, none of them can explain all the experimental results. From these facts, the coherent pion production has drawn much attention in the neutrino interaction physics community. Especially, a precise measurement of the CC coherent pion production in a few GeV neutrino energy has been desired to test the null results from K2K and SciBooNE. Therefore, we measured the CC coherent pion production cross section in a few GeV neutrino energy using INGRID.

*Some of the models are based on the PCAC theorem as with the Rein-Sehgal model [318, 319]. On the other hand, there are also microscopic models which describe the coherent pion production process in terms of a coherent sum of neutrino-nucleon interactions where the final-state nucleon is constrained to remain in the same quantum state [320–324]. See Appendix D for details.

Table 9.1: List of past measurements of coherent pion production. $\langle A \rangle$ is the average atomic number of the target nucleus.

Experiment	Beam	Interaction	E_ν (GeV)	Target	$\langle A \rangle$	Reference
Aachen-Padova	$\nu_\mu/\bar{\nu}_\mu$	NC	2	Al	27	[305]
Gargamelle	$\nu_\mu/\bar{\nu}_\mu$	NC	3.5	Freon	30	[306]
SKAT	$\nu_\mu/\bar{\nu}_\mu$	CC/NC	3–30	Freon	30	[307]
CHARM	$\nu_\mu/\bar{\nu}_\mu$	NC	10–160	Marble	20	[308]
CHARM II	$\nu_\mu/\bar{\nu}_\mu$	CC	3–300	Glass	20.1	[309]
BEBC	$\nu_\mu/\bar{\nu}_\mu$	CC	5–150	Ne	20	[310, 311]
FNAL E632	$\nu_\mu/\bar{\nu}_\mu$	CC	10–300	Ne	20	[312, 313]
K2K	ν_μ	CC	1.3	C	12	[223]
MiniBooNE	ν_μ	NC	1.2	C	12	[314]
SciBooNE	ν_μ	CC/NC	1.2	C	12	[224, 225]
NOMAD	ν_μ	NC	25	C	12	[315]

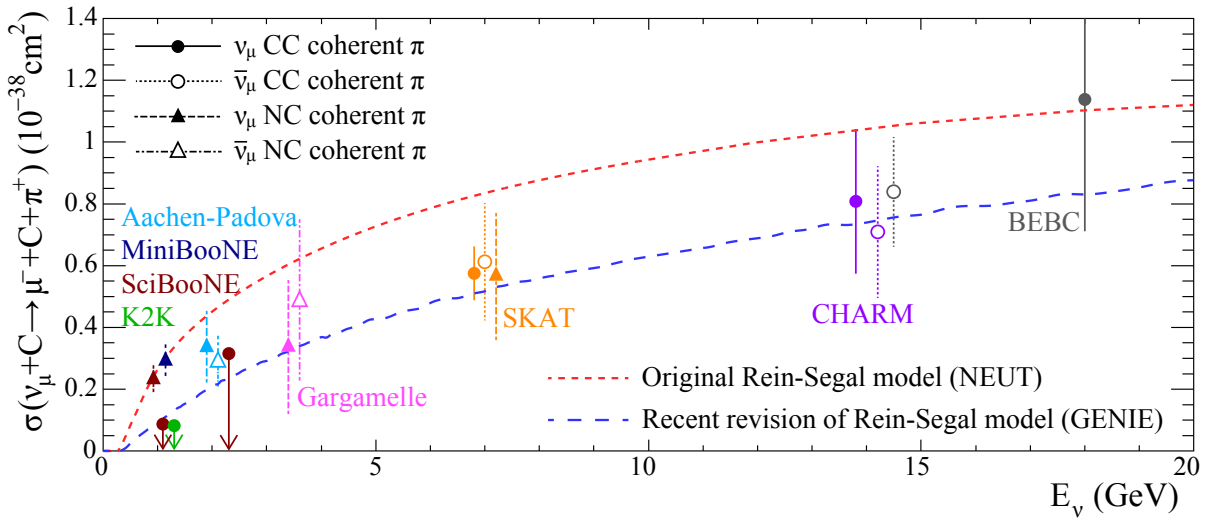

Figure 9.1: Existing experimental results on the coherent pion production cross section below 20 GeV [223–225, 305–311, 314]. The results are scaled to the cross section for the CC coherent pion production on C ($\nu_\mu + \mathrm{C} \to \mu^- + \pi^+ + \mathrm{C}$) by assuming $\sigma(\mathrm{CC}) = 2\sigma(\mathrm{NC})$, $\sigma(\nu_\mu) = \sigma(\bar{\nu}_\mu)$, $\sigma(A) \propto A^{1/3}$ where A is the atomic number. These assumptions come from the Rein-Sehgal model as described in Chapter 4. The downward arrows represent the 90% confidence level upper limits.

9.2 Event selection

9.2.1 Overview of event selection

As the first step, the same event selection as the one in Chapter 7 is applied to enrich the CC interaction events in the Proton Module and to reduce NC interaction events and background events from outside. After this selection, CC coherent pion production events make up 2.76% of the MC sample. To increase the selection purity for CC coherent pion production events, additional CC coherent pion production selection cuts are applied. The overall flow of the CC coherent pion production event selection is as follows: number of tracks = 2, particle identification, kinematic cut, and vertex activity cut.

9.2.2 Event selection criteria

The number of tracks

The CC coherent pion production generally produces two particles in the final state (a muon and a pion). In most cases, they are separately reconstructed as shown in Fig. 9.2. Thus, only events with two reconstructed tracks coming from the vertex are selected (Fig. 9.3).

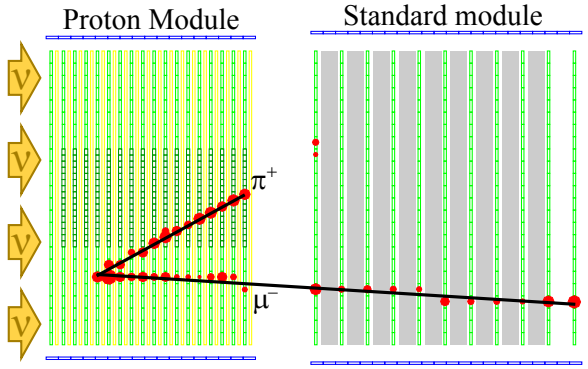

Figure 9.2: Event display of an MC CC coherent pion production event in the Proton Module.

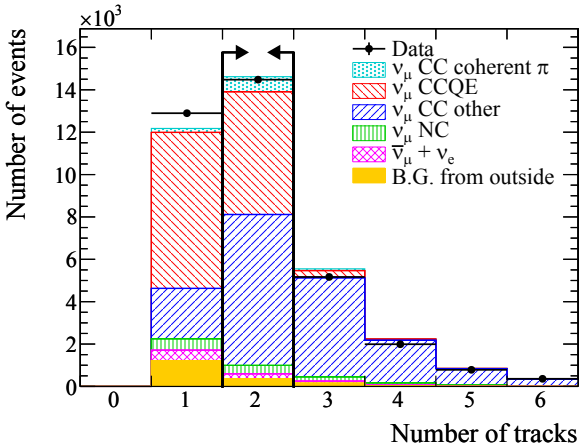

Figure 9.3: The number of reconstructed tracks from a vertex in the Proton Module.

Particle identification

Particle identification (PID) is performed using dE/dx information. As with Chapter 8, MuCL is used for the particle identification. In Chapter 8, tracks whose MuCL is more than 0.6 are identified as muon-like and those less than 0.6 are identified as proton-like. However, for the separation of protons and pions in this analysis, tracks whose MuCL is more than 0.25 are identified as pion-like and those less than 0.25 are identified as proton-like. In the CC coherent pion production, the longer reconstructed track is expected to be the muon track and the shorter is expected to be the pion track. Thus, the MuCL for the longer track is required to be more than 0.6 and that for the shorter track is required to be more than 0.25 to select muons and pions respectively (Fig. 9.4).

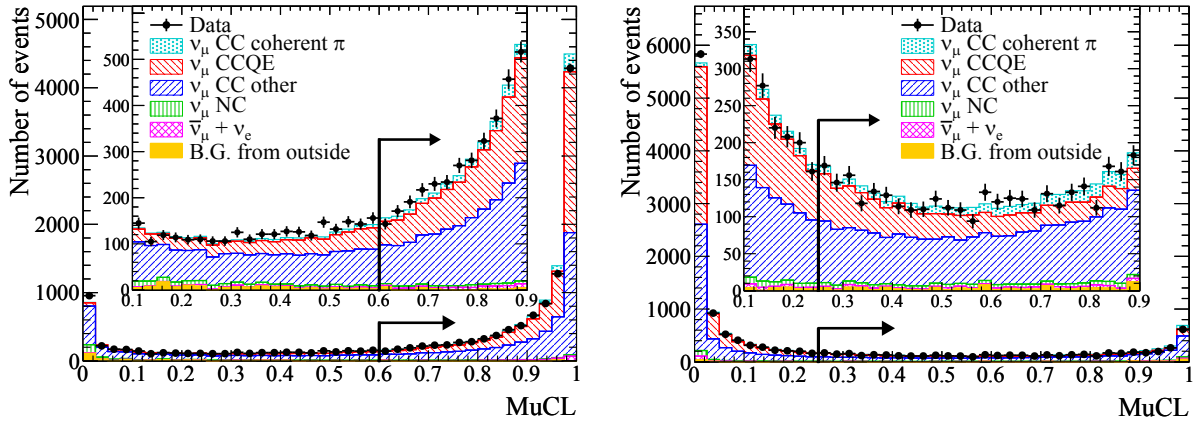

Figure 9.4: MuCL distributions of the longer track (left) and the shorter track (right) for the two-track sample.

Kinematic cut

In the CC coherent pion production, the muon tends to be scattered extremely forward as shown in Fig. 9.5 because the four-momentum transfer to the target nucleus is generally small. Thus, events in which the reconstructed angle between the longer track (the muon candidate track) and the beam axis is less than 15° are selected[†]. The reconstructed angle of the shorter track (the pion candidate track) is not used in the event selection since it is affected by the uncertainties associated with pion re-scattering.

Vertex activity cut

In a charged current resonant pion event ($\nu_\mu + p \to \mu^- + p + \pi^+$), the proton track is often not reconstructed due to its low momentum, and thus the event is identified as a $\mu^- + \pi^+$ event. Even if the proton track is not reconstructed, dense energy deposition by the proton is expected to be observed around the vertex because the Proton Module is a fully-active detector. Thus, in order to separate CC coherent pion events from CC resonant pion events, the vertex activity, which is defined as the sum of the energy deposition around the vertex, is used to see if there are additional low energy protons. Figure 9.6 shows the sum of the energy deposit around the vertex in the volume of ±15cm in the X and Y directions and ±2 layers in the Z direction. This volume is defined from the typical pass length of the proton track which is not reconstructed. The peak around 25 MeV corresponds to the energy deposited by two minimum ionizing particles, and the high energy deposit tail is mainly due to the extra low energy proton. Events with an energy deposit less than 34 MeV around the vertex are selected as the CC coherent pion production candidates.

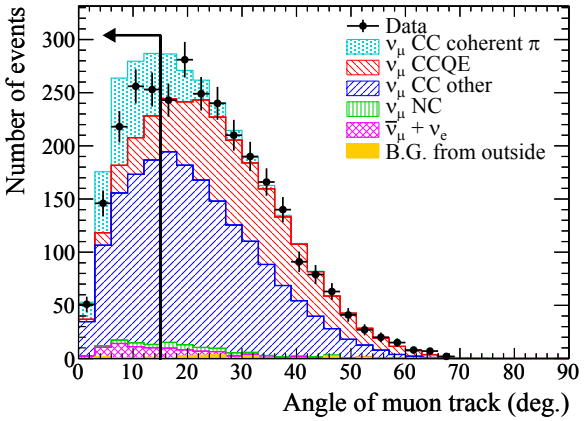

Figure 9.5: Distribution of the reconstructed angle between the longer track and the beam axis, following the PID cut.

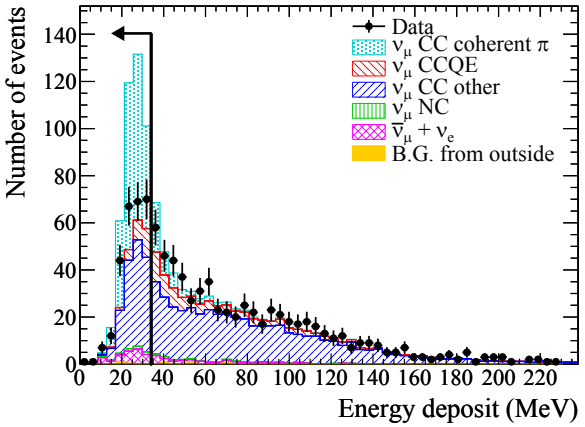

Figure 9.6: Distribution of the vertex activity following the PID and kinematic cuts.

9.2.3 Summary of event selection

The results of the event selection are summarized in Table 9.2. Finally, 271 events are selected as the CC coherent pion candidate events. After the event-pileup correction, the number of selected events becomes 271.9. The expected purity of the CC coherent pion events is 53.31%.

[†]Generally, squared four-momentum transfer, Q^2 or $|t|$, is used for the kinematic cut for the coherent pion production selection. However, we cannot reconstruct them because we cannot measure the muon momentum. Therefore, the muon angle is alternatively used for the kinematic cut.

Table 9.2: The number of events passing each step of the CC coherent pion event selection. The efficiency is defined as the number of selected ν_μ CC coherent pion events divided by the number of ν_μ CC coherent pion productions in the FV. The purity is defined as the ratio of the selected ν_μ CC coherent pion events to the total selected events.

Selection	Data	MC	Efficiency	Purity
Number of tracks = 2	14479	1.473×10^4	49.64%	4.82%
Particle identification	3412	3.546×10^3	29.47%	11.88%
Kinematic cut	924	1.072×10^3	19.92%	26.56%
Vertex activity cut	271	4.301×10^2	16.04%	53.31%

9.3 Analysis strategy

As with the CC inclusive cross section analysis, the flux averaged CC coherent pion production cross section is calculated from the number of selected CC coherent pion candidate events using the background subtraction and efficiency correction:

$$\sigma_{\mathrm{CCcoh.}\pi} = \frac{N_{\mathrm{sel}} - N_{\mathrm{BG}}}{\phi T \varepsilon}, \tag{9.1}$$

where N_{sel} is the number of selected CC coherent pion candidate events from real data, N_{BG} is the number of selected background events predicted by the MC simulation, ϕ is the integrated ν_μ flux, T is the number of target nuclei, and ε is the detection efficiency for CC coherent pion events predicted by the MC simulation. These quantities are summarized in Table 9.3. The background events for this analysis consist of CC incoherent events, NC events, $\bar{\nu}_\mu$ events, ν_e events and external background events created by neutrino interactions in the material surrounding the detector. They are dominated by the CC resonant pion events as shown in Table 9.4.

Table 9.3: Summary of the inputs for the CC coherent pion production cross section calculation.

N_{sel}	N_{BG}	ϕ	T	ε
271.90	202.94	$3.025\times10^{13}\mathrm{cm}^{-2}$	1.384×10^{28}	0.1604

Table 9.4: The expected breakdown of the background events for the CC coherent pion cross section analysis. Ratio to the total number of selected events is shown in parenthesis.

Category	Number of events
CCQE events	27.96 (6.50%)
CC resonant pion events	104.79 (24.36%)
CC other events	38.71 (9.00%)
NC events	4.98 (1.16%)
$\bar{\nu}_\mu$ events	22.45 (5.22%)
ν_e events	0.27 (0.06%)
Background events from outside	1.68 (0.39%)

9.4 Systematic errors

The total systematic error on the CC coherent pion cross section measurement is $^{+68.45\%}_{-65.93\%}$. The breakdown of the error is summarized in Table 9.5. As with the CC inclusive and CCQE cross section measurements, systematic error from the neutrino flux uncertainty is the largest. It is

Table 9.5: Summary of the systematic errors on the CC coherent pion cross section measurement.

Item	Error
Neutrino flux	$-35.68\% + 43.20\%$
M_A^{QE}	$-11.20\% + 7.98\%$
M_A^{RES}	$-23.84\% + 21.39\%$
CCQE normalization (E_ν <1.5 GeV)	$-0.69\% + 0.68\%$
CCQE normalization (1.5< E_ν <3.5 GeV)	$-0.80\% + 0.79\%$
CCQE normalization (E_ν >3.5 GeV)	$-2.69\% + 2.67\%$
CC1π normalization (E_ν <2.5 GeV)	$-11.47\% + 11.17\%$
CC1π normalization (E_ν >2.5 GeV)	$-18.55\% + 18.21\%$
CC other E_ν shape	$-3.51\% + 3.41\%$
NC1π^0 normalization	$-0.46\% + 0.45\%$
NC1$\pi^\pm$ normalization	$-0.06\% + 0.06\%$
NC coherent π normalization	$-0.11\% + 0.11\%$
NC other normalization	$-0.81\% + 0.70\%$
π-less Δ decay	$-11.54\% + 13.11\%$
Spectral function	$-0.29\% + 0.00\%$
Fermi momentum	$-0.09\% + 0.17\%$
Binding energy	$-0.89\% + 0.92\%$
Pion absorption	$-6.06\% + 4.66\%$
Pion charge exchange (low energy)	$-0.41\% + 0.29\%$
Pion charge exchange (high energy)	$-3.02\% + 2.80\%$
Pion QE scattering (low energy)	$-6.12\% + 4.97\%$
Pion QE scattering (high energy)	$-0.46\% + 0.18\%$
Pion inelastic scattering	$-5.65\% + 5.04\%$
Nucleon elastic scattering	$-1.24\% + 1.11\%$
Nucleon single π production	$-4.01\% + 3.96\%$
Nucleon two π production	$-0.10\% + 0.27\%$
Target mass	$\pm 0.90\%$
MPPC dark noise	$\pm 0.74\%$
Hit efficiency	$\pm 5.36\%$
Light yield	$\pm 15.37\%$
Event pileup	$\pm 0.31\%$
Beam-induced external background	$\pm 0.00\%$
Cosmic-ray background	$\pm 0.00\%$
2D track reconstruction	$\pm 1.92\%$
Track matching	$\pm 4.28\%$
3D tracking	$\pm 12.73\%$
Vertexing	$\pm 12.00\%$
Timing cut	$\pm 0.00\%$
Veto cut	$\pm 10.42\%$
Fiducial volume cut	$\pm 14.38\%$
Secondary interactions	$\pm 6.72\%$
Total	$-60.72\% + 63.95\%$

much more than the neutrino flux uncertainty of about 10% because the uncertainty affects not only the integrated neutrino flux (ϕ) but also the predicted number of background events (N_{BG}). Meanwhile, systematic errors due to the CC resonant pion interaction uncertainties (M_A^{RES} and CC1π normalizations) are comparably large because CC resonant pion events are the dominant background events for this measurement.

9.5 Results

The measured CC coherent pion production cross section on carbon is

$$\sigma_{\mathrm{CCcoh.}\pi} = (1.03 \pm 0.25(stat.)^{+0.66}_{-0.63}(syst.)) \times 10^{-39}\mathrm{cm}^2/\mathrm{nucleus}, \tag{9.2}$$

at a mean neutrino energy of 1.51 GeV [325]. The 90% confidence level (C.L.) upper limit on the CC coherent pion production cross section is set as

$$\begin{aligned} \sigma_{\mathrm{CCcoh.}\pi} &< (1.03 + 1.28 \times \sqrt{0.25^2 + 0.66^2}) \times 10^{-39}\mathrm{cm}^2/\mathrm{nucleus} \\ &= 1.93 \times 10^{-39}\mathrm{cm}^2/\mathrm{nucleus}, \end{aligned} \tag{9.3}$$

where 1.28 is the ratio of the one-sided 90% confidence interval to the 1σ interval. Since the significance of the CC coherent pion signal excess is 1.7σ, this result indicates the existence of the CC coherent pion production in a few GeV region for the first time although it is too weak to claim the observation. The NEUT and GENIE predictions of the flux averaged CC coherent pion production cross section on carbon are 3.22×10^{-39}cm^2/nucleus and 1.37×10^{-39}cm^2/nucleus respectively. NEUT uses the original Rein-Sehgal model while GENIE uses a recent revision of the Rein-Sehgal model. As a result, their predictions in the T2K energy region differ by a factor of two. The difference mainly stems from the different pion-nucleon cross section data used in the model as described in Chapter 4. Our result agrees with the prediction by GENIE, but is significantly smaller than the prediction by NEUT. The cross section result is shown in Fig. 9.7 together with the predictions and the results of other experiments. Our result is compatible

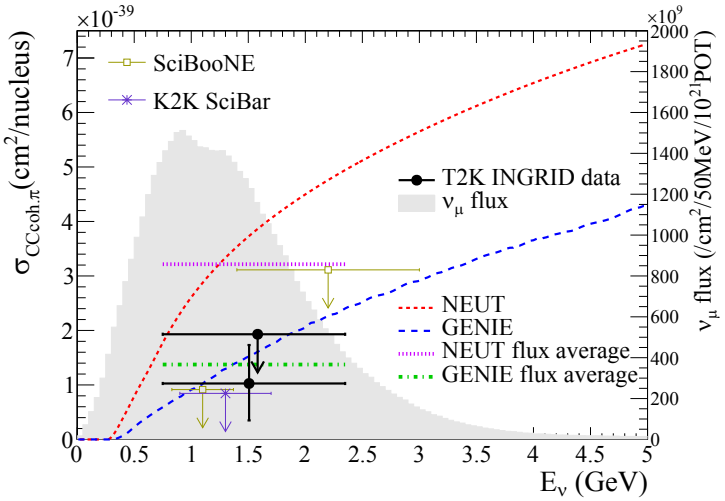

Figure 9.7: The CC coherent pion production cross section result with predictions by NEUT and GENIE. Our data point is placed at the flux mean energy. The vertical error bar represents the total (statistical and systematic) uncertainty, and the horizontal bar represents 68% of the flux at each side of the mean energy. The K2K and SciBooNE results are also plotted [223, 224]. The downward arrows represent the 90% C.L. upper limits.

with the K2K and SciBooNE results [223, 224]. Figure 9.8 shows the angular distributions of reconstructed muon and pion tracks of the selected events with respect to the beam axis. In both distributions, the signal excesses are observed in the smaller angle region than the MC predictions with NEUT. A similar tendency is seen in the SciBooNE CC coherent pion measurement [224] as shown in Fig. 9.9. They might indicate that the original Rein-Sehgal model implemented in NEUT does not correctly predict these kinematic distributions. GENIE predicts slightly smaller angular distributions of the CC coherent pion events than NEUT. For example, averages of the reconstructed muon (pion) angle of the selected CC coherent pion events predicted with NEUT and GENIE are 13.0° and 11.5° (29.4° and 26.0°), respectively. Thus, the predictions with GENIE have better agreements with our data. Consequently, we verify that the original Rein-Sehgal model breaks down at the neutrino energy of a few GeV and indicate that the pion-nucleon cross section data in the original Rein-Sehgal model needs to be replaced with the modern value as is done in GENIE.

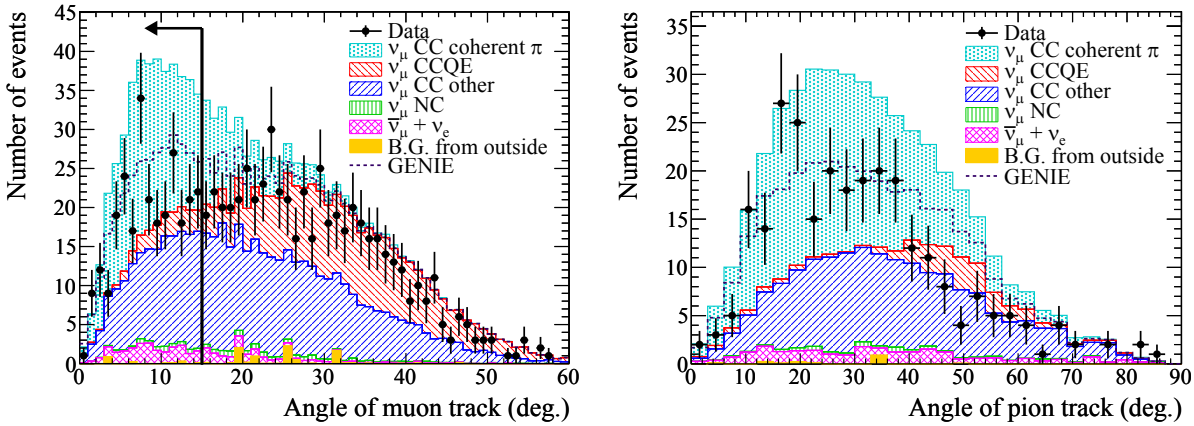

Figure 9.8: Distributions of reconstructed angles of muon tracks (left) and pion tracks (right) of selected events with respect to the beam axis. Colored histograms show the MC predictions with NEUT and dashed lines show those with GENIE for the CC coherent pion production. The muon angel distribution is without the muon angle cut, and the arrowed line shows the muon angle cut.

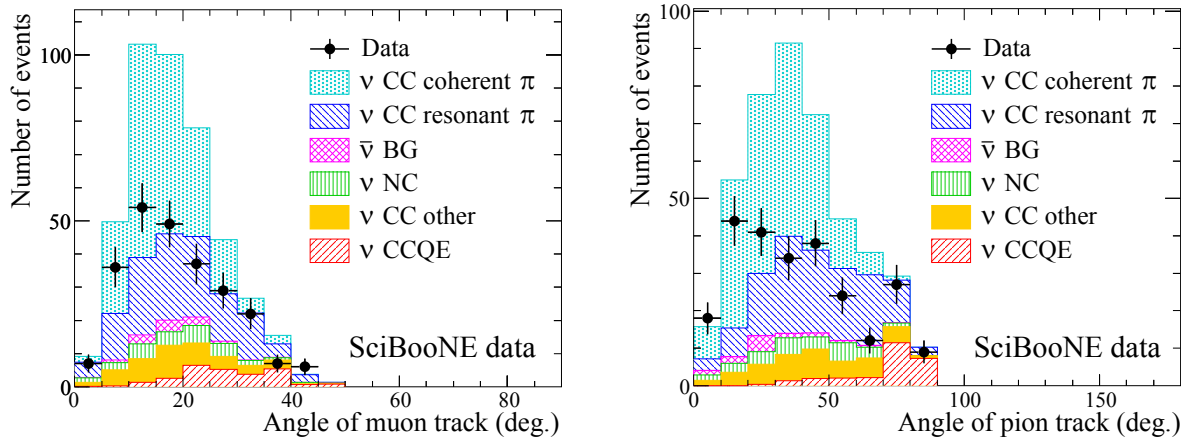

Figure 9.9: Distributions of reconstructed angles of muon tracks (left) and pion tracks (right) of the SciBooNE CC coherent pion candidate sample with respect to the beam axis [224]. Colored histograms show the MC predictions with NEUT. This figure was taken from Ref. [326].

9.6 Considerations

9.6.1 Impact of our CC coherent pion cross section result

Although our result is inconsistent with the neutrino interaction model used in T2K (*i.e.* the original Rein-Sehgal model in NEUT), it is within the considered uncertainty because 100% uncertainty is assigned to the CC coherent pion cross section in T2K. Hence, this inconsistency is not a problem for the neutrino oscillation measurement and other neutrino cross section measurements in T2K.

To reduce the 100% uncertainty, the revisions of the neutrino interaction model are required. We measured the CC coherent pion cross section in a few GeV region with an accuracy of 60% and demonstrated a consistency with the revised Rein-Sehgal model implemented in GENIE. Thus, if the Rein-Sehgal model in NEUT is revised as with GENIE or GENIE is used for the simulation of the coherent pion production in T2K, the 100% uncertainty on the CC coherent pion cross section will be reduced to 60%. In addition, the discrepancy in the angular distributions we observed will be helpful to revise the neutrino interaction model. For example, a new calculation of the coherent pion angular distribution was recently proposed [327], which predicts the smaller angular distribution than the Rein-Sehgal model. If such a calculation is implemented in the neutrino interaction model, the predicted angular distribution will be more consistent with our experimental result. In this thesis, only the Rein-Sehgal model is used for the comparisons of the cross section result and the angular distributions because other models are not implemented in the simulators. In the future, many other models should be used for the comparisons.

9.6.2 Dependence on the kinematics of the CC coherent pion production

In the CC coherent pion event selection, events in which the reconstructed muon angle is less than 15° are selected. On the other hand, the reconstructed pion angle is not used for the event selection. They were determined before checking the real data in order to avoid a subjective bias. If the selection criteria for these kinematic cuts are changed, the CC coherent pion cross section result varies as shown in Fig. 9.10. The variations of cross section result due to the muon angle cut are within the error size. However, if the pion angle cut is introduced, it causes more significant variations. For example, when events in which the reconstructed pion angle is less than 20° are selected, the cross section result becomes about twice larger than the default

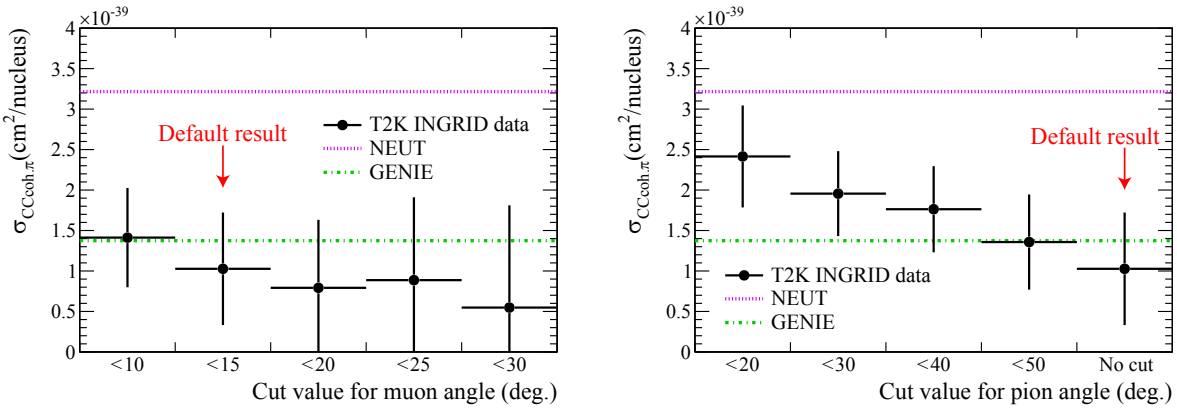

Figure 9.10: Variation of the CC coherent pion cross section result when the cut criteria for the muon angle (left) and pion angle (right) are changed. The vertical error bar represents the total (statistical and systematic) uncertainty. Predictions by NEUT and GENIE are shown for the comparison.

result. In that case, the cross section result is compatible with the prediction by NEUT, and the significance of the signal excess is as high as 3.7σ although these results are biased. It means that the result of the CC coherent pion cross section measurement is dependent on the kinematics used for the analysis especially when the pion kinematics is used. Almost all the existing coherent pion cross measurements use similar kinematic cuts. Some of them use not only the muon kinematics but also the pion kinematics. Therefore, the inconsistencies of the existing coherent pion cross section results may stem from the difference in the used kinematics.

9.6.3 Future prospects of CC coherent pion cross section measurement

Currently, 48% out of the total 61% systematic error on our CC coherent pion cross section measurement arises from the uncertainty of the CC resonant pion background events. To reduce the uncertainty, the CC resonant pion cross section should be measured with INGRID. If it is actually measured, the systematic error on the measured CC resonant pion cross section will have a strong anti-correlations with the neutrino flux uncertainty. Thus, we will be able to precisely predict the number of CC resonant pion background events in the CC coherent pion candidate sample owing to the cancellation of the neutrino flux uncertainty and the cross section uncertainty.

Moreover, several experiments also attempt precise measurements of the CC coherent pion production. In T2K, a measurement of the CC coherent pion production using the ND280 detector is going on [328]. It is expected to have a higher sensitivity to search for the CC coherent pion production at around 0.6 GeV. In addition, the MINERνA experiment is measuring the neutrino energy dependence of the CC coherent pion production in the neutrino energy range up to 20 GeV [329, 330]. It is expected to bridge the gap between the measurements at a few GeV region where the signal deficits were observed and those at higher energy where the signals were observed as predicted. Most recently, the MINERνA experiment reported the first preliminary result which is consistent with the Rein-Sehgal model in GENIE [331]. Besides, the liquid argon TPC (Time Projection Chamber) [332] is also a promising detector for the measurement of the CC coherent pion production because it is able to observe nuclear stubs from the coherent pion production, hence it is able to eliminate most incoherent backgrounds from coherent signals. The ArgoNeuT liquid argon TPC [333] is taking neutrino beam data at Fermilab, and reported the first preliminary result quite recently [334]. In addition, several other liquid argon TPC experiments are projected [335–338].

In conclusion, although the CC coherent pion production in a few GeV region had been poorly understood for many years, it is being revealed by the recent neutrino experiments. In the future, more precise measurements of the NC coherent pion production in a few GeV region are also required for a comprehensive understanding of the coherent pion production.

Chapter 10

Measurement of Neutrino Oscillations

This chapter describes the measurements of the T2K neutrino beam at ND280 (Secs. 10.2 and 10.3) and Super-K (Sec. 10.4), and the methods (Secs. 10.5, 10.6 and 10.7) and results (Secs. 10.8 and 10.9) of the neutrino oscillation analysis.

10.1 Analysis overview

The T2K neutrino beam properties in Run 1-4 were precisely measured with INGRID, which reduced the neutrino flux uncertainty and assured the Run 1-4 neutrino beam quality and the consistency of the neutrino flux prediction as presented in Chapter 6.

The neutrino interaction cross sections were also measured with INGRID as presented in Chapters 7, 8 and 9. The measured CC inclusive cross section and CCQE cross section are consistent with predictions by the neutrino interaction models used in T2K. It indicates that the CC resonant pion cross section is also consistent because the CC interactions in the T2K neutrino energy region are dominated by a comparable amount of CCQE interactions and CC resonant pion interactions. Although the measured CC coherent pion cross section is significantly smaller than the model prediction, the discrepancy is covered by the systematic uncertainty assigned in T2K. In addition, the result of the CC inclusive cross section ratio on different targets demonstrates that the nuclear effect of the target material is correctly treated in the neutrino interaction models. Consequently, we have demonstrated the validity of the T2K neutrino interaction models and their uncertainties using the T2K internal data although they had been evaluated dependently only on a few external data.

The measurement of the neutrino beam properties and the neutrino cross sections with INGRID enables us to perform the neutrino oscillation analysis on the firm ground of the assured neutrino flux prediction, neutrino interaction models, and Run 1-4 beam data. The procedure for the neutrino oscillation analysis is as follows.

1. Uncertainties on the neutrino flux prediction and the neutrino interaction models are constrained by the ND280 measurement.

2. The ν_e and ν_μ candidate events are separately selected at Super-K.

3. A maximum likelihood fit is performed to the measured energy spectra of the ν_e and ν_μ candidate events at Super-K to extract the neutrino oscillation parameters.

In this chapter, neutrino oscillation parameters, earth matter density and baseline length listed in Table 10.1 are assumed as nominal values unless otherwise noted.

Table 10.1: Nominal values of the neutrino oscillation parameters, earth matter density, baseline length, and their derivations.

Parameter	Nominal value	Derivation
$\sin^2 2\theta_{12}$	0.857	Global oscillation analysis [339]
$\sin^2 2\theta_{13}$	0.1	Reactor $\bar{\nu}_e$ disappearance [49–51]
$\sin^2 \theta_{23}$	0.5	T2K Run 1-3 ν_μ disappearance [114]
Δm^2_{12}	$7.5 \times 10^{-5}\text{eV}^2$	Global oscillation analysis [339]
Δm^2_{32}	$2.4 \times 10^{-3}\text{eV}^2$	T2K Run 1-3 ν_μ disappearance [114]
δ_{CP}	0	(Unknown)
Mass hierarchy	Normal hierarchy	(Unknown)
Earth matter density	2.6g/cm^3	Geophysical measurement [340]
Baseline length	295km	GPS measurement

10.2 Measurement at ND280

The ND280 data set for Run 1-4 is used for this measurement. It corresponds to 5.90×10^{20} POT.

10.2.1 CC event selection

First, ν_μ CC interactions are selected by identifying muon track originated from the upstream FGD (FGD1). The selection criteria are as follows:

(1) Negative track originated from FGD1
Negatively charged tracks are identified from the track curvature and is required to start inside the FGD1 fiducial volume (FV) that begins 48 mm inward from the edges of FGD1 in X and Y and 21 mm inward from the upstream FGD1 edge in Z.

(2) Upstream veto
To reduce the background events from neutrino interactions upstream of the FGD1 FV, any tracks which pass through the upstream TPC (TPC1) are rejected.

(3) Muon PID with TPCs
The particle identification (PID) is performed based on the energy loss and momentum measured by TPCs. Those of the negative track from FGD1 are required to be consistent with a muon.

Table 10.2 summarizes the numbers of events passing each CC selection step for the Run 1+2+3+4 data and the MC expectation. There are 25917 events selected as the inclusive CC candidate events.

Table 10.2: The numbers of events passing each ND280 CC selection step.

	Data	MC	Purity of CC events
Negative track from FGD1	48731	47751.9	55.7%
Upstream veto	34804	36833.2	70.2%
Muon PID	25917	27082.1	90.7%

10.2.2 CC event classification

The selected CC events are divided into three sub-samples which are sensitive to different neutrino interaction types:

CC0π sample

For this sample, only one muon track and no pion tracks are required in the final states as shown in Fig. 10.1(a). Thus, no additional tracks which pass through both FGD1 and TPC2 other than the muon track and no electrons from muon decay at rest in FGD1 (Michel electron) are required. This sample is dominated by CCQE interactions.

CC1π^+ sample

For this sample, one muon track and one π^+ track are required in the final states as shown in Fig. 10.1(b). In order to reject π^0 and π^-, no e^-, e^+ or π^- are required in TPCs. This sample is dominated by CC resonant pion productions.

CC other sample

The rest of the CC events which are not included in the previous two samples are included in this sample. Figure 10.1(c) shows an example of the event in this sample. This sample is dominated by CC deep inelastic scatterings.

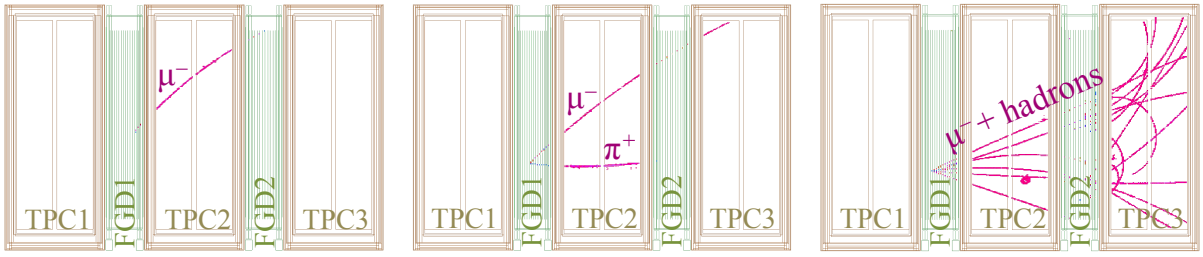

(a) CC0π event (b) CC1π^+ event (c) CC other event

Figure 10.1: Example of selected events in three event topologies.

Table 10.3 summarizes the expected event compositions for the three sub-samples. Figure 10.2 shows the momentum distributions of the muon candidate tracks for the CC inclusive sample and the three sub-samples.

Table 10.3: Expected event compositions for the three sub-samples.

	CC0π sample	CC1π^+ sample	CC other sample
CCQE	**63.3%**	5.3%	3.9%
CC resonant π	20.3%	**39.4%**	14.2%
CC DIS	7.5%	31.3%	**67.7%**
CC coherent π	1.4%	10.6%	1.4%
NC	1.9%	4.7%	6.8%
$\bar{\nu}_\mu$	0.2%	1.7%	0.9%
ν_e	0.2%	0.4%	0.9%
External	5.2%	6.6%	4.1%

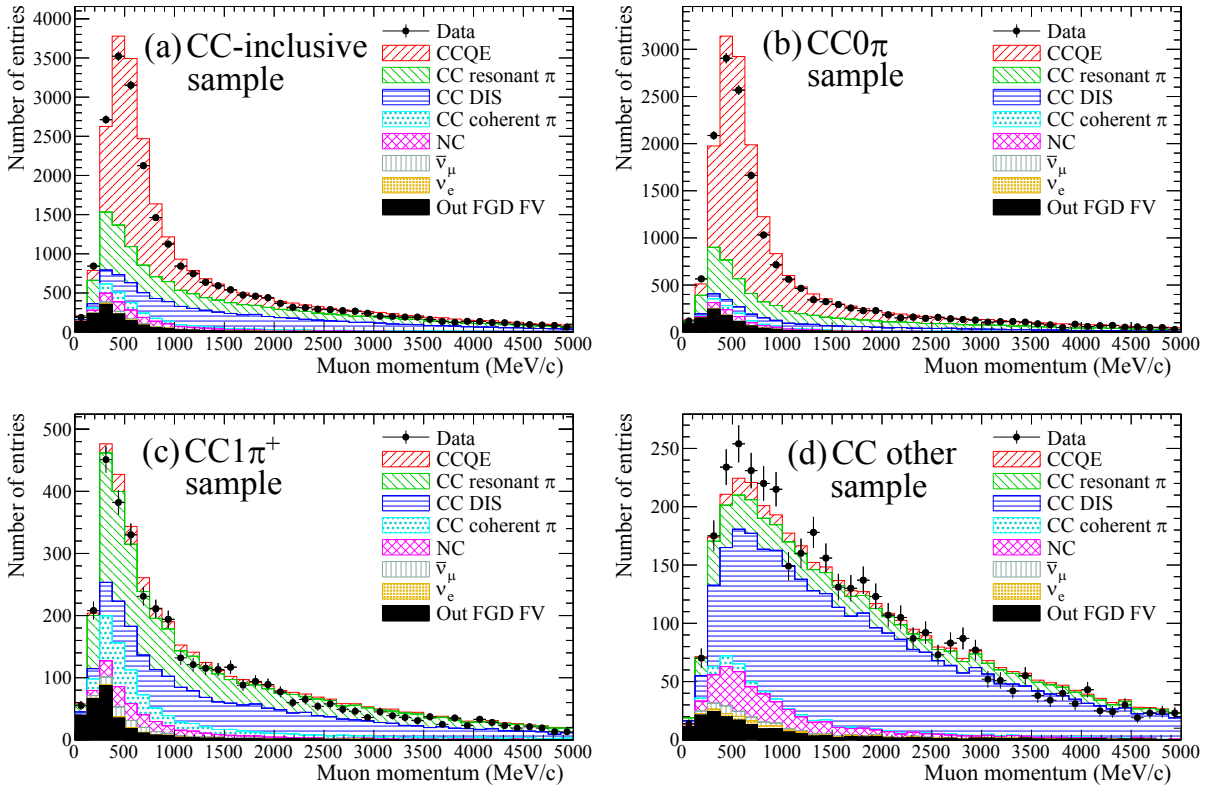

Figure 10.2: Momentum distributions of the muon candidate tracks in (a) CC inclusive sample, (b) CC0π sample, (c) CC1π^+ sample and (d) CC other sample overlaid with the nominal MC predictions.

10.3 Constraint from the ND280 measurement

In order to constrain the uncertainties of flux and cross section by the ND280 measurement, the muon momentum and angular distributions measured in three categories are fitted with 25 beam flux parameters at ND280 (11 E_{ν_μ}, 5 $E_{\bar{\nu}_\mu}$, 7 E_{ν_e}, and 2 $E_{\bar{\nu}_e}$ bins) and 21 cross section parameters (M_A^{QE}, M_A^{RES}, spectral function parameter, binding energy, Fermi momentum, π-less Δ decay parameter, nine normalization parameters, and six pion intra-nuclear interaction parameters) as well as 210 parameters describing the ND280 detector systematics (10 momentum $\times$ 7 angle bins for each sample). Figure 10.3 shows the muon momentum and $\cos\theta_\mu$ distributions for the data and the nominal and best-fit MC predictions. A χ^2 goodness-of-fit test returns a p-value of 0.66, indicating no disagreement between the data and the MC prediction using best-fit parameters. The ND280 measurement constrains the Super-K flux parameters due to the flux covariance between ND280 and Super-K derived from the neutrino beam simulation. Likewise, it also constrains eight cross section parameters (M_A^{QE}, M_A^{RES} and normalization parameters for CCQE, CC1π and NC1π^{0*}) which are strongly correlated between ND280 and Super-K (CH and H_2O targets). Figure 10.4 and Table 10.4 show the Super-K ν_μ and ν_e flux normalization parameters and the correlated cross section parameters with and without the ND280 constraint. Uncertainties on these parameters are reduced by the ND280 constraint. When the ND280 constraint is applied, strong anti-correlations between the Super-K flux parameters and the cross section parameters appear as shown in Fig. 10.5. This implies that the uncertainty on the product of the Super-K flux and the cross section is greatly reduced by the ND280 constraint.

*Although the NC1π^0 events constitute only small percentages of the ND280 selected samples, the NC1π^0 normalization is constrained owing to the correlation between CC1π^+ and NC1π^0 interactions.

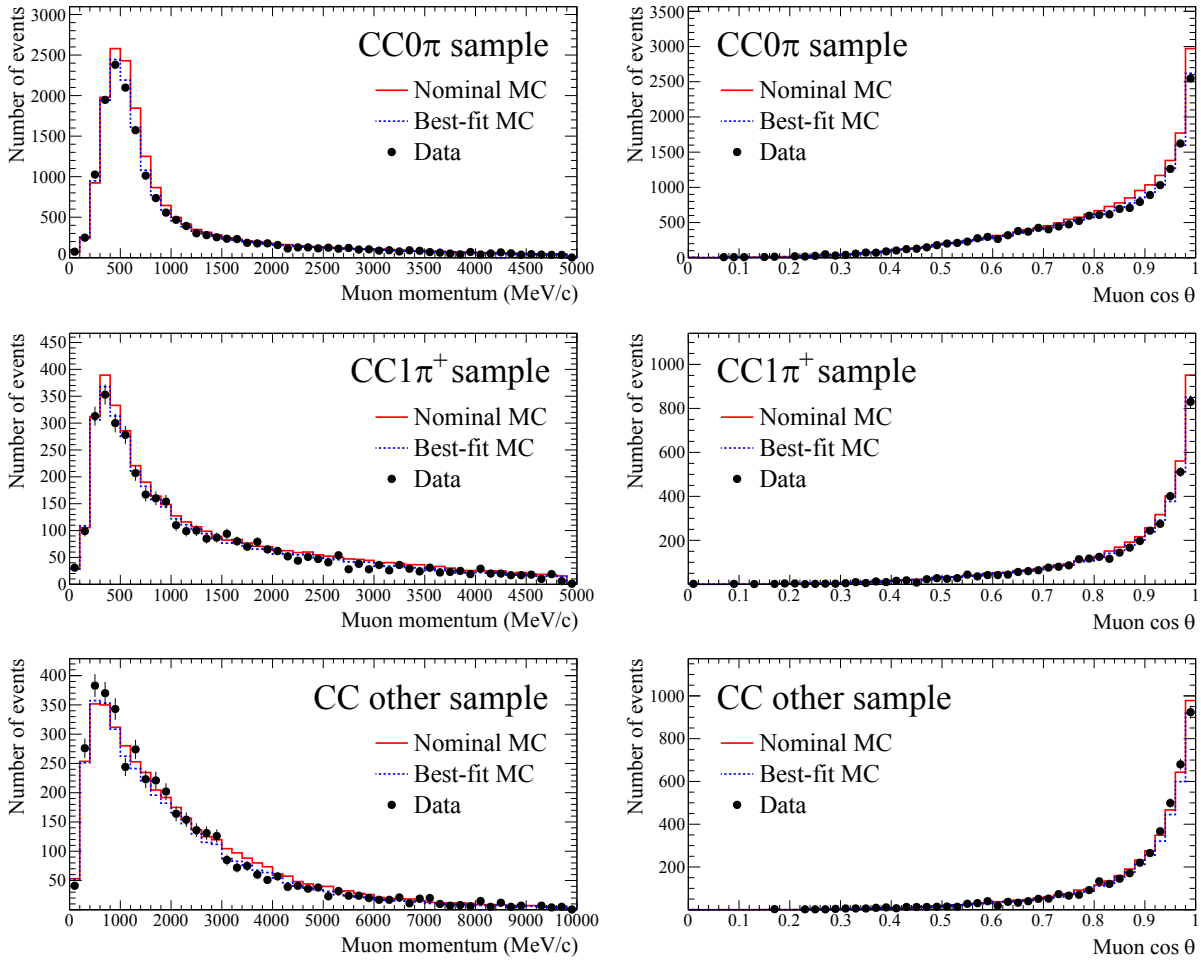

Figure 10.3: Muon momentum distributions (left) and $\cos\theta_\mu$ distributions (right) for CC0π sample (top), CC1π^+ sample (middle) and CC other sample (bottom) overlaid with the nominal and best-fit MC predictions.

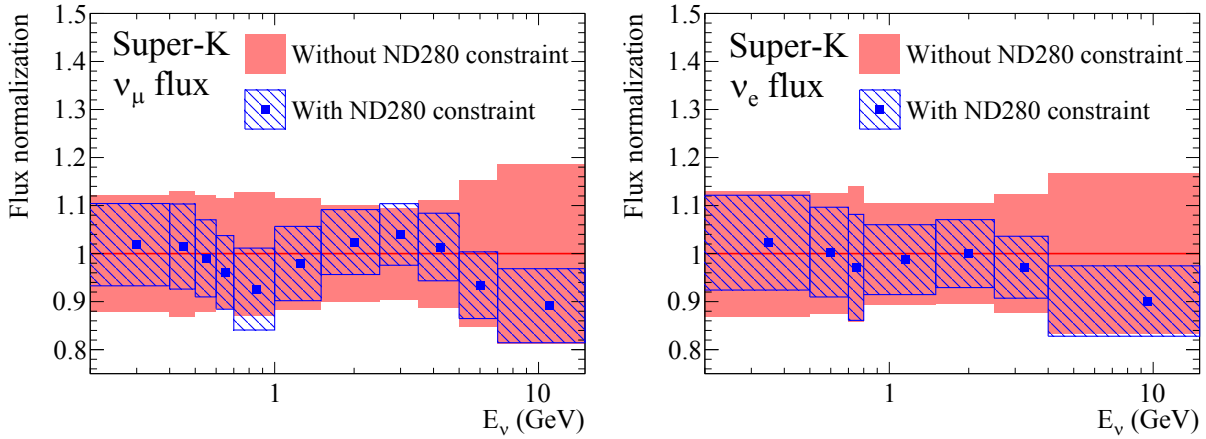

Figure 10.4: Super-K ν_μ (left) and ν_e (right) flux normalization parameters and their error band with and without the ND280 constraint.

Table 10.4: Cross section parameters and their errors with and without the ND280 constraint.

Cross section parameter	Without ND280 constraint	With ND280 constraint
M_A^{QE}	1.21±0.45 GeV/c^2	1.24±0.072 GeV/c^2
M_A^{RES}	1.41±0.22 GeV/c^2	0.96±0.068 GeV/c^2
CCQE norm. ($E_\nu < 1.5$ GeV)	1.00±0.11	0.97±0.076
CCQE norm. ($1.5 < E_\nu < 3.5$ GeV)	1.00±0.30	0.93±0.10
CCQE norm. ($E_\nu > 3.5$ GeV)	1.00±0.30	0.85±0.11
CC1π norm. ($E_\nu < 2.5$ GeV)	1.15±0.32	1.26±0.16
CC1π norm. ($E_\nu > 2.5$ GeV)	1.00±0.40	1.12±0.17
NC1π^0 norm.	0.96±0.33	1.14±0.25

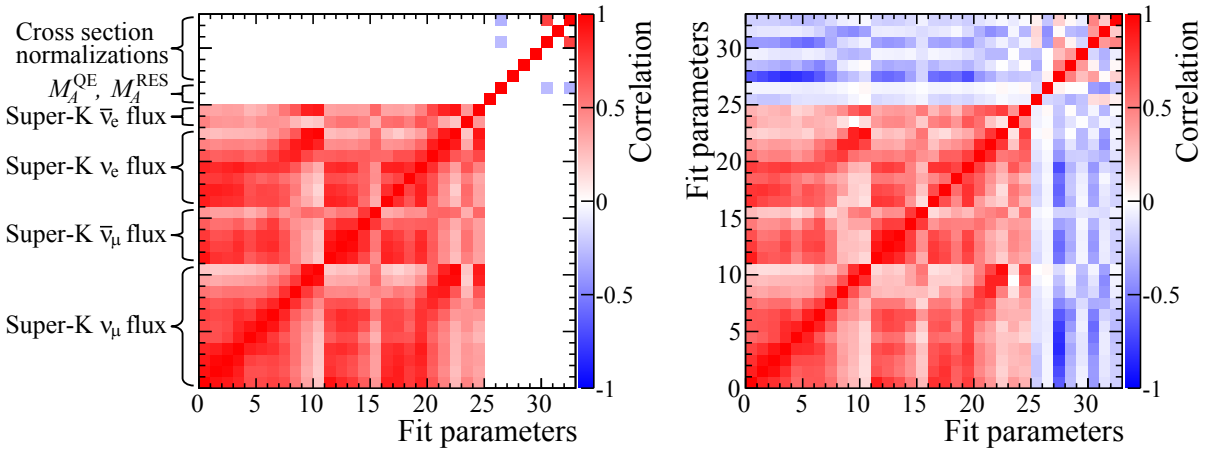

Figure 10.5: The parameter correlations with (left) and without (right) the ND280 constraint. The parameters are 0-24 Super-K flux normalization, 25 M_A^{QE}, 26 M_A^{RES}, 27-29 CCQE normalization, 30-31 CC1π normalization, 32 NC1π^0 normalization.

10.4 Measurement at Super-K

The Super-K data set for Run 1-4 is used for this measurement. It corresponds to 6.57×10^{20} POT. The CCQE interaction events of ν_μ and ν_e are counted at Super-K, which produce charged leptons of their respective flavor. A muon, counted to measure the $\nu_\mu \to \nu_\mu$ oscillation, generally travels in a straight line through the detector and produces a well-defined Cherenkov light cone. As a result, a clear, sharp ring of PMT hits is observed as shown in Fig. 10.6 (a). In contrast, an electron, counted to measure the $\nu_\mu \to \nu_e$ oscillation, scatters more easily because of its smaller mass, and almost always induces electromagnetic showers. As a result, many Cherenkov light cones from the electromagnetic showers overlap, and a fuzzy ring of PMT hits is observed as shown in Fig. 10.6 (b). The difference between sharp and fuzzy ring patterns is used to designate whether the ring was produced from muon-like or electron-like particles. The CCQE interaction is chosen as the signal interaction mode because it is the dominant interaction in the T2K neutrino energy region, and the neutrino energy for a CCQE interaction (E_{rec}) can be reconstructed from the emitted charged lepton as:

$$E_{\mathrm{rec}} = \frac{m_p^2 - (m_n - E_b)^2 - m_l^2 + 2(m_n - E_b)E_l}{2(m_n - E_b - E_l + p_l \cos\theta_l)}, \tag{10.1}$$

where m_n, m_p and m_l are masses of neutron, proton and charged lepton, E_b is the neutron binding energy in oxygen (27 MeV) and E_l, p_l and θ_l are energy of charged lepton, its momentum and its emission angle relative to the beam direction, respectively. The reconstructed neutrino energy is needed for a precise neutrino oscillation measurement because the neutrino oscillation probabilities depend on the neutrino energy.

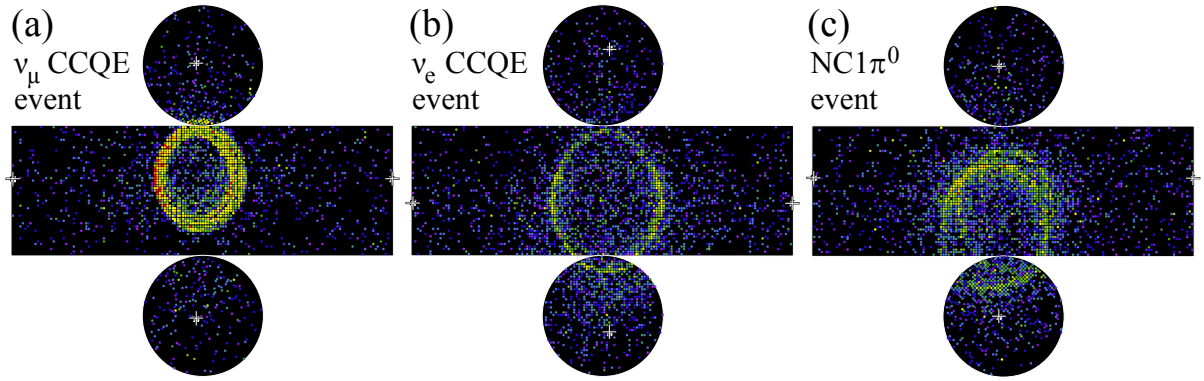

Figure 10.6: MC event displays of (a) ν_μ CCQE event, (b) ν_e CCQE event and (c) NC1π^0 event in Super-K, where the cylindrical detector is unrolled onto a plane. The colored points represent hit PMTs, with the color corresponding to the amount of charge (blue→yellow→red is small→large charge). The white crosses indicate the location of the reconstructed vertex.

10.4.1 ν_e event selection

To detect the CCQE events of the oscillated ν_e, we select events with a single electron-like Cherenkov ring. The main backgrounds come from the NC π^0 production interactions and intrinsic ν_e contamination in the beam. The π^0 decaying into two photons generally produces two fuzzy rings as shown in Fig. 10.6 (c). However, one of the two photons is not sometimes reconstructed due to highly asymmetric energies or a small opening angle between the two photons, resulting in the misidentification as a single electron ring from ν_e CC interaction. The intrinsic beam ν_e is mainly produced by the muon decay ($\mu^+ \to e^+ + \bar{\nu}_\mu + \nu_e$). In order to reduce these backgrounds and the CC-nonQE events, four further event selections (a visible energy cut, a decay electron cut, a reconstructed neutrino energy cut and a π^0 rejection) are applied. The event selection criteria are described below[†].

(1) Fully contained events in the fiducial volume (FCFV)

A fully-contained (FC) event is defined as an event in which a neutrino interacts in the Super-K inner detector (ID) and the neutrino-induced charged particles deposit all the energy in ID not in the outer detector (OD) so that the energy of the charged particles can be reconstructed. The fiducial volume (FV) is defined as shown in Sec 2.5. The FV cut requires the neutrino interaction vertex reconstructed from the PMT hit timing to be in the FV. As the first step in the event selection, the FCFV events are selected.

(2) Single ring

In the CCQE events, a charged lepton and a proton are produced, then only one Cherenkov ring by the charged lepton is observed because the proton generally does not exceed the Cherenkov radiation threshold energy[‡]. In contrast, in CC-nonQE events, for example

[†]More details about the Super-K event selection and reconstruction are found in Y. Ashie *et al.* [341].

[‡]Cherenkov radiation threshold energies of electron, muon, pion and proton in water are 0.775MeV, 160MeV, 212MeV and 1423MeV, respectively.

CC1π events, a pion is produced in addition to a charged lepton, then more than one Cherenkov ring is observed if a Cherenkov ring by the pion is observed. Thus, single ring events are selected to enhance CCQE events as shown in Fig. 10.7(a).

(3) Electron-like PID

The particle identification (PID) is performed based on the Cherenkov ring pattern and opening angle. Figure 10.7(b) shows the distribution of the PID likelihood parameter where negative (positive) value is recognized as e-like (μ-like). In order to select ν_e CC events, e-like events are selected.

(4) Visible energy greater than 100 MeV

The events having the visible energy ($E_{\rm vis}$) above 100 MeV are selected as shown in Fig. 10.7(c). $E_{\rm vis}$ is calculated from the total amount of Cherenkov light assuming the ring was produced by an electron. This cut removes low energy NC interactions and electrons from the decay of invisible muons and pions, such as cosmic muons outside the beam time window or muons below Cherenkov threshold.

(5) No decay electron

Decay electrons are tagged by searching for delayed hit clusters after the primary event. Events without the delayed hit clusters are selected (Fig. 10.7(d)) because the decay electrons indicate a presence of invisible muons or pions in addition to an electron.

(6) Reconstructed neutrino energy less than 1250 MeV

Events are required to have a reconstructed neutrino energy ($E_{\rm rec}$) below 1250 MeV since the signal at high energy is expected to be small from the past measurements of $|\Delta m^2_{32}|$, and the intrinsic ν_e background is dominant in the high energy region, as shown in Fig. 10.7(e). The $E_{\rm rec}$ is calculated assuming a CCQE interaction (Eq. 10.1).

(7) π^0 rejection

To separate π^0 background events from signal ν_e CC events, the reconstructed π^0 mass (m_{π^0}) and the ratio of the best-fit likelihoods of the π^0 and electron fits (L_{π^0}/L_e) are used. The m_{π^0} is reconstructed by a search for a second photon ring and a calculation assuming the two rings from the π^0 decay. The likelihoods are constructed from charge and time probability density functions (PDFs) for every PMT hit for a given particle hypothesis with a set of seven parameters: the vertex position, the timing, the direction and the momentum. Figure 10.7(f) shows $\ln(L_{\pi^0}/L_e)$ vs m_{π^0} distribution. Events that satisfy

$$\ln(L_{\pi^0}/L_e) < 175 - 0.875 \times m_{\pi^0} \tag{10.2}$$

constitute the final ν_e candidate sample[§].

Table 10.5 summarizes the numbers of events passing each ν_e selection step for the Run 1+2+3+4 data and the MC expectation. There are 28 events selected as the final ν_e candidate events, whereas the expected number of the selected background events other than $\nu_\mu \to \nu_e$ signal events is 4.27.

[§]This π^0 rejection cut was developed in 2013. It removes 69% of the π^0 background events relative to the previous π^0 rejection cut, with only a 2% loss in signal efficiency.

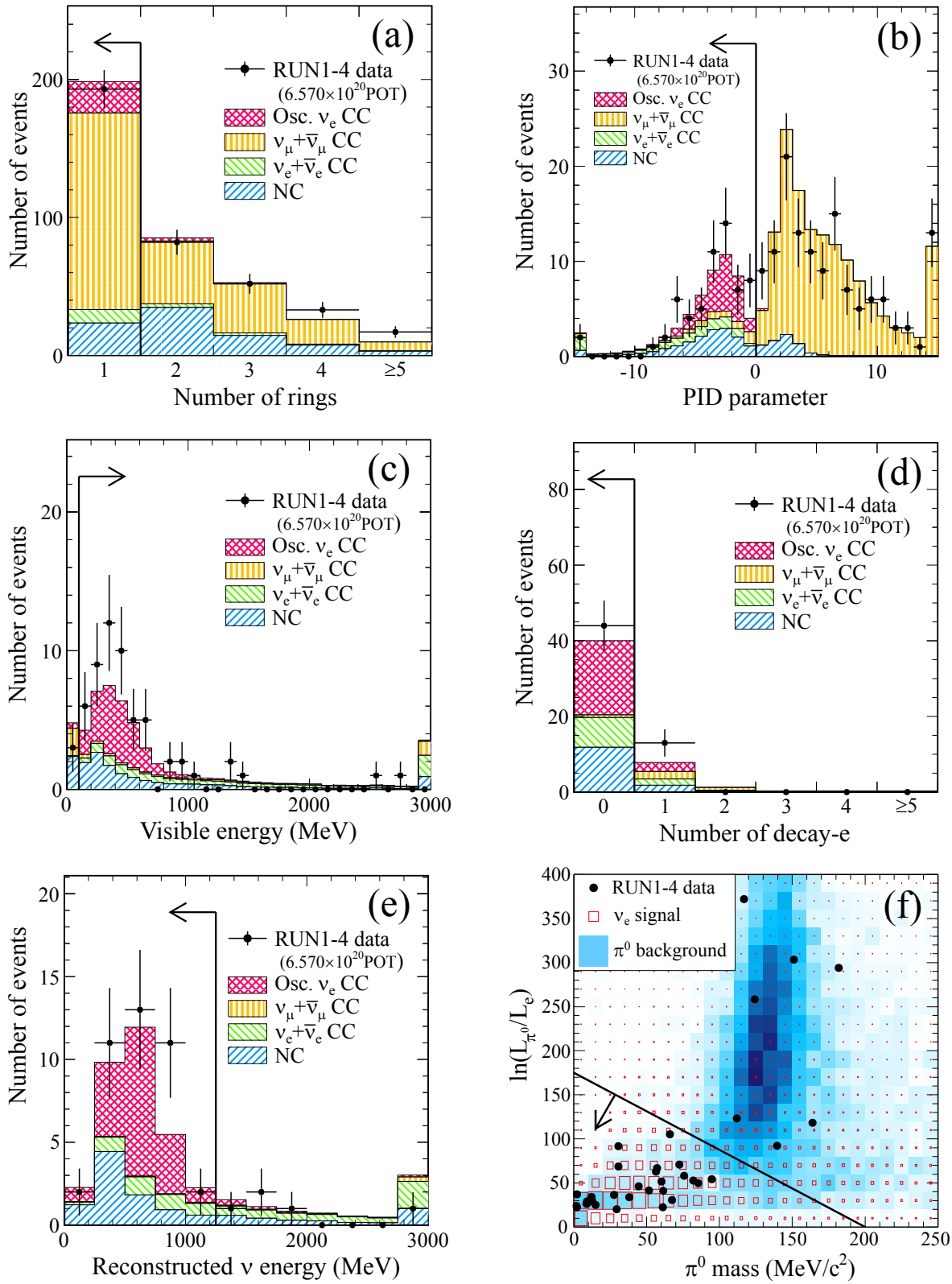

Figure 10.7: Distributions of ν_e event selection variables at each selection step. (a) The number of rings, (b) PID parameter, (c) visible energy, (d) the number of decay electrons, (e) reconstructed neutrino energy and (f) π^0 cut variables. The MC predictions assume the nominal oscillation parameters.

Table 10.5: The numbers of events passing each ν_e selection step. Efficiency is defined as the number of selected events divided by the number of interactions in FV. The MC predictions assume the nominal oscillation parameters.

	Data	MC				
		MC total	$\nu_\mu \to \nu_e$ CC signal	$\nu_\mu + \bar{\nu}_\mu$ CC	$\nu_e + \bar{\nu}_e$ CC	NC
Interactions in FV	–	656.8	27.07	325.67	15.97	288.11
FCFV	377	372.4	26.22	247.75	15.36	83.02
Single-ring	193	198.4	22.72	142.44	9.82	23.46
Electron-like PID	60	54.2	22.45	5.63	9.74	16.35
E_{vis} >100MeV	57	49.4	22.04	3.66	9.68	13.99
No decay electron	44	40.0	19.63	0.69	7.87	11.84
E_{rec} <1250MeV	39	31.7	18.82	0.21	3.73	8.99
π^0 rejection	28	21.6	17.32	0.07	3.24	0.96
Efficiency	–	3.3%	64.0%	0.0%	20.3%	0.3%

10.4.2 ν_μ event selection

To detect the CCQE events of the surviving ν_μ, we select events with a single muon-like Cherenkov ring. Then, two further event selections (a reconstructed momentum cut and a decay electron cut) are applied in order to keep the performance of the particle identification and enrich CCQE events. The event selection criteria are described below.

(1) Fully contained events in the fiducial volume (FCFV)
Definitions of fully contained and the fiducial volume are the same as ν_e event selection.

(2) Single ring
Along with the ν_e event selection, single ring events are selected to select CCQE events as shown in Fig. 10.8(a).

(3) Muon-like PID
The same likelihood parameter as the ν_e event selection is used for the PID. In order to select ν_μ CC events, μ-like events are selected as shown in Fig. 10.8(b).

(4) Reconstructed muon momentum is greater than 200 MeV/c
Events with the reconstructed muon momentum greater than 200 MeV/c are selected as shown in Fig. 10.8(c). This cut is to ensure the PID performance and remove contamination of charged pions and misidentified electrons from the decay of invisible muons and pions.

(5) Less than two decay electrons
In order to eliminate the events with invisible charged pions, events with less than two decay electrons are selected as the final ν_μ candidate sample.

Table 10.6 summarizes the numbers of events passing each ν_μ selection step for the Run 1+2+3+4 data and the MC expectation. There are 120 events selected as the final ν_μ candidate events, whereas the expected number of selected events without neutrino oscillation is 446.0.

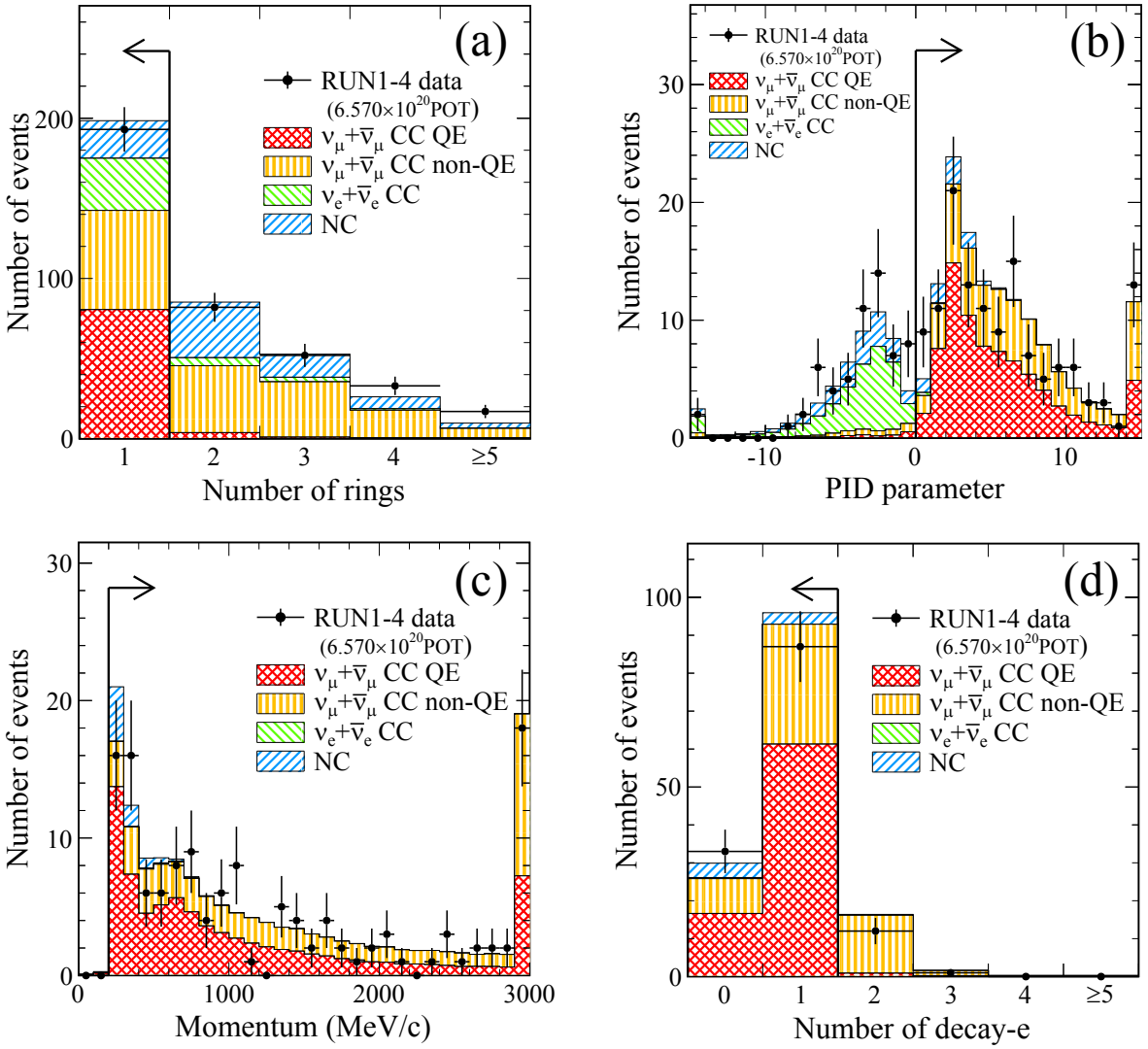

Figure 10.8: Distributions of ν_μ event selection variables at each selection step. (a) The number of rings, (b) PID parameter, (c) reconstructed muon momentum and (d) the number of decay electrons. The MC predictions assume the nominal oscillation parameters.

Table 10.6: The numbers of events passing each ν_μ selection step. Efficiency is defined as the number of selected events divided by the number of interactions in FV. The MC predictions assume the nominal oscillation parameters.

	Data	MC				
		MC total	$\nu_\mu + \bar{\nu}_\mu$ CCQE	$\nu_\mu + \bar{\nu}_\mu$ CC non-QE	$\nu_e + \bar{\nu}_e$ CC	NC
Interactions in FV	–	656.83	111.71	213.96	43.05	288.11
FCFV	377	372.35	85.55	162.20	41.58	83.02
Single-ring	193	198.44	80.57	61.87	32.54	23.46
Muon-like PID	133	144.28	79.01	57.80	0.35	7.11
p_μ >200MeV/c	133	143.99	78.83	57.77	0.35	7.04
$N_{\mathrm{decay-e}}$ <2	120	125.85	77.93	40.78	0.35	6.78
Efficiency	–	19.2%	69.8%	19.1%	0.8%	2.4%

10.4.3 Super-K detector uncertainties

Selection efficiency uncertainty

The systematic uncertainties of the Super-K detector on event selection efficiency and reconstruction have been studied using comparisons of the data and MC control samples. In the past, the Super-K systematic uncertainties on the ν_e event selection and those on the ν_μ event selection have been estimated separately for the stand-alone $\nu_\mu \to \nu_e$ and $\nu_\mu \to \nu_\mu$ oscillation analyses. For the joint neutrino oscillation analysis, they are re-estimated in consideration of the correlation between the ν_e event selection and the ν_μ event selection. The Super-K event selection uncertainties are evaluated for every event selection step using various control samples. Appendix E gives detailed descriptions of the evaluation of the Super-K selection efficiency uncertainties. Figure 10.9 shows the correlation matrix and the fractional error of the Super-K selection efficiency, where the binning is based on the neutrino flavor, neutrino interaction type, and reconstructed neutrino energy at Super-K.

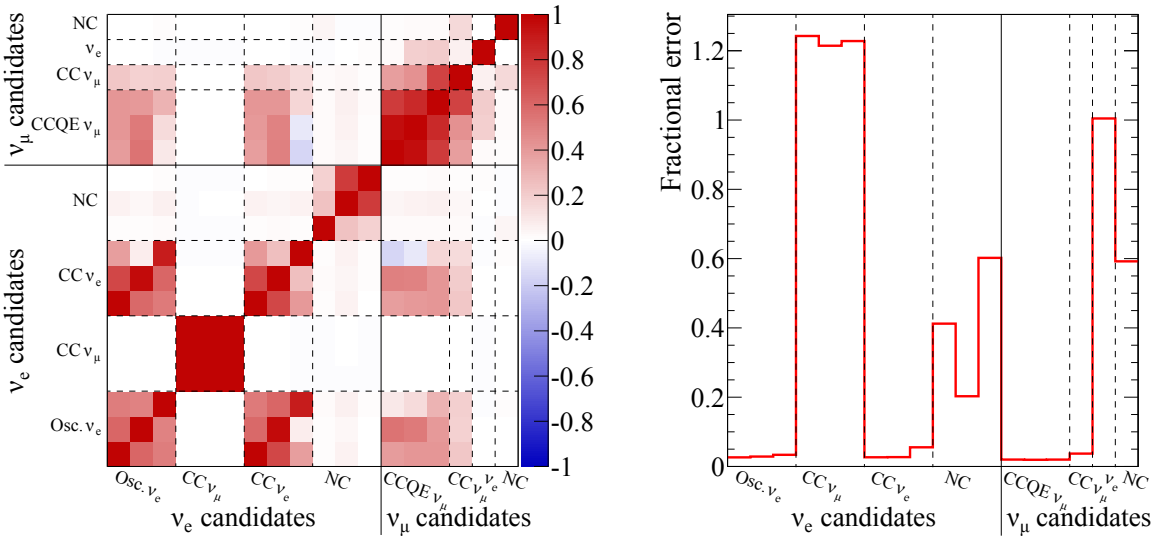

Figure 10.9: Correlation matrix (left) and the fractional error (right) of the Super-K selection efficiency. The binning is based on the neutrino flavor, neutrino interaction type, and reconstructed neutrino energy at Super-K. "Osc. ν_e" denotes the oscillated ν_e events.

Energy scale uncertainty

The energy scale uncertainty of Super-K is estimated to be 2.4% from comparisons of distributions between the cosmic-ray data and the MC samples (Fig. 4.14). The effect of the energy scale uncertainty is not included in Fig. 10.9 because it is implemented in a different way as we shall describe later.

Photo-nuclear effect uncertainty

The photo-nuclear effect is the interactions of the photon with a nucleus. It leads to the absorption of a photon before it induces electromagnetic showers. When one of the two photons from a π^0 decay is absorbed, the event is misidentified as ν_e CCQE event in Super-K. Accordingly, this affects the π^0 background for the $\nu_\mu \to \nu_e$ oscillation measurement. Thus, this effect and its uncertainty are added to the Super-K MC simulation.

Pion interaction uncertainty

When a pion from CC resonant pion production ($\nu_l + N \rightarrow l^- + N' + \pi$) is absorbed, the event is misidentified as CCQE event in Super-K. Uncertainties of pion interactions in the target nucleus and the Super-K detector are treated in the same way as the near detectors (see Chapter 4 for details).

10.5 Introduction to the three-flavor neutrino oscillation analysis

The $\nu_\mu \rightarrow \nu_e$ oscillation probability in T2K is particularly sensitive to $\sin^2 2\theta_{13}$ and δ_{CP}, while the $\nu_\mu \rightarrow \nu_\mu$ oscillation probability is particularly sensitive to $\sin^2 \theta_{23}$ and Δm^2_{32}. Therefore, analysis for the measurement of $\sin^2 2\theta_{13}$ and δ_{CP} via the $\nu_\mu \rightarrow \nu_e$ oscillation and that of $\sin^2 \theta_{23}$ and $|\Delta m^2_{32}|$ via the $\nu_\mu \rightarrow \nu_\mu$ oscillation had been performed separately to date [47,112–116]. However, the $\nu_\mu \rightarrow \nu_e$ and $\nu_\mu \rightarrow \nu_\mu$ oscillation probabilities actually depend also on $\sin^2 \theta_{23}$ and $|\Delta m^2_{32}|$, and $\sin^2 2\theta_{13}$, respectively as shown in Eq. 1.11 and 1.17. In the past neutrino oscillation analyses, these oscillation parameters were fixed or constrained from the other experimental results. For example, in the latest $\nu_\mu \rightarrow \nu_e$ oscillation analysis, $\sin^2 \theta_{23}$ and $|\Delta m^2_{32}|$ are constrained by the result of the T2K $\nu_\mu \rightarrow \nu_\mu$ oscillation analysis since the measurement precisions of T2K on these oscillation parameters reach to the world's highest level. However, the correlation of the common systematic errors between the $\nu_\mu \rightarrow \nu_e$ and $\nu_\mu \rightarrow \nu_\mu$ oscillation analyses was not taken into account. The three-flavor joint oscillation analysis of $\nu_\mu \rightarrow \nu_e$ and $\nu_\mu \rightarrow \nu_\mu$ is therefore performed in order to determine $\sin^2 2\theta_{13}$, $\sin^2 \theta_{23}$, $|\Delta m^2_{32}|$ and δ_{CP} simultaneously with consideration of the correlation among the oscillation parameters and the systematic errors.

10.6 Analysis strategy

10.6.1 Treatment of oscillation parameters

In the oscillation analysis fit, $\sin^2 2\theta_{13}$, $\sin^2 \theta_{23}$, Δm^2_{32} and δ_{CP} are fitted as free parameters which are totally unknown prior to the fit, whereas $\sin^2 2\theta_{12}$, Δm^2_{12}, earth matter density and baseline length are fixed to the nominal values (Table 10.1) because the effects of the uncertainties on these parameters to the fitted parameters are negligible. While the mass hierarchy is also treated as fixed during the fit procedure, both mass hierarchy cases are checked. The largest mass-squared difference is Δm^2_{32} for the normal hierarchy and Δm^2_{13} for the inverted hierarchy. Hence, Δm^2_{13} is used instead of Δm^2_{32} for the inverted hierarchy in order to make a direct comparison between the normal and inverted hierarchies.

10.6.2 Fitting methods

We performed a binned maximum likelihood fit to the reconstructed neutrino energy spectra of the ν_e and ν_μ candidate events. The reconstructed neutrino energy is calculated from the measured kinematics of a charged lepton assuming a CCQE interaction (Eq. 10.1). We use 25 and 73 bins for the reconstructed neutrino energy of ν_e candidate events and ν_μ candidate events, respectively. The likelihood function for the three-flavor joint fit with the ν_e and ν_μ candidate events is defined as:

$$\mathcal{L}(\boldsymbol{N}^{\mathbf{obs}}_{\boldsymbol{\nu_e}}, \boldsymbol{N}^{\mathbf{obs}}_{\boldsymbol{\nu_\mu}}, \boldsymbol{o}, \boldsymbol{f}) = \mathcal{L}_{\nu_e}(\boldsymbol{N}^{\mathbf{obs}}_{\boldsymbol{\nu_e}}, \boldsymbol{o}, \boldsymbol{f}) \times \mathcal{L}_{\nu_\mu}(\boldsymbol{N}^{\mathbf{obs}}_{\boldsymbol{\nu_\mu}}, \boldsymbol{o}, \boldsymbol{f}) \times \mathcal{L}_{\mathrm{syst}}(\boldsymbol{o}, \boldsymbol{f}), \tag{10.3}$$

where the variables have the following meanings:

- $\boldsymbol{N^{\mathrm{obs}}_{\nu_e}}$ and $\boldsymbol{N^{\mathrm{obs}}_{\nu_\mu}}$ are the observed numbers of ν_e and ν_μ candidate events at Super-K in bins of the reconstructed neutrino energy.
- $\boldsymbol{o}$ represents the oscillation parameters we measure (θ_{13}, θ_{23}, Δm^2_{32} and δ_{CP}).
- $\boldsymbol{f}$ corresponds to the nuisance parameters describing the systematic uncertainties.

The ν_e and ν_μ spectrum terms, $\mathcal{L}_{\nu_e}$ and $\mathcal{L}_{\nu_\mu}$, are defined by the Poisson probability to the observed number of events, N^{obs}, when the predicted number of events is N^{pred}:

$$\mathcal{L}_{\nu_e}(\boldsymbol{N^{\mathrm{obs}}_{\nu_e}}, \boldsymbol{o}, \boldsymbol{f}) = \prod_{i=1}^{25} \left(\frac{\exp(-N^{\mathrm{pred}}_{\nu_e,i}(\boldsymbol{o},\boldsymbol{f})) \cdot (N^{\mathrm{pred}}_{\nu_e,i}(\boldsymbol{o},\boldsymbol{f}))^{N^{\mathrm{obs}}_{\nu_e,i}}}{N^{\mathrm{obs}}_{\nu_e,i}!} \right), \tag{10.4}$$

$$\mathcal{L}_{\nu_\mu}(\boldsymbol{N^{\mathrm{obs}}_{\nu_\mu}}, \boldsymbol{o}, \boldsymbol{f}) = \prod_{i=1}^{73} \left(\frac{\exp(-N^{\mathrm{pred}}_{\nu_\mu,i}(\boldsymbol{o},\boldsymbol{f})) \cdot (N^{\mathrm{pred}}_{\nu_\mu,i}(\boldsymbol{o},\boldsymbol{f}))^{N^{\mathrm{obs}}_{\nu_\mu,i}}}{N^{\mathrm{obs}}_{\nu_\mu,i}!} \right), \tag{10.5}$$

where $N_{\nu_e,i}$ and $N_{\nu_\mu,i}$ denote the numbers of ν_e and ν_μ candidate events in the i^{th} reconstructed energy bin. The systematic error term, $\mathcal{L}_{\mathrm{syst}}$, is the prior probability density function for the nuisance parameters[¶]. The maximization of the likelihood is performed as the minimization of χ^2 which is defined as:

$$\chi^2(\boldsymbol{N^{\mathrm{obs}}_{\nu_e}}, \boldsymbol{N^{\mathrm{obs}}_{\nu_\mu}}, \boldsymbol{o}, \boldsymbol{f}) = -2\ln\mathcal{L}(\boldsymbol{N^{\mathrm{obs}}_{\nu_e}}, \boldsymbol{N^{\mathrm{obs}}_{\nu_\mu}}, \boldsymbol{o}, \boldsymbol{f}), \tag{10.6}$$

using the ROOT Minuit2 minimization package [342, 343].

10.6.3 Determination of the confidence regions of the oscillation parameters

To determine the confidence region of one of the four oscillation parameters, the effect of the uncertainties of other three oscillation parameters must be taken into account. Thus, the confidence region of an oscillation parameter (o) is determined in the following way.

1. The χ^2 is minimized with fixing the oscillation parameter to a trial value. During the minimization procedure, the other three oscillation parameters are treated as free parameters.
2. The minimum χ^2 is scanned for many trial values of the oscillation parameter, and the χ^2 map of the oscillation parameter, $\chi^2_{\mathrm{trial}}(o)$, is obtained.
3. The $\Delta\chi^2$ map is composed as:

$$\Delta\chi^2(o) = \chi^2_{\mathrm{trial}}(o) - \chi^2_{\mathrm{min}}, \tag{10.7}$$

   where χ^2_{min} is the global minimum χ^2 value.
4. The confidence region of the oscillation parameter is determined as the region where the $\Delta\chi^2$ is lower than a critical limit[‖].

The two-dimensional confidence region of two oscillation parameters is also determined in the similar say.

[¶] The reason why the systematic error term is a function of the oscillation parameters as well as the nuisance parameters is described in the next section.

[‖] The critical limit for the 90% C.L region for single degree of freedom is 2.71.

10.6.4 Neutrino event prediction at Super-K

The likelihood calculation requires predictions of the reconstructed neutrino energy spectra for ν_e and ν_μ candidate events at Super-K as a function of the oscillation parameters and the systematic error nuisance parameters. When the systematic uncertainties are not considered, the number of ν_e candidate events in i^{th} reconstructed neutrino energy bin is predicted as:

$$\begin{aligned} N^{\mathrm{pred}}_{\nu_e,i}(\boldsymbol{o}) &= \sum_{F}\sum_{F'}\int_{E^i_{\mathrm{rec}}}^{E^{i+1}_{\mathrm{rec}}} dE_{\mathrm{rec}} \int dE_\nu \; \Phi^F(E_\nu)\cdot P^{F\to F'}(E_\nu,\boldsymbol{o})\cdot T \\ &\times \sum_{I}\sigma^{F',I}(E_\nu)\cdot\varepsilon^{F',I}_{\nu_e}(E_\nu)\cdot R^{F',I}(E_\nu\to E_{\mathrm{rec}}), \end{aligned} \tag{10.8}$$

where,

- E_ν and E_{rec} are the true and reconstructed energies of neutrino. E^i_{rec} is the lower edge of the i^{th} reconstructed neutrino energy bin.
- The indexes F and F' indicate the neutrino flavor categories, where ν_e, $\bar{\nu}_e$, ν_μ, $\bar{\nu}_\mu$, ν_τ and $\bar{\nu}_\tau$ are included.
- $\Phi^F(E_\nu)$ is the predicted neutrino flux of flavor F at Super-K without neutrino oscillations.
- $P^{F\to F'}(E_\nu,\boldsymbol{o})$ is the neutrino oscillation probability of $F\to F'$, depending on the chosen values of the oscillation parameters, $\boldsymbol{o}$. This factor is calculated using the Prob3++ software package** [344], which is based on three-flavor neutrino oscillation framework with the matter effect taken into account.
- T is a constant representing the number of target nuclei in Super-K.
- The index I indicates the neutrino interaction type, where CCQE, CC1π, CC other, and NC interactions are used.
- $\sigma^{F',I}(E_\nu)$ is the neutrino-nucleus interaction cross-section on the Super-K target material (H_2O) for flavor F' and interaction type I. It is extracted from NEUT.
- $\varepsilon^{F',I}_{\nu_e}(E_\nu)$ is the Super-K detection efficiency for the ν_e event selection estimated with NEUT and SKDETSIM (Fig. 10.10).
- $R^{F',I}(E_\nu\to E_{\mathrm{rec}})$ accounts for the Super-K detector response function representing the probability of observing an event with E_ν as one with E_{rec} (Fig. 10.11). It is also estimated with NEUT and SKDETSIM.

The number of ν_μ candidate events in bins of the reconstructed neutrino energy is also predicted in the same way using the Super-K detection efficiency and response function for the ν_μ event selection (Figs. 10.10 and 10.11).

**Prob3++ calculates oscillation probabilities based on the work of Barger *et al.* [345].

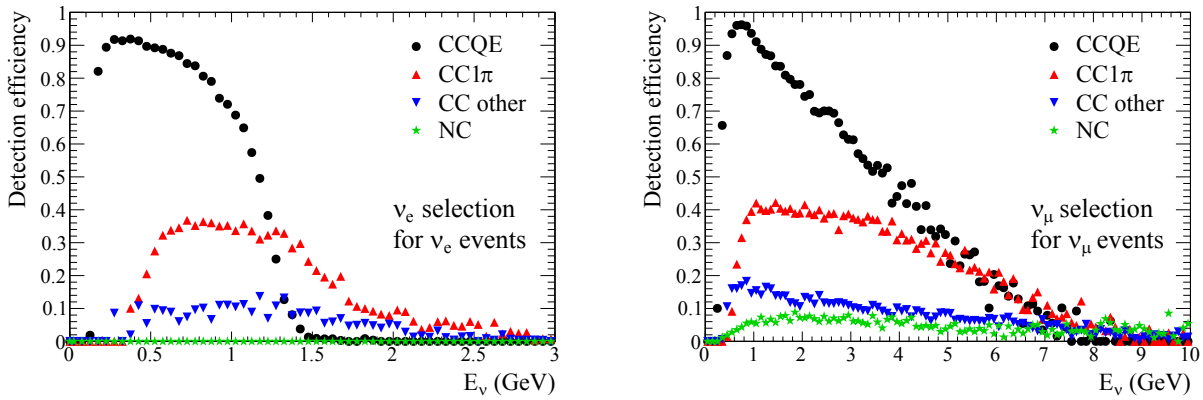

Figure 10.10: Super-K detection efficiency of ν_e events in the ν_e event selection (left) and ν_μ events in the ν_μ event selection (right) for each interaction type as a function of the neutrino energy.

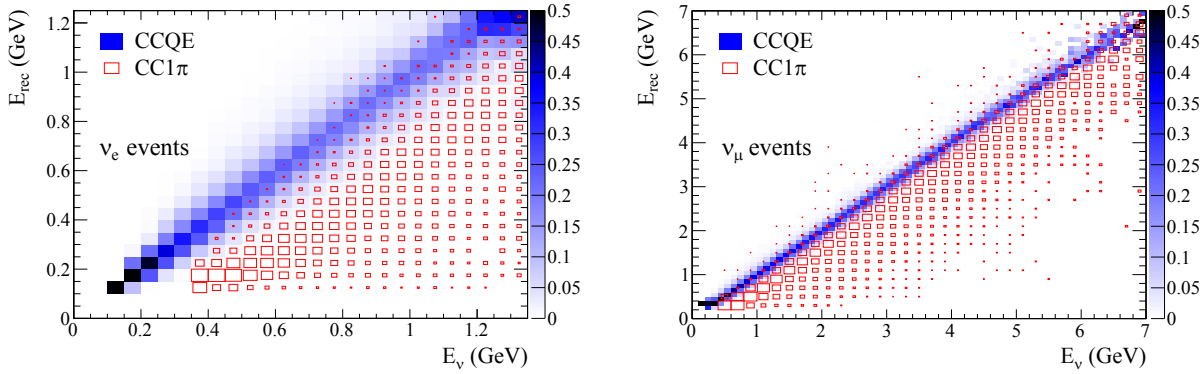

Figure 10.11: Probability of observing CCQE or CC1π event of ν_e (left) or ν_μ (right) with E_ν as one with $E_{\rm rec}$ in Super-K.

10.7 Systematic errors

10.7.1 Treatment of systematic errors

The neutrino flux uncertainties are implemented as normalization parameters in bins of neutrino energy and flavor. The neutrino interaction uncertainties are implemented as the model parameters and the ad hoc parameters as described Chapter 4. The neutrino flux uncertainties and part of the neutrino interaction uncertainties are constrained by the ND280 measurement. In addition, the Super-K detector uncertainties other than the energy scale error are implemented as normalization parameters on the detection efficiency in bins of reconstructed neutrino energy, neutrino flavor and neutrino interaction type. In total, there are 65 systematic error parameters (15 for the neutrino flux prediction, 19 for the neutrino interaction models, 21 for the Super-K detector). In the existing T2K oscillation analysis, they have been directly included as nuisance parameters in the oscillation analysis fit. This treatment makes the T2K oscillation analysis complicate and requires long CPU times for the oscillation analysis fit. It has been a problem existing in the T2K experiment. In order to avoid complexity and long CPU times, the treatment of the systematic errors should be simple yet accurate. Since this analysis involves a fit to the reconstructed neutrino energy, one simple solution is to propagate all the systematic

uncertainties to bins of reconstructed neutrino energy, and to represent these uncertainties by a covariance matrix. Therefore, we have developed a new method of the systematic error treatment, where 63 out of 65 systematic errors are encoded into a single covariance matrix. The Super-K energy scale error and the spectral function error are treated differently because they cannot be encoded into a covariance matrix as will be discussed in detail later.

10.7.2 Method of generating covariance matrix

The fractional uncertainties on the number of events in the reconstructed energy bins and their correlations among the bins are evaluated in the form of the covariance matrix. The covariance matrix is produced as follows.

1. 10,000 sets of 63 systematic error parameters are randomly generated based on the constraints and covariances for the systematic error parameters.
2. An expected reconstructed energy distribution is made for each parameter set.
3. The covariance matrix is made by checking the bin-by-bin correlations of the 10,000 reconstructed energy distributions:

$$V_{i,j}(\boldsymbol{o}) = \frac{1}{10000}\sum_{k=1}^{10000}\frac{(n_{i,k}^{\mathrm{pred}}(\boldsymbol{o}) - n_i^{\mathrm{pred}}(\boldsymbol{o}))(n_{j,k}^{\mathrm{pred}}(\boldsymbol{o}) - n_j^{\mathrm{pred}}(\boldsymbol{o}))}{n_i^{\mathrm{pred}}(\boldsymbol{o})n_j^{\mathrm{pred}}(\boldsymbol{o})}, \tag{10.9}$$

where $n_{i,k}^{\mathrm{pred}}(\boldsymbol{o})$ is the expected number of events in the i^{th} bin obtained from the k^{th} set of the systematic error parameters, and $n_i^{\mathrm{pred}}(\boldsymbol{o})$ is that of the nominal case without systematic errors.

This covariance matrix correctly treats the correlation between ν_e candidate events and ν_μ candidate events as well as that between the reconstructed energy bins. In order to speed up the oscillation analysis fitting procedure, we adopted a coarser binning in the covariance matrix by merging the original fine bins as shown in Fig. 10.12. The merging is applied to the bins which have similar covariances and those which have low sensitivities to the neutrino oscillation analysis so that it has negligible effects on the analysis result. Figure 10.13 shows the covariance matrices with original fine binning and merged coarse binning. The course binning contains 20 bins where first to eighth and ninth to twentieth bins correspond to the reconstructed energy bins

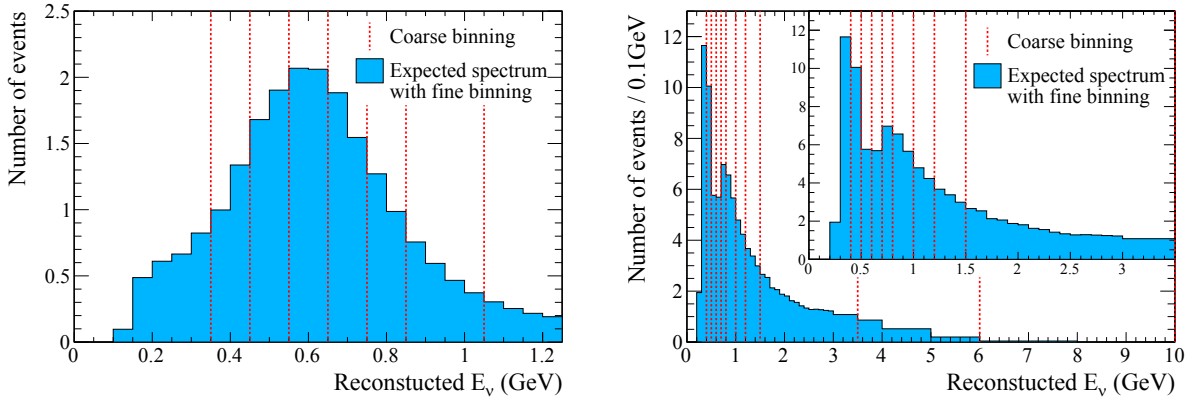

Figure 10.12: Definition of the coarse binning for the reconstructed energy of ν_e candidate events (left) and ν_μ candidate events (right) overlaid with expected spectra with the original fine binning.

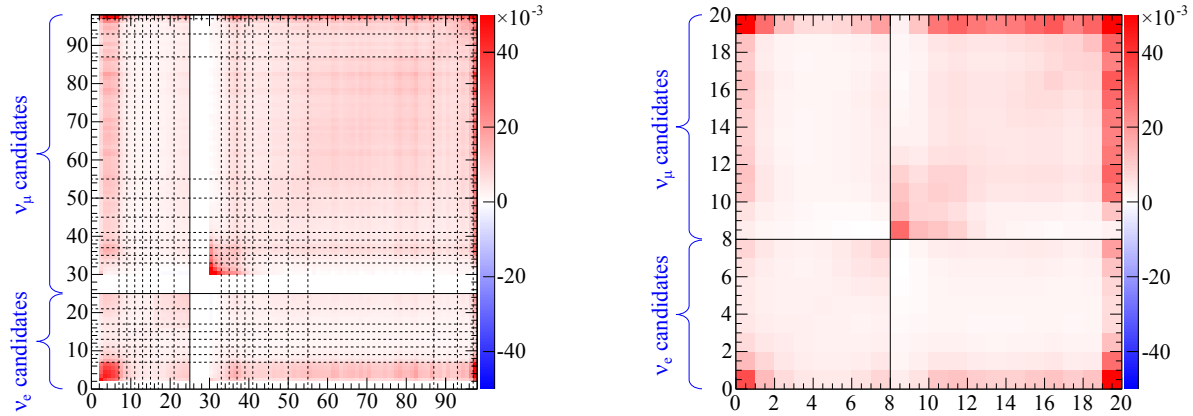

Figure 10.13: Covariance matrices with original fine binning (left) and merged coarse binning (right) when the nominal oscillation parameters are assumed. Dashed lines in the matrix with the fine binning represent groups in the course binning.

of ν_e candidate events and ν_μ candidate events, respectively. After establishing the method of oscillation analysis fit, the effect of the bin merging to the oscillation analysis result is confirmed to be negligibly small by fitting pseudo data as described in Appendix H.

10.7.3 Oscillation parameter dependence of the covariance matrix

The systematic error on the number of selected events at Super-K depends on the neutrino oscillation parameters as shown in Fig. 10.14. It means that the systematic error covariance matrix also depends on the neutrino oscillation parameters. Figure 10.14 shows that the vari-

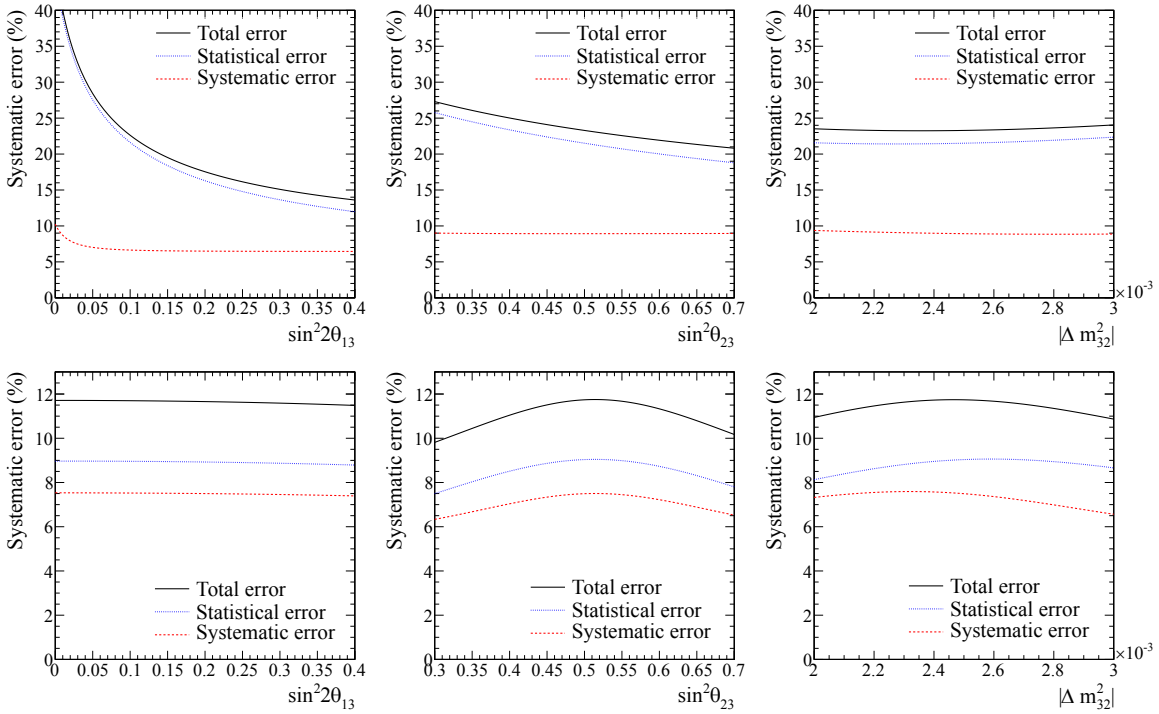

Figure 10.14: Variation of the errors on the number of ν_e candidate events (top) and ν_μ candidate events (bottom) at Super-K as a function of each oscillation parameter.

ation of the systematic error on the number of ν_e and ν_μ candidate events due to changes in $\sin^2 2\theta_{13}$ is negligibly small compared to the total error size. However, the variation of the systematic error on the number of ν_μ candidate events due to $\sin^2\theta_{23}$ and $|\Delta m^2_{32}|$ is not negligible, meaning that the variation of the covariance matrix due to changes in $\sin^2\theta_{23}$ and $|\Delta m^2_{32}|$ is not negligible. In order to take into account the dependence on $\sin^2\theta_{23}$ and $|\Delta m^2_{32}|$, 201×201 sets of covariance matrices in the plane of $\sin^2\theta_{23}$ and $|\Delta m^2_{32}|$ were generated. The oscillation parameters used to generate the covariance matrices are equally-spaced in a sufficiently wide region ($0.3 < \sin^2\theta_{23} < 0.7$ and $2.0\times10^{-3}\mathrm{eV}^2 < |\Delta m^2_{32}| < 3.0\times10^{-3}\mathrm{eV}^2$). Figure 10.15 shows the covariance matrices for the oscillation parameters at the edges and center of the $\sin^2\theta_{23}$ and $|\Delta m^2_{32}|$ region. Then, the covariance matrix for the oscillation analysis is defined as a function of the oscillation parameters ($\sin^2\theta_{23}$ and $|\Delta m^2_{32}|$), where the covariance matrix generated assuming oscillation parameters which are the closest to the input oscillation parameters is chosen among 201×201 sets of covariance matrices.

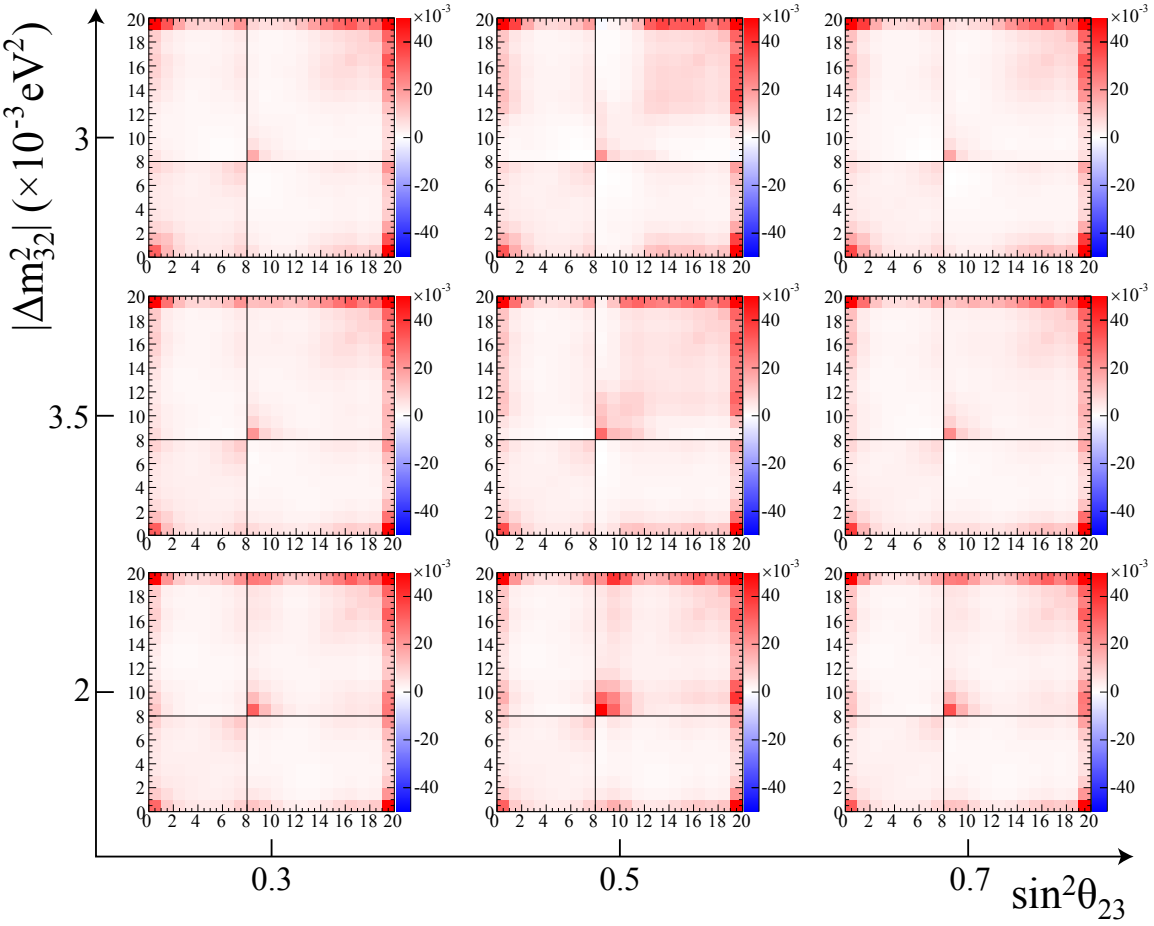

Figure 10.15: Covariance matrices for the oscillation parameters at the edges and the center of the $\sin^2\theta_{23}$ and $|\Delta m^2_{32}|$ region. First to eighth bins are for ν_e candidate events, and ninth to twentieth bins are for ν_μ candidate events.

10.7.4 Systematic error implementation with the covariance matrix

We assign a nuisance parameter, f_i $(1 \leq i \leq 20)$, to each reconstructed energy bin of the covariance matrix. It scales the number of events in the reconstructed energy bin by a factor of $(1 + f_i)$. They are included as nuisance parameters in the oscillation analysis fit. A penalized likelihood which constrains the nuisance parameters is given by using the covariance matrix as:

$$\mathcal{L}_{\rm cov}(\boldsymbol{o}, f_1, \cdots, f_{20}) = \prod_{i=1}^{20}\prod_{j=1}^{20} \exp\left(-\frac{f_i (V(\boldsymbol{o})^{-1})_{i,j} f_j}{2}\right), \tag{10.10}$$

where the covariance matrix is a function of the oscillation parameters. We can simply and accurately treat the systematic errors by including the scaling and the penalty term in the oscillation analysis fit.

10.7.5 Super-K energy scale error implementation

The Super-K energy scale error is treated separately from the systematic error covariance matrix. This is because the covariance matrix method cannot properly take into account the migration of events between reconstructed energy bins which may be caused by this error. In addition, the migration of events between merged bins in the covariance matrix is also unable to be treated. Thus, a systematic error nuisance parameter for the energy scale error, $f_{\rm ES}$, is introduced, which allows the mean energy of each reconstructed energy bin ($E_{\rm rec}$) to vary as:

$$E_{\rm rec} \rightarrow (1 + f_{\rm ES}) E_{\rm rec}. \tag{10.11}$$

The bin content is then modified for each reconstructed energy bin assuming that the content is flat across each bin. A graphical representation of this implementation is given in Fig. 10.16. The Super-K energy scale nuisance parameter is constrained by the total Super-K energy scale error size (2.4%) by multiplying an additional penalized likelihood

$$\mathcal{L}_{\rm ES}(f_{\rm ES}) = \exp\left(-\frac{f_{\rm ES}^2}{2 \times 0.024^2}\right) \tag{10.12}$$

to the likelihood function.

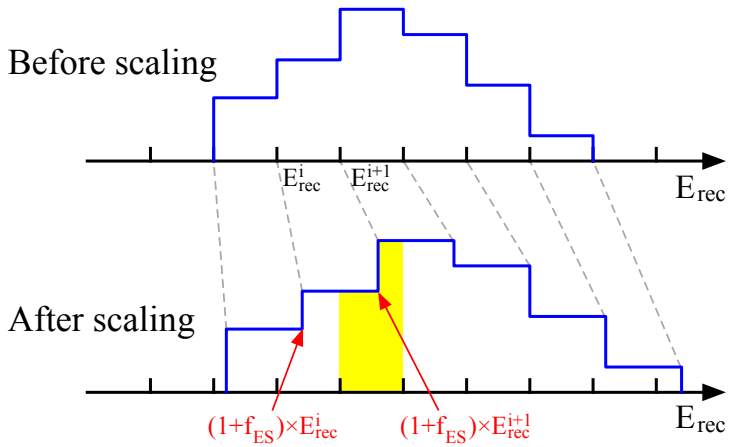

Figure 10.16: An illustration of the implementation of the Super-K energy scale error.

10.7.6 Spectral function error implementation

The spectral function parameter, $f_{\rm SF}$, is introduced to take into account the difference in the nuclear model between the relativistic Fermi gas model and the spectral function, and is truncated between zero and one as described in Chapter 4. However, the systematic error covariance matrix method by definition can handle only errors which are fully Gaussian. Therefore, the spectral function parameter is also treated as the systematic error nuisance parameter separately from the systematic error covariance matrix. The nuisance parameter is constrained by a Gaussian and is limited between zero and one, where the penalized likelihood is given by

$$\mathcal{L}_{\rm SF}(f_{\rm SF}) = \exp\left(-\frac{f_{\rm SF}^2}{2}\right), \ (0 \leq f_{\rm SF} \leq 1). \tag{10.13}$$

10.7.7 Summary of the systematic error treatment

In total, 22 nuisance parameters, $\boldsymbol{f} = (f_1, \cdots, f_{20}, f_{\rm ES}, \ f_{\rm SF})$, are included in the oscillation analysis fit. The systematic error term in Eq. 10.3 is given by the product of the three penalized likelihoods:

$$\mathcal{L}_{\rm syst}(\boldsymbol{o}, \boldsymbol{f}) = \mathcal{L}_{\rm cov}(\boldsymbol{o}, f_1, \cdots, f_{20}) \times \mathcal{L}_{\rm ES}(f_{\rm ES}) \times \mathcal{L}_{\rm SF}(f_{\rm SF}). \tag{10.14}$$

Owing to the simple treatment of the systematic errors, the CPU time for the neutrino oscillation analysis fit is reduced to about one-tenth of that with the original error treatment.

10.7.8 Systematic errors on the number of events at Super-K

After implementing all the systematic uncertainties, we studied their effects on the predicted number of events at Super-K. The total systematic uncertainties on the numbers of ν_e and ν_μ candidate events with (without) the ND280 constraint are 6.80% and 7.68% (26.85% and 24.17%), respectively. The systematic uncertainties on the predicted reconstructed energy spectra are shown in Fig. 10.17. They show that the ND280 constraint significantly reduces the systematic uncertainties. The systematic uncertainties from individual error sources are summarized in Table 10.7. Although the systematic uncertainties from the neutrino flux alone are large even with the ND280 constraint, their contributions to the total systematic uncertainties are actually small because great parts of them are cancelled out with the systematic uncertainties from the neutrino interaction parameters. Currently, the contributions of the neutrino interaction uncertainties (especially the π-less Δ decay uncertainty) are the largest.

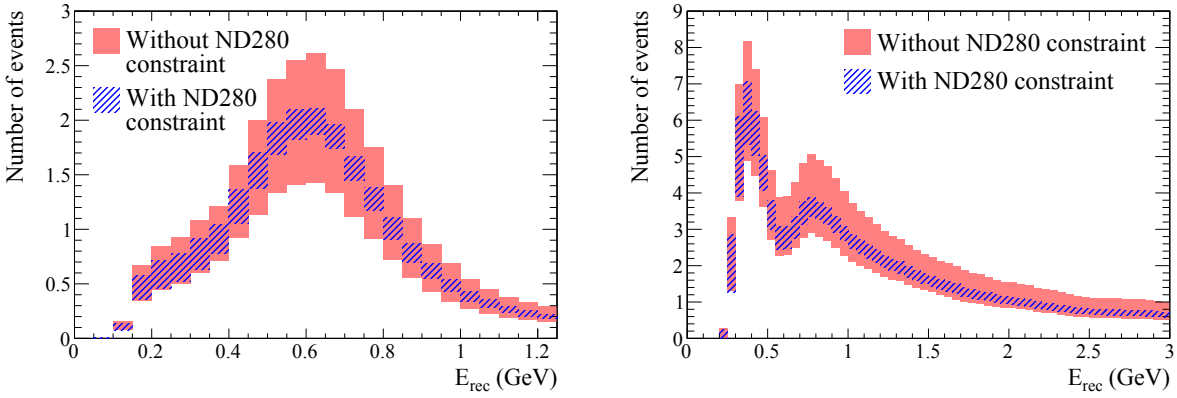

Figure 10.17: Systematic uncertainties on the predicted reconstructed energy spectra for the ν_e candidate events (left) and ν_μ candidate events (right) with and without the ND280 constraint. The nominal oscillation parameters are assumed.

Table 10.7: Systematic uncertainties on the predicted number of ν_e candidate events and ν_μ candidate events due to each individual error source with (without) the ND280 constraint. The nominal oscillation parameters are assumed. Dashes (–) denote that contributions from the error sources are skipped because they are negligibly small.

Source		ν_e candidate event		ν_μ candidate event	
Correlated with ND280	Neutrino flux	3.32% (26.19%)	7.51% (11.48%)	3.19% (23.14%)	7.23% (15.91%)
	M_A^{QE}		3.10% (20.05%)		2.79% (17.09%)
	M_A^{RES}		1.06% (3.51%)		2.33% (7.53%)
	CCQE normalization (E_ν <1.5 GeV)		6.24% (8.99%)		3.34% (4.81%)
	CCQE normalization (1.5< E_ν <3.5 GeV)		0.00% (0.01%)		1.61% (4.67%)
	CCQE normalization (E_ν >3.5 GeV)		0.00% (0.00%)		0.54% (1.42%)
	CC1π normalization (E_ν <2.5 GeV)		2.04% (4.02%)		1.98% (3.90%)
	CC1π normalization (E_ν >2.5 GeV)		0.01% (0.03%)		1.56% (3.68%)
	NC1π^0 normalization		0.43% (0.58%)		–
Uncorrelated interactions	CC coherent π normalization	4.83%	0.24%	4.88%	0.93%
	CC other E_ν shape		0.10%		0.88%
	NC1$\pi^\pm$ normalization		–		0.76%
	NC coherent π normalization		0.24%		–
	NC other normalization		0.50%		0.85%
	W shape		0.23%		0.26%
	π-less Δ decay		3.69%		4.39%
	Spectral function		1.09%		0.26%
	Fermi momentum		0.09%		0.13%
	ν_e normalization		2.84%		0.01%
	$\bar{\nu}$ normalization		–		1.19%
Super-K	Super-K detection efficiency	3.45%	2.42%	5.00%	4.02%
	Super-K energy scale		0.49%		0.00%
	Photo nuclear effect		0.78%		–
	Pion interaction		2.28%		2.98%
Total			6.80% (26.85%)		7.68% (24.17%)

10.8 Results

10.8.1 Results without prior constraints on oscillation parameters

First, we present the results of the oscillation analysis without constraining any of θ_{13}, θ_{23}, Δm^2_{32} or δ_{CP} prior to the fit. Figure 10.18 shows the reconstructed neutrino energy spectra for ν_e and ν_μ candidate events at Super-K. The observed spectra agree well with the best-fit MC expectations. The best fit points, as well as the 1D 1σ and 90% C.L. limits on the oscillation parameters assuming either mass hierarchy are given in Tables 10.8 and 10.9. The 90% C.L. contours for δ_{CP} vs $\sin^2 2\theta_{13}$ plane and Δm^2_{32} (Δm^2_{13}) vs $\sin^2\theta_{23}$ plane are given in Figs. 10.19 and 10.20 respectively [346]. The difference of χ^2 values between the best fit and $\theta_{13} = 0$ is 54. It is equivalent to an exclusion significance of 7.3σ. Therefore, we observed the $\nu_\mu \to \nu_e$ oscillation via the finite θ_{13} with more than 5σ significance[††]. In addition, our measurement of $\sin^2 2\theta_{13}$ via $\nu_\mu \to \nu_e$ oscillation is compatible with that via the disappearance of anti-electron neutrinos from reactors in short baseline. It demonstrates the consistency of the three-flavor

[††]T2K's $\nu_\mu \to \nu_e$ observation is the first discovery of the neutrino appearance signal with more than 5σ significance although there are indications with less than 5σ significance by other experiments [347, 348].

neutrino oscillation scheme of the PMNS framework. Meanwhile, our measurement of $\sin^2\theta_{23}$ is consistent with the maximal mixing[‡‡] as with the results from the Super-K atmospheric neutrino data [349] and the MINOS experiment [350]. Our result is the world's most precise measurement of $\sin^2\theta_{23}$. On the other hand, we cannot give a significant constraint on δ_{CP} only from the T2K data. Moreover, difference of minimum χ^2 assuming the normal and inverted hierarchies ($\chi^2_{\mathrm{min,NH}}$ and $\chi^2_{\mathrm{min,IH}}$) is

$$\chi^2_{\mathrm{min,NH}} - \chi^2_{\mathrm{min,IH}} = 0.001. \tag{10.15}$$

The T2K data does not favor either mass hierarchy because the difference of the minimum χ^2 is marginal.

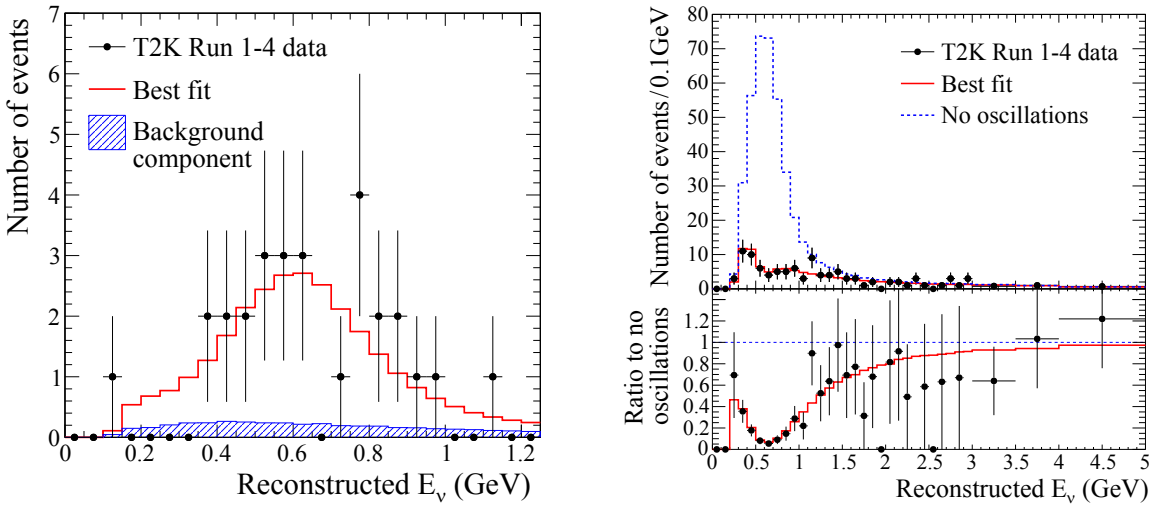

Figure 10.18: Reconstructed neutrino energy spectra for ν_e candidate events (left) and ν_μ candidate events (right) at Super-K with the MC best fit spectra. The ratio of the ν_μ spectrum to the no oscillation hypothesis is also shown.

Table 10.8: Results of four dimensional fitting for the T2K Run 1-4 data assuming the normal mass hierarchy.

	Best fit	-1σ	$+1\sigma$	-90%	$+90\%$
$\sin^2 2\theta_{13}$	0.1646	0.0917	0.2085	0.0723	0.2429
$\sin^2\theta_{23}$	0.5243	0.4663	0.5819	0.4356	0.6086
$\Delta m^2_{32}(\times 10^{-3}\mathrm{eV}^2)$	2.5010	2.3887	2.6064	2.3162	2.6726
δ_{CP}	1.75	–	–	–	–

Table 10.9: Results of four dimensional fitting for the T2K Run 1-4 data assuming the inverted mass hierarchy.

	Best fit	-1σ	$+1\sigma$	-90%	$+90\%$
$\sin^2 2\theta_{13}$	0.1909	0.1065	0.2472	0.0857	0.2852
$\sin^2\theta_{23}$	0.5238	0.4669	0.5821	0.4358	0.6090
$\Delta m^2_{13}(\times 10^{-3}\mathrm{eV}^2)$	2.4778	2.3698	2.5917	2.2964	2.6594
δ_{CP}	1.13	–	–	–	–

[‡‡]Minor deviation of the best fit value of $\sin^2\theta_{23}$ from 0.5 is due to the secondary term of the $\nu_\mu \to \nu_\mu$ oscillation probability formula (Eq. 1.11).

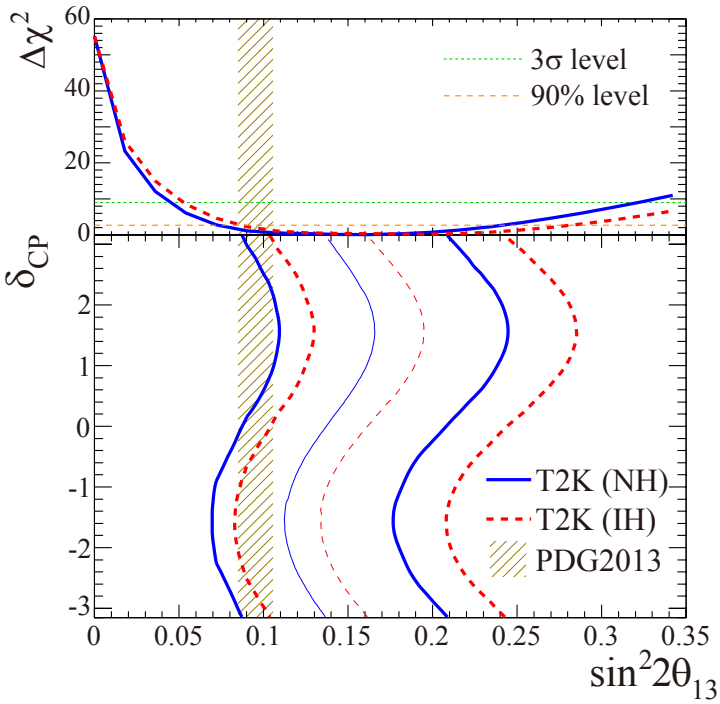

Figure 10.19: The 90% C.L. allowed regions for $\sin^2 2\theta_{13}$ and δ_{CP}. The central thin lines represent the best fit $\sin^2 2\theta_{13}$ value for given δ_{CP} values. The average value and error of $\sin^2 2\theta_{13}$ measured by the reactor experiments is taken from PDG2013 [36] for comparison. The 1D χ^2 profile for $\sin^2 2\theta_{13}$ is also shown at the top.

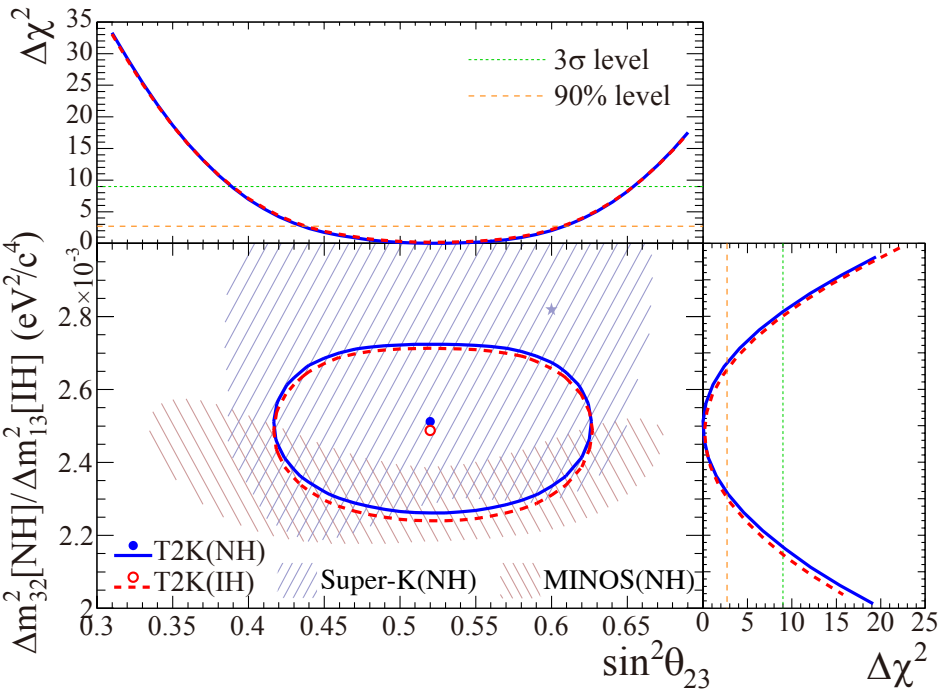

Figure 10.20: The 90% C.L. allowed regions and best-fit points for $\sin^2\theta_{23}$ and Δm^2_{32} (NH) or Δm^2_{13}(IH). The Super-K [349] and MINOS [350] 90% C.L. allowed regions for NH are shown for comparison. The Super-K result is derived from the atmospheric neutrino data, and the MINOS result is derived from the combination of the accelerator and atmospheric neutrino data. The 1D χ^2 profile for each oscillation parameter is also shown at the top and right.

10.8.2 Results with reactor θ_{13} constraint

Currently, $\sin^2 2\theta_{13}$ was precisely measured via the disappearance of anti-electron neutrinos from reactors in short baseline [49–51] as described in Chapter 1. The global value and error of $\sin^2 2\theta_{13}$ in PDG2013 [36] are 0.095 and 0.01, respectively. We add the constraint on $\sin^2 2\theta_{13}$ to measure $\sin^2\theta_{23}$ and Δm^2_{32} more precisely and to give a significant constraint on δ_{CP}. In order to include the reactor constraint on $\sin^2 2\theta_{13}$, an additional likelihood ($\mathcal{L}_{\rm react}$) is introduced to Eq. 10.3:

$$\begin{aligned}\mathcal{L}(\boldsymbol{N^{obs}_{\nu_e}}, \boldsymbol{N^{obs}_{\nu_\mu}}, \boldsymbol{o}, \boldsymbol{f}) &= \mathcal{L}_{\nu_e}(\boldsymbol{N^{obs}_{\nu_e}}, \boldsymbol{o}, \boldsymbol{f}) \times \mathcal{L}_{\nu_\mu}(\boldsymbol{N^{obs}_{\nu_\mu}}, \boldsymbol{o}, \boldsymbol{f}) \\ &\times \mathcal{L}_{\rm syst}(\boldsymbol{o}, \boldsymbol{f}) \times \mathcal{L}_{\rm react}(\theta_{13}), \qquad (10.16)\\ \mathcal{L}_{\rm react}(\theta_{13}) &= \exp\left(-\frac{(\sin^2 2\theta_{13} - 0.095)^2}{2\times 0.01^2}\right). \qquad (10.17)\end{aligned}$$

The best fit points, as well as the 1D 1σ and 90% C.L. limits on the oscillation parameters with the reactor constraint assuming either mass hierarchy are given in Tables 10.10 and 10.11. The 90% C.L. contours for δ_{CP} vs $\sin^2 2\theta_{13}$ plane and Δm^2_{32} (Δm^2_{13}) vs $\sin^2\theta_{23}$ plane with the reactor constraint are given in Figs. 10.21 and 10.22 respectively [346].

Table 10.10: Results of four dimensional fitting for the T2K Run 1-4 data with the θ_{13} constraint by the reactor experiments assuming the normal mass hierarchy.

	Best fit	-1σ	$+1\sigma$	-90%	$+90\%$
$\sin^2 2\theta_{13}$	0.0968	0.0877	0.1062	0.0816	0.1125
$\sin^2\theta_{23}$	0.5277	0.4685	0.5783	0.4397	0.6033
$\Delta m^2_{32}(\times 10^{-3}\mathrm{eV}^2)$	2.4990	2.3965	2.5998	2.3283	2.6672
δ_{CP}	-1.50	-2.98	-0.05	2.32	0.84

Table 10.11: Results of four dimensional fitting for the T2K Run 1-4 data with the θ_{13} constraint by the reactor experiments assuming the inverted mass hierarchy.

	Best fit	-1σ	$+1\sigma$	-90%	$+90\%$
$\sin^2 2\theta_{13}$	0.0985	0.0891	0.1079	0.0833	0.1140
$\sin^2\theta_{23}$	0.5352	0.4762	0.5812	0.4451	0.6048
$\Delta m^2_{13}(\times 10^{-3}\mathrm{eV}^2)$	2.4834	2.3795	2.5861	2.3112	2.6519
δ_{CP}	-1.62	-2.75	-0.45	2.85	0.28

The precisions on the measurements on Δm^2_{32} (Δm^2_{13}) and $\sin^2\theta_{23}$ become a little better by adding the reactor constraint. Difference of minimum χ^2 assuming the normal and inverted hierarchies is

$$\chi^2_{\rm min,NH} - \chi^2_{\rm min,IH} = -1.17. \qquad (10.18)$$

It means that the T2K data with the reactor constraint favors the normal hierarchy with a significance of 1.1σ. However, it is still too marginal to conclude. On the other hand, it becomes possible to give a significant constraint on δ_{CP}. The best fit value of δ_{CP} is close to $-\pi/2$*.

*Minor deviation of the best fit value of δ_{CP} from $-\pi/2$ is due to the solar term of the $\nu_\mu \to \nu_e$ oscillation probability formula (Eq. 1.17).

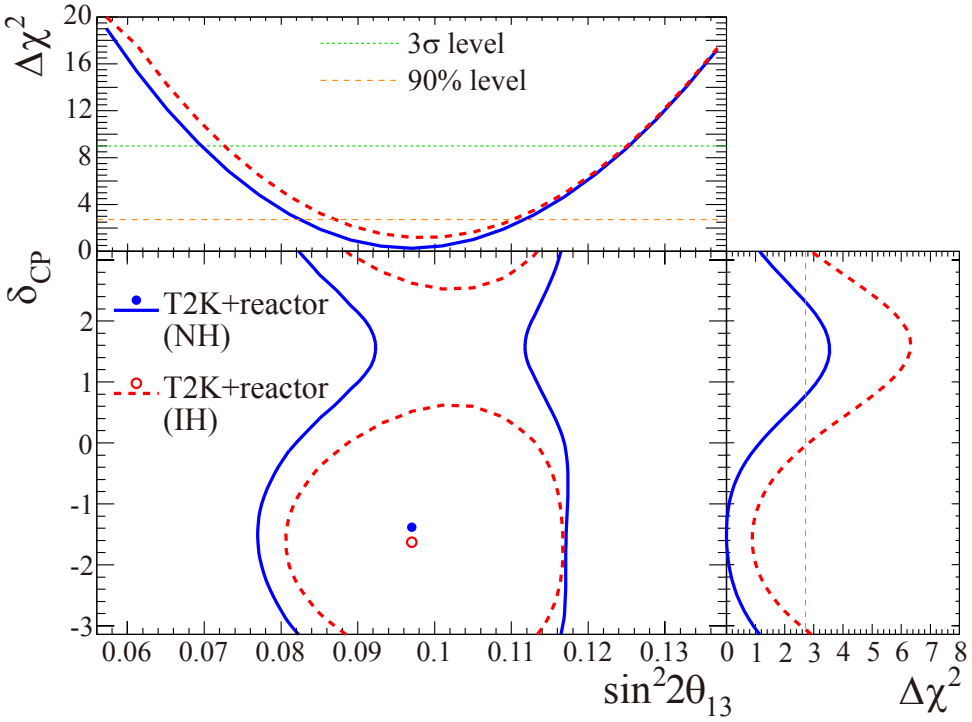

Figure 10.21: The 90% C.L. allowed regions and best-fit points for $\sin^2 2\theta_{13}$ and δ_{CP} with the reactor θ_{13} constraint. The 1D χ^2 profile for each oscillation parameter is also shown at the top and right.

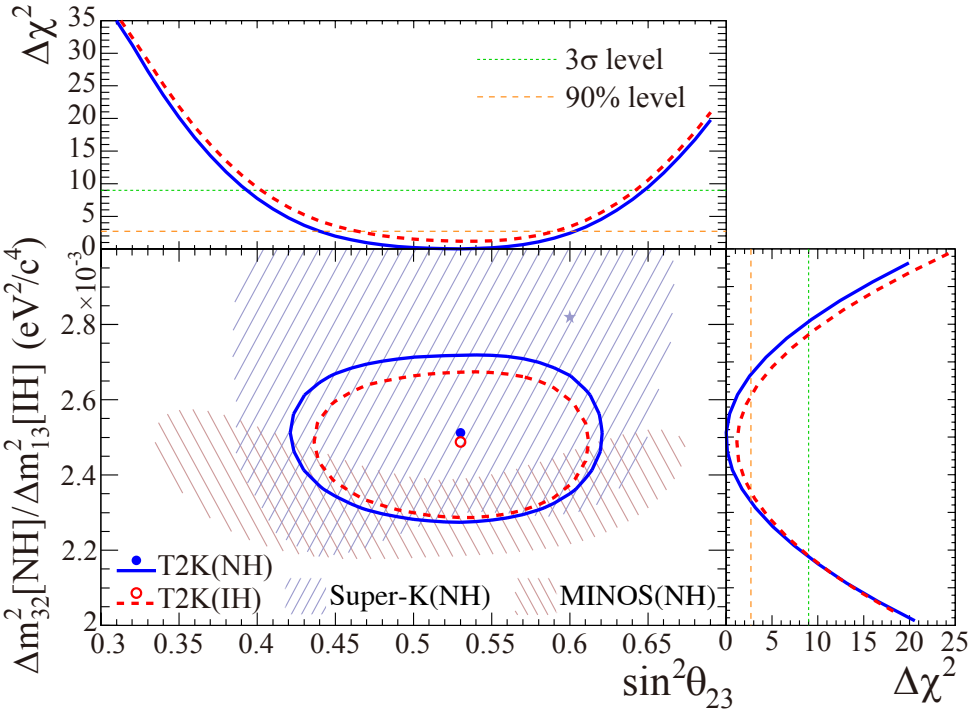

Figure 10.22: The 90% C.L. allowed regions and best-fit points for $\sin^2\theta_{23}$ and Δm^2_{32} (NH) or Δm^2_{13}(IH) with reactor θ_{13} constraint. The Super-K [349] and MINOS [350] 90% C.L. allowed regions for NH are shown for comparison. The 1D χ^2 profile for each oscillation parameter separately is also shown at the top and right.

For the estimation of the allowed region around a physical boundary, the constant $\Delta\chi^2$ limit is not strictly accurate because this method is fully based on the Gaussian approximation. In order to evaluate the accurate critical $\Delta\chi^2$ limit, the Feldman-Cousins method [351] is used. Since the value of the critical $\Delta\chi^2$ limit depends on the value of δ_{CP} and the mass hierarchy, it is estimated at 20 discrete values of δ_{CP} in both mass hierarchy cases. For example, the value of the critical $\Delta\chi^2$ limit at $\delta_{CP} = x$ in the normal mass hierarchy case is derived in the following way:

1. Generate 10,000 toy MC experiments assuming $\delta_{CP} = x$ and the normal hierarchy. The systematic error nuisance parameters, $\sin^2 2\theta_{13}$, $\sin^2\theta_{23}$, and Δm^2_{32} are thrown according to the probability density functions for them. The probability density function for $\sin^2 2\theta_{13}$, $\sin^2\theta_{23}$, and Δm^2_{32} is based on the 3D $\Delta\chi^2$ map of T2K Run 1-4 data joint fit with the PDG 2013 reactor constraint shown in Fig. 10.23.

2. Fit each toy MC experiment assuming both normal and inverted hierarchies, and calculate the χ^2 as
$$\Delta\chi^2 = \chi^2_{\text{true}} - \chi^2_{\text{min}}, \tag{10.19}$$
where χ^2_{true} is the value of χ^2 minimized for δ_{CP} fixed at $\delta_{CP} = x$ and the normal hierarchy, and χ^2_{min} is the global minimum value of χ^2 from the normal and inverted hierarchies when all oscillation parameters are fit.

3. Calculate the critical $\Delta\chi^2$ limit for 90% C.L. ($\Delta\chi^2_{\text{crit}}$), such that 90% of toy MC experiments have $\Delta\chi^2 < \Delta\chi^2_{\text{crit}}$ (Fig. 10.24).

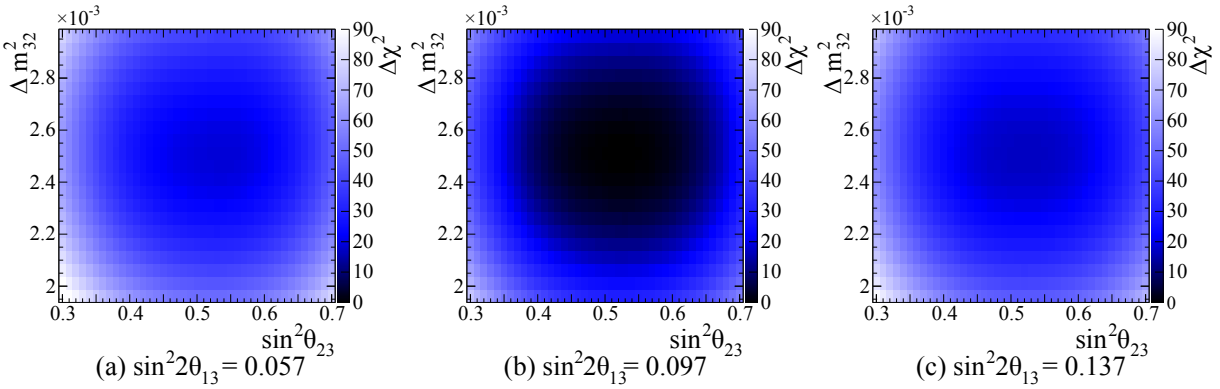

Figure 10.23: The $\Delta\chi^2$ contour as a function of $\sin^2 2\theta_{13}$, $\sin^2\theta_{23}$, and Δm^2_{32} in the normal hierarchy case calculated from the T2K Run 1-4 data joint fit with the reactor constraint.

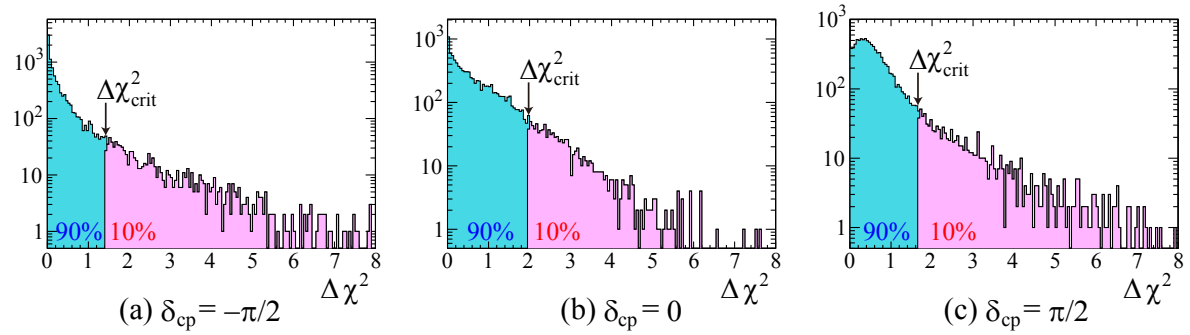

Figure 10.24: The $\Delta\chi^2$ distribution at (a) $\delta_{CP} = -\pi/2$, (b) $\delta_{CP} = 0$, and (c) $\delta_{CP} = \pi/2$ in the normal hierarchy case for 10,000 toy MC experiments.

Figure 10.25 shows the critical $\Delta\chi^2$ limits evaluated by the Feldman-Cousins method drawn on top of the $\Delta\chi^2$ curve for δ_{CP} for T2K Run 1-4 data with the reactor constraint. The 90% C.L. allowed regions of δ_{CP} are defined as the regions where the $\Delta\chi^2$ curve is lower than the critical $\Delta\chi^2$ limits, which are summarized in Table 10.12. Constraint on δ_{CP} is also given by the recent results of MINOS [352] and the Super-K atmospheric neutrino measurement [349]. However, our constraint is the strongest. Although it is still weak to claim a discovery of non-zero $\sin\delta_{CP}$, this result is an important step towards the discovery of CP violation in the lepton sector.

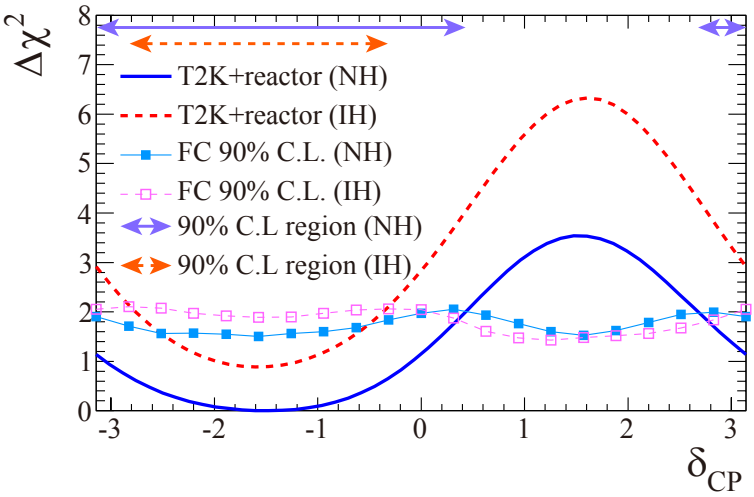

Figure 10.25: The $\Delta\chi^2$ as a function of δ_{CP} with the critical $\Delta\chi^2$ 90% C.L. limit extracted by using the Feldman-Cousins method.

Table 10.12: The 90% C.L. allowed regions of δ_{CP} extracted using the Feldman-Cousins method.

	Best fit point	90% C.L. allowed region
Normal hierarchy	-1.51 (-0.48π)	$-3.59 \sim 0.43$ $(-1.14\pi \sim 0.14\pi)$
Inverted hierarchy	-1.57 (-0.50π)	$-2.84 \sim -0.32$ $(-0.90\pi \sim -0.10\pi)$

10.9 Considerations

10.9.1 Three-flavor joint neutrino oscillation analysis

We simultaneously determined the four oscillation parameters ($\sin^2 2\theta_{13}$, $\sin^2\theta_{23}$, $|\Delta m^2_{32}|$ and δ_{CP}) for the first time by the joint fit to the ν_e and ν_μ candidate samples. This joint analysis treats the correlations among the oscillation parameters and systematic errors in the optimal way. In addition, the measurement precision with this joint analysis was found to be better than that with the stand-alone oscillation analyses as described in Appendix H because the systematic errors from the uncertainties of other oscillation parameters are suppressed in the joint fit procedure. Therefore, it will be a standard approach for the future neutrino oscillation measurement.

This analysis technique will be applicable to the neutrino cross section analysis. In this thesis, the cross section analysis for each neutrino interaction type was performed separately. However, if a simultaneous cross section analysis fit is performed to the enriched samples of various neutrino interaction types, cross sections for these interaction types can be determined simultaneously. In the exclusive cross section analyses in this thesis (the CCQE and CC coherent

pion analyses), systematic errors from the uncertainties of background interaction events are large. In the simultaneous cross section analysis, they can be suppressed in the fit procedure, and the precision of the cross section measurement is expected to be improved.

10.9.2 New method of the systematic error treatment

Although the treatment of the systematic errors in T2K had been very complicated, we succeed in simplifying it. It reduced the CPU time for the neutrino oscillation analysis fit to about one-tenth of that with the original error treatment. For example, a neutrino oscillation analysis with original error treatment requires more than two weeks for the Feldman-Cousins method when 500 CPUs are used. On the one hand, our analysis requires less than two days under the same conditions by virtue of the simple treatment of the systematic errors. Thus, from the next year's beam operation, we will be able to get the result of the neutrino oscillation analysis immediately after the data taking by using our method of the error treatment.

In 2014, T2K started to take the antineutrino beam data by inverting the horn current polarity because a combination of the neutrino beam data and the antineutrino beam data has better sensitivity to δ_{CP} as described in Chapter 1. After taking more antineutrino beam data, a combined neutrino oscillation analysis with the neutrino and antineutrino beam data will be performed in the near future. However, it will require further long CPU time because it needs to use almost twice the number of the systematic error parameters than the current neutrino oscillation analysis. Therefore, our method of the error treatment will be very helpful for this combined analysis and may be an essential method in the near future.

10.9.3 Matter-antimatter asymmetry in the universe

As described in Chapter 1, the CP violation found in the quark sector [65–67] is too small to explain the observed matter-antimatter asymmetry in the universe [68, 69]. A model suggests that if $|\sin\theta_{13}\sin\delta_{CP}| > 0.11$ and the mass hierarchy is normal, the CP violation in neutrino can explain the matter-antimatter asymmetry [353,354]. The T2K neutrino oscillation measurement favors the normal hierarchy and $|\sin\theta_{13}\sin\delta_{CP}| = 0.16$ as the best fit value although the precisions are not high enough to discuss the effect on the matter-antimatter asymmetry in the universe. However, if similar results are achieved with much higher precision, we may be able to give an explanation of the matter-antimatter asymmetry.

10.9.4 Future prospects of neutrino oscillation measurement

Although we achieved the world's highest precision in the measurement of δ_{CP} and $\sin^2\theta_{23}$, more precise measurements are required in order to reveal whether $\sin\delta_{CP}$ is non-zero and whether θ_{23} is maximal mixing. Currently, the statistical error is predominant in the neutrino oscillation measurement in T2K. Thus, the most important task for T2K is to accumulate more beam data with increasing the beam power. When the T2K goal statistic (7.8×10^{21} POT) is achieved, the measurement precisions of $\sin^2 2\theta_{13}$, $\sin^2\theta_{23}$ and $|\Delta m^2_{32}|$ which are currently 0.06, 0.06 and $1.1 \times 10^{-4}\text{eV}^2$ are expected to be improved to 0.04, 0.03 and $0.4 \times 10^{-4}\text{eV}^2$ assuming the same systematic error size. In addition, we are expected to be able to indicate the non-zero $\sin\delta_{CP}$ with 90% C.L. if true δ_{CP} is $-\pi/2$ and the true mass hierarchy is normal. To achieve even better precisions, the uncertainties of the systematic error sources should be reduced. Especially, the reduction of the neutrino interaction uncertainties is the most important because the systematic error from these uncertainties is the largest at present as shown in Table 10.7. The uncertainties on CCQE and CC coherent pion cross sections which are currently 30% and 100% can be reduced to 15% and 60% on the ground of the cross section results from INGRID as presented in Chapters 8 and 9 although model revisions are needed as for the CC coherent pion production.

In addition, our result of the CC inclusive cross section ratio on different targets may be a trigger to improve the uncorrelated treatment of the neutrino interaction uncertainties between ND280 and Super-K as described in Chapter 7. In the future, more precise and various neutrino cross section measurements are required in order to reduce further the neutrino interaction uncertainties. In the near future, many neutrino cross section measurements will be performed in T2K because we have established a strong basis of the neutrino cross section measurement.

In 2014, the NOνA experiment [72] started the beam operation. Since T2K and NOνA have complementary nature, we can give stronger constraints on the oscillation parameters and the mass hierarchy by combining the neutrino oscillation measurements of the two experiments. Ultimately, the combination of T2K and NOνA is expected to be able to indicate the non-zero $\sin\delta_{CP}$ with 2.5σ level and the normal hierarchy with 3.5σ level if true δ_{CP} is $-\pi/2$ and the true mass hierarchy is normal. The expected future sensitivities of the T2K experiment and the combination of T2K and NOνA are discussed in detail in Appendix H. In addition, a next generation neutrino oscillation experiment using a larger water Cherenkov detector, "Hyper-Kamiokande" [355], is being proposed. I hope these experiments reveal whether $\sin\delta_{CP}$ is non-zero, whether θ_{23} is maximal mixing, and the mass hierarchy in the near future.

Chapter 11

Conclusions

In this thesis, we reported the measurement of the neutrino interaction cross sections and neutrino oscillation parameters in the T2K experiment.

Since T2K adopts the off-axis beam configuration, in which the neutrino beam intensity and energy spectrum are sensitive to the neutrino beam direction, the neutrino beam direction has to be controlled within 1 mrad and be measured with a much better precision. Thus, we precisely measured the neutrino beam direction using the INGRID detector. The average horizontal and vertical beam directions relative to the nominal directions were measured as

$$\begin{aligned} \bar{\theta}_X^{\text{beam}} &= 0.030 \pm 0.011(stat.) \pm 0.095(syst.) \text{ mrad}, \\ \bar{\theta}_Y^{\text{beam}} &= 0.011 \pm 0.012(stat.) \pm 0.105(syst.) \text{ mrad}, \end{aligned}$$

respectively. This result reduced the neutrino flux uncertainty from the neutrino beam direction which was originally 7.0% at 1 GeV to 2.5%. In addition, the measured neutrino event rate and neutrino beam width are consistent with the predictions based on the T2K neutrino flux simulation. Moreover, all the neutrino beam properties were confirmed to be stable within the physics requirements. Therefore, the T2K beam data quality and the consistency of the neutrino flux prediction were assured.

In the neutrino oscillation measurement in T2K, uncertainties of the neutrino interaction are the dominant systematic error sources because the neutrino interaction in a few GeV region is poorly understood. Thus, we developed and constructed a new neutrino detector, the Proton Module, and measured the neutrino interaction cross section in a few GeV region. First, the CC inclusive cross section was measured from the number of CC interaction events in the INGRID standard module and the Proton Module whose target elements are dominated by iron and hydrocarbon respectively. The measured CC inclusive cross sections on iron and hydrocarbon and their cross section ratio are

$$\begin{aligned} \sigma_{\text{CC}}^{\text{Fe}} &= (1.444 \pm 0.002(stat.)^{+0.189}_{-0.157}(syst.)) \times 10^{-38}\text{cm}^2/\text{nucleon}, \\ \sigma_{\text{CC}}^{\text{CH}} &= (1.379 \pm 0.009(stat.)^{+0.178}_{-0.147}(syst.)) \times 10^{-38}\text{cm}^2/\text{nucleon}, \\ \sigma_{\text{CC}}^{\text{Fe}}/\sigma_{\text{CC}}^{\text{CH}} &= 1.047 \pm 0.007(stat.) \pm 0.035(syst.), \end{aligned}$$

at a mean neutrino energy of 1.51 GeV. They agree well with the predictions of neutrino interaction models. Since the neutrino cross section in a few GeV region is sensitive to the nuclear effect of the target material, this result demonstrates that the nuclear effect of iron and hydrocarbon targets is well understood and correctly treated in the models. Then, further event selections were applied to the CC interaction events in the Proton Module in order to enrich CCQE events and CC coherent pion events. From the enriched samples, the exclusive cross sections of these

interaction types were measured. The CCQE cross section on carbon was measured to be

$$\begin{aligned}\sigma_{\mathrm{CCQE}}(1.94\mathrm{GeV}) &= (11.95 \pm 0.19(stat.)^{+1.82}_{-1.47}(syst.)) \times 10^{-39}\mathrm{cm}^2/\mathrm{neutron},\\ \sigma_{\mathrm{CCQE}}(0.93\mathrm{GeV}) &= (10.64 \pm 0.37(stat.)^{+2.03}_{-1.65}(syst.)) \times 10^{-39}\mathrm{cm}^2/\mathrm{neutron},\end{aligned}$$

at mean neutrino energies of 1.94 GeV and 0.93 GeV, respectively. They are also compatible with the predictions of neutrino interaction models. In addition, we found that the CCQE cross section measurement is sensitive to the nuclear model and the existence of the multi-nucleon interaction at 10% level. The measured CC coherent pion production cross section on carbon is

$$\sigma_{\mathrm{CCcoh.}\pi} = (1.03 \pm 0.25(stat.)^{+0.66}_{-0.63}(syst.)) \times 10^{-39}\mathrm{cm}^2/\mathrm{nucleus},$$

and the 90% C.L. upper limit on the CC coherent pion production cross section is

$$\sigma_{\mathrm{CCcoh.}\pi} < 1.93 \times 10^{-39}\mathrm{cm}^2/\mathrm{nucleus},$$

at a mean neutrino energy of 1.51 GeV. Although the CC coherent pion production signal had never observed in this energy region, our signal significance corresponds to 1.7σ. However, the measured CC coherent pion production cross section is significantly smaller than the prediction of the original Rein-Sehgal model while it is consistent with the prediction of the Rein-Sehgal model with recent revisions. Therefore, we revealed that the original Rein-Sehgal model breaks down in a few GeV region and it needs the recent revisions. Since this inconsistency is within the originally assigned uncertainty, all the cross section results from INGRID demonstrate the validity of the neutrino interaction models and their uncertainties in T2K which had been evaluated only by a few external data. In addition, they provided helpful clues to the existing problems in the neutrino interaction physics.

Finally, we performed the three-flavor joint oscillation analysis of $\nu_\mu \to \nu_e$ and $\nu_\mu \to \nu_\mu$ using the neutrino flux prediction, the neutrino interaction models and the beam data in the near and far detectors (ND280 and Super-K). The ND280 measurement further constrained the uncertainties of the neutrino flux prediction and the neutrino interaction models. In Super-K, 28 ν_e candidate events and 120 ν_μ candidate events were observed. We performed a maximum likelihood to the energy spectra of the ν_e and ν_μ candidate events in Super-K in order to determine $\sin^2 2\theta_{13}$, $\sin^2\theta_{23}$, $|\Delta m^2_{32}|$ and δ_{CP} simultaneously. In addition, we sped up the neutrino oscillation analysis procedure by simplifying the treatment of the systematic errors using covariance matrices. As the result of the oscillation analysis, we obtained the value of $\sin^2 2\theta_{13}$ for the normal (inverted) mass hierarchy to be

$$\sin^2 2\theta_{13} = 0.165^{+0.044}_{-0.073} \quad (0.191^{+0.056}_{-0.084}).$$

We concluded that the electron neutrino appearance in a muon neutrino beam was observed because the appearance signal corresponds to a significance of 7.3σ. This result is compatible with the result of $\sin^2 2\theta_{13}$ measurements via the disappearance of anti-electron neutrinos from reactors in short baseline. It demonstrates the consistency of the three-flavor neutrino oscillation scheme of the PMNS framework. The values of $\sin^2\theta_{23}$ and Δm^2_{32} (Δm^2_{13}) for the normal (inverted) hierarchy were determined to be

$$\begin{aligned}\sin^2\theta_{23} &= 0.524 \pm 0.058 \quad (0.524^{+0.058}_{-0.057}),\\ \Delta m^2_{32} &= (2.50 \pm 0.11) \times 10^{-3}\mathrm{eV}^2 \quad (\Delta m^2_{13} = (2.48 \pm 0.11) \times 10^{-3}\mathrm{eV}^2).\end{aligned}$$

Measured $\sin^2\theta_{23}$ is consistent with the maximal mixing and is the most precise in the world. Furthermore, when the T2K result was combined with the result of θ_{13} measurements by reactor experiments, 90% C.L allowed region for δ_{CP} was obtained to be

$$-3.59 < \delta_{CP} < 0.43 \quad (-2.84 < \delta_{CP} < -0.32),$$

for the normal (inverted) hierarchy. Although it is still weak to claim the discovery of non-zero $\sin\delta_{CP}$, it is the world strongest constraint on δ_{CP}.

Appendix A

Development and Construction of Proton Module

The basic idea of the Proton Module was proposed in 2008. Then, we started to develop it in 2009 and constructed it in 2010. The development and the construction of the Proton Module are introduced here.

A.1 Performance measurement of detector components

Performances of detector components were measured before the detector designing.

A.1.1 Light yield of scintillators

For the high detection efficiency and the high ability of the particle identification using dE/dx, light yield substantially more than 10 photoelectrons is required. The light yield of the INGRID-type and SciBar-type scintillators with WLS fiber-MPPC readout is measured with cosmic rays. Figure A.1 shows the typical light yield distributions. Average light yields for the INGRID-type and SciBar-type scintillators are 28.70 and 57.46 photoelectrons, which are substantially more than the requirement.

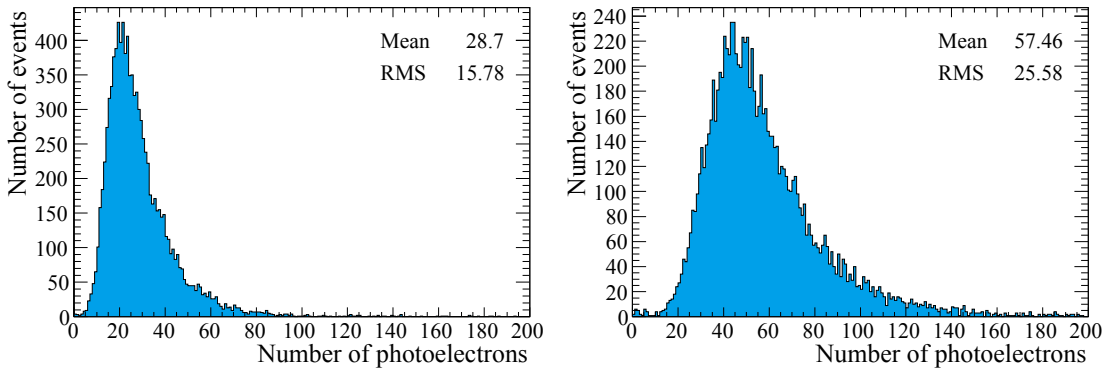

Figure A.1: Typical light yield distribution of an INGRID-type scintillator (left) and a SciBar-type scintillator (right) for cosmic rays.

A.1.2 Weights of scintillators

The weights of all scintillators for the Proton Module were measured in advance within a precision of 0.1g. The standard deviations of the weights for the INGRID-type and SciBar-type scintillators are 0.20% and 0.52%, respectively. The measured weights are used to calculate the number of nucleons, neutrons and nuclei as described in Appendix F, which are needed to calculate the neutrino interaction cross sections.

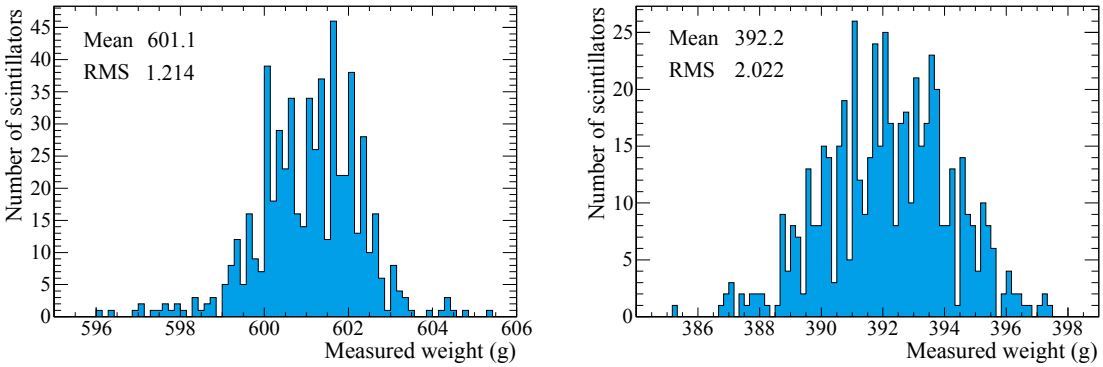

Figure A.2: Measured weights of INGRID-type scintillators (left) and the SciBar-type scintillators (right) for the Proton Module.

A.1.3 Basic characteristics of MPPCs

Basic characteristics of the all MPPCs for the Proton Module were measured in advance. Requirements to the basic characteristics are summarized in Table A.1.

Table A.1: Requirements to the basic characteristics of MPPCs.

Item	Requirement
Breakdown voltage	> 65V and < 70V
Gain	$> 5 \times 10^5$
Dark rate	< 1.5MHz
Crosstalk and afterpulse rate	< 0.3

Gain

Figure A.3 shows a typical ADC distribution of the MPPC dark counts in a channel. In the distribution, the pedestal peak and one photoelectron peak can be seen clearly. The pedestal peak and one photoelectron peak are fitted by the double Gaussian function. The MPPC gain is calculated from the difference of the peak position of the pedestal and that of one photoelectron.

Breakdown voltage

The MPPC gain depends linearly on the applied voltage. Thus, when we measure the gain as a function of the applied voltage, the breakdown voltage can be derived by linearly extrapolating the gain-voltage relation to the point where gain becomes zero as shown in Fig. A.4.

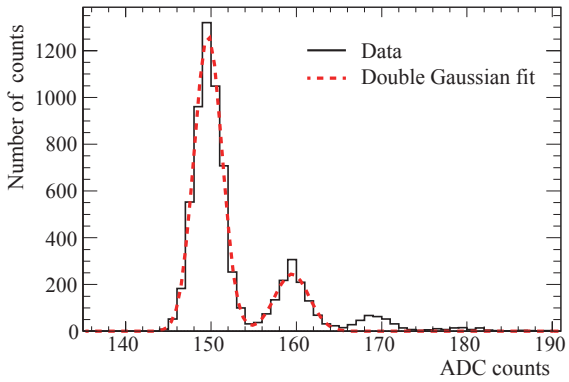

Figure A.3: Typical ADC distribution of MPPC dark counts with double Gaussian fitting.

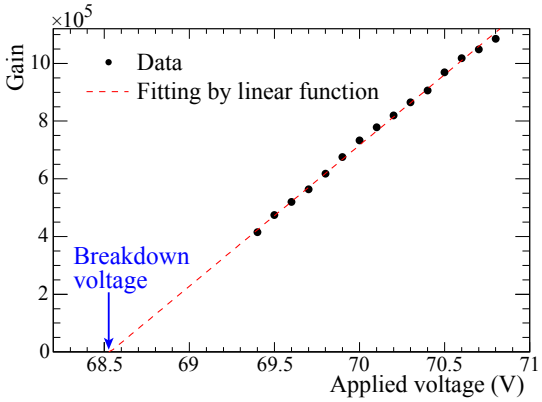

Figure A.4: Determination of breakdown voltage from gain-voltage extrapolation.

Dark rate

The dark rate is measured from the data without external light. In the absence of crosstalk and afterpulse, the number of detected photoelectrons follows the Poisson statistics. Thus, the dark rate is estimated from the number of pedestal events assuming the Poisson statistics as:

$$\begin{aligned} \text{Dark rate} &= \frac{\sum_{i=1}^{\infty} iN_i}{T_{\text{gate}} N_{\text{tot}}} \\ &= \frac{\lambda}{T_{\text{gate}}} \\ &= \frac{-\ln(N_0/N_{\text{tot}})}{T_{\text{gate}}}, \end{aligned} \tag{A.1}$$

where T_{gate} is the gate time width, N_i is the number of i photoelectron events, N_{tot} is the total number of events, and λ is the expected number of photoelectron.

Crosstalk and afterpulse rate

We are able to estimate the number of 1 photoelectron events, in the absence of crosstalk and afterpulse, from the fraction of pedestal events and Poisson statistics. Comparing this number with the observed number of events at 1 photoelectron peak and assuming the difference comes from the effects of crosstalk and afterpulse, we can estimate the rate of crosstalk and afterpulse as:

$$\begin{aligned} \text{Cross talk and after pulse rate} &= \frac{N_1^{\text{exp}} - N_1}{N_1^{\text{exp}}} \\ &= \frac{\lambda N_0 - N_1}{\lambda N_0} \\ &= \frac{-N_0 \ln(N_0/N_{\text{tot}}) - N_1}{-N_0 \ln(N_0/N_{\text{tot}})}, \end{aligned} \tag{A.2}$$

where N_1^{exp} is the expected number of 1 photoelectron events assuming the Poisson distribution.

Figure A.5 shows the results of the measurement. Basic characteristics of all the MPPCs fulfill the requirements.

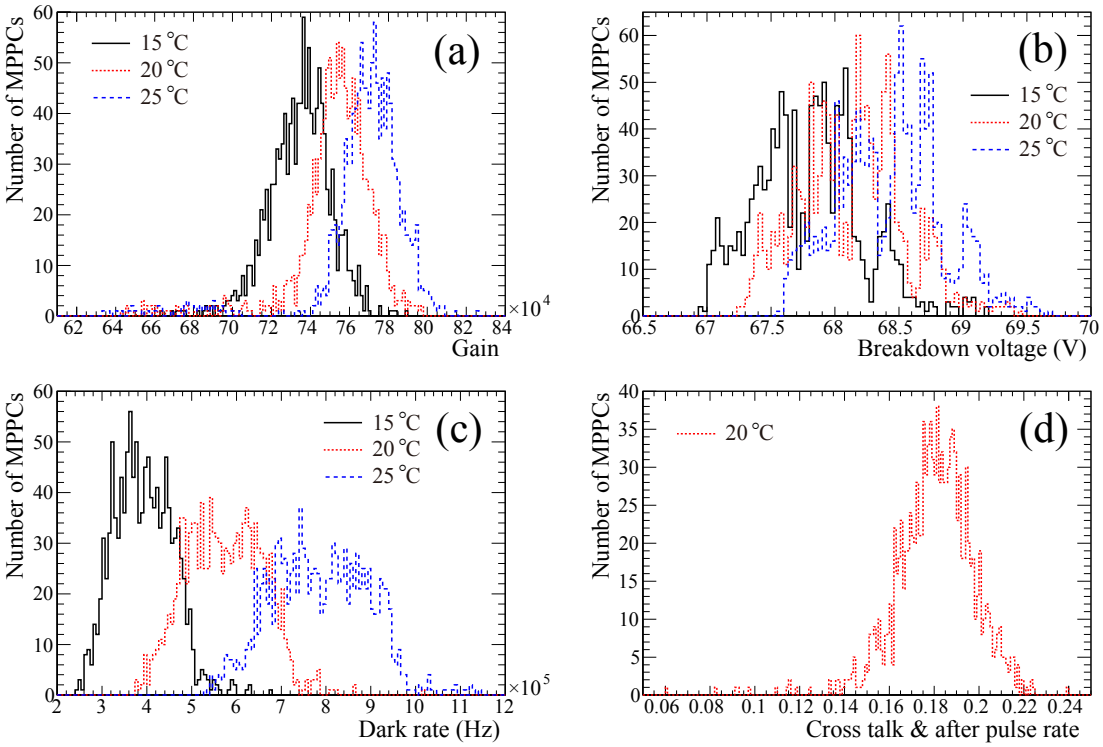

Figure A.5: Result of the measurements of the MPPC basic characteristics. (a) Gain, (b) breakdown voltage, (c) dark rate and (d) crosstalk and afterpulse rate.

A.2 Designing

A.2.1 Scintillator planes

The arrangement of the scintillators for the Proton Module was optimized with the MC simulation. For the cross section analysis with the Proton Module, the reconstruction efficiency of the second track in addition to a muon track (a proton track for CCQE and a pion track for CC coherent pion) is important. Thus, the optimization was performed to maximize the efficiency of detecting both a muon and a proton from CCQE interaction separately. As a result, SciBar-type scintillators were decided to be arranged in the inner region of the tracking planes and the distance between planes was decided to be 23mm. The veto plane was designed to be large enough to surround the tracking planes. Figure A.6 shows the schematic drawings of the tracking planes and the veto plane.

A.2.2 Support structure

The scintillators for the tracking planes of the standard modules are fixed by glues. However, if those for the Proton Module are fixed by glues, they become dead materials which are not sensitive to the energy deposit by charged particles. In addition, neutrino interactions on the glues must be taken into account*. Therefore, the scintillators for the Proton Module are fixed in a different way. We developed a dedicated frame (Fig. A.7 (a)) for the scintillator fixation. There are holes for the readout on the top and right side surfaces of the frame seen from the upstream. Grooved plates (Fig. A.7 (b)) were installed on the inside walls of the frame. Scintillators are fixed by being mounted on the grooves of the plates as shown in Fig. A.7 (c).

*In case of the standard module, ratio of the glues is vanishingly small relative to the iron plates.

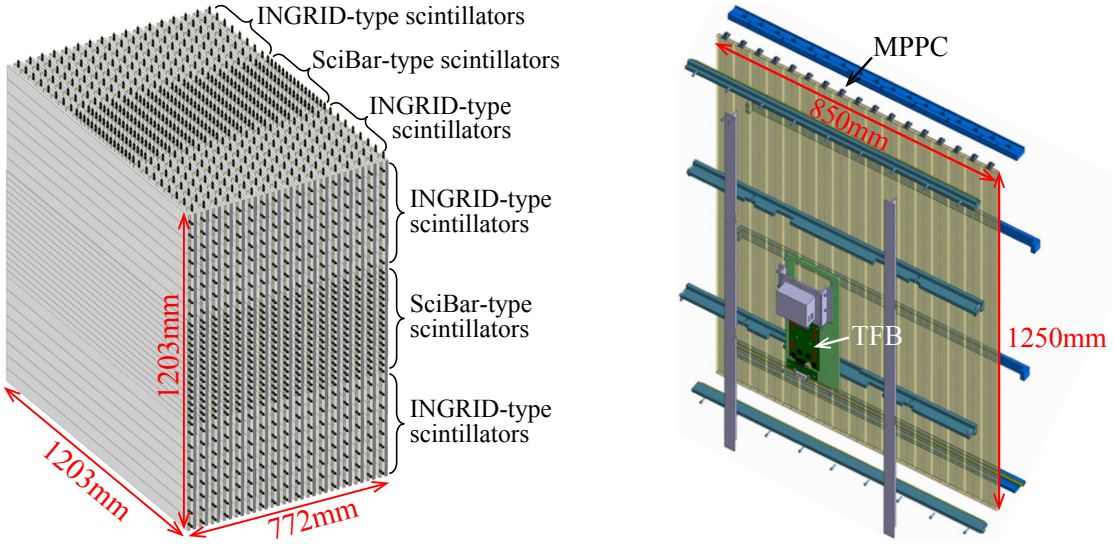

Figure A.6: Schematic drawings of the tracking planes (left) and the veto plane (right).

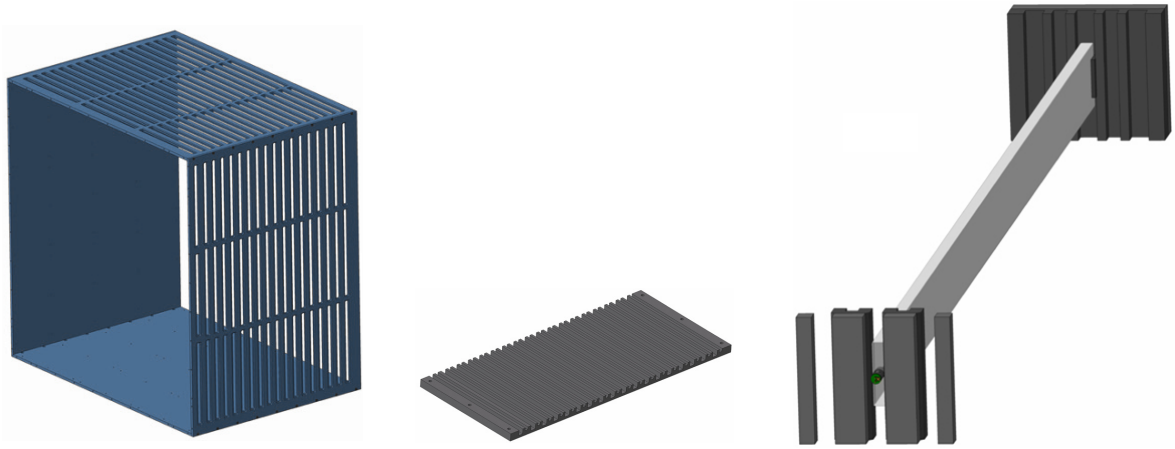

(a) Frame (b) Grooved plate (c) Method of fixation

Figure A.7: Support structure to fix the scintillators for the Proton Module.

A.2.3 Readout system

The readout system is designed as shown in A.8. The readout surfaces are on the top and either side of the frame. The optical connectors attached to the WLS fibers stick out of the holes on the frame. They are fixed on the surface by dedicated locks. Nine TFBs for the tracking planes are housed in an electronics box attached on the top of the Proton Module. The coaxial cables are connected to the TFBs through the holes on the electronics box. Since the inside of electronics box is optically connected to the inside of the frame through the holes, it is completely shaded.

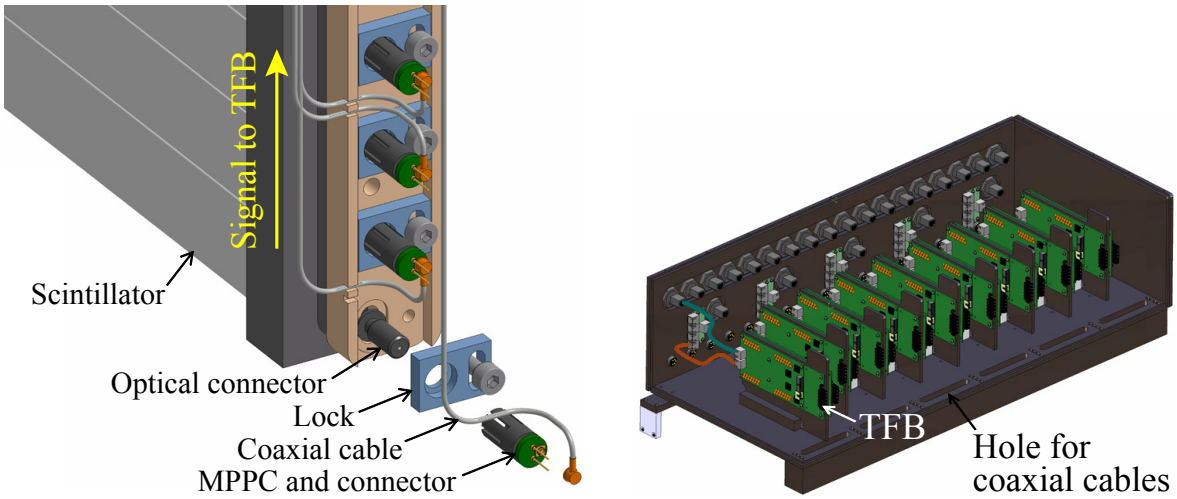

Figure A.8: Schematic drawings of the readout surface (left) and the electronics box (right).

A.3 Construction

The construction of the Proton Module was started in April 2010. First, the preparations of the detector components were done. The scintillators and WLS fibers were cut to the required length. The ends the WLS fibers were polished by a diamond turning tool. Reflective material was painted the ends of the WLS fibers and the scintillators. The optical connectors were attached to the WLS fibers and MPPCs. The PCB connectors were attached to the coaxial cables. The dedicated frame of the Proton Module (Fig. A.9) was produced in June. At the end of June, the detector assembly was started. The process of the assembly is as follows.

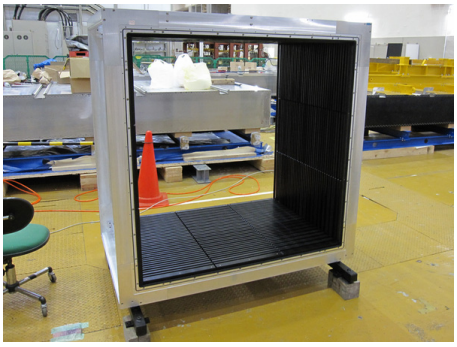

Figure A.9: Dedicated frame of the Proton Module

1. Attach the scintillator strips for the tracking planes (Fig. A.10).
2. Attach the scintillator strips for the veto planes (Fig. A.11).
3. Insert the WLS fibers to the holes of the scintillator strips (Fig. A.12).

Figure A.10: Attachment of the scintillator strips for the tracking planes.

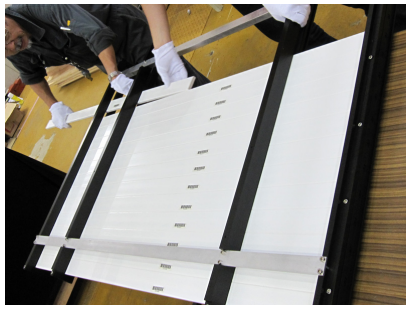

Figure A.11: Attachment of the scintillator strips for the veto planes.

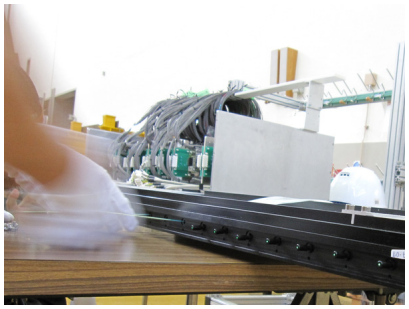

Figure A.12: Insertion of the WLS fiber.

4. Attach MPPCs to the end of the WLS fibers (Fig. A.13).
5. Attach cables to the TFBs (Fig. A.14).
6. Attach TFBs to the electronics box (Fig. A.15).
7. Attach the electronics box on the frame and connect the cables with MPPCs (Figs. A.16 and A.17).
8. Attach the veto planes and the shading panels (Fig. A.18).

Figure A.13: Attachment of the MPPCs.

Figure A.14: Attachment of cables to TFBs.

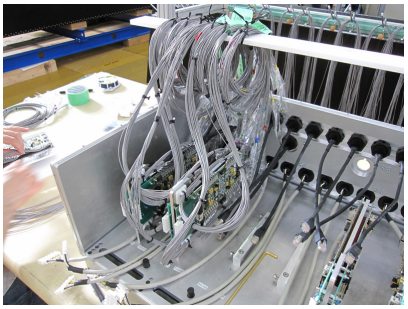

Figure A.15: Attachment of TFBs to the electronics box.

Figure A.16: Connection of the cables with MPPCs on the side readout surface.

Figure A.17: Connection of the cables with MPPCs on the top readout surface.

Figure A.18: Attachment of the veto planes.

Proton Module was completed as scheduled on July 30, 2010 (Fig. A.19). Figure A.20 show the photographs of the readout surface and the electronics box of the Proton Module.

After the basic tests, Proton Module was installed in the ND280 hall. Then, the TFBs of the Proton Module were cable-connected with the back-end boards (Fig. A.21).

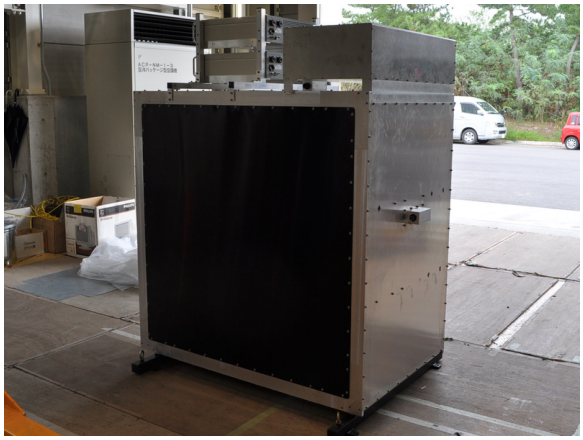

Figure A.19: Photograph of the completed Proton Module

Figure A.20: Photographs of the readout surface (left) and the inside of the electronics box (right).

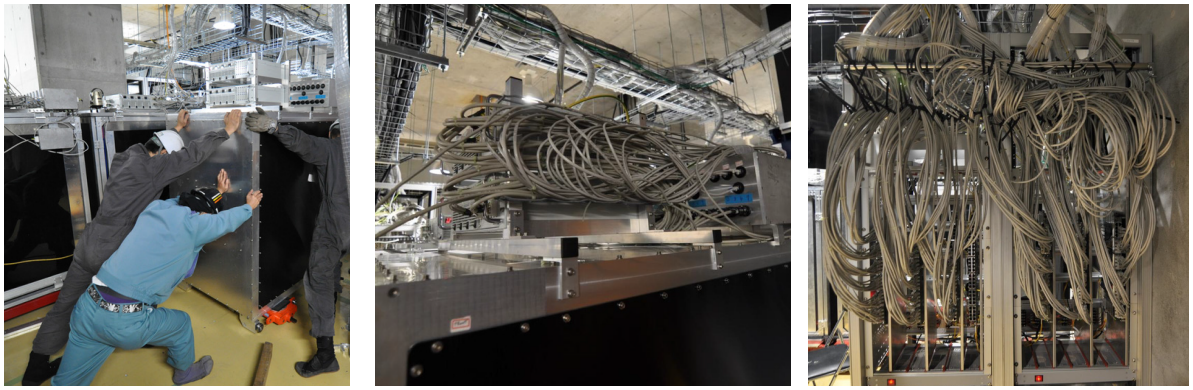

Figure A.21: Photographs of the installation work of the Proton Module (left) and the cables between the Proton Module and the back-end board (center, right).

A.4 First data taking

The first beam operation after the installation of the Proton Module was started on November 16. On November 18, the first neutrino candidate event in the Proton Module was observed (Figs. A.22 and A.23).

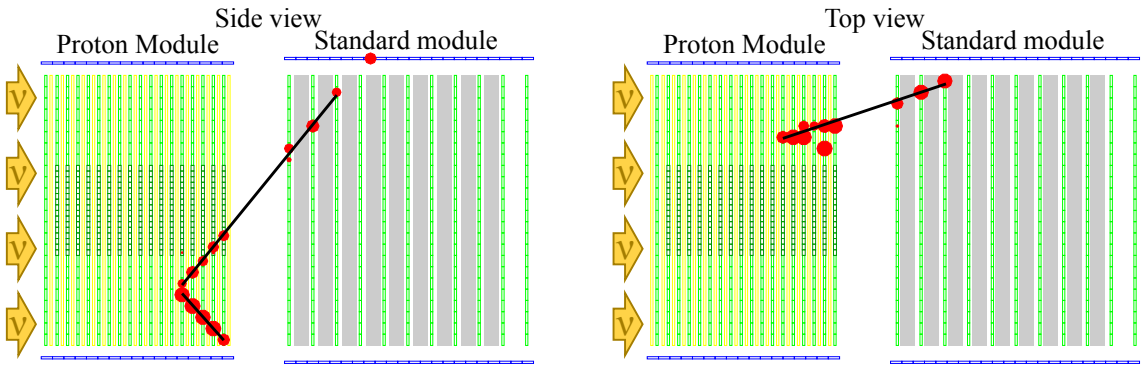

Figure A.22: Event display of the first neutrino candidate event in the Proton Module.

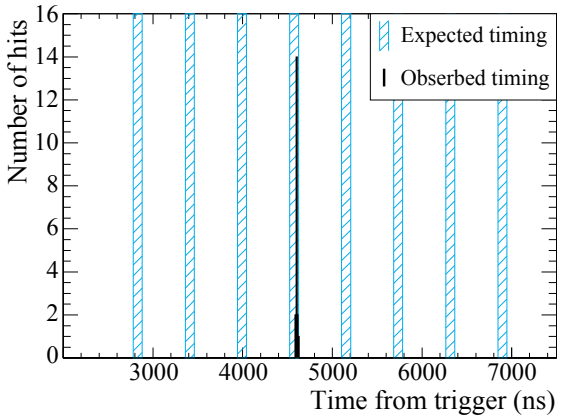

Figure A.23: Hit timing distribution of the first neutrino candidate event in the Proton Module.

Appendix B

Calibration and Data Quality of INGRID

The detector stability is essential for the measurement of the neutrino beam stability. Thus, we calibrated MPPCs for INGRID and validated the data quality of INGRID by checking the stability of the detector responses. Details of the calibration and the data quality of INGRID are described here.

B.1 MPPC calibration

The gains of all MPPCs for INGRID were calibrated by tuning the applied voltage channel-by-channel because MPPC is sensitive to the temperature and has considerable individual difference. First, the MPPC dark count data is taken by the periodic trigger. Then, the gain of each MPPC is estimated as described in Appendix A. Since the MPPC gain is proportional to the gap between the applied voltage and the breakdown voltage*, the applied voltage is tuned from the measured gain as follows:

$$V_{\mathrm{app}}^{\mathrm{new}} = (V_{\mathrm{app}}^{\mathrm{old}} - V_{\mathrm{bd}}) \times \frac{G_{\mathrm{nom}}}{G_{\mathrm{meas}}} + V_{\mathrm{bd}}, \tag{B.1}$$

where, V_{app} is the applied voltage, V_{bd} is the breakdown voltage, and G_{nom} and G_{meas} are nominal and measured gain values. We set the nominal gain value 7×10^5. After this calibration process, the gains of all the MPPCs become nearly uniform as shown in Fig. B.1.

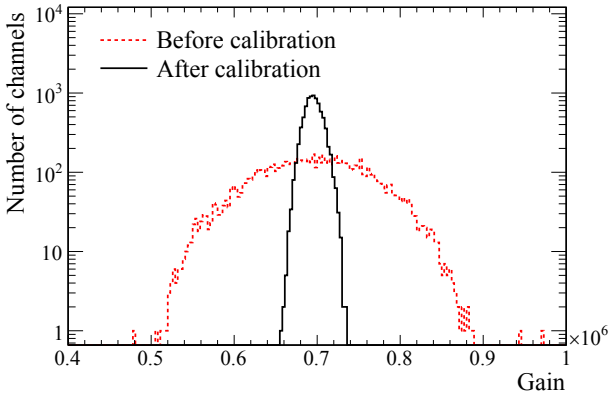

Figure B.1: Typical gain distribution of all MPPCs for INGRID before and after the calibration.

*The gap between the applied voltage and the breakdown voltage is generally referred to as the over voltage.

B.2 MPPC gain stability

During the entire data taking period, the MPPC status has been monitored by looking at the MPPC gain. The MPPC dark count distribution is obtained using the beam trigger data because the fraction of the beam induced hits is small. The gain is measured every 300 beam triggers, which correspond to about 13 minutes when repetition cycle is 2.56 nsec. Figure B.2 shows the gains for all MPPCs for INGRID as a function of time. Because of the variation of temperature, the gains varied slightly. Nevertheless the gains are stable within the 10% level.

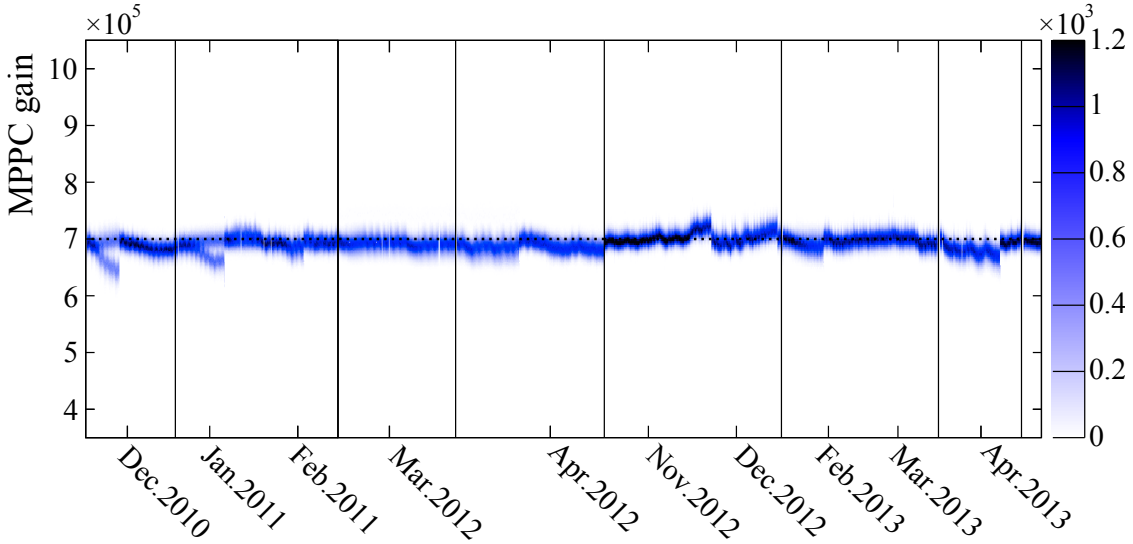

Figure B.2: Stability of the gains of all MPPCs for INGRID. Some discontinuities are attributed to the MPPC calibrations.

B.3 Hit efficiency

The hit efficiency is evaluated by using beam-induced external muon tracks with the following procedure.

1. All the hits in the test plane are masked (Fig. B.3 (1)).
2. The track is reconstructed using the same algorithm as the beam data analysis (see Chapter 6 for details). The expected track position in the test plane is interpolated with the reconstructed track (Fig. B.3 (2)).
3. The mask is opened and check if hits exist within ±10cm from the expected track position (Fig. B.3 (3)).
4. The above routine is repeated for many beam-induced external muon tracks. Then, the hit efficiency is calculated as the number of tests which observe hits divided by the total number of tests.

Figure B.4 shows the hit efficiency as a function of the track angle for each run period. The difference in the hit efficiency between run periods is very small.

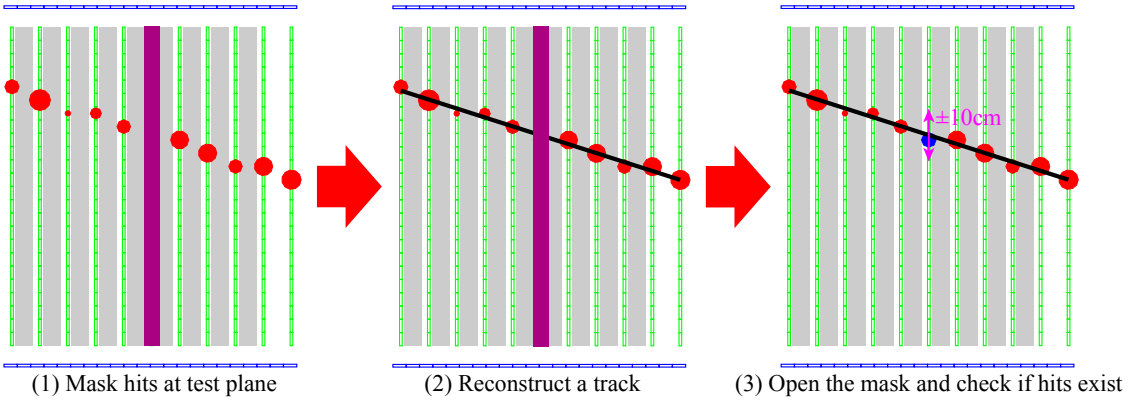

Figure B.3: Method of estimating the hit efficiency.

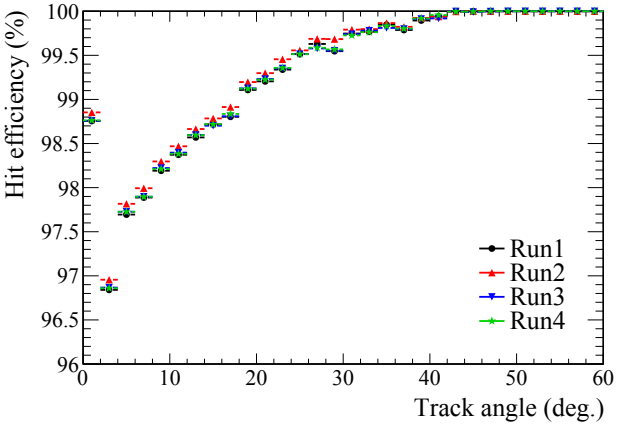

Figure B.4: Hit efficiency for beam-induced external muons for each run as a function of the track angle.

B.4 Light yield

The light yield per length of a muon track is monitored with inter-spill cosmic-ray data. The cosmic trigger is fired by CTM (Cosmic Trigger Module) when certain four scintillator trackers have two hits altogether. The inter-spill cosmic data is analyzed in the similar method as the hit efficiency test. All the hits in the test plane are masked, and the track is reconstructed. Then, the hits of the test plane within ±10cm[†] from the expected track position are used for the light yield test. A typical light yield distribution of a normal channel is shown in Fig. B.5. The distribution is consistent with the Landau distribution. Figure B.6 shows the light yields of all MPPCs over a run period, and Fig. B.7 shows the mean light yields as a function of time. It is stable over the entire run period.

[†]Precision of the track reconstruction is much better than 10cm (Fig. 6.3).

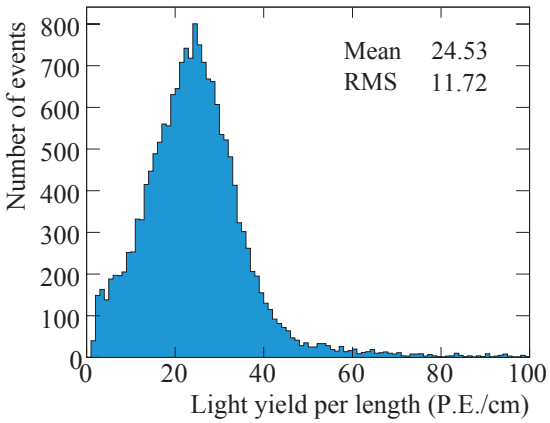

Figure B.5: Typical cosmic light yield distribution in a channel.

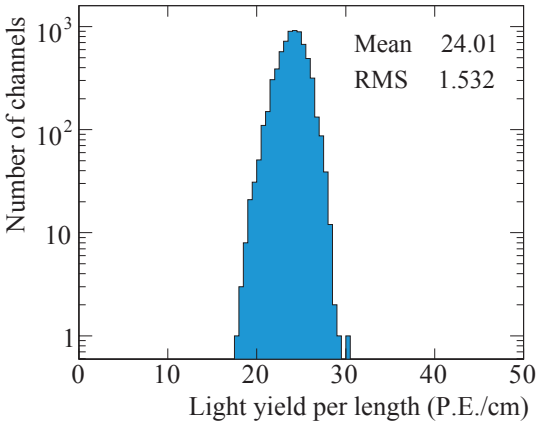

Figure B.6: Typical distribution of mean cosmic light yields of all the channels.

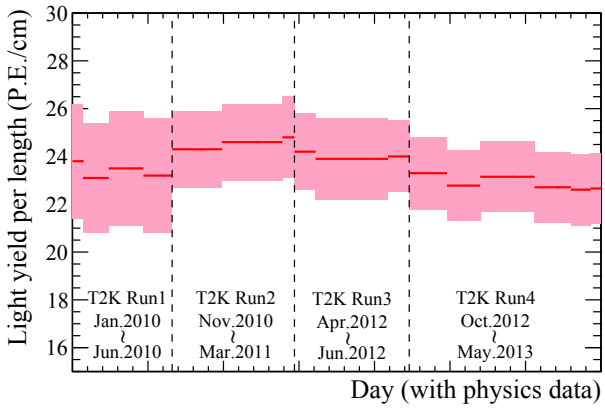

Figure B.7: Stability of mean cosmic light yields of all the channels. Red line and pink band show average and standard deviation, respectively.

Appendix C

Neutrino Beam Simulation

The neutrino fluxes and energy spectra at Super-K, ND280 and INGRID are predicted by the MC simulation based on the external hadron production data as described in Chapter 4. Details of the neutrino flux prediction are described here.

C.1 Hadronic interaction in the target

The interactions of the primary beam protons with the graphite of the baffle and the target are simulated with FLUKA2008. Incident protons are generated according to the measured proton beam spatial distribution and divergence. The kinetic energy of the incident protons is set to 30 GeV. The geometry in FLUKA2008 is shown in Fig. C.1. The baffle is depicted as a graphite block with the dimensions $29 \times 40 \times 171.145$ cm^3 and a 3.0 cm diameter cylindrical hole through the center. The target is modeled as a graphite cylinder of 90 cm in length and 2.6 cm in diameter. The volume inside the baffle hole and that between the baffle and the target are filled with He gas. The generated particles are traced until they emerge from the model geometry, then information such as kinematic variables and hadron interaction history is recorded at that point.

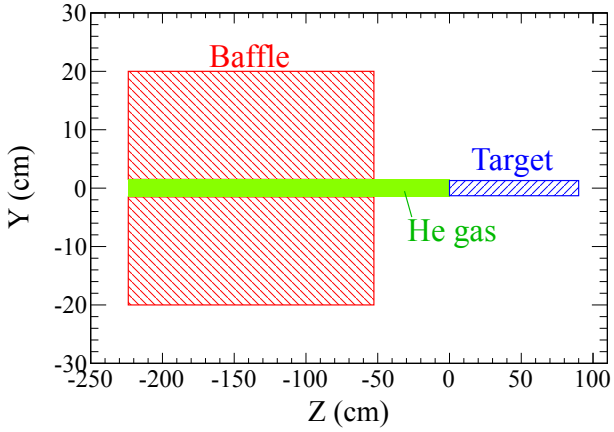

Figure C.1: Two-dimensional projected view of the geometrical setup in the FLUKA simulation of the baffle and the target.

C.2 Tracking inside horns and helium vessel.

Particles are generated in JNUBEAM according to the recorded information in FLUKA2008, and then are tracked through the horns and helium vessel. The graphite tube and titanium case surrounding the target are modeled in JNUBEAM. The thicknesses of graphite tube and titanium case are 2 mm and 0.3 mm, respectively. The interactions of particles with the materials are modeled by GCALOR in JNUBEAM.

C.3 Magnetic field of the horn inside inner conductors

The horn conductor is made of aluminum, and the thickness of the inner conductor is 3 mm. Since the low frequency pulsed current (3.6 msec full width) is loaded into the horn, the skin effect is small (the estimated skin depth is approximately 5 mm). Therefore, it is assumed that the current flows in the conductor uniformly. On this assumption, the magnetic field at radius r in the inner conductor is calculated with the Ampère's law as:

$$B(r) = \frac{\mu_0 I}{2\pi r}\frac{r^2 - a^2}{b^2 - a^2}, \tag{C.1}$$

where μ_0 is the magnetic permeability, I is the current, and a and b are the inner and outer radii of the inner conductor.

C.4 Neutrino production

Particles travel in the horn, the helium vessel, the decay volume, and the surrounding concrete shield including the beam dump, and then decay into neutrinos or stop when their kinetic energy drops below 10 MeV. In JNUBEAM, decays of $\pi^{\pm}$, $K^{\pm}$, K^0_L and $\mu^{\pm}$ are considered as neutrino sources. The current best knowledge [36] on the branching ratios and $K^{\pm}_{\ell 3}$ decay ($K^+ \to \pi^0 l^+ \nu_l$ or $K^- \to \pi^0 l^- \bar{\nu}_l$) form factors are used to simulate the decays. When a muon is generated from the decay of pion or kaon, its polarization information is stored. This polarization is taken into account at the muon decay.

When a particle decays into neutrino(s), the neutrino(s) are forced to point in the direction of Super-K or a randomly chosen point in the near detector planes. The neutrino energy in the center-of-mass frame is assigned based on the decay kinematics. The neutrino is then boosted into the laboratory frame under the assumption that it points in the selected direction. In addition, the probability of neutrino production in the selected direction is stored. Finally, the neutrino flux spectrum is obtained by scaling each event with the stored probability. This method enables us to save the CPU time for the simulation.

C.5 Hadronic interaction weight

Particles traversing in the target encounter a significant amount of material and can undergo multiple interactions. In addition, the particles can also interact with the material outside the target. The hadronic interaction weight is therefore applied to the each hadronic interaction of the interaction history in each event. The weight factor is estimated so that the hadron interaction model (FLUKA2008 or GCALOR) reproduces the hadron interaction data. The data include measurements of inelastic cross sections and differential hadron production. The hadron interaction weights are composed of the following processes:

1. Weight for the $\pi^{\pm}$ differential production cross-section.
2. Weight for the $K^{\pm}$ and K^0_L differential production cross-section.
3. Weight for the hadronic interaction rate (production cross-section).

Figure C.2 shows the differential production weights from NA61/SHINE data for π^+, and Fig. C.3 shows the ratio of the weighted flux over the non-weighted flux for ν_μ at Super-K. The weighting for the pion differential production has the largest effect at the energy around oscillation maximum ($\sim$ 1 GeV), while that for the kaon differential production is dominant at high energies.

The produced hadrons are labeled as secondary (tertiary) hadrons if they are produced in interactions of the original protons (hadrons other than original protons) as shown in Fig. C.4. The breakdown of the predicted flux for each flavor is described in Table C.1 according to the final parent hadron in the interaction history. The ν_e and $\bar{\nu}_e$ mainly come from the decays of muons originating from secondary or tertiary pions. A significant fraction of the fluxes comes from tertiary pions and kaons. Thus, it is important to investigate the hadron interaction data not only for the incident proton momentum (30 GeV) but also for the lower momentum. The used hadron differential production data are summarized in Table C.2 and the used hadronic interaction rate data are summarized in Table C.3.

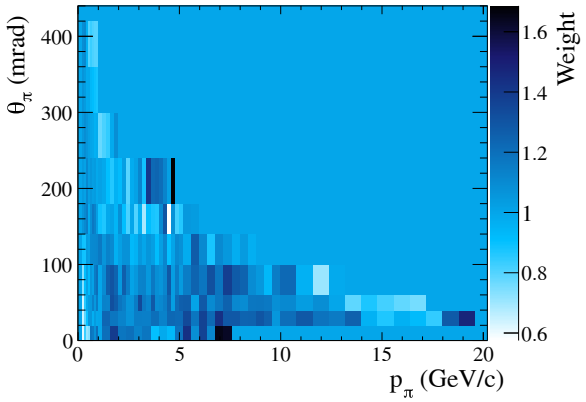

Figure C.2: The differential production weights from NA61/SHINE data for π^+.

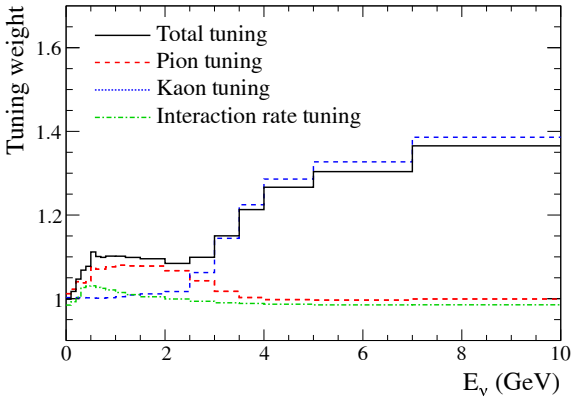

Figure C.3: Ratio of the weighted flux over the non-weighted flux for ν_μ at Super-K.

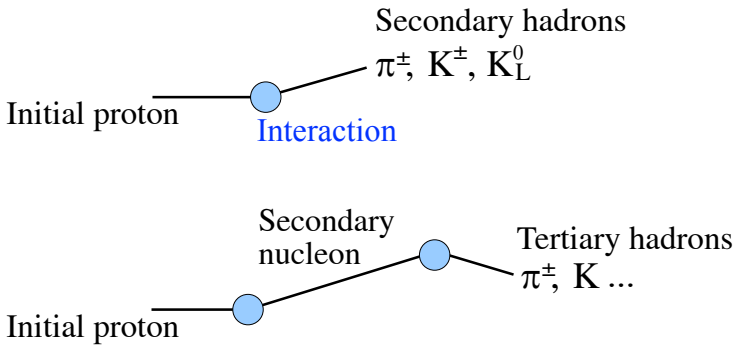

Figure C.4: Labels of hadrons produced in each hadronic interaction.

Table C.1: The fraction of the neutrino flux by the final hadron in the interaction history.

	Flux percentage of each (all) flavors			
Parent	ν_μ	$\bar{\nu}_\mu$	ν_e	$\bar{\nu}_e$
Secondary				
$\pi^\pm$	60.0(55.6)%	41.8(2.5)%	31.9(0.4)%	2.8(0.0)%
$K^\pm$	4.0(3.7)%	4.3(0.3)%	26.9(0.3)%	11.3(0.0)%
K^0_L	0.1(0.1)%	0.9(0.1)%	7.6(0.1)%	49.0(0.1)%
Tertiary				
$\pi^\pm$	34.4(31.9)%	50.0(3.0)%	20.4(0.2)%	6.6(0.0)%
$K^\pm$	1.4(1.3)%	2.6(0.2)%	10.0(0.1)%	8.8(0.0)%
K^0_L	0.0(0.0)%	0.4(0.1)%	3.2(0.0)%	21.3(0.0)%

Table C.2: Differential hadron production data used for the T2K neutrino flux predictions.

Experiment	Particle	Target	Beam momentum
NA61/SHINE [158, 159]	$\pi^\pm$, K^+	C	31 GeV/c
Eichten *et al.* [160]	p, $\pi^\pm$, $K^\pm$	Be, Al, ...	24 GeV/c
Allaby *et al.* [161]	p, $\pi^\pm$, $K^\pm$	Be, Al, ...	19.2 GeV/c
BNL-E910 [356]	$\pi^\pm$	Be	6.4 – 17.5 GeV/c

Table C.3: Inelastic and production cross-section data used for the T2K neutrino flux predictions.

Data	Particle	Target	Beam momentum	Measurement
Abrams *et al.* [357]	$K^\pm$	C, Cu	1 – 3.3 GeV/c	Inelastic cross section
Allaby *et al.* [358]	π^-, K^-	C, Al, ...	20 – 65 GeV/c	Inelastic cross section
Allardyce *et al.* [359]	$\pi^\pm$	C, Al, ...	0.71 – 2 GeV/c	Inelastic cross section
Bellettini *et al.* [360]	p	C, Al, ...	19.3, 21.5 GeV/c	Inelastic cross section
Bobchenko *et al.* [361]	π^-, p	C, Al, ...	1.75 – 9 GeV/c	Inelastic cross section
Carroll *et al.* [362]	$\pi^\pm$, $K^\pm$, p	C, Al, ...	60 – 280 GeV/c	Production cross section
Cronin *et al.* [363]	π^-	C, Al	0.73 – 1.33 GeV/c	Inelastic cross section
Chen *et al.* [364]	p	C, Al, ...	1.53 GeV/c	Inelastic cross section
Denisov *et al.* [365]	$\pi^\pm$, $K^\pm$, p	C, Al, ...	6 – 60 GeV/c	Inelastic cross section
Longo *et al.* [366]	π^+, p	C, Al	3 GeV/c	Inelastic cross section
NA61/SHINE [158]	p	C	31 GeV/c	Production cross section
Vlasov *et al.* [367]	π^-	C, Al	2 – 6.7 GeV/c	Inelastic cross section

Appendix D

Neutrino Interaction Models

The neutrino interaction models used in T2K were described in Chapter 4. Supplemental remarks of the models, and the methods of estimating their uncertainties are given here.

D.1 Nuclear models

At the T2K neutrino energies, the neutrino interaction cross section (especially the CCQE cross section) is highly dependent on the nuclear model. The relativistic Fermi gas model is used as the default model, and the spectral function is used as the alternative model as described in Chapter 4. This section describes the details of these nuclear models.

D.1.1 Fermi gas model

In the Fermi gas model, the nucleus is considered as an ideal gas composed of weakly interacting fermions. In the nucleus, neutrons and protons are considered as distinguishable fermions, creating two potentials as shown in Fig. D.1. All states are filled up to the Fermi level, above which no states are filled. The number of nucleons that can be contained in a certain volume of space is obtained by dividing that volume by the volume of one state in phase space, $(2\pi)^3$:

$$\mathrm{d}n = \frac{V 4\pi p^2 \mathrm{d}p}{(2\pi)^3}, \tag{D.1}$$

where V is the nuclear volume and n is the number of protons or neutrons. The total number of protons or neutrons will be then given by,

$$n = \frac{V 4\pi \int_0^{p_F} p^2 \mathrm{d}p}{(2\pi)^3} = \frac{p_F^3 V}{6\pi^2}. \tag{D.2}$$

The nucleon-nucleon correlation is described by used of the mean-field approximation. The momentum-energy distribution of nucleons in the Fermi gas model is given by.

$$P(\boldsymbol{p}, E) = \theta(p_F - |\boldsymbol{p}|)\delta(E + \sqrt{M_N^2 + |\boldsymbol{p}|^2} - E_B), \tag{D.3}$$

where $\theta(x) = 0$ for $x < 0$ and $\theta(x) = 1$ for $x \geq 0$ is the step function, p_F is the Fermi momentum, M_N is the nucleon mass, and E_B is the binding energy.

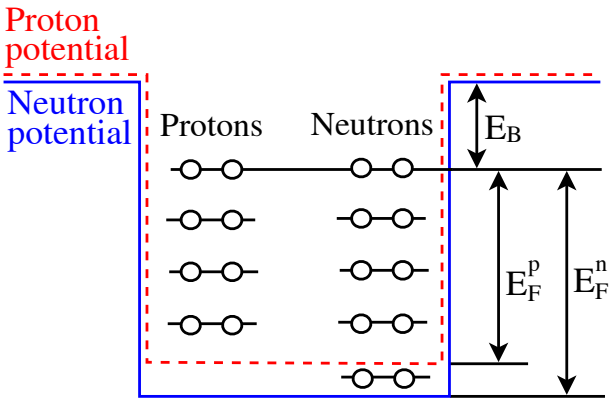

Figure D.1: The proton and neutron potential wells and states in the Fermi gas model.

D.1.2 Spectral function

The spectral function gives the probability to find in a nucleus a nucleon with momentum $\boldsymbol{p}$ and removal energy E as:

$$P(\boldsymbol{p}, E) = |\langle \psi_n^{A-1} | a_{\boldsymbol{p}}^\dagger | \psi_0^A \rangle|^2 \times \delta(E - E_0 + E_n), \tag{D.4}$$

where ψ_n^{A-1} is the n-th eigenstate of $(A-1)$ nucleon system, ψ_0^A is the nuclear ground state, $a_{\boldsymbol{p}}^\dagger$ is the creation operator for nucleon with momentum $\boldsymbol{p}$, E_0 and E_n are energies for the ground state and the n-th eigenstate. For the realistic many-body calculation, it is split into a term for single particles, and a term from correlated pairs of nucleons:

$$P(\boldsymbol{p}, E) = P_{SP}(\boldsymbol{p}, E) + P_{corr}(\boldsymbol{p}, E). \tag{D.5}$$

The single-particle term corresponds to the contribution from one-hole intermediate states. This term is calculated from mean-field calculation and electron scattering data. It goes to zero around the Fermi surface, and accounts for roughly 80% of the total spectral function.

The correlation term corresponds to the contribution from n-hole-$(n-1)$-particle intermediate states. This term is calculated by use of local-density approximation. It leads to a very long tail in both momentum and binding energy, and accounts for roughly 20% of the total spectral function.

In the Fermi gas model, all states up to the Fermi level are filled, so particles cannot be ejected in momentum states lower than this level. This naturally leads to Pauli blocking with a hard momentum cut off reducing the cross section. In the spectral function model, Pauli blocking does not arise so naturally, as there is no hard cut-off in the momentum spectrum. A possible approach to Pauli blocking in the spectral function model is to use the local density at the interaction point to determine a "local Fermi momentum". The Fermi momentum is only relevant for Pauli blocking in the spectral function model, whereas it also affects the initial nucleon momentum distribution in the Fermi gas model.

D.2 Coherent pion production models

There are mainly two different approaches to model the coherent pion production. One is based on the partially conserved axial current (PCAC) theorem, and the other is based on a microscopic dynamical model.

D.2.1 PCAC-based models

The Rein-Sehgal model used in T2K is based on the PCAC theorem as described in Chapter 4. Berger-Sehgal model [318] and Schalla-Paschos model [319] are also based on the PCAC theorem. Here, the details of PCAC-based approach are explained. When the final-state lepton's scattering angle is small, the cross section for weak scattering from an initial hadronic system, α, to a final hadronic system, β, can be related to the analogous process in pion scattering, as shown in Fig. D.2. The amplitude for the process of $\nu_l + \alpha \to l^- + \beta$ is described by the product of the leptonic and hadronic weak currents:

$$\mathcal{M}(\nu_l + \alpha \to l^- + \beta) = \frac{G_F}{\sqrt{2}} \bar{\mu}_l \gamma_\mu (1 - \gamma_5) \mu_\nu \langle \beta | V^\mu + A^\mu | \alpha \rangle, \tag{D.6}$$

where V^μ and A^μ are hadronic vector and axial-vector currents. Assuming the final-state lepton emerges parallel to the incoming neutrino and neglecting its mass, the amplitude, squared and averaged over the lepton's spin, is:

$$\begin{aligned}
\langle |\mathcal{M}(\nu_l + \alpha \to l^- + \beta)|^2 \rangle &= 2G_F^2 \frac{E_\nu E_l}{q_0^2} q^2 |\langle \beta | V^\mu + A^\mu | \alpha \rangle|^2 \\
&= 2G_F^2 \frac{E_\nu E_l}{q_0^2} q_\mu \langle \beta | V^\mu + A^\mu | \alpha \rangle q_\nu \langle \beta | V^\nu + A^\nu | \alpha \rangle^* \\
&= 2G_F^2 \frac{E_\nu E_l}{q_0^2} \langle \beta | \partial_\mu (V^\mu + A^\mu) | \alpha \rangle \langle \beta | \partial_\nu (V^\nu + A^\nu) | \alpha \rangle^* \\
&= 2G_F^2 \frac{E_\nu E_l}{q_0^2} |\langle \beta | \partial_\mu (V^\mu + A^\mu) | \alpha \rangle|^2.
\end{aligned} \tag{D.7}$$

In the limit of $Q^2 \to 0$, the divergence of the vector current must go to zero ($\partial_\mu V^\mu \to 0$). And thus, the amplitude is:

$$\langle |\mathcal{M}(\nu_l + \alpha \to l^- + \beta)|^2 \rangle = 2G_F^2 \frac{E_\nu E_l}{q_0^2} |\langle \beta | \partial_\mu A^\mu | \alpha \rangle|^2. \tag{D.8}$$

The divergence of the axial-vector current can be related to another weak process: pion decay ($\pi \to \mu + \nu_\mu$). The amplitude for this process is:

$$\mathcal{M}(\pi \to \mu + \nu_\mu) = \frac{G_F}{\sqrt{2}} \bar{\mu}_l \gamma_\mu (1 - \gamma_5) \mu_\nu \langle 0 | V^\mu + A^\mu | \pi \rangle. \tag{D.9}$$

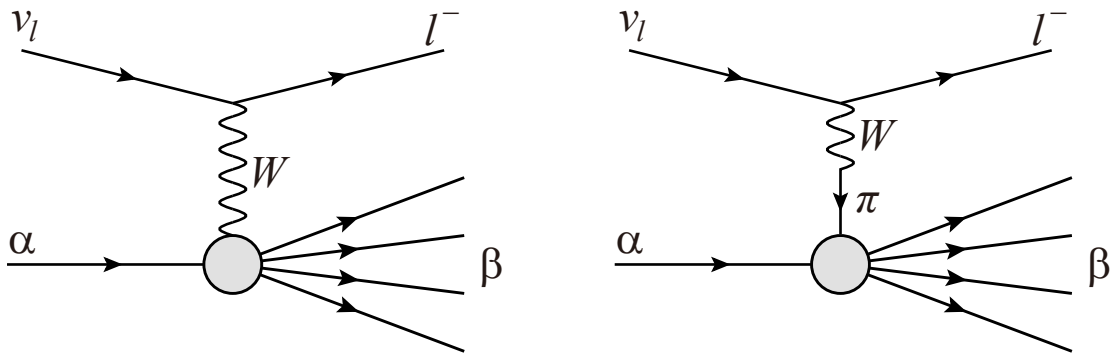

Figure D.2: Feynman diagrams of $\nu_l + \alpha \to l^- + \beta$ (left) and $\pi + \alpha \to \beta$ (right) which are related in Adler's PCAC theorem.

Lorentz invariance of this amplitude requires $\langle 0|V^\mu + A^\mu|\pi\rangle$ to be either vector or axial-vector, but since the pion has no spin and the only four-vector available is the pion four-momentum P_π, we have

$$\langle 0|V^\mu + A^\mu|\pi\rangle = f_\pi P_\pi^\mu \Phi_\pi, \tag{D.10}$$

where Φ_π is the pion field, and the form-factor f_π is known as the pion decay constant. Since it is represented by a vector, only the axial current contributes because both the vacuum and the axial current have even parity and the pion has odd parity.

$$\langle 0|A^\mu|\pi\rangle = f_\pi P_\pi^\mu \Phi_\pi. \tag{D.11}$$

Taking the divergence of this expression gives:

$$\begin{aligned} \langle 0|\partial_\mu A^\mu|\pi\rangle &= f_\pi P_{\pi\mu} P_\pi^\mu \Phi_\pi \\ &= f_\pi P_\pi^2 \Phi_\pi \\ &= f_\pi m_\pi^2 \Phi_\pi, \end{aligned} \tag{D.12}$$

where m_π is the pion mass. The matrix elements of the divergence of the axial current are given by the following expression:

$$\langle \beta|\partial_\mu A^\mu|\alpha\rangle = \frac{f_\pi m_\pi^2}{m_\pi^2 + Q^2}\mathcal{M}(\pi + \alpha \to \beta). \tag{D.13}$$

In the limit of $Q^2 \to 0$,

$$\langle \beta|\partial_\mu A^\mu|\alpha\rangle = f_\pi \mathcal{M}(\pi + \alpha \to \beta). \tag{D.14}$$

Putting Eq. D.14 into Eq. D.8 gives:

$$\langle|\mathcal{M}(\nu_l + \alpha \to l^- + \beta)|^2\rangle = 2G_F^2 \frac{E_\nu E_l}{q_0^2} f_\pi^2 |\mathcal{M}(\pi + \alpha \to \beta)|^2. \tag{D.15}$$

In the coherent pion production, $\alpha = A$, and $\beta = \pi + A$:

$$\langle|\mathcal{M}(\nu_l + A \to l^- + \pi + A)|^2\rangle = 2G_F^2 \frac{E_\nu E_l}{q_0^2} f_\pi^2 |\mathcal{M}(\pi + A \to \pi + A)|^2. \tag{D.16}$$

From this relation, Eq. 4.21 is derived.

D.2.2 Microscopic models

Whereas the PCAC-based model describes the coherent pion production in terms of a single interaction channel with a nucleus, the microscopic model describes the process in terms of a coherent sum of neutrino-nucleon interactions where the final-state nucleon is constrained to remain in the same quantum state. The microscopic model includes four such neutrino-nucleon pion producing channels, shown in Fig. D.3, two of which involve the intermediate propagation of a Δ, and two the propagation of a nucleon. The nuclear medium effect on the Δ-propagation and the pion-nucleus interaction are also taken into account. This model is reliable only for low energy neutrinos ($E_\nu \lesssim 1$ GeV). Thus, it is not applicable to the T2K on-axis neutrinos while it is applicable to the T2K off-axis neutrinos (Fig. 2.3). Alvarez-Ruso model [320–322], Hernandez model [323], and Nakamura model [324] are examples of the microscopic models.

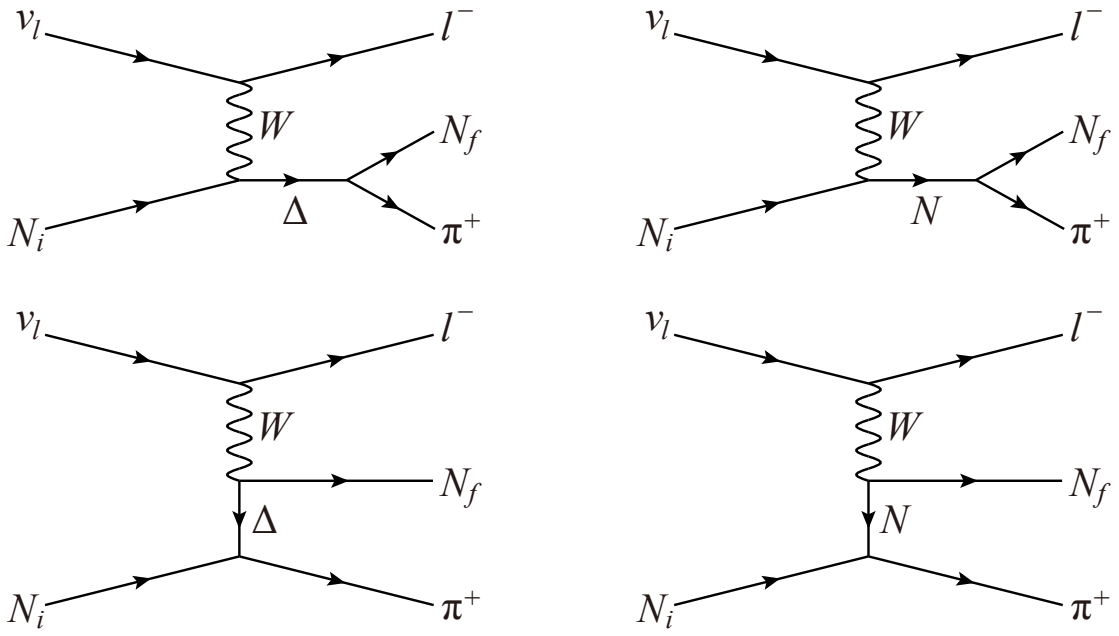

Figure D.3: Feynman diagrams of the interaction processes which contribute to the microscopic models. The interaction can utilize a Δ (left) or nucleon (right) propagator, and proceed via an s-channel (top) or t-channel (bottom) diagram.

D.3 Neutrino interaction model uncertainties

The neutrino interaction model uncertainties are driven from the experimental data. We compared the NEUT predictions to external neutrino-nucleus interaction data in the energy region relevant for T2K. Details of the evaluation of the uncertainties are described here.

D.3.1 Quasi-elastic scattering

The uncertainty in the CCQE cross section is estimated by comparing data from the MiniBooNE experiment to NEUT. In this comparison, NEUT CCQE interactions are simulated using the predicted MiniBooNE flux and tuned to the MiniBooNE double-differential CCQE data in the muon kinetic energy and angle [213] to fit for the best value of $M_{\rm QE}^A$ and CCQE normalization (Fig. D.4). The error on each NEUT parameter is determined as the difference between the fitted value of the parameter and the nominal. For CCQE, we take the MiniBooNE data below 1.5 GeV, and assign the uncertainty of 11% as reported by the MiniBooNE Collaboration. To allow for the discrepancy in the CCQE cross section between NOMAD at E_ν >3.5 GeV [222] and MiniBooNE at E_ν <1.5 GeV [221], a 30% error has been set above 3.5 GeV. The 30% error also has been assigned to the intermediate region (1.5< E_ν <3.5 GeV).

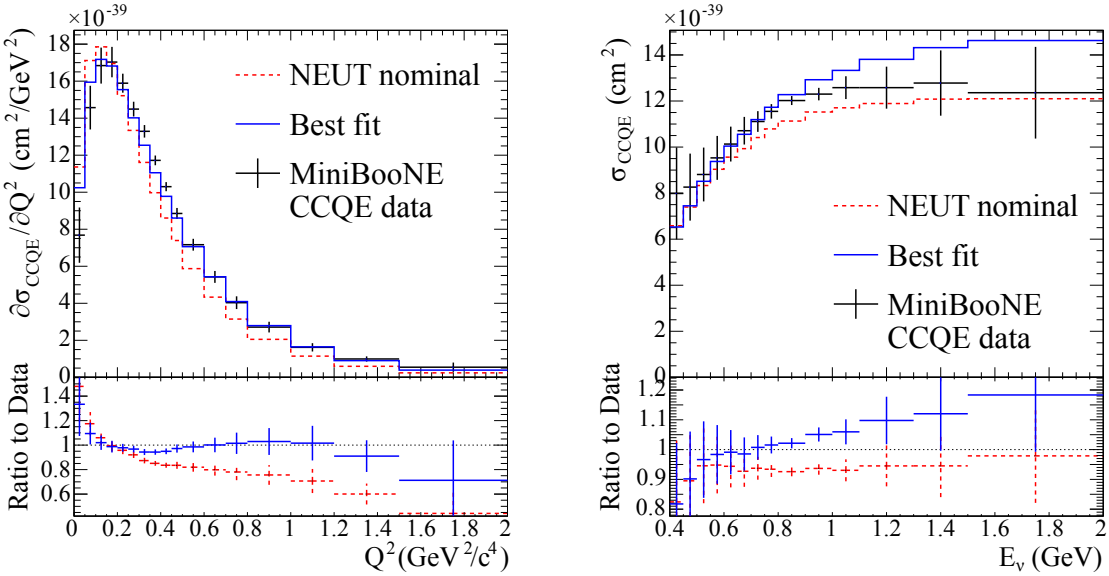

Figure D.4: Differential cross section for CCQE Q^2 used in CCQE fits to MiniBooNE data, and NEUT nominal and best-fit predictions (left), and CCQE cross section as a function of neutrino energy (right).

D.3.2 Single resonant meson via baryon resonances

To constrain the single pion production, we perform a joint fit to the MiniBooNE data sets for CC1π^+, CCπ^0 and NC1π^0 production since these sets are connected in the underlying model (the Rein-Sehgal model). We fit to the reconstructed Q^2 distributions in the CC channels and the pion momentum distribution in the NC channel [214–216] (Fig. D.5). Nine parameters are included in the fit: M_A^{RES}, W-shape parameter, CC1π normalizations below and above 2.5 GeV, CC other E_ν shape, NC1π^0 normalization, NC1$\pi^\pm$ normalization, NC coherent pion normalization, NC other normalization. The MiniBooNE data directly constrain M_A^{RES}, CC1π normalization below 2.5 GeV and NC1π^0 normalization. For energies above 2.5 GeV, we assign a conservative 40% error to the normalization of CC1π production, motivated primarily by NOMAD data [278]. The W-shape parameter allows an adjustment of the shape of the pion momentum spectrum of the NC1π^0 channel to improve agreement with data. The error on this parameter is taken to be 50%. As there is little NC1$\pi^\pm$ data, the uncertainty on the NC1$\pi^\pm$ normalization is set to be the same size as that for the NCπ^0 resonant normalization (30%). In addition, π-less Δ decay parameter is considered. This parameter varies the rate of the π-less Δ decay process. An absolute error of 20% is assigned to this process.

D.3.3 Coherent pion production

A 100% error has been set for the CC coherent pion production. This is driven by the fact that K2K and SciBooNE data [223, 224] indicate there is much less coherent charged pion production by neutrinos with energy below 2 GeV than predicted by the original models as shown in Fig. D.6. A 30% uncertainty on the NC coherent normalization factor is used. This conservative estimation is motivated by the observation of a 15% discrepancy between the NEUT prediction and the SciBooNE measurement of NC coherent production, together with a 20% systematic error in those data [225] (Fig. D.6).

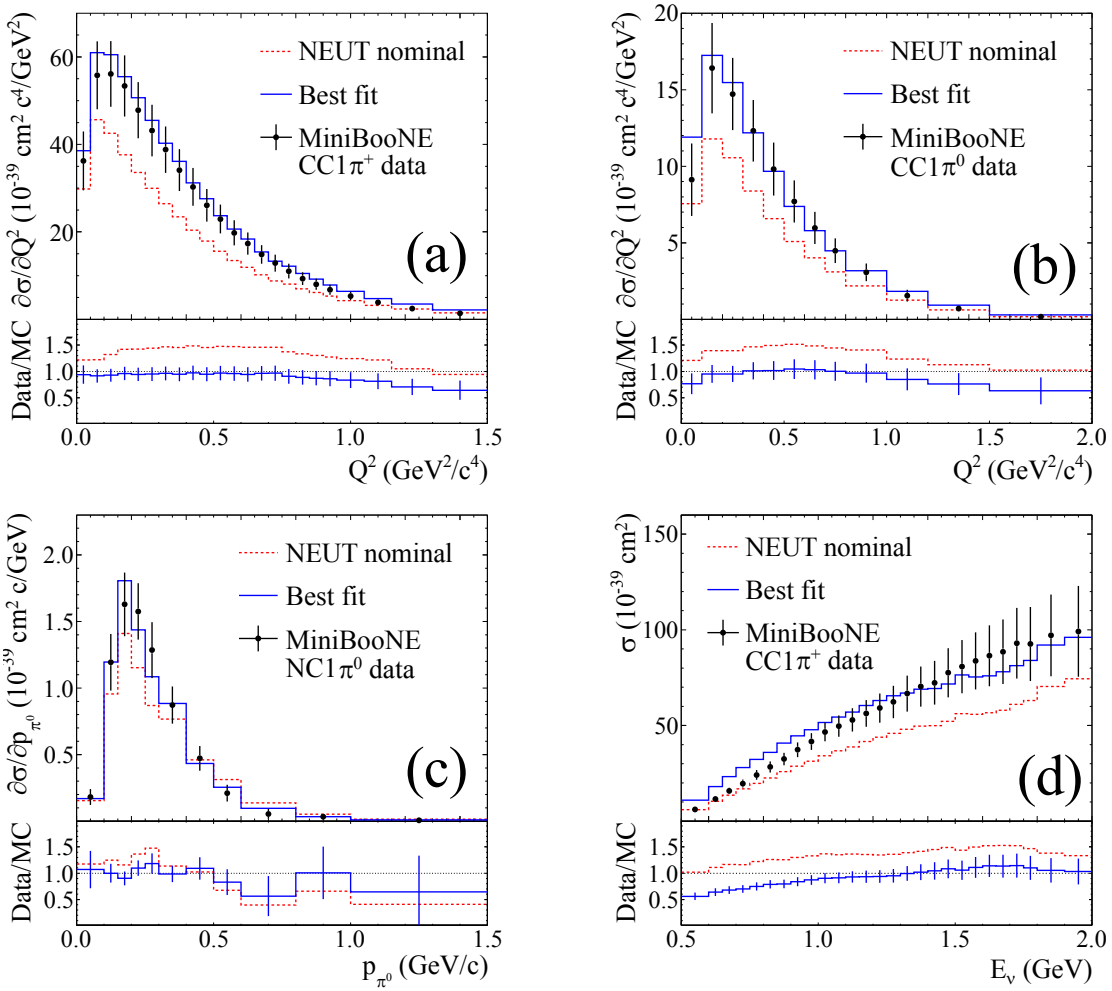

Figure D.5: Differential cross sections for (a) CC1π^+ Q^2, (b) CC1π^0 Q^2 and (c) NC1π^0 p_{π^0} used in single-pion fits to MiniBooNE data, and NEUT nominal and best-fit predictions, and (d) CC1π^+ cross section as a function of the neutrino energy.

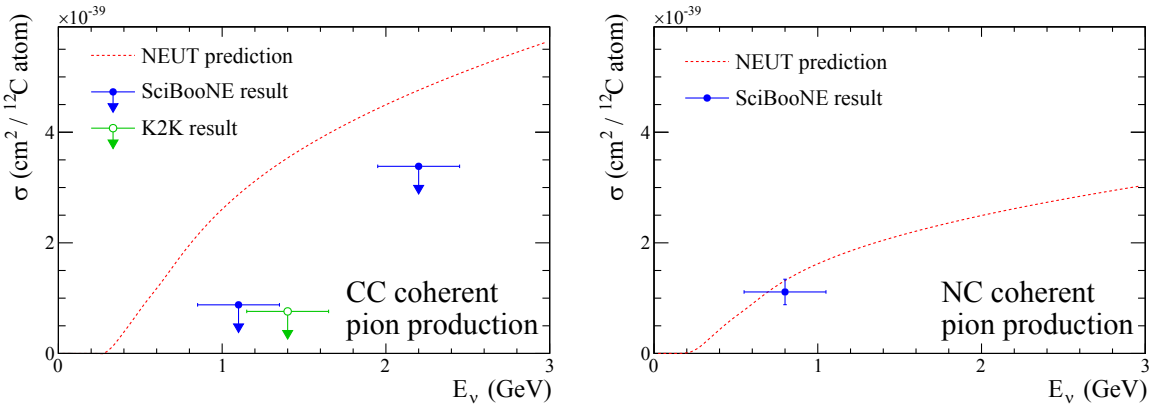

Figure D.6: The coherent pion production cross section via CC (right) and NC (left) predicted by NEUT compared to external data. The downward arrows show 90% C.L. upper limits.

D.3.4 Other interactions

At energies greater than 4 GeV, CC multi-pion/DIS interactions dominate the CC inclusive cross section and are constrained by measurements of the CC inclusive cross section with ∼10% uncertainties [278] (Fig. D.7). At lower energies the constraint from the CC inclusive cross section measurements is weaker since other interaction modes are significant. Hence, we apply an uncertainty that is 10% at high energies and increases to 40% near the threshold for multi-pion production. The model is adjusted by applying a weight:

$$w = 1 + \frac{x_{\mathrm{CCother}}}{E_\nu}, \tag{D.17}$$

where x_{CCother} is allowed to vary around a nominal value of 0 with a prior uncertainty of 0.4 GeV.

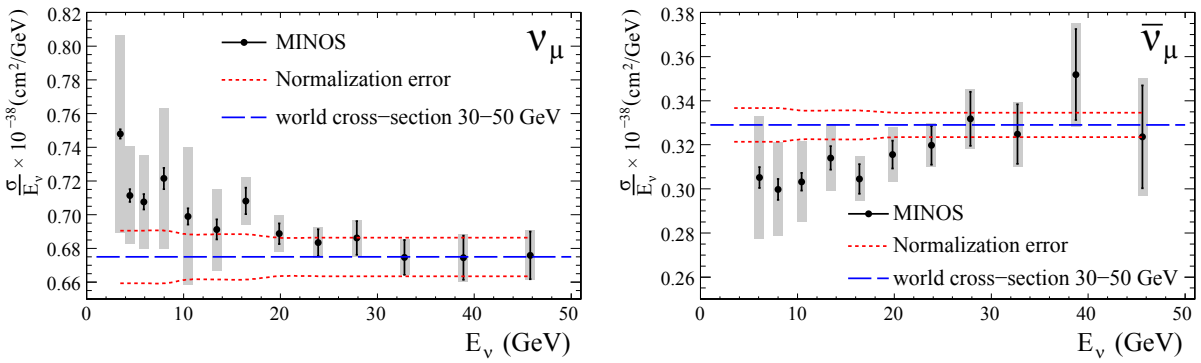

Figure D.7: The CC inclusive cross section for ν_μ (left) and $\bar{\nu}_\mu$ (right) reported by MINOS. The error around 4 GeV is on the order of 10%.

D.3.5 Intra-nuclear interaction

In theory, the uncertainties on the intra-nuclear interaction parameters (absorption, charge exchange, quasi-elastic scattering and inelastic scattering) are correlated with the other cross-section parameters. In this analysis, however, we assume them to be independent, as a first approximation. Therefore, the uncertainty on the intra-nuclear interaction contribution is added in quadrature to the other sources in the reported cross section. The values and uncertainties of the parameters that scale the microscopic interaction probabilities have been estimated from comparison to external π-^{12}C scattering data. Figure D.8 shows the tuned cascade model compared to macroscopic measurements of the pion absorption cross section and the maximum variation of the model parameters chosen to cover the uncertainties on the data. Table D.1 summarizes the external data sets used for this estimation.

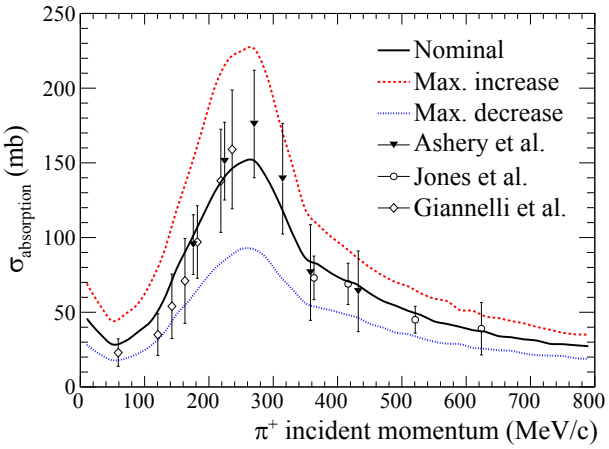

Figure D.8: Pion absorption cross section as a function of pion momentum overlaid with π^+-^{12}C scattering data [228, 232].

Table D.1: External data sets used to tune the scaling parameters of intra-nuclear interactions. ABS, CX and INEL denote absorption, charge exchange and inelastic scattering, respectively.

Data	Interaction channel	Pion momentum (MeV/c)
D. Ashery *et al.* [228]	π^+-C Reactive, ABS+CX	175.7, 224.4, 270.4, 314.7, 358.0, 432.2
D. Ashery *et al.* [228]	π^--C Reactive, ABS+CX	224.4, 270.4
A. Saunders *et al.* [229]	π^+-C Reactive	115.9, 133.9, 149.3
E. Bellotti *et al.* [230]	π^+-C ABS	230.6
S. M. Levenson *et al.* [231]	π^+-C INEL	194.4, 331.0
M. K. Jones *et al.* [232]	π^+-C INEL, CX	363.3, 416.4
D. Ashery *et al.* [233]	$\pi^\pm$-C CX	270.4
E. Bellotti *et al.* [234]	π^+-C CX	230.6
I. Navon *et al.* [235]	$\pi^\pm$-C ABS+CX, CX	224.8
I. Navon *et al.* [236]	π^+-C ABS+CX	128.3
F. Binon *et al.* [237]	π^--C Reactive	218.5, 253.4, 287.1, 309.2, 341.8, 374.0, 395.3
H. Hilscher *et al.* [238]	π^--C CX	156.3
R. H. Miller *et al.* [239]	π^--C ABS+CX	253.4

Appendix E

Measurement at Super-Kamiokande

The measurement of the ν_e and ν_μ events in Super-K was described in Chapter 10. Details of the neutrino event observation and the detector error estimation of Super-K are described here.

E.1 Event timing

Figure E.1 shows the relative event timing at Super-K to the spill head timing (ΔT_0), accounting for the travel time of the neutrino from production to detection. The spill duration is about 5 μs. A clear peak at $\Delta T_0 = 0$ is seen for the FC sample. We observe ten FC events outside of the 5 μs spill window. The expected number of such out-of-time FC events, mainly low energy events and atmospheric neutrino events, is estimated to be 5.2 from data collected when the beam is not present. The Super-K event timing clearly exhibits the eight bunch beam timing structure.

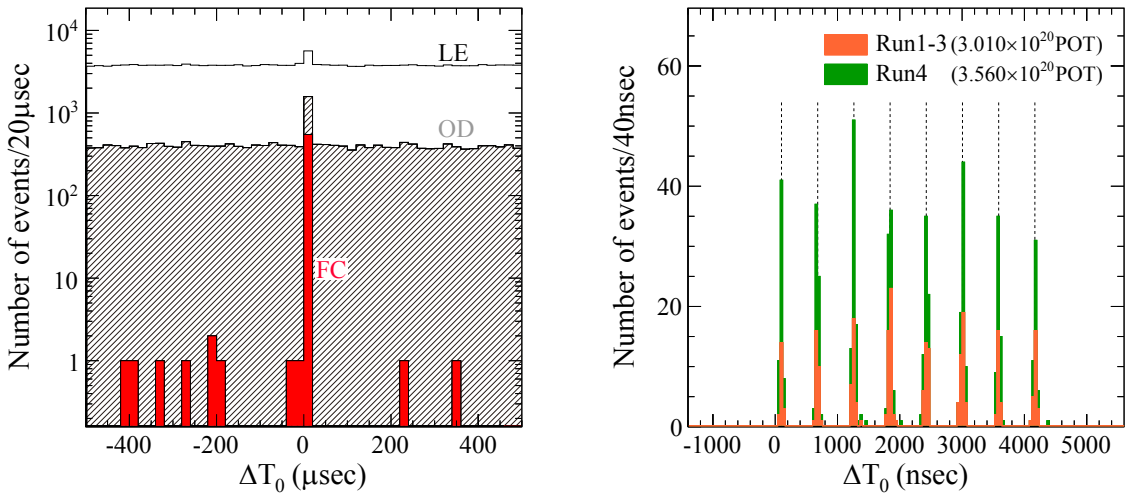

Figure E.1: Distribution of the relative event timing to the spill head timing of all FC, OD and LE events at Super-K observed in the $\pm 500\mu$s window (left) and that of FC events zoomed in the spill time (right).

E.2 Vertex distributions

Figures E.2 and E.3 show the distributions of the reconstructed vertices of observed ν_e candidate events and ν_μ candidate events at Super-K, respectively. Although the distribution of the eleven ν_e candidate events observed in Run 1-3 period is asymmetric, such an asymmetry is not observed in the newly observed 17 events. Thus, it would be due to the statistical fluctuation. In addition, the distribution of the ν_μ candidate events is homogeneous.

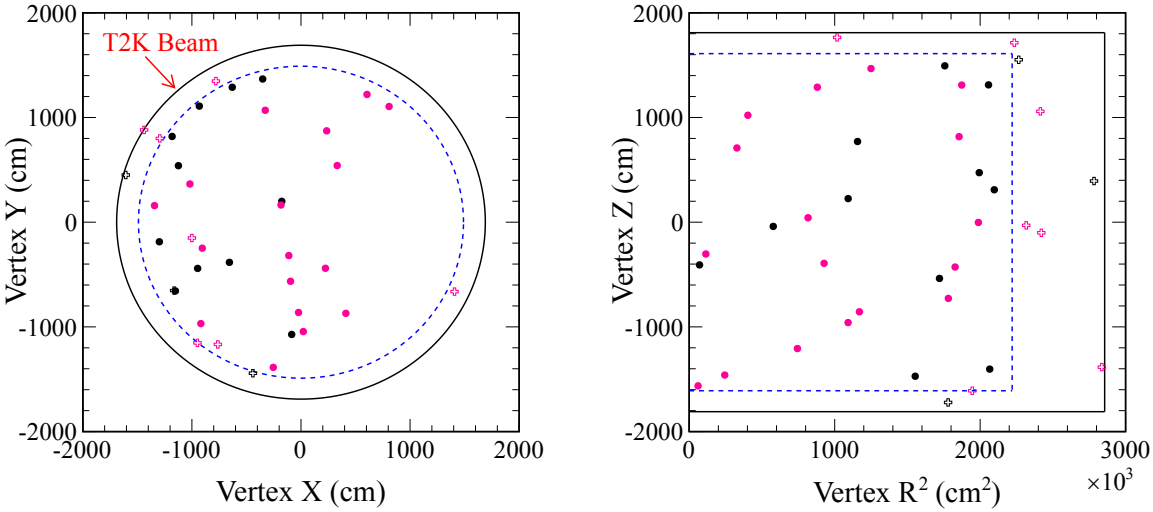

Figure E.2: Vertex distribution of ν_e candidate events at Super-K. Vertex R^2 is calculated as $R^2 = X^2 + Y^2$. Black markers are events observed during Run 1-3, and pink markers are events from Run 4. Dashed blue line indicates the fiducial volume boundary, and open crosses represent events which passed all the ν_e selection cuts except for the fiducial volume cut.

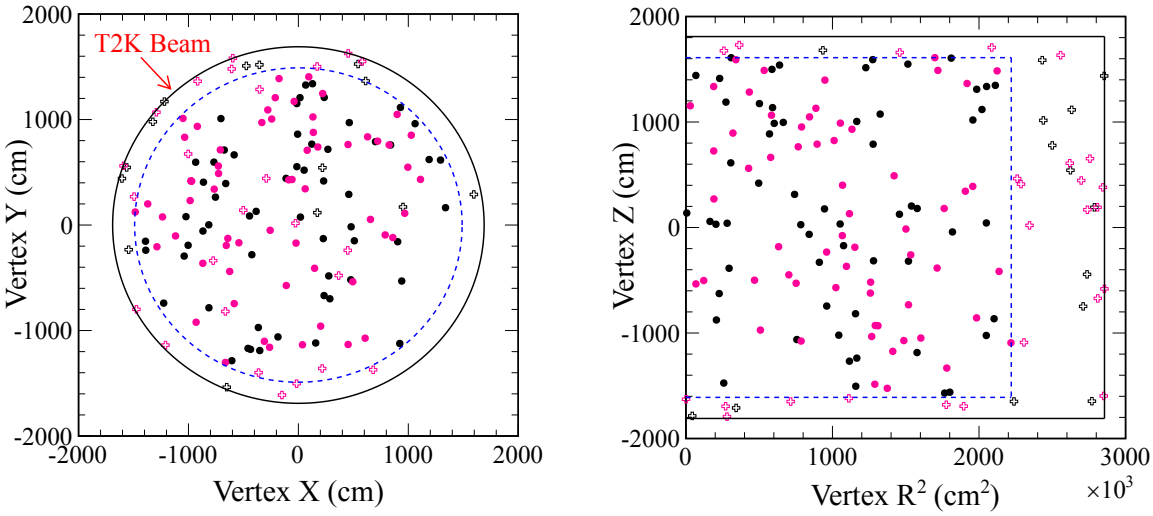

Figure E.3: Vertex distribution of ν_μ candidate events at Super-K. Legend definitions are the same as Fig. E.2.

E.3 Systematic error evaluation

Table E.1 shows the summary of the systematic errors on the FCFV and decay electron cuts. The error on the FC event selection is estimated to be 1% from the difference in the cut efficiency between the atmospheric neutrino data and the MC simulation. We estimate the uncertainty on the fiducial volume definition to be 1% by comparing the reconstructed vertex distribution of observed and simulated cosmic-ray muons which have been independently determined to have stopped inside the inner detector (ID). Errors of 0.2–0.4% are assigned for the decay electron cut for the ν_e candidate sub-samples and 1% for the ν_μ sample from the comparison of the efficiency to find delayed signals in data and MC for the cosmic-ray muons which stopped in Super-K.

Table E.1: List of the systematic error values assigned for each event type due to the FCFV and decay electron cuts.

Event type	FC cut	FV cut	Decay electron cut
Oscillated ν_e CC in ν_e selection	1.0%	1.0%	0.2%
Intrinsic beam ν_μ CC in ν_e selection	1.0%	1.0%	0.4%
Intrinsic beam ν_e CC in ν_e selection	1.0%	1.0%	0.2%
All NC in the ν_e selection	1.0%	1.0%	0.4%
All ν_μ selection	1.0%	1.0%	1.0%

Tables E.2 and E.3 show summaries of the systematic errors on topological cuts (ring-counting, PID, π^0 rejection cuts) in the ν_e selection and ν_μ selection, respectively. The errors for the ν_e CC interactions in the ν_e selection and the ν_μ CC interactions in the ν_μ selection are estimated by using the atmospheric neutrino data. The atmospheric neutrino data is useful because it covers the same energy range of the T2K neutrino beam and the similar detector response is expected. We fit the atmospheric neutrino data to derive the efficiencies of the topological cuts and their errors. In the fit, we define the efficiency parameters for three topological cuts and the nuisance parameters which represents the atmospheric neutrino flux and cross section uncertainties. The fractional uncertainties are calculated from the difference between the nominal value and the best fit value, and the uncertainties in the fit which is dominated by the statistical uncertainty. On the other hand, for the interactions with π^0 in the final state, the errors are estimated by using hybrid π^0 sample. The hybrid π^0 sample consists of one electron ring events from the real data which has overlaid with a simulated gamma-ray event to create a composite π^0. The one electron ring data is derived from atmospheric data sample or from the decay-electrons of cosmic ray muon data sample. A 126% error is assigned for the ν_e selection ν_μ CC events, which is the combined error from muons which decay in flight and those which decay at rest, weighted by their fraction in the MC. The same error shift as introduced for the ν_e selection ν_e CC single electron event type is used for the NC gamma event type but with an additional 1% error shift included (correlated in all energy and angular bins). A conservative 100% uncorrelated error for each of the ring-counting, PID and π^0 rejection cuts is assigned to the ν_e selection NC $1\pi^\pm$ and NC other event type. The ν_μ selection NC sample is assigned errors determined using an independent fit to atmospheric data. A 100% uncertainty is applied to the ν_e CC sample within the ν_μ selection.

Table E.2: List of the systematic error values assigned for each event type due to topological cuts (ring-counting, PID, π^0 rejection cuts) in the ν_e selection.

Event type	Ring-counting	Particle ID	π^0 rejection
ν_e CC1e	Atmospheric neutrino fit		
ν_e CC other	Atmospheric neutrino fit		
ν_μ CC	126%	126%	126%
ν_μ CC π^0 other	Hybrid π^0 sample		
NC1π^0	Hybrid π^0 sample		
NCπ^0 other	Hybrid π^0 sample		
NCγ	ν_e CC1e + 1%		
NC1$\pi^\pm$	100%	100%	100%
NC other	100%	100%	100%

Table E.3: List of the systematic error values assigned for each event type due to topological cuts (ring-counting, PID) in the ν_μ selection.

Event type	Ring-counting	Particle ID
ν_μ CC1μ	Atmospheric neutrino fit	0.3%
ν_μ CC other	Atmospheric neutrino fit	0.3%
ν_e CC	100%	100%
NC	21.8%	55%

Appendix F

Neutrino Interaction Target of INGRID

Precise neutrino interaction measurement requires accurate information of the neutrino interaction target. Details of the neutrino interaction target of INGRID are explained here.

F.1 Elemental composition

The scintillator strip for INGRID consists of inner scintillator material and outer reflector coating material as described in Chapter 3 (Fig. 3.9). The composition of the scintillator material is 98.97% of polystyrene (C_8H_8), 1% of PPO ($C_{15}H_{11}NO$), and 0.03% of POPOP ($C_{24}H_{16}N_2O_2$) by weight. The composition of the reflector coating material is 85% of polystyrene and 15% of titanium dioxide (TiO_2) by weight. The densities of polystyrene, PPO, POPOP, and titanium dioxide are 1.03g/cm^3, 1.06g/cm^3, 1.20g/cm^3, and 4.23g/cm^3, respectively, and their elemental compositions are shown in Table F.1. From the above quantities, the elemental compositions of the scintillator material and the reflector coating material are calculated as shown in Table F.2.

Since the mass ratio of reflector coating material is 10.12% for the INGRID-type scintillator and 6.57% for the SciBar-type scintillator, their elemental compositions are calculated as shown in Table F.3.

The fiducial volume of the standard module consists of 96.23% of iron (Fe) and 3.77% of INGRID-type scintillator by weight. The fiducial volume of the Proton Module consists of 324 INGRID-type scintillators and 432 SciBar-type scintillators. As a result, the elemental compositions of materials in the fiducial volume of the standard module and the Proton Module are calculated as shown in Table F.4.

Table F.1: The elemental compositions of polystyrene, PPO, POPOP, and titanium dioxide by weight.

	H	C	N	O	Ti
Polystyrene	7.74%	92.26%	0%	0%	0%
PPO	4.43%	79.11%	7.69%	8.78%	0%
POPOP	5.01%	81.43%	6.33%	7.23%	0%
Titanium dioxide	0%	0%	0%	40.07%	59.93%

Table F.2: The elemental composition of the scintillator material and the reflector coating material by weight.

	H	C	N	O	Ti
Scintillator material	7.71%	92.12%	0.08%	0.09%	0%
Reflector coating material	6.58%	78.42%	0%	6.01%	8.99%

Table F.3: The elemental compositions of the INGRID-type and SciBar-type scintillators by weight.

	H	C	N	O	Ti
INGRID-type scintillator	7.59%	90.74%	0.07%	0.69%	0.91%
SciBar-type scintillator	7.63%	91.22%	0.07%	0.48%	0.59%

Table F.4: The elemental compositions of the materials in the fiducial volume of the standard module and the Proton Module by weight.

	H	C	N	O	Ti	Fe
Standard module	0.29%	3.42%	0.003%	0.03%	0.03%	96.23%
Proton Module	7.61%	90.96%	0.07%	0.59%	0.76%	0%

F.2 Number of target nucleons

The number of the target nucleons in the fiducial volume of the standard module and the Proton Module is needed to measure the CC inclusive cross section per nucleon. It is calculated from the target mass measured before the detector assembly. The measured masses of the iron plates of the central standard module are summarized in Table F.5.

The iron mass in the fiducial volume region of the standard module ($M_{\mathrm{SM}}^{\mathrm{iron}}$) is calculated as follows:

$$M_{\mathrm{SM}}^{\mathrm{iron}} = 6276\mathrm{kg} \times \frac{100^2}{124^2} = 4081.7\mathrm{kg}, \tag{F.1}$$

where 6276kg is the total mass of iron layers 0∼7 from Table F.5, and $124^2(\mathrm{cm}^2)$ and $100^2(\mathrm{cm}^2)$ are dimensions of the iron plate and the fiducial volume. Iron layer 8 is not included since it is outside the fiducial volume.

The scintillator mass in the fiducial volume region of the Proton Module ($M_{\mathrm{PM}}^{\mathrm{sci}}$) is calculated as follows:

$$M_{\mathrm{PM}}^{\mathrm{sci}} = 364.19\mathrm{kg} \times \frac{100}{120.3} = 302.73\mathrm{kg}, \tag{F.2}$$

where 364.19kg is the total mass of scintillators for layers 4∼31, excluding the four outermost scintillators in each layer that lie outside of the fiducial volume, and 120.3(cm) and 100(cm) are lengths of the scintillator strip and the fiducial volume. Besides, the total mass of the WLS fibers in the fiducial region of the Proton Module ($M_{\mathrm{PM}}^{\mathrm{fib}}$) is calculated as follows:

$$M_{\mathrm{PM}}^{\mathrm{fib}} = 0.05(\mathrm{cm}) \times 0.05(\mathrm{cm}) \times \pi \times 100(\mathrm{cm}) \times 0.00103(\mathrm{kg/cm}^3) \times 756 = 0.612\mathrm{kg}, \tag{F.3}$$

where 0.05cm is the radius of the fiber, 756 is the number of fibers in the fiducial region of the Proton Module. From the masses in the fiducial module, the numbers of target nucleons for the

Table F.5: The measured masses of the iron plates of the central standard module.

Layer	0	1	2	3	4	5	6	7	8
Mass(kg)	783	783	783	780	790	784	784	789	789

standard module and the Proton Module ($T^N_{\rm SM}$ and $T^N_{\rm PM}$) are calculated as follows:

$$T^N_{\rm SM} = M^{\rm iron}_{\rm SM} \times \frac{n^{\rm Fe}_p + n^{\rm Fe}_n}{A^{\rm Fe}_r/N_A} = 2.4609 \times 10^{30}, \quad \text{(F.4)}$$

$$T^N_{\rm PM} = (M^{\rm sci}_{\rm PM} + M^{\rm fib}_{\rm PM}) \times (R^C + R^H) \times \frac{n^C_p + n^C_n + n^H_p + n^H_n}{(A^C_r + A^H_r)/N_A} = 1.7993 \times 10^{29}, \quad \text{(F.5)}$$

where R is the, n_p and n_n are the number of protons and neutrons per atom, A_r is the atomic weight and N_A is the Avogadro number (6.02214×10^{23}). Table F.6 summarizes n_p, n_n and N_A for H, C and Fe.

Table F.6: The number of protons and neutrons per atom and the atomic weight of H, C and Fe.

	H	C	Fe
Protons per atom (n_p)	1	6	26
Neutrons per atom (n_n)	0.0001	6.0107	29.9099
Atomic weight (A_r)	1.008	12.011	55.845

F.3 Number of target neutrons

The number of the target neutrons in the fiducial volume of the Proton Module is needed for the measurement the CCQE cross section per neutron. It includes neutrons in all kinds of nuclei because our CCQE cross section measurement does not discriminate the target nuclei. The calculation of the number of the target neutrons ($T^n_{\rm PM}$) is as follows:

$$T^n_{\rm PM} = (M^{\rm sci}_{\rm PM} + M^{\rm fib}_{\rm PM}) \times \frac{\sum_{i=H,C,N,O,Ti}(n^i_n \times R^i_A)}{\sum_{i=H,C,N,O,Ti}(A^i_r \times R^i_A)/N_A} = 8.4525 \times 10^{28}, \quad \text{(F.6)}$$

where R is the atomic rate in the target material, and others are the same as Eq. F.4 and F.5. Table F.7 summarizes n_n, R, and N_A for H, C, N, O and Ti.

Table F.7: The number of neutrons per atom, atomic weight, and the atomic rate in the target material.

	H	C	N	O	Ti
Neutrons per atom (n_n)	0.00015	6.011	7.00366	8.00441	25.93
Atomic weight (A_r)	1.008	12.011	14.007	15.994	47.867
Atomic rate (R_A)	49.73%	49.89%	0.03%	0.24%	0.10%

F.4 Number of target nuclei

The number of the target nuclei in the fiducial volume of the Proton Module ($T^A_{\rm PM}$) is needed to measure the CC coherent pion cross section per nuclei. It is calculated as follows:

$$T^A_{\rm PM} = (M^{\rm sci}_{\rm PM} + M^{\rm fib}_{\rm PM}) \times \frac{R^C_A}{\sum_{i=H,C,N,O,Ti}(A^i_r \times R^i_A)/N_A} = 1.3837 \times 10^{28}. \quad \text{(F.7)}$$

Appendix G

Supplemental Remarks of INGRID Analyses

The measurements of the neutrino beam properties and the neutrino interaction cross sections with INGRID were presented in Chapters 6, 7, 8 and 9. Supplemental remarks of the analyses for these measurements are given here.

G.1 Performance comparisons between the original and new beam analyses

The original analysis method for the INGRID beam measurement was established in 2010. In 2012, we developed a totally new analysis method. In this section, thorough performance comparisons between the original and new analysis methods are described.

G.1.1 Susceptibility to MPPC dark count

Figure G.1 shows the expected variations of the selection efficiency due to the MPPC dark count with original and new beam analysis methods. The effect of the MPPC dark count with the new analysis method is less than one tenth of that with the original analysis method. The difference mainly comes from the track reconstruction. The original analysis applied the event correction to compensate the effect of the MPPC dark count. It is no longer needed in the new analysis method because the effect of the MPPC dark count is vanishingly small.

G.1.2 Susceptibility to event pileup

Figure G.2 shows the expected variations of the selection efficiency due to the event pileup with original and new beam analysis methods. The effect of the event pileup with the new analysis method is less than one quarter of that with the original analysis method. The original analysis method cannot reconstruct more than one event in a bunch. Hence, when event pileup occurs, it inevitably loses events. Nevertheless, this effect was not regarded although it is significant. By contrast, in the new analysis method, even when event pileup occurs, events are handled correctly as long as the vertices are distinguishable. In addition, the remaining effect of the event pileup is properly treated by applying event correction and imposing the systematic error for it.

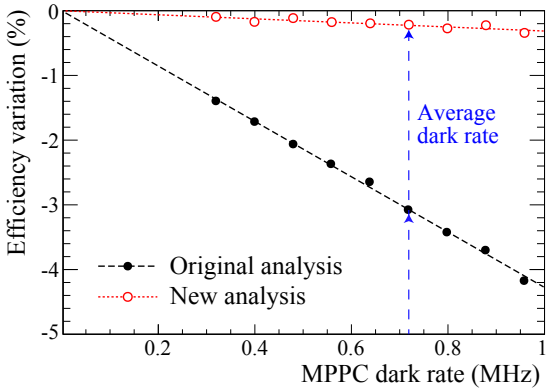

Figure G.1: Variation of the selection efficiency due to the MPPC dark count with the original and new analysis methods.

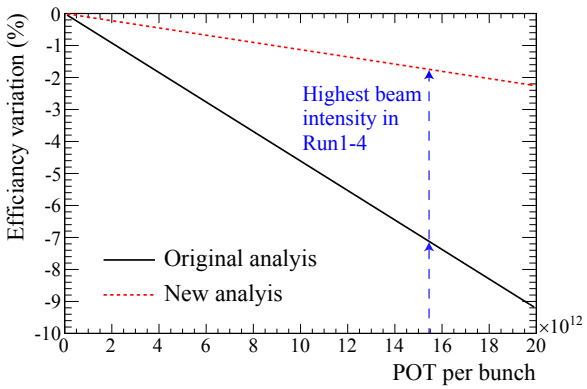

Figure G.2: Variation of the selection efficiency due to the event pileup with the original and new analysis methods.

G.1.3 Neutrino event selection efficiency

The neutrino event selection efficiency with the new analysis method is higher than that with the original analysis method as shown in Fig. G.3. The overall difference in the selection efficiency for the T2K on-axis neutrino flux is 13.2%. It is mainly attributable to the track reconstruction efficiency. The difference is especially noticeable in the high energy region. Neutrino interactions in the high energy region are dominated by the deep inelastic scatterings. Since the deep inelastic scatterings produce many particles, messy hits are observed around the neutrino interaction vertex. The track reconstruction algorithm of the new analysis method can accurately reconstruct even such messy events, whereas that of the original analysis method often fails.

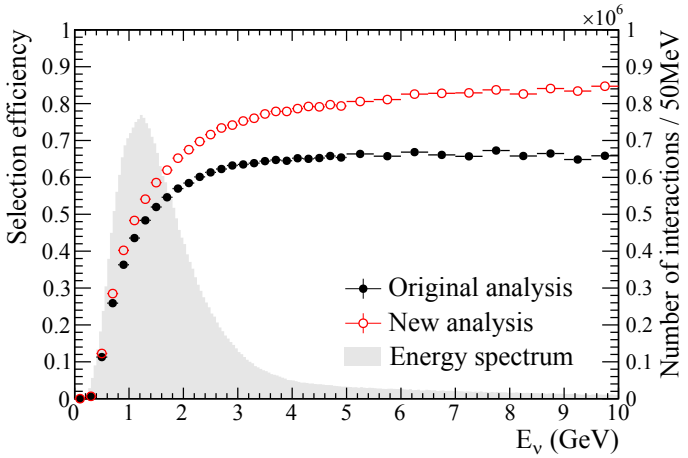

Figure G.3: Neutrino event selection efficiency as a function of true neutrino energy with the original and new analysis methods overlaid with the energy spectrum of the neutrino interactions in the standard modules.

G.1.4 Systematic error

Table G.1 shows the comparison of the systematic errors with the original and new analysis methods. In the new analysis method, the systematic errors from the event pileup and the veto cut are properly included, whereas they are not regarded in the original analysis method. Total systematic error with the new analysis method (0.91%) is less than one quarter of that with the original analysis method (3.82%). The systematic error from the hit efficiency with the original analysis is large because the uncertainty of the hit efficiency was overestimated. It is reduced in the new analysis method by re-estimating the uncertainty of the hit efficiency in a reasonable way. In addition, the systematic error for the two-dimensional track reconstruction is reduced in the new analysis method by virtue of the high track reconstruction efficiency. Furthermore, the systematic error from the three-dimensional tracking is so large in the original analysis method because of the too tight criterion of the three-dimensional tracking. In the new analysis method, the error becomes smaller since the criterion of the three dimensional tracking is improved.

Table G.1: Summary of systematic errors on the beam measurement with the original and new analysis methods.

Item	Original analysis	New analysis
Target mass	0.13%	0.13%
MPPC dark count	0.72%	0.27%
Hit efficiency	1.84%	0.39%
Event pileup	–	0.14%
Beam-induced external background	0.19%	0.27%
Cosmic-ray background	0.01%	0.01%
2D track reconstruction	1.62%	0.49%
3D tracking	2.84%	0.19%
Vertexing	–	0.43%
Timing selection	0.01%	0.01%
Veto cut	–	0.13%
Fiducial volume cut	0.28%	0.09%
Total	3.82%	0.91%

G.2 Measurement of the antineutrino beam

In 2014, T2K started to take the antineutrino beam data by inverting the horn current polarity because a combination of the neutrino beam data and the antineutrino beam data has better sensitivity to δ_{CP}. The beam property measurement with INGRID is also essential for the antineutrino beam. Thus, we studied the measurement of the antineutrino beam properties with INGRID by the MC simulation. For this study, we used the same analysis method as Chapter 6. The expected event rate in INGRID for the antineutrino beam operation is 4.94×10^{-15} per POT. It is about one-third of that for the neutrino beam operation, 1.71×10^{-14} per POT. In addition, the expected fraction of the neutrino events in INGRID for the antineutrino beam operation is 33.7%, while that of the antineutrino events for the neutrino beam operation is no more than 1.9%. These differences mainly come from the difference in the interaction cross section because the antineutrino-nucleus interaction cross section is about one-third of the neutrino-nucleus interaction cross section in a few GeV neutrino energy region as shown in Fig. G.4. Figure G.5 shows the expected antineutrino beam profile reconstructed by the INGRID measurement. Although the beam profile is well reconstructed, the reconstructed

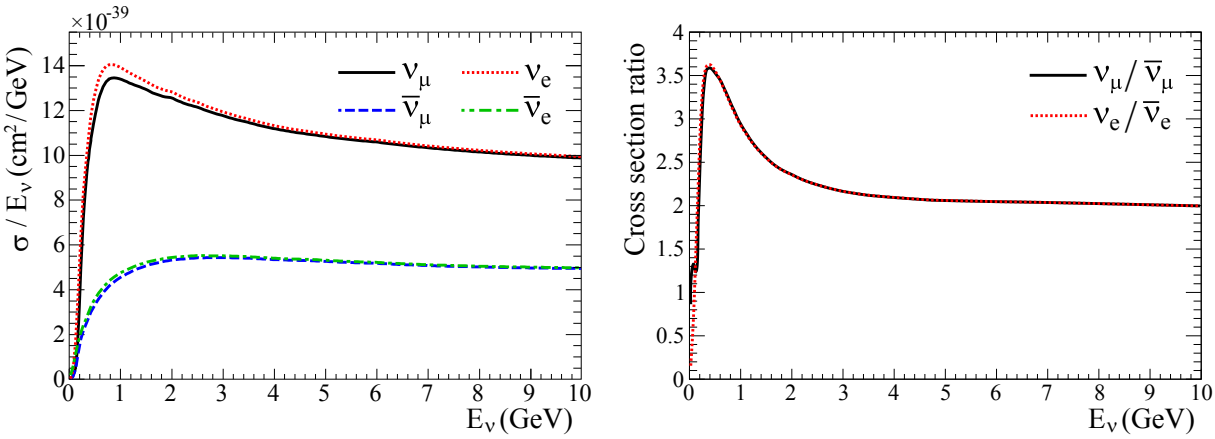

Figure G.4: Total neutrino-nucleus cross sections per nucleon divided by the neutrino energy for ν_μ, $\bar{\nu}_\mu$, ν_e and $\bar{\nu}_e$ (left) and cross section ratios for $\nu_\mu/\bar{\nu}_\mu$ and $\nu_e/\bar{\nu}_e$ (right) modeled in NEUT.

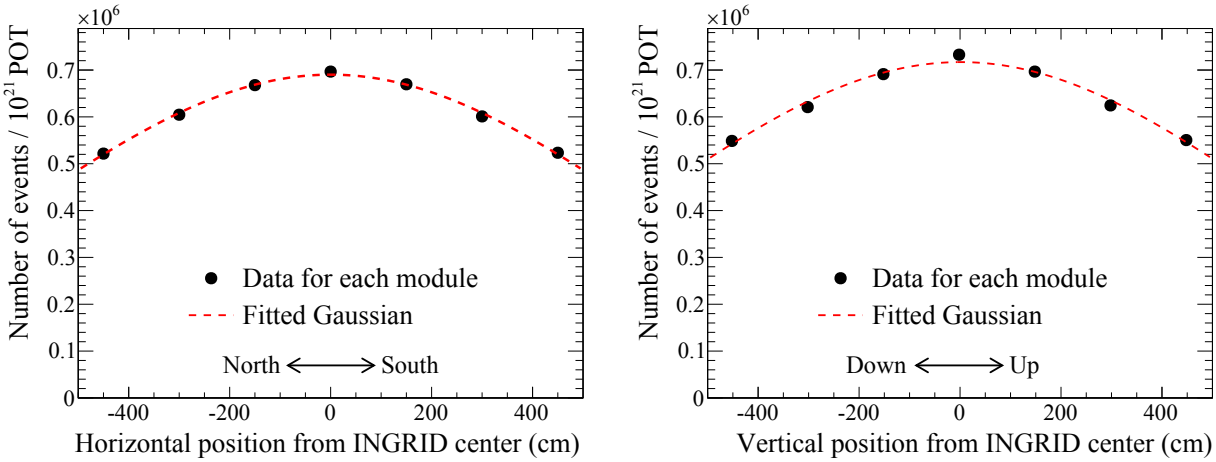

Figure G.5: Expected antineutrino beam profiles in INGRID for horizontal (left) and vertical (right) directions. Each point represents the number of selected events in each module per 10^{21} POT.

vertical profile slightly deviates from a Gaussian distribution. The spatial width of the neutrino (antineutrino) events is larger than that of the antineutrino (neutrino) events in antineutrino (neutrino) beam operation as shown in Table G.2. Thus, the reconstructed beam profile is actually a superposition of the two Gaussian distributions with different width. However, a deviation from a Gaussian distribution is not apparent in the neutrino beam operation because the fraction of the antineutrino events is very small. On the other hand, it is apparent in the antineutrino beam operation because of the large fraction of the neutrino events. However, the profile center can be accurately reconstructed even for the antineutrino beam measurement, and thus the deviation is no problem for the beam direction measurement. Consequently, the analysis method for the neutrino beam measurement is directly applicable to the antineutrino beam measurement.

Table G.2: Expected spatial width of the neutrino events and antineutrino events in neutrino and antineutrino beam operations.

	Neutrino events		Antineutrino events	
	Horizontal	Vertical	Horizontal	Vertical
Neutrino beam operation	586 cm	605 cm	683 cm	728 cm
Antineutrino beam operation	703 cm	754 cm	564 cm	589 cm

G.3 Angular distributions

The angular distributions of the CC coherent pion sample are discussed in Chapter 9. The angular distributions of other neutrino interactions also greatly depend on the neutrino interaction models as well as the CC coherent pion production. For example, when the axial-vector mass (M_A) is changed, the angular distribution greatly changes as shown in Figs.G.6 and G.7, where the angle represents the track angle with respect to the beam axis. Therefore, the angular distributions of the CC inclusive samples and the CCQE samples of INGRID are also compared with the MC predictions to test the neutrino interaction model. Figure G.8 shows the reconstructed track angle of the CC inclusive samples for the standard module and the Proton Module. Figures G.9 and G.10 show the angles of the reconstructed muon tracks and proton tracks of the CCQE samples, respectively. The angular distributions of the CC inclusive samples agree very well with the MC predictions. Although small data-MC differences exist in some angular distributions of the CCQE samples, they are also substantially consistent with the MC predictions. The CC resonant pion events make up a sizable portion of the CC inclusive samples. These facts demonstrate that the CCQE interaction and the CC resonant pion production are well understood and correctly treated in the neutrino interaction model.

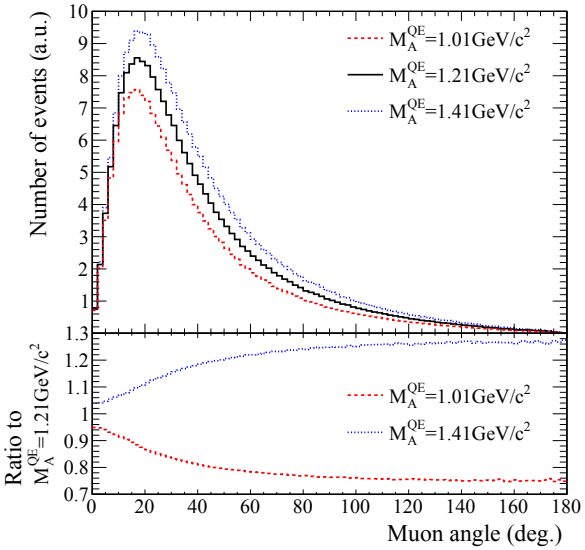

Figure G.6: Distributions of true muon angle from CCQE interactions in the Proton Module for several values of M_A^{QE}.

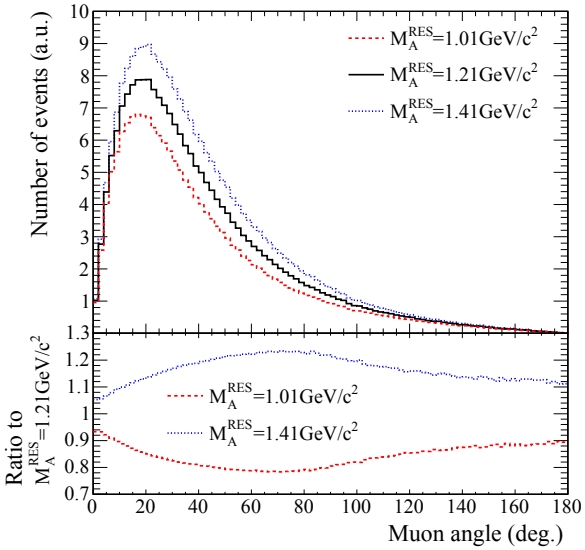

Figure G.7: Distributions of true muon angle from CC resonant pion productions in the Proton Module for several values of M_A^{RES}.

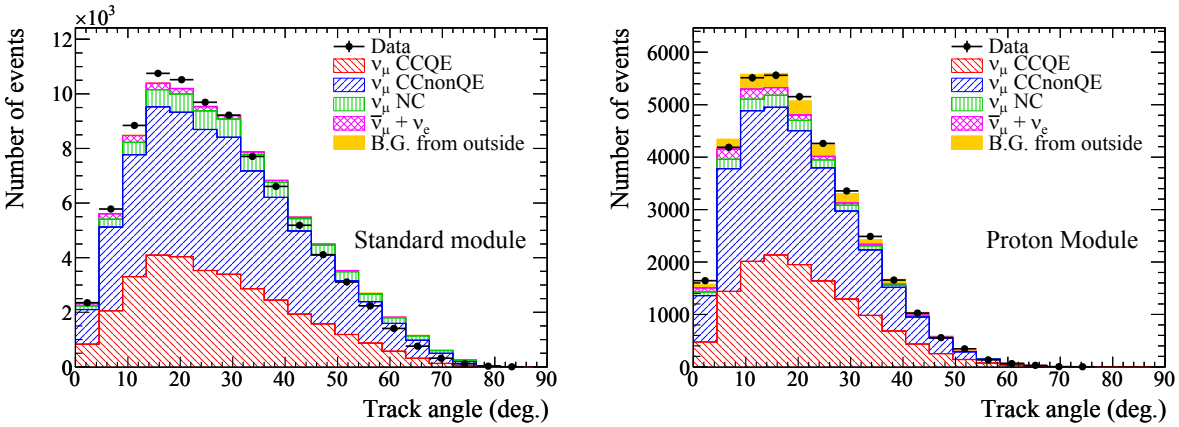

Figure G.8: Distributions of reconstructed track angle of the CC inclusive samples for the standard module (left) and the Proton Module (right). The acceptance cut is not applied to the standard module.

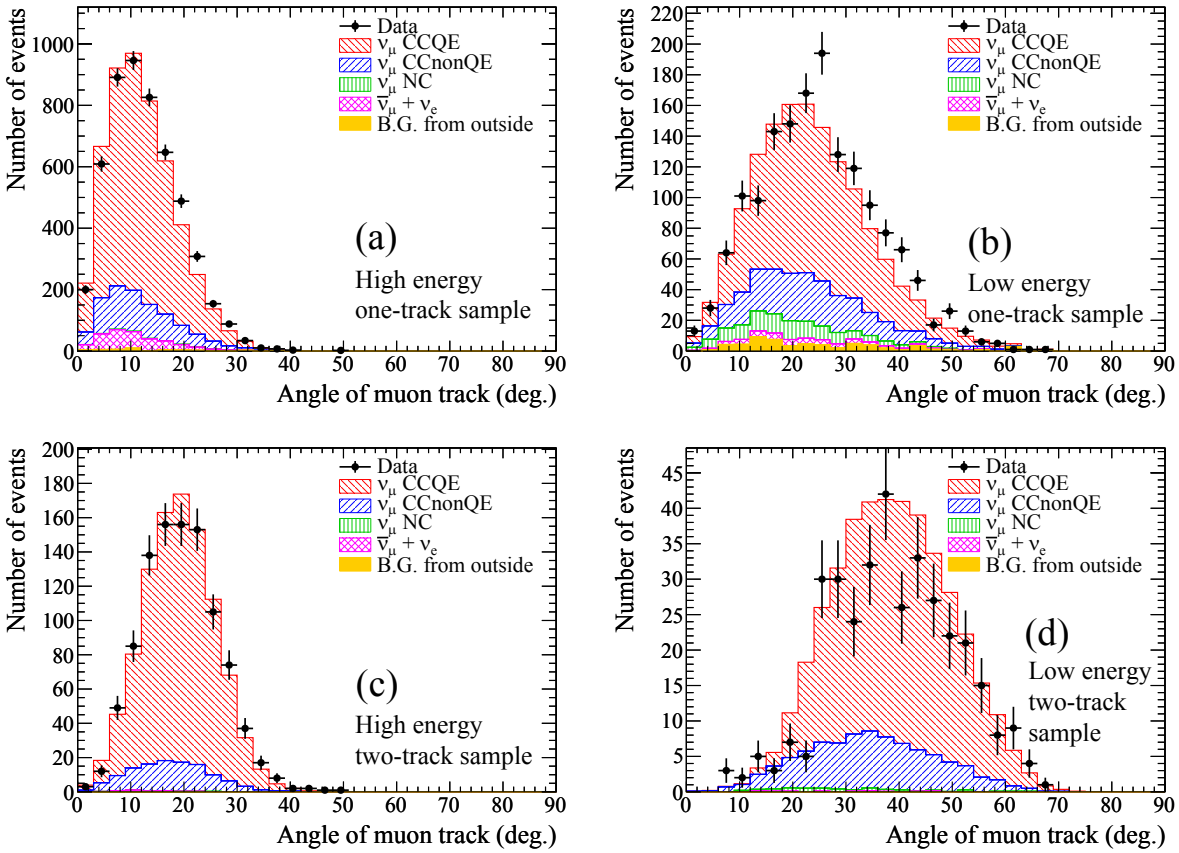

Figure G.9: Distributions of reconstructed muon track angle of the CCQE samples for the Proton Module. The CCQE sample falls into four categories: (a) high energy one-track sample, (b) low energy one-track sample, (c) high energy two-track sample, and (d) low energy two-track sample.

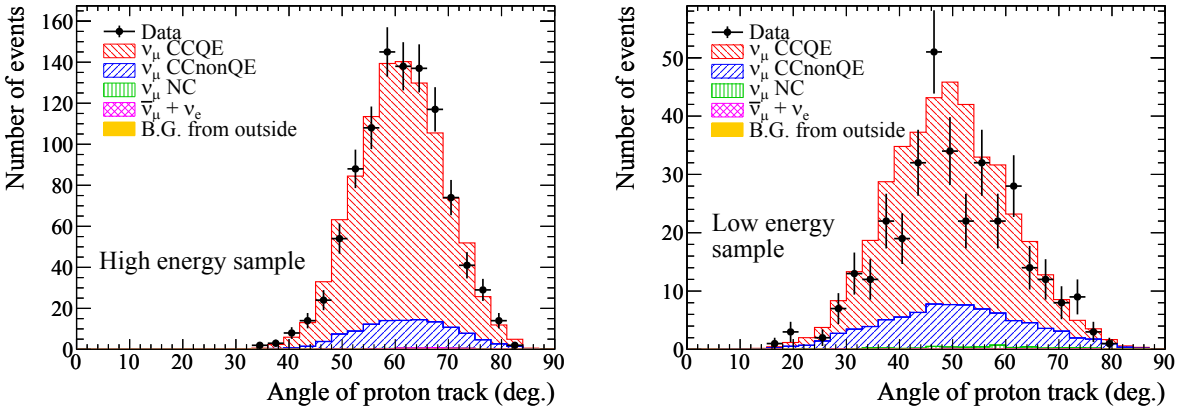

Figure G.10: Distributions of reconstructed proton track angle of the high energy CCQE sample (left) and the low energy CCQE sample (right) for the Proton Module.

G.4 Prospect of the neutrino cross section measurements of other interaction types

In this thesis, the measurements of the CC inclusive cross section, the CCQE cross section and the CC coherent pion cross section with INGRID were presented (see Chapter 7, 8 and 9 for details). However, other various neutrino cross section measurements are required in order to gain a better understanding of the neutrino interactions and reduce the systematic errors for the neutrino oscillation measurement. Thus, the prospect of the neutrino cross section measurements of some other interaction types with INGRID is discussed here.

G.4.1 CC resonant pion production

The ν_μ CC resonant pion production ($\nu_\mu + N \to \mu^- + \Delta \to \mu^- + N' + \pi$) is the main background for the ν_μ disappearance measurement in T2K because it is misidentified as the ν_μ CCQE event when the pion is not detected. In a type of the CC resonant pion production, there are a muon, a proton and a positive pion in the final state, $\nu_\mu + p \to \mu^- + \Delta^{++} \to \mu^- + p + \pi^+$. Thus, three tracks of the charged particles are expected to be reconstructed as shown in Fig. G.11. However, as with the CCQE interaction, the proton track often fails to be reconstructed. Therefore, we have to analyze not only the three-track sample but also the two-track sample for the cross section measurement of this CC resonant pion production.

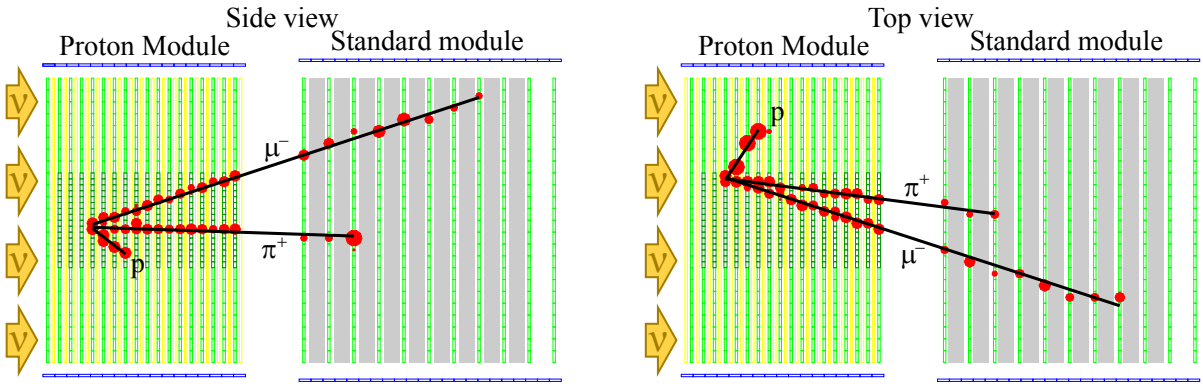

Figure G.11: Event display of an MC CC resonant pion production event in the Proton Module.

G.4.2 NC resonant pion production and NC coherent pion production

The NC resonant π^0 production ($\nu_l + N \rightarrow \nu_l + \Delta \rightarrow \nu_l + N + \pi^0$) and the NC coherent π^0 production ($\nu_l + A \rightarrow \nu_l + A + \pi^0$) are the main backgrounds for the measurement of the $\nu_\mu \rightarrow \nu_e$ oscillation in T2K because they are misidentified as the ν_e CCQE events when one of the two photons from the π^0 decay is not reconstructed. Figure G.12 shows the typical event display of an MC NC resonant π^0 production event in the Proton Module. A photon in T2K energy range (a few hundred MeV) generally makes one main track and additional hits or short tracks around the main track in the Proton Module. Thus, we will be able to identify π^0 by the two reconstructed photons. In addition, we can reduce the background events without π^0 by reconstructing the π^0 mass from the measured energies of two photons. Therefore, this measurement requires the accurate photon identification and π^0 mass reconstruction. Although the NC coherent π^0 production also generates π^0, it will be discriminable by using the vertex activity as with the CC coherent pion cross section analysis presented in Chapter 9.

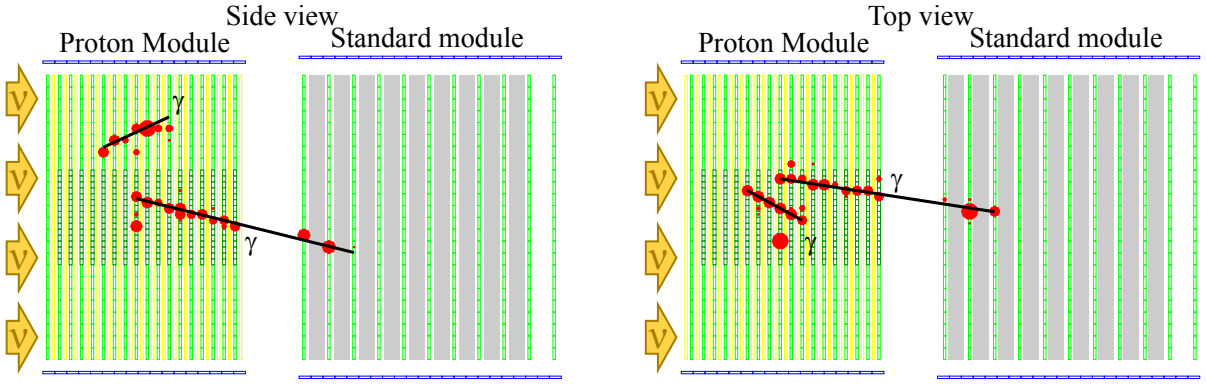

Figure G.12: Event display of an MC NC resonant π^0 production event in the Proton Module.

G.4.3 NC elastic scattering

The NC elastic scattering ($\nu_l + N \rightarrow \nu_l + N$) is of capital interest to the neutrino interaction physics community because it is the most elementary neutrino-nucleon interaction. The NC elastic scattering with a proton in the Proton Module generates a proton track with large dE/dx as shown in Fig. G.13. However, a neutron coming from the outside of the Proton Module also can scatter a proton in the Proton Module. Thus, it will be the main background for the NC elastic cross section measurement. This background component will be able to be reduced by

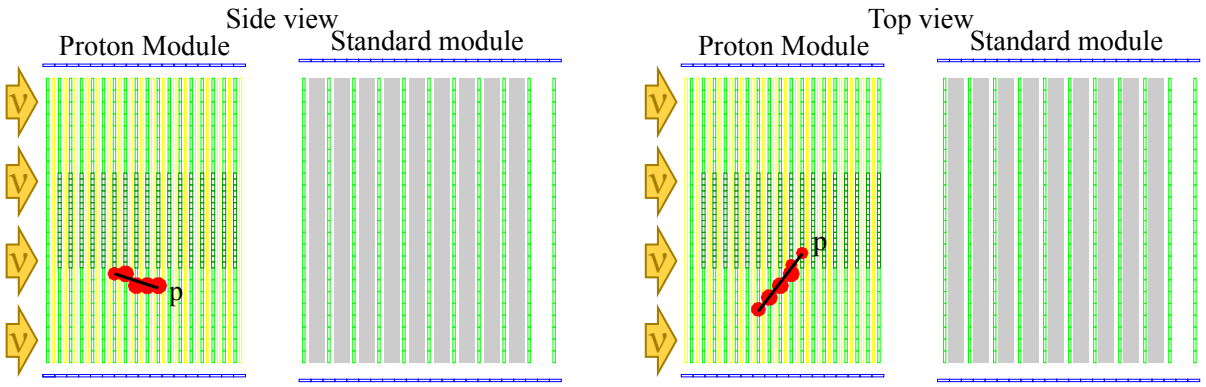

Figure G.13: Event display of an MC NC elastic scattering event in the Proton Module.

selecting the events in the central volume of the Proton Module because many of the background neutrons from outside will scatter the protons in the outer volume of the Proton Module.

Appendix H

Supplemental Remarks of Neutrino Oscillation Analysis

The measurement of the neutrino oscillations in T2K was presented in Chapters 10. Supplemental remarks of the neutrino oscillation analysis are given here.

H.1 Binning of the covariance matrix

In our neutrino oscillation analysis, the oscillation analysis fitting procedure can be sped up by decreasing the number of bins in the covariance matrix since a systematic error nuisance parameter is allocated to each bin in the covariance matrix. However, if the oscillation analysis results are sensitive to the number of bins, it should not be decreased. Therefore, we tested the results of the fitting with some different binnings for the covariance matrix. We define three binnings; the fine binning using the original 98 bins, the medium binning using 50 bins, and the coarse binning using 20 bins. The systematic error covariance matrix with each binning is shown in Fig. H.1. Figure H.2 shows the results of fitting a pseudo data using each binning for the covariance matrix. Even if the number of bins is decreased, the oscillation analysis result stays at the same. It is true of the results of fitting any other pseudo data which were generated assuming various sets of oscillation parameters. Meanwhile, the fitting procedure actually becomes faster by decreasing the number of bins. Therefore, we used the coarse binning for the covariance matrix.

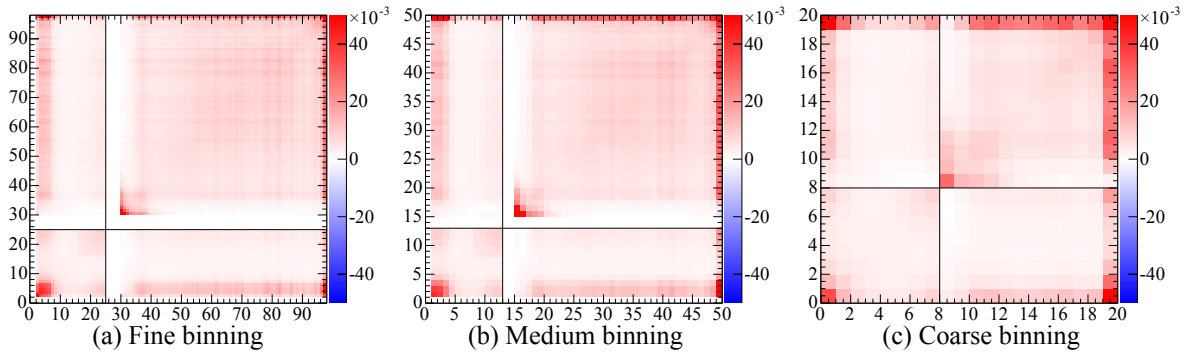

Figure H.1: Systematic error covariance matrices for the nominal oscillation parameters with different binnings. Dashed lines show partings between ν_e candidate events and ν_μ candidate events.

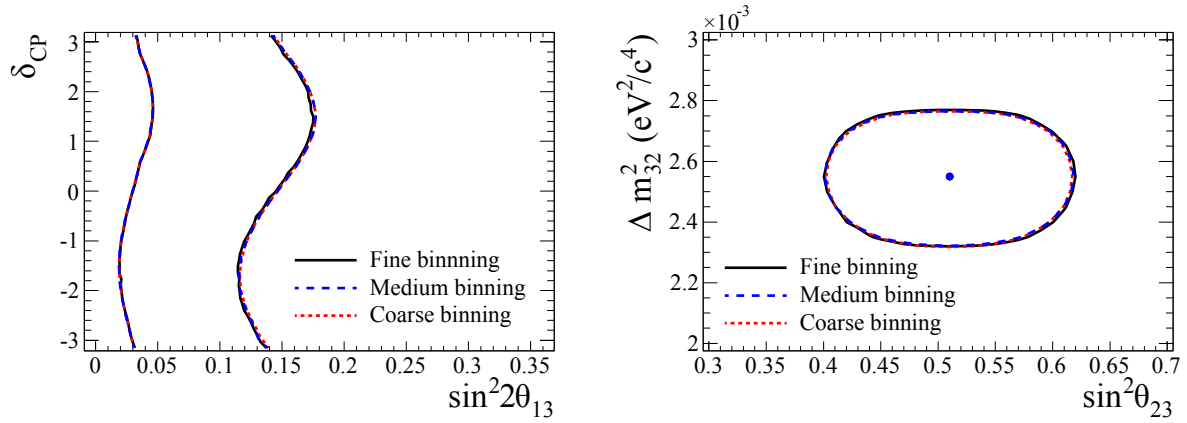

Figure H.2: The 90% C.L. allowed regions for δ_{CP} vs $\sin^2 2\theta_{13}$ (left) and $\sin^2\theta_{23}$ vs Δm^2_{32} (right) extracted by fitting a pseudo data with different binnings for the covariance matrix.

H.2 Oscillation parameter dependence of the covariance matrix

The systematic error covariance matrix depends on the oscillation parameters as described in Chapter 10. Its effect on the neutrino oscillation analysis is checked. Figure H.3 shows the results of fitting pseudo data with single covariance matrix assuming the nominal oscillation parameters and multiple covariance matrices which depend on the oscillation parameters. There are apparent differences in the results. Therefore, we conclude that this effect is not negligible for the oscillation analysis, and use multiple covariance matrices which depend on the oscillation parameters.

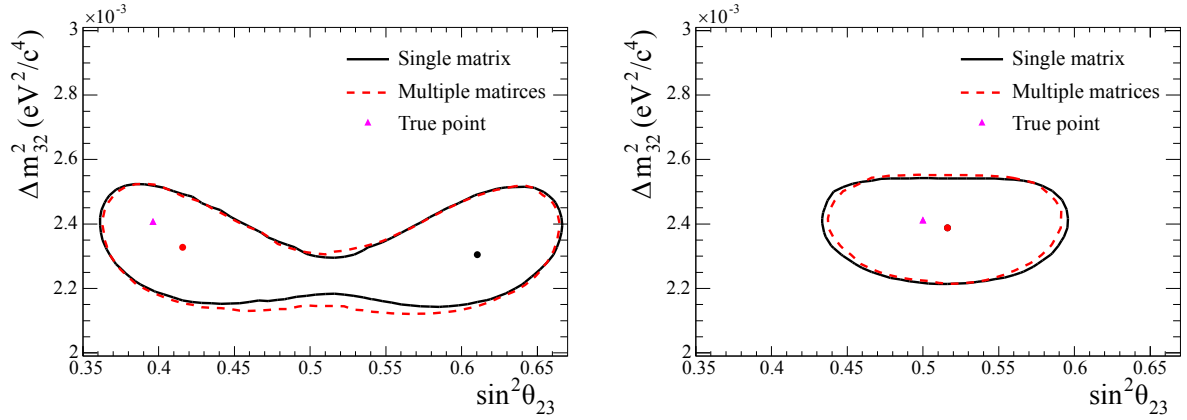

Figure H.3: The 90% C.L. allowed regions for $\sin^2\theta_{23}$ and Δm^2_{32} extracting by fitting pseudo data with single systematic error covariance matrix and 201×201 sets of covariance matrices. One pseudo data assumes $\sin^2\theta_{23} = 0.4$ (left), and the other assumes $\sin^2\theta_{23} = 0.5$ (right).

H.3 Bias check

The potential bias of the fitter was verified by checking the pull distributions [368] of the fit parameters. First, toy MC data sets were generated for fixed oscillation parameters according to the following procedure:

1. A set of the systematic error parameters is randomly generated following the constraints on those parameters.

2. The predicted reconstructed neutrino energy spectrum for an assumed condition of oscillation parameters and data statistics (*i.e.* POT) is calculated using the generated systematic error parameter values.

3. The number of events in each reconstructed neutrino energy bin is statistically fluctuated following a Poisson distribution.

Then, the number of observed events and their reconstructed neutrino energy for this toy MC data set are input into the oscillation fit algorithm and the $\Delta\chi^2$ contours are calculated as described in Chapter 10. Finally, the "pull" of this measurement result is calculated as

$$\text{Pull} = \begin{cases} \frac{\tau_{\text{fit}} - \tau_{\text{true}}}{\sigma_+} & (\text{if } \tau_{\text{fit}} < \tau_{\text{true}}) \\ \frac{\tau_{\text{fit}} - \tau_{\text{true}}}{\sigma_-} & (\text{if } \tau_{\text{fit}} > \tau_{\text{true}}) \end{cases} \tag{H.1}$$

where τ_{fit} is the best fit value of the oscillation parameters, τ_{true} is an assumed value of the oscillation parameters, and σ_+ (σ_-) is the positive (negative) side 1σ error as illustrated in Fig. H.4. If no bias exists on the measurement in this analysis, the pull distribution derived

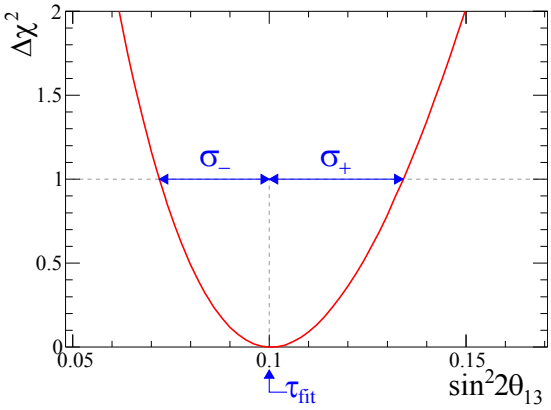

Figure H.4: Definition of σ_+ and σ_- in Eq. H.1.

from many toy MC data sets should be the standard normal distribution (mean=0, standard deviation=1). In this study, fits of 500 toy MC data sets are performed to check possible biases via the pull distributions. Table H.1(a) shows the means and standard deviations of the pulls of the oscillation parameters when the toy MC data assume $\sin^2 2\theta_{13} = 0.1$, $\sin^2\theta_{23} = 0.517^*$, $\Delta m^2_{32} = 2.4 \times 10^{-3}\text{eV}^2$, $\delta_{CP} = 0$ and the normal hierarchy. The mean of the pulls for Δm^2_{23} and the standard deviation of the pulls for $\sin^2 2\theta_{13}$ are a little shifted from zero and one, respectively. On the other hand, when the value of δ_{CP} is fixed to zero in the fit, the means and standard deviations for the pulls are closer to zero and one as shown in Table H.1(b). This can be explained by the fact that δ_{CP} is basically unconstrained by a fit to the T2K Run 1-4 data alone, so fitting this unconstrained parameter may cause slight biases in the fit values of the other parameters. Likewise, when the reactor constraint is applied, the means and standard deviations of the pulls are also close to zero and one as shown in Table H.2 because the δ_{CP} is constrained. Therefore, we concluded that there are no unknown biases in the fitter.

*When θ_{13} is fixed at $\sin^2 2\theta_{13} = 0.1$, the ν_μ disappearance probability becomes maximal at $\sin^2\theta_{23} = 0.517$.

Table H.1: Means and standard deviations of the pulls of the oscillation parameters when the toy MC data assume $\sin^2 2\theta_{13} = 0.1$, $\sin^2\theta_{23} = 0.517$, $\Delta m^2_{32} = 2.4 \times 10^{-3}\text{eV}^2$, $\delta_{CP} = 0$ and the normal hierarchy.

	(a) δ_{CP} is free.			(b) δ_{CP} is fixed to zero.		
	$\sin^2 2\theta_{13}$	$\sin^2\theta_{23}$	Δm^2_{32}	$\sin^2 2\theta_{13}$	$\sin^2\theta_{23}$	Δm^2_{32}
Mean	0.14	−0.07	0.25	0.12	0.15	0.09
Standard deviation	0.86	0.92	1.13	1.07	1.05	0.94

Table H.2: Means and standard deviations of the pulls of the oscillation parameters with the reactor constraint when the toy MC data assume $\sin^2 2\theta_{13} = 0.1$, $\sin^2\theta_{23} = 0.517$, $\Delta m^2_{32} = 2.4 \times 10^{-3}\text{eV}^2$, $\delta_{CP} = 0$ and the normal hierarchy.

	$\sin^2 2\theta_{13}$	$\sin^2\theta_{23}$	Δm^2_{32}	δ_{CP}
Mean	−0.10	0.13	0.07	0.08
Standard deviation	0.94	1.02	0.93	0.99

H.4 Comparisons with the stand-alone neutrino oscillation analysis results

So far, the analysis for the measurement of θ_{13} and δ_{CP} via the $\nu_\mu \to \nu_e$ oscillation and that of θ_{23} and Δm^2_{32} via the $\nu_\mu \to \nu_\mu$ oscillation had been performed independently [47, 112–116]. In these stand-alone oscillation analyses, the likelihood functions for the $\nu_\mu \to \nu_e$ and $\nu_\mu \to \nu_\mu$ oscillation measurements have been given as:

$$\mathcal{L}(\boldsymbol{N}^{\mathbf{obs}}_{\boldsymbol{\nu_e}}, \theta_{13}, \delta_{CP}, \boldsymbol{f}) = \mathcal{L}_{\nu_e}(\boldsymbol{N}^{\mathbf{obs}}_{\boldsymbol{\nu_e}}, \theta_{13}, \delta_{CP}, \boldsymbol{f}) \times \mathcal{L}_{\text{syst}}(\boldsymbol{f}), \tag{H.2}$$

$$\mathcal{L}(\boldsymbol{N}^{\mathbf{obs}}_{\boldsymbol{\nu_\mu}}, \theta_{23}, \Delta m^2_{23}, \boldsymbol{f}) = \mathcal{L}_{\nu_\mu}(\boldsymbol{N}^{\mathbf{obs}}_{\boldsymbol{\nu_\mu}}, \theta_{23}, \Delta m^2_{23}, \boldsymbol{f}) \times \mathcal{L}_{\text{syst}}(\boldsymbol{f}), \tag{H.3}$$

where $\mathcal{L}_{\nu_e}$ and $\mathcal{L}_{\nu_\mu}$ are the ν_e and ν_μ spectrum terms, and $\mathcal{L}_{\text{syst}}$ is the systematic error term in analogy with Eq. 10.3. In this thesis, the first results of the joint neutrino oscillation analysis are presented. This section describes the comparisons of the results between the joint analysis and the stand-alone analyses. Figures H.5 and H.5 show the results of the T2K joint oscillation analysis compared with those of the T2K stand-alone $\nu_\mu \to \nu_e$ and $\nu_\mu \to \nu_\mu$ oscillation analyses [115, 116]. Figure H.7 shows the $\Delta\chi^2$ as a function of δ_{CP} of the T2K stand-alone $\nu_\mu \to \nu_e$ oscillation analysis with the critical $\Delta\chi^2$ 90% C.L. limit. Comparison of the 90% allowed regions of δ_{CP} between the T2K joint oscillation analysis and the T2K stand-alone $\nu_\mu \to \nu_e$ oscillation analysis is given in Fig. H.8. They all use the T2K Run 1-4 data set. However, there are some other differences than the simultaneous treatment of the ν_e candidate events and the ν_μ candidate events:

- The joint oscillation analysis uses the reconstructed neutrino energy spectrum for the maximum likelihood fit, while the stand-alone $\nu_\mu \to \nu_e$ oscillation analysis uses the momentum and angular distribution of the outgoing electrons.
- The joint oscillation analysis uses the reactor θ_{13} constraint from PDG2013 ($\sin^2 2\theta_{13} = 0.095 \pm 0.010$), while the stand-alone $\nu_\mu \to \nu_e$ oscillation analysis uses that from PDG2012 ($\sin^2 2\theta_{13} = 0.098 \pm 0.013$).
- The joint oscillation analysis truncates the spectral function parameter between 0 and 1[†], while the stand-alone $\nu_\mu \to \nu_e$ and $\nu_\mu \to \nu_\mu$ oscillation analyses do not truncate it.

[†]This treatment is approved as a more reasonable treatment in the T2K collaboration.

The results of the joint oscillation analysis are compatible with those of the stand-alone analyses. Moreover, the precisions of the oscillation parameter measurements with the joint analysis are a little better than those with the stand-alone analyses. The impact of the joint oscillation analysis is currently small because the precision of the oscillation parameter measurements is dominated by the statistical error. In the future, the impact of the joint oscillation analysis will be larger as more beam data is accumulated.

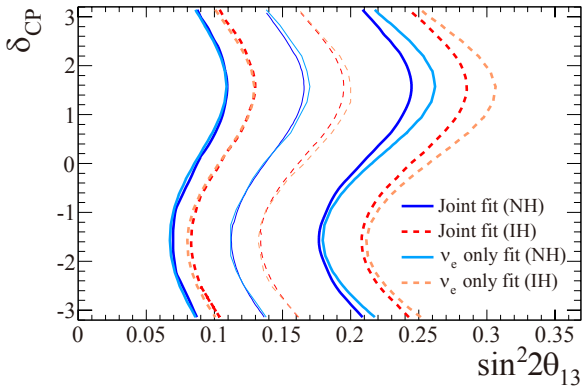

Figure H.5: The 90% C.L. allowed regions for $\sin^2 2\theta_{13}$ and δ_{CP} extracted by the T2K joint oscillation analysis and the T2K stand-alone $\nu_\mu \to \nu_e$ oscillation analysis. [115]. The reactor θ_{13} constraint is not applied.

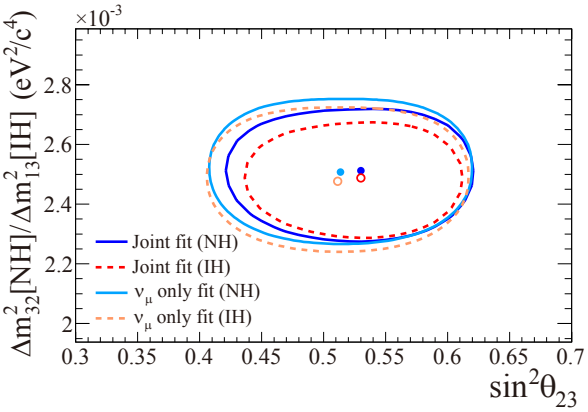

Figure H.6: The 90% C.L. allowed regions for $\sin^2\theta_{23}$ and Δm^2_{32} (NH) or Δm^2_{13}(IH) with reactor θ_{13} constraint extracted by the T2K joint oscillation analysis and the T2K stand-alone $\nu_\mu \to \nu_\mu$ oscillation analysis [116].

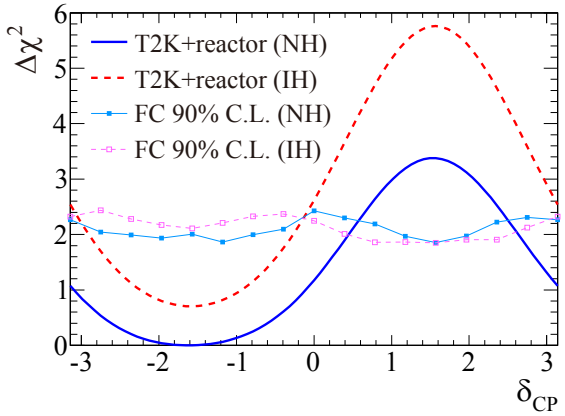

Figure H.7: The $\Delta\chi^2$ as a function of δ_{CP} of the T2K stand-alone $\nu_\mu \to \nu_e$ oscillation analysis with the critical $\Delta\chi^2$ 90% C.L. limit extracted by using the Feldman-Cousins method [115].

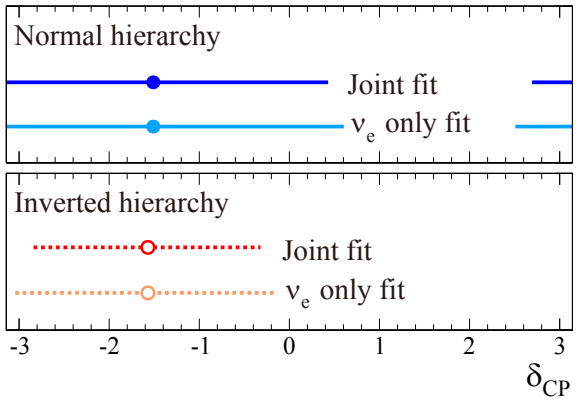

Figure H.8: The 90% allowed regions of δ_{CP} extracted by the T2K joint oscillation analysis and the T2K stand-alone $\nu_\mu \to \nu_e$ oscillation analysis [115].

H.5 Future sensitivity of the neutrino oscillation measurement

H.5.1 T2K sensitivity

To demonstrate the physics potential of T2K, we studied the expected future sensitivity to the oscillation parameters using the same analysis method as Chapter 10, where systematic errors

are implemented as the covariance matrices. The T2K neutrino beamline can generate either neutrino beam or antineutrino beam by changing the polarity of the horn current. In the Run 1-4 periods, the neutrino beam data had been taken (ν mode). In 2014, we started to take the antineutrino beam data ($\bar{\nu}$ mode). Thus, we explored the sensitivities for the cases of 100% ν mode and 50% ν mode plus 50% $\bar{\nu}$ mode. The sensitivities depend on the true oscillation parameter values. In this study, the nominal oscillation parameters (Table 10.1) are assumed as the true values unless otherwise noted.

Measurement precisions vs POT

Figure H.9 shows the expected measurement precisions of $\sin^2 2\theta_{13}$, $\sin^2 \theta_{23}$ and Δm^2_{32} as a function of the accumulated POT. Although the statistical errors are currently dominant, they will

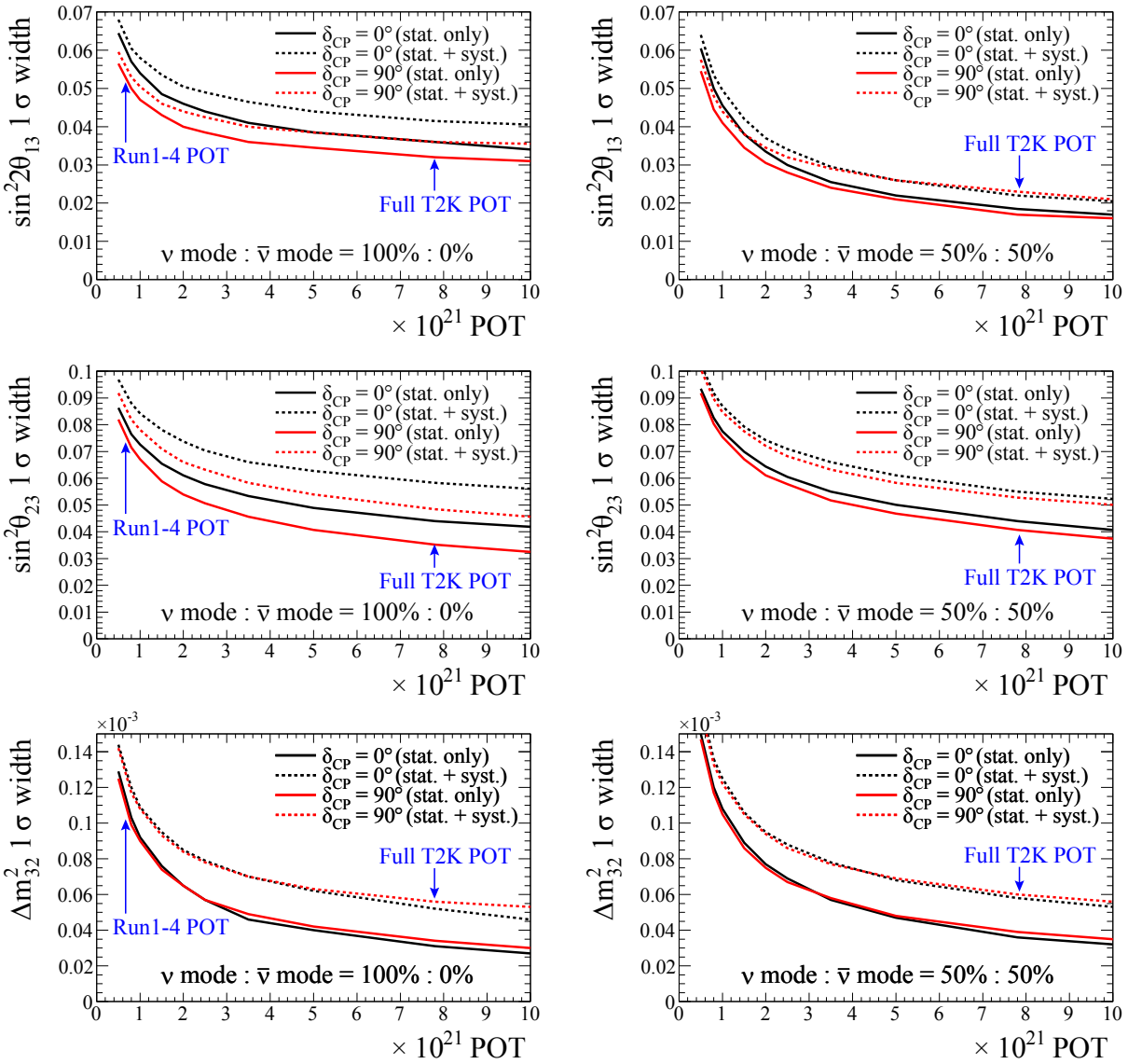

Figure H.9: The expected measurement precisions of $\sin^2 2\theta_{13}$ (top), $\sin^2 \theta_{23}$ (middle) and Δm^2_{32} (bottom) as a function of the accumulated POT for the cases of 100% ν mode (left) and 50% ν mode plus 50% $\bar{\nu}$ mode (right). The reactor θ_{13} constraint is used to estimate the precisions of $\sin^2 \theta_{23}$ and Δm^2_{32}.

be gradually reduced with increasing the accumulated POT. The expected measurement precision of $\sin^2 2\theta_{13}$ is much better for the case of 50% ν mode plus 50% $\bar{\nu}$ mode. By contrast, those of $\sin^2\theta_{23}$ and Δm^2_{32} does not have significant differences between the neutrino running modes. The expected measurement precisions of $\sin^2 2\theta_{13}$, $\sin^2\theta_{23}$ and Δm^2_{32} for the approved full T2K statistics, 7.8×10^{21} POT, are 0.042, 0.058 and $5.6{\times}10^{-5}\mathrm{eV}^2$ (0.022, 0.055 and $5.8{\times}10^{-5}\mathrm{eV}^2$), respectively, for the case of 100% ν mode (50% ν mode plus 50% $\bar{\nu}$ mode) when the nominal oscillation parameters are assumed. They will be further improved if the systematic errors are reduced.

Sensitivity for resolving non-maximal mixing θ_{23}

Figure H.10 shows the $\sin^2\theta_{23}$ region where the non-maximal mixing of θ_{23} ($\theta_{23} \neq \pi/4$) is expected to be resolved as a function of POT. When the approved full T2K statistics are achieved, the non-maximal mixing of θ_{23} is expected to be resolved with 90% C.L. if $\sin^2\theta_{23} < 0.44$ or $\sin^2\theta_{23} > 0.59$.

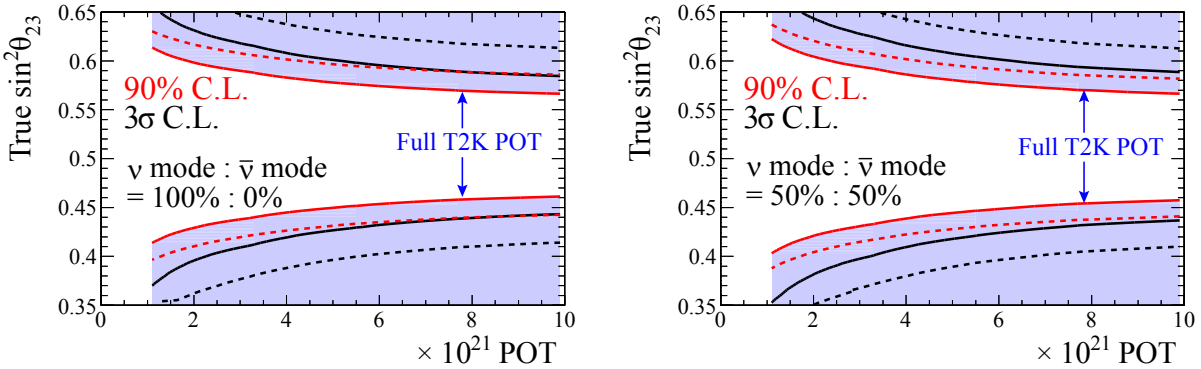

Figure H.10: The $\sin^2\theta_{23}$ region where the non-maximal mixing of θ_{23} ($\theta_{23} \neq \pi/4$) is expected to be resolved as a function of POT for the cases of 100% ν mode (left) and 50% ν mode plus 50% $\bar{\nu}$ mode (right).

Sensitivity for resolving non-zero $\sin\delta_{CP}$

Figure H.11 shows the expected $\Delta\chi^2$ for resolving $\sin\delta_{CP} \neq 0$ as a function of POT when true $\delta_{CP} = -\pi/2$. The statistical error which is currently dominant, will be gradually reduced with

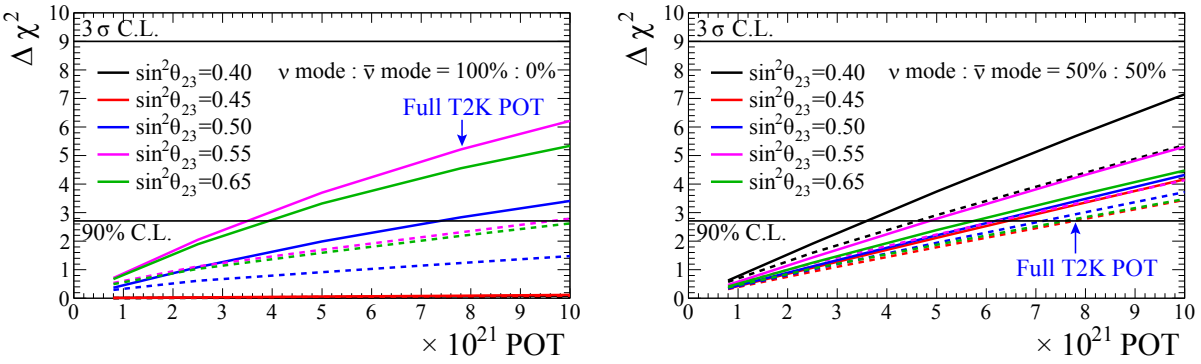

Figure H.11: The expected $\Delta\chi^2$ for resolving $\sin\delta_{CP} \neq 0$ as a function of POT for the cases of 100% ν mode (left) and 50% ν mode plus 50% $\bar{\nu}$ mode (right) when true $\delta_{CP} = -\pi/2$. The solid lines assume statistical error only, while the dashed lines include systematic errors.

increasing the accumulated POT. Figure H.12 shows the expected $\Delta\chi^2$ for resolving $\sin\delta_{CP} \neq 0$ as a function of true δ_{CP} for full T2K POT (7.8×10^{21} POT). When the mass hierarchy is the normal hierarchy (the inverted hierarchy), the sensitivity becomes maximal at true $\delta_{CP} = -\pi/2$ (true $\delta_{CP} = \pi/2$). The maximal sensitivity is the 2σ level.

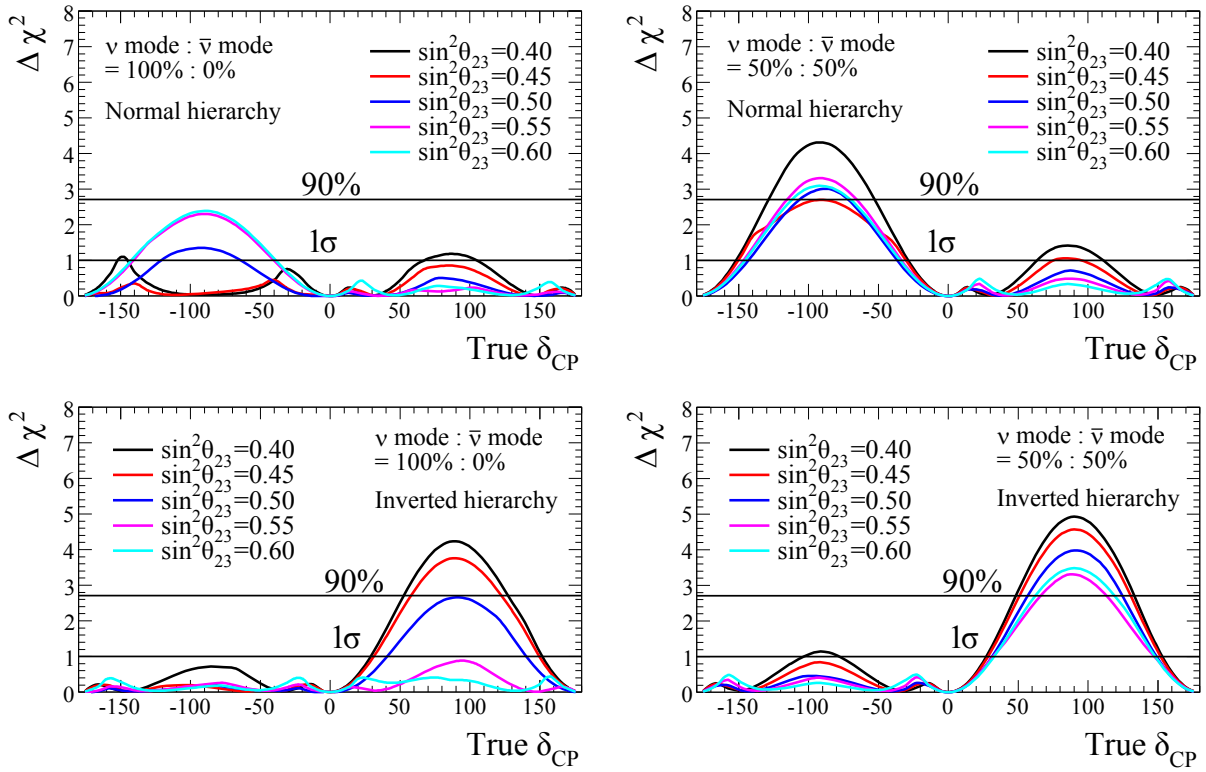

Figure H.12: The expected $\Delta\chi^2$ for resolving $\sin\delta_{CP} \neq 0$ as a function of true δ_{CP} for full T2K POT (7.8×10^{21} POT). Systematic errors are included. The true mass hierarchy is assumed to be the normal hierarchy (top) or the inverted hierarchy (bottom). The run mode is assumed to be 100% ν mode (left) or 50% ν mode plus 50% $\bar{\nu}$ mode (right).

H.5.2 T2K–NOνA combined sensitivity

The NOνA experiment [72], which has a longer baseline (810 km) and higher peak neutrino energy (2 GeV) than T2K, started the beam operation in 2014. By virtue of the longer baseline, the $\nu_\mu \to \nu_e$ oscillation measurement in the NOνA experiment is more sensitive to the matter effect, thus has a greater sensitivity to the mass hierarchy. Thus, we can attain better sensitivities to the oscillation parameters and the mass hierarchy by combining the neutrino oscillation measurements of the two experiments.

Sensitivity for resolving non-zero $\sin\delta_{CP}$

Figure H.13 shows the expected $\Delta\chi^2$ for resolving $\sin\delta_{CP} \neq 0$, as a function of δ_{CP} for T2K, NOνA, and T2K+NOνA[‡]. It demonstrates that the combination of T2K and NOνA will considerably enhance the sensitivity for resolving non-zero $\sin\delta_{CP}$. The maximal sensitivity is the 3σ level.

[‡]The inputs describing the NOνA experiment were developed in conjunction with NOνA collaborators.

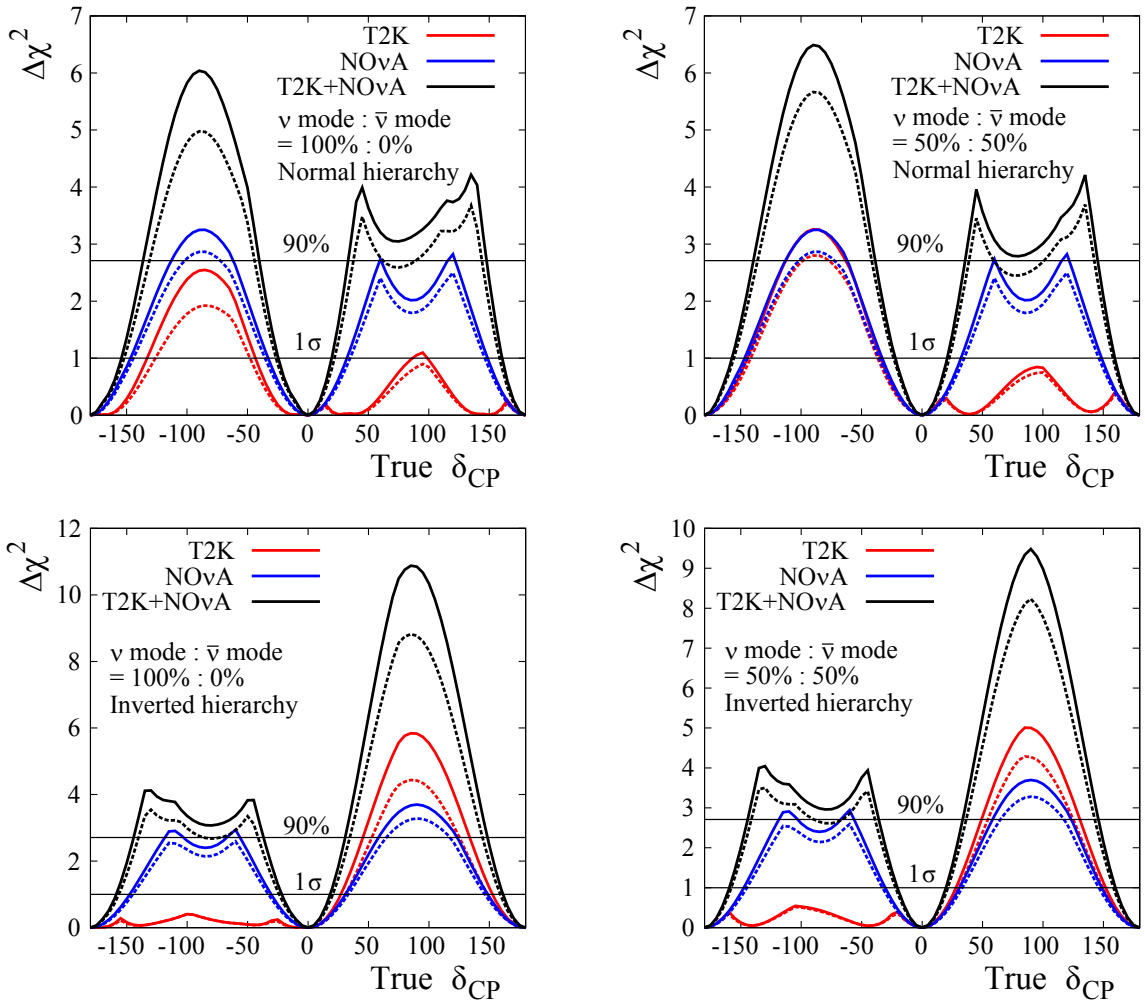

Figure H.13: The expected $\Delta\chi^2$ for resolving $\sin\delta_{CP} \neq 0$, as a function of true δ_{CP} for T2K, NOνA, and T2K+NOνA. Dashed (solid) indicate studies where normalization systematics are (not) considered. The true mass hierarchy is assumed to be the normal hierarchy (top) or the inverted hierarchy (bottom). The T2K run mode is assumed to be 100% ν mode (left) or 50% ν mode plus 50% $\bar{\nu}$ mode (right). The NOνA run mode is assumed to be 50% ν mode plus 50% $\bar{\nu}$ mode.

Sensitivity for resolving mass hierarchy

Figure H.14 shows the expected $\Delta\chi^2$ for resolving the mass hierarchy as a function of true δ_{CP} for T2K, NOνA, and T2K+NOνA. As with the sensitivity for resolving non-zero $\sin\delta_{CP}$, the sensitivity for resolving the mass hierarchy also becomes maximal at true $\delta_{CP} = -\pi/2$ (true $\delta_{CP} = \pi/2$) when the mass hierarchy is the normal hierarchy (the inverted hierarchy).

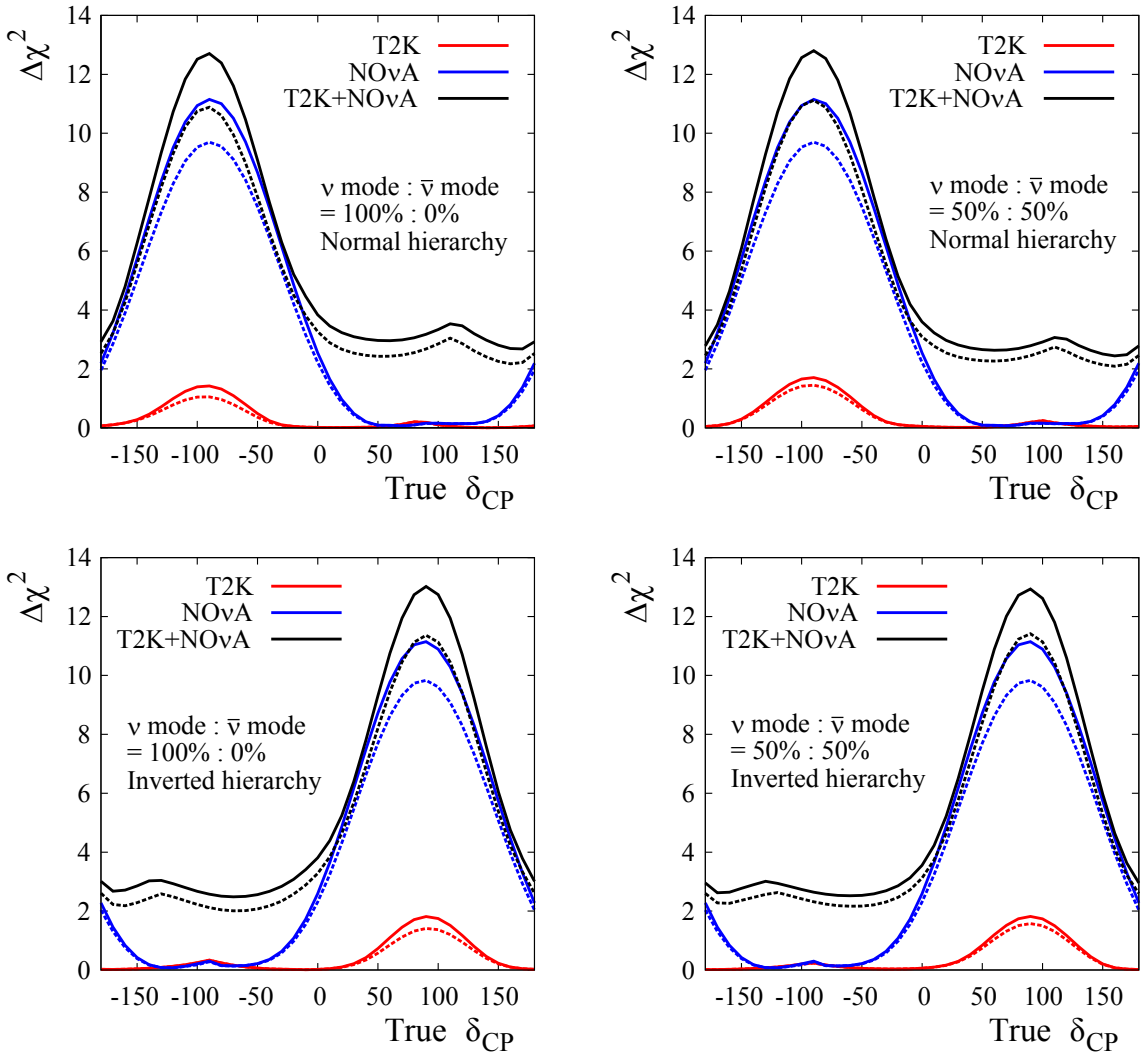

Figure H.14: The expected $\Delta\chi^2$ for resolving the mass hierarchy as a function of true δ_{CP} for T2K, NOνA, and T2K+NOνA. Dashed (solid) indicate studies where normalization systematics are (not) considered. The true mass hierarchy is assumed to be the normal hierarchy (top) or the inverted hierarchy (bottom). The T2K run mode is assumed to be 100% ν mode (left) or 50% ν mode plus 50% $\bar{\nu}$ mode (right). The NOνA run mode is assumed to be 50% ν mode plus 50% $\bar{\nu}$ mode.

List of Tables

List of Figures

List of Abbreviations

ASIC ..... Application Specific Integrated Circuit

ADC ..... Analog to Digital Converter

APD ..... Avalanche Photodiode

BEB ..... Back-End Board

BG ..... Background

CC ..... Charged Current

CCQE ..... Charged Current Quasi-Elastic

CL ..... Confidence Level

CP ..... Charge conjugation and Parity

CPU ..... Central Processing Unit

CTM ..... Cosmic-ray Trigger Module

DAC ..... Digital to Analog Converters

DAQ ..... Data Acquisition

DIS ..... Deep Inelastic Scattering

ECal ..... Electromagnetic Calorimeter

FC ..... Fully Contained

FGD ..... Fine Grained Detector

FPGA ..... Field-Programmable Gate Array

FV ..... Fiducial Volume

GPS ..... Global Positioning System

ID ..... Inner Detector

IH ..... Inverted Hierarchy

INGRID ..... Interactive Neutrino GRID

J-PARC ..... Japan Proton Accelerator Research Complex

LINAC ..... Linear Accelerator

MC ..... Monte Carlo

MCM ..... Master Clock Module

MEC ..... Meson Exchange Current

MIDAS ..... Maximum Integrated Data Acquisition System

MPPC ..... Multi-Pixel Photon Counter

MR ..... Main Ring

MuCL ..... Muon Confidence Level

MUMON ..... Muon Monitor

NC ..... Neutral Current

NH ..... Normal Hierarchy

OD ..... Outer Detector

P0D ..... Pi-Zero Detector

PCAC ..... Partially Conserved Axial-vector Current

PCB ..... Printed Circuit Board

PDG ..... Particle Data Group

PE ..... Photoelectron

PID ..... Particle Identification

PMNS ..... Pontecorvo Maki Nakagawa Sakata

PMT ..... Photomultiplier Tube

POT ..... Protons On Target

QE ..... Quasi Elastic

RCS ..... Rapid-Cycling Synchrotron

RES ..... Resonance

RMM ..... Readout Merger Module

SMRD ..... Side Muon Range Detector

SSM ..... Standard Solar Model

Super-K ..... Super-Kamiokande

T2K ..... Tokai to Kamioka

TDC ..... Time to Digital Converter

TFB ..... Trip-t Front-end Board

TPC ..... Time Projection Chamber

WLS ..... Wavelength Shifting

Bibliography

[1] W. Pauli, Letter to L. Meitner and her colleagues (1930)

[2] F. Reines and C. L. Cowan *et al.*, *Phys. Rev.* **117** (1960)

[3] G. Danby *et al.*, *Phys. Rev. Lett.* **9**, 36 (1962).

[4] S. Schael *et al.* (ALEPH, DELPHI, L3, OPAL, SLD, LEP Electroweak Working Group, SLD Electroweak Group, SLD Heavy Flavour Group), *Phys. Rept.* **427** 257 (2006)

[5] K. Kodama *et al.* (DONUT Collaboration), *Phys. Lett. B* **504**, 218 (2001).

[6] G. Aad *et al.* (ATLAS Collaboration), *Phys. Lett. B* **716** 1 (2012)

[7] S. Chatrchyan *et al.* (CMS Collaboration), *Phys. Lett. B* **716** 30 (2012)

[8] R. D. Peccei and H. R. Quinn, *Phys. Rev. Lett.* **38** 1440 (1977)

[9] B. Pontecorvo, *Zh. Eksp. Teor. Fiz.* **33** 549 (1957)

[10] B. Pontecorvo, *Zh. Eksp. Teor. Fiz.* **34** 247 (1958)

[11] M. Gell-Mann and A. Pais *Phys. Rev.* **97** 1387 (1955)

[12] Z. Maki, M. Nakagawa, and S. Sakata, *Prog. Theor. Phys.* **28**, 870 (1962)

[13] S. Tanaka, Y. Katayama, K. Matsumoto and E. Yamada, *Prog. Theor. Phys.* **28** 675 (1962)

[14] L. Wolfenstein, *Phys. Rev. D* **17** 2369 (1978).

[15] S. P. Mikheyev and A. Yu. Smirnov, *Yad. Fiz.* **42** 1441 (1985)

[16] S. P. Mikheyev and A. Yu. Smirnov, *Sov. J. Nucl. Phys.* **42** 913 (1985)

[17] S. P. Mikheyev and A. Yu. Smirnov, *Nuovo Cim. C* **9** 17 (1986)

[18] C. F. von Weizsäcker, *Physikalische Zeitschrift* **39** 633 (1938)

[19] H. A. Bethe, *Phys. Rev.* **55** 434 (1939)

[20] J. Davis, Raymond, D. S. Harmer and K. C. Hoffman, *Phys. Rev. Lett.* **20** 1205 (1968)

[21] B. Pontecorvo, Chalk River Lab. report PD-205, (1946)

[22] J. N. Bahcall, W. A. Fowler, I. Iben Jr. and R. L. Sears, *Astrophys. J* **137** 344 (1963)

[23] R. L. Sears, *Astrophys. J* **140** 477 (1964)

[24] H. R. P. Pochoda, *Planet. Space Sci.* **12** 119 (1964)

[25] K. S. Hirata *et al.*, *Phys. Rev. Lett.* **63** 16 (1989)

[26] P. Anselmann *et al.* (GALLEX Collaboration), *Phys. Lett. B* **285** 376 (1992)

[27] W. Hampel *et al.* (GALLEX Collaboration), *Phys. Lett. B* **447** 127 (1999)

[28] M. Altmann *et al.* (GNO Collaboration), *Phys. Lett. B* **616** 174 (2005)

[29] J. N. Abdurashitov *et al.* (SAGE Collaboration), *Phys. Rev. C* **80** 015807 (2009)

[30] Y. Fukuda *et al.* (Super-Kamiokande Collaboration), *Phys. Rev. Lett.* **81** 1158 (1998)

[31] T. K. Gaisser and M. Honda, *Ann. Rev. Nucl. Part. Sci.* **52** 153 (2002)

[32] K. S. Hirata *et al.*, *Phys. Lett. B* **205** 416 (1988)

[33] Y. Fukuda *et al.* (Super-Kamiokande Collaboration), *Phys. Rev. Lett.* **81** 1562 (1998)

[34] Q. R. Ahmad *et al.* (SNO Collaboration), *Phys. Rev. Lett.* **87** 071301 (2001)

[35] S. Fukuda *et al.* (Super-Kamiokande Collaboration), *Phys. Rev. Lett.* **86** 5651 (2001)

[36] J. Beringer *et al.* (Particle Data Group), *Phys. Rev. D* **86** 010001 (2012) and 2013 partial update for the 2014 edition

[37] K. Abe *et al.* (Super-Kamiokande Collaboration), *Phys. Rev. D* **83** 052010, 1010.0118 (2011)

[38] B. Aharmim *et al.* (SNO Collaboration) *Phys. Rev. C* **88** 025501 (2013)

[39] G. Bellini *et al.* (Borexino Collaboration), *Phys. Rev. Lett.* **107** 141302, 1104.1816. (2011)

[40] S. Abe *et al.* (KamLAND Collaboration), *Phys. Rev. Lett.* **100** 221803 0801.4589 (2008)

[41] J. Hosaka *et al.* (Super-Kamiokande Collaboration), *Phys.Rev. D* **73** 112001 (2006)

[42] M. Ahn *et al.* (K2K Collaboration), *Phys. Rev. D* **74** 072003 (2006)

[43] D. Michael *et al.* (MINOS Collaboration), *Phys. Rev. Lett.* **97** 191801 (2006)

[44] M. Apollonio *et al.*, *Phys. Lett. B* **466**, 415 (1999)

[45] F. Boehm *et al.*, *Phys. Rev. D* **64** 112001 (2001)

[46] S. Yamamoto *et al.* (K2K Collaboration), *Phys. Rev. Lett.* **96** 181801 (2006)

[47] K. Abe *et al.* (T2K Collaboration), *Phys. Rev. Lett.* **107** 041801 (2011)

[48] F. An *et al.* (DAYA-BAY Collaboration), *Phys. Rev. Lett.* **108** 171803 (2012)

[49] F. An *et al.* (DAYA-BAY Collaboration), *Chinese Phys. C* **37** 011001 (2013)

[50] J. Ahn *et al.* (RENO Collaboration), *Phys. Rev. Lett.* **108** 191802 (2012)

[51] Y. Abe *et al.* (Double Chooz Collaboration), *Phys. Rev. D* **86** 052008 (2012)

[52] C. Zhang (DAYA-BAY Collaboration), The 26th International Conference on Neutrino Physics and Astrophysics (2014)

[53] N. Cabibbo, *Phys. Rev. Lett.* **10** 531 (1963)

[54] M. Kobayashi and T. Maskawa, *Prog. Theor. Phys.* **49** 652 (1973)

[55] D. H. Perkins, P. F. Harrison and W. G. Scott, *Phys. Rev. B* **530** 167 (2002)

[56] S. Antusch and S. F. King, *Phys. Rev. B* **631** 42 (2005)

[57] H. Murayama, L. Hall and N. Weiner, *Phys. Rev. Lett.* **84** 2572 (2000)

[58] S. F. King and C. Luhn, *Rept. Prog. Phys.* **76** 056201 (2013)

[59] C. H. Albright, A. Dueck, and W. Rodejohann, *Eur. Phys. J. C* **70** 1099 (2010)

[60] G. Altarelli and F. Feruglio, *Rev. Mod. Phys.* **82**, 2701 (2010)

[61] H. Ishimori, T. Kobayashi, H. Ohki, Y. Shimizu, H. Okada *et al.*, *Prog. Theor. Phys. Suppl.* **183** 1 (2010)

[62] C. H. Albright and M. C. Chen, *Phys.Rev. D* **74** 113006 (2006)

[63] R. Mohapatra and A. Smirnov, *Ann. Rev. Nucl. Part. Sci.* **56** 569 (2006)

[64] A. D. Sakharov, *Sov. Phys. Usp.* **34** 392 (1991)

[65] J. H. Christenson, J. W. Cronin, V. L. Fitch, and R. Turlay, *Phys. Rev. Lett.* **13** 138 (1964)

[66] B. Aubert *et al.* (BABAR Collaboration), *Phys. Rev. Lett.* **86** 2515 (2001)

[67] K. Abe *et al.* (Belle Collaboration), *Phys. Rev. Lett.* **87** 091802 (2001)

[68] G. C. Branco, L. Lavoura, and J. P. Silva, *CP Violation*, Oxford University Press (1999)

[69] I. I. Y. Bigi and A.I. Sanda, *Phys. Nucl. Phys. Cosmol.* **9** 1 (2000)

[70] M. Fukugita and T. Yanagida, *Phys. Lett. B* **174** 45 (1986)

[71] R. Wendell (Super-Kamiokande Collaboration), The 26th International Conference on Neutrino Physics and Astrophysics (2014)

[72] D. Ayres *et al.* (NOνA Collaboration), Fermilab-Proposal-0929 (2005)

[73] C. Kraus *et al.*, *Eur. Phys. J. C* **40** 447 (2005)

[74] V. N. Aseev *et al.* (Troitsk Collaboration), *Phys.Rev. D* **84** 112003 (2011)

[75] K. Assamagan *et al.*, *Phys.Rev. D* **53** 6065 (1996)

[76] R. Barate *et al.* (ALEPH Collaboration), *Eur.Phys.J. C* **2** 395 (1998)

[77] P. A. R. Ade *et al.* (Planck Collaboration), arXiv:1303.5076 (2013)

[78] J. Wolf *et al.* (KATRIN Collaboration), *Nucl. Instrum. Meth. A* **623** 442 (2010)

[79] A. Nucciotti *et al.* (MARE Collaboration), *Nucl. Phys. Proc. Suppl.* **229** 155 (2012)

[80] B. Monreal and J. Formaggio, *Phys. Rev. D* **80** 051301 (2009)

[81] E. Ma and P. Roy, *Phys. Rev. D 52* **52** 4780 (1995).

[82] R. Foot and R. R. Volkas, *Phys. Rev. D* **52** 6595 (1995).

[83] E. J. Chuna, A. S. Joshipura, and A. Yu. Smirnov, *Phys. Lett. B* **357** 608 (1995).

[84] A. Aguilar *et al.* (LSND Collaboration), *Phys. Rev. D* **64**, 112007 (2001)

[85] A. A. Aguilar-Arevalo et al. (The MiniBooNE Collaboration), *Phys. Rev. Lett* **105** 181801 (2010)

[86] G. Mention *et al.*, *Phys. Rev. D* **83** 073006 (2011)

[87] C. Giunti and M. Laveder, *Phys. Rev. C* **83** 065504 (2011)

[88] A. A. Aguilar-Arevalo *et al.* (MiniBooNE Collaboration), *Phys. Rev. Lett.* **98**, 231801 (2007)

[89] B. Armbruster *et al.*, *Phys. Rev. D* **65** 112001 (2002)

[90] K. B. M. Mahn *et al.*, *Phys. Rev. D* **85** 032007 (2012)

[91] P. Adamson *et al.*, *Phys. Rev. Lett.* **107** 011802 (2011)

[92] N. Okada and O. Yasuda, *Int. J. Mod. Phys. A* **12** 3669 (1997)

[93] V. Barger, B. Kayser, J. Learned, T. Weiler, and K. Whisnant, *Phys. Lett. B* **489** 345 (2000)

[94] O. L. G. Peres and A. Yu. Smirnov, *Nucl. Phys. B* **599** 3 (2001)

[95] A. Boyarsky, J. Lesgourgues, O. Ruchayskiy, and M. Viel, *Phys. Rev. Lett.* **102** 201304 (2009)

[96] K. N. Abazajian, *Phys. Rev. Lett.* **112** 161303 (2014)

[97] E. Majorana, *Nuovo Cim.* **14** 171 (1937)

[98] E. Andreotti *et al. Phys. Rev. C* **85** 045503 (2012)

[99] M. Agostini *et al.* (GERDA Collaboration), *Phys. Rev. Lett.* **111** 122503 (2013)

[100] M. Auger *et al. Phys. Rev. Lett.* **109** 032505 (2012)

[101] A. Gando *et al. Phys. Rev. C* **85** 045504 (2012)

[102] S. L. Glashow, *Nucl. Phys.* **22** 579 (1961)

[103] S. Weinberg, *Phys. Rev. Lett.* **19** 1264 (1967)

[104] J. Goldstone, *Nuovo Cim.* **19** 154 (1961)

[105] Y. Nambu, *Phys.Rev.* **117** 648 (1960)

[106] P. W. Higgs, *Phys. Lett.* **12** 132 (1964)

[107] L. G. Liu *et al.*, *Phys. Rev. C.* **51** 2302 (1995)

[108] L. G. Liu *et al.*, *Phys. Rev. C.* **51** 3421 (1995)

[109] L. G. Liu *et al.*, *Phys. Rev. C.* **56** 800 (1997)

[110] J. E. Amaro *et al.*, *AIP Conf. Proc.* **1189** 24 (2009)

[111] K. Abe *et al.* (T2K Collaboration), *Nucl. Instrum. Meth. A* **659** 106 (2011)

[112] K. Abe *et al.* (T2K Collaboration), *Phys. Rev. D* **85** 031103 (2012)

[113] K. Abe *et al.* (T2K Collaboration), *Phys. Rev. D* **88** 032002 (2013)

[114] K. Abe *et al.* (T2K Collaboration), *Phys. Rev. Lett.* **111** 211803 (2013)

[115] K. Abe *et al.* (T2K Collaboration), *Phys. Rev. Lett.* **112** 061802 (2014)

[116] K. Abe *et al.* (T2K Collaboration), *Phys. Rev. Lett.* **112** 181801 (2014)

[117] Y. Yamazaki *et al.*, KEK-Report 2002-13; JAERI-Tech 2003-044 (2003)

[118] D. Beavis, A. Carroll, I. Chiang *et al.*, Physics Design Report, BNL 52459 (1995)

[119] T. Nakamoto *et al.*, *IEEE Trans. on Appl. Superconductivity* **14**, 616 (2004).

[120] T. Nakamoto *et al.*, *Proc. of 2005 Particle Acc. Conf.*, (2005).

[121] T. Ogitsu *et al.*, *IEEE Trans. on Appl. Superconductivity* **15**, 1175 (2005).

[122] S. Bhadra *et al.*, *Nucl. Instrum. Meth. A* **703** 45 (2013)

[123] T. Nakadaira *et al.*, *AIP Conf. Proc.* **981** 290 (2008)

[124] A. K. Ichikawa, *Nucl. Instrum. Meth. A* **690** 27 (2012)

[125] S. van der Meer, CERN-61-07 (1961).

[126] R. Palmer, CERN-65-32 (1965).

[127] K. Matsuoka *et al.*, *Nucl. Instrum. Meth. A* **623** 385 (2010)

[128] K. Matsuoka *et al.*, *Nucl. Instrum. Meth. A* **624** 591 (2010)

[129] K. Abe *et al.* (T2K Collaboration), *Nucl. Instrum. Meth. A* **694** 211 (2012)

[130] S. Assylbekov *et al.*, *Nucl. Instrum. Meth. A* **686** 48 (2012)

[131] N. Abgrall *et al.*, *Nucl. Instrum. Meth. A* **637** 25 (2011)

[132] P. A. Amaudruz *et al.*, *Nucl. Instrum. Meth. A* **696** 1 (2012)

[133] D. Allan *et al.*, *Journal of Instrum.* **8** 10019 (2013)

[134] M. B. Luque *et al.* (UA1 Collaboration), *Nucl. Instrum. and Meth.* **176** 175 (1980)

[135] J. Altegoer *et al.* (NOMAD Collaboration), *Nucl. Instrum. Meth. A* **404** 96 (1998)

[136] S. Aoki *et al.*, *Nucl. Instrum. Meth. A* **698** 135 (2013)

[137] I. Giomataris *et al.*, *Nucl. Instrum. Meth. A* **560** 405 (2006)

[138] Y. Fukuda *et al.* (Super-Kamiokande Collaboration), *Nucl. Instrum. Meth. A* **501** 418 (2003)

[139] T. Kikawa, *Nucl. Phys. B, Proc. Suppl.* **229** 451 (2012)

[140] A. Pla-Dalmau *et al.*, FERMILAB-PUB-05-344 (2005)

[141] K. Nitta *et al.*, *Nucl. Instrum. Meth. A* **535** 147 (2004)

[142] Kuraray Co., Ltd., *Scintillator Fiber Products* (1994)

[143] M. Yokoyama *et al.*, *Nucl. Instrum. Meth. A* **610** 128 (2009)

[144] M. Yokoyama *et al.*, *Nucl. Instrum. Meth. A* **622** 567 (2010)

[145] Hamamatsu Photonics K.K., *MPPC Selection Guide* (2009)

[146] H. Kawamuko *et al.*, PoS PD07, 043 (2007)

[147] Hirose Electronics Co., Ltd., *Ultra Small Surface Mount Coaxial Connectors* (2009)

[148] A. Vacheret *et al.*, Nuclear Science Symposium Conference Record, 2007. NSS '07. IEEE **3** 1084 (2007)

[149] L. Bellantoni and P. Rubinov, D0 note 4845 (2005)

[150] Xilinx Inc., *Spartan-3 FPGA Family Data Sheet* (2013)

[151] Xilinx Inc., *Virtex-II Pro and Virtex-II Pro X Platform FPGAs Complete Data Sheet* (2011)

[152] S. Ritt, P. Amaudruz, K. Olchanski, http://midas.psi.ch (2001)

[153] K. Abe *et al.* (T2K Collaboration), *Phys. Rev. D* **87** 012001 (2013)

[154] A. Ferrari, P. R. Sala, A. Fasso, and J. Ranft, CERN-2005-010, SLAC-R-773 and INFN-TC-05-011 (2005)

[155] G. Battistoni *et al.*, *AIP Conf. Proc.* **896**, 31 (2007)

[156] R. Brun *et al.*, CERN Program Library Long Write-up W5013 (1993)

[157] C. Zeitnitz and T. A. Gabriel, *Nucl. Instrum. Meth. A* **349** 106 (1994)

[158] N. Abgrall *et al.*, (NA61/SHINE Collaboration), *Phys. Rev. C* **84**, 034604 (2011)

[159] N. Abgrall *et al.*, (NA61/SHINE Collaboration), *Phys. Rev. C* **85**, 035210 (2012)

[160] T. Eichten *et al.*, *Nucl. Phys. B* **44**, 333 (1972)

[161] J. V. Allaby, F. G. Binon, A. N. Diddens, P. Duteil, A. Klovning, and R. Meunier, Report No. CERN-70-12, (1970)

[162] Y. Hayato, *Nucl. Phys. Proc. Suppl. B* **112** 171 (2002)

[163] Y. Hayato, *Acta Phys. Polon. B* **40** 2477 (2009)

[164] G. Mitsuka, *AIP Conf. Proc.* **981** 262 (2008)

[165] C. Andreopoulos *et al.*, *Nucl. Instrum. Meth. A* **614** 87 (2010)

[166] D. Casper, *Nucl. Phys. Proc. Suppl.* **112** 161 (2002)

[167] A. Gazizov and M. P. Kowalski, *Comput. Phys. Commun.* **172** 203 (2005)

[168] O. Buss *et al.*, *Phys. Rept.* **512** 1 (2012)

[169] C. Juszczak, *Acta Phys. Polon. B* **40** 2507 (2009)

[170] C. H. Llewellyn Smith, *Phys. Rept.* **3** 261 (1972)

[171] R. G. Sachs, *Phys. Rev.* **126** 2256 (1962)

[172] D. Dubbers *et al.*, *Europhys. Lett.* **11** 195 (1990)

[173] J. Liu *et al.* (UCNA Collaboration), *Phys. Rev. Lett.* **105** 181803 (2010)

[174] D. Mund *et al.*, *Phys. Rev. Lett.* **110** 172502 (2012)

[175] R. Gran, *et al.*, *Phys. Rev. D* **74** 052002 (2006)

[176] A. A. Aguilar-Arevalo, *et al.*, *Phys. Rev. Lett.* **100** 032301, (2008)

[177] L. A. Ahrens *et al.*, *Phys. Rev. Lett.* **56** 1107 (1986)

[178] C. H. Albright, C. Quigg, R. E. Shrock, and J. Smith, *Phys. Rev. D* **14** 1780, (1976)

[179] R. A. Smith and E. J. Moniz, *Nucl. Phys. B* **43** 605 (1972)

[180] D. Rein and L. M. Sehgal *Ann. Phys.* **133** 79 (1981)

[181] G. Breit, E. Wigner, *Phys. Rev.* **49** 519 (1936)

[182] R. P. Feynman, M. Kislinger, and F. Ravndal, *Phys. Rev. D* **3** 2706 (1971)

[183] C. H. Berger and L. M. Sehgal, *Phys. Rev. D* **76** 113004 (2007)

[184] K. S. Kuzmin, V. V. Lyubushkin, and V. A. Naumov, *Mod. Phys. Lett. A* **19** 2815 (2004)

[185] D. Rein, *Zeit. Phys. C* **35** 43 (1987)

[186] T. Kitagaki, *et al.*, *Phys. Rev. D* **34** 2554 (1986)

[187] S. K. Singh, M. J. Vicente-Vacas, and E. Oset, *Phys. Lett. B* **416** 23 (1998)

[188] D. Rein and L. M. Sehgal *Nucl. Phys. B* **223** 29 (1983)

[189] D. Rein and L. M. Sehgal *Nucl. Phys. B* **657** 207 (2007)

[190] S. L. Adler, *Phys. Rev.* **135** 963 (1964)

[191] J. J. Sakurai, *Ann. Phys.* **11** 1 (1960)

[192] V. Flaminino *et al.*, CERN-HERA 79-01 (1979)

[193] M. Glück, E. Reya, and A. Vogt, *Eur. Phys. J. C* **5** 461 (1998)

[194] A. Bodek and U. K. Yang, *AIP Conf. Proc.* **670** 110 (2003)

[195] A. Bodek, I. Park, and U.K. Yang, *Nucl. Phys. B, Proc. Suppl.* **139** 113 (2005)

[196] M. Nakahata *et al.*, *J. Phys. Soc. Jpn.* **55** 3786 (1986)

[197] M. Derrick *et al.*, *Phys. Rev. D* **17** 1 (1978)

[198] Z. Koba, H. B. Nielsen and P. Olesen, *Nucl. Phys. B* **40** 317 (1972)

[199] T. Sjostrand, *Comput. Phys. Commun.* **82** 74 (1994)

[200] P. Musset and J. P. Vialle, *Phys. Rept.* **39** 1 (1978)

[201] J. E. Kim, P. Langacker, M. Levine, and H. H. Williams, *Rev. Mod. Phys.* **53** 211, (1981)

[202] A. Bodek and J. L. Ritchie, *Phys. Rev. D* **24** 1400 (1981)

[203] T. Yang, C. Andreopoulos, H. Gallagher, K. Hoffmann, and P. Kehayias, *Eur. Phys. J. C* **63** 1 (2009)

[204] C. Amsler *et al.* (Particle Data Group), *Phys. Lett. B* **667** 1 (2008)

[205] N. Metropolis *et al.*, *Phys. Rev.* **110** 185 (1958)

[206] R. D. Woods, D. S. Saxon, *Phys. Rev.* **95** 577 (1954)

[207] C. W. De Jager, H. De Vries, and C. De Vries, *Atom. Data Nucl. Data Tabl.* **14** 479 (1974)

[208] L. L. Salcedo, E. Oset, M. J. Vicente-Vacas, and C. Garcia-Recio, *Nucl. Phys. A* **484** 557 (1988)

[209] D. Ashery *et al.*, *Phys. Rev. C* **23** 2173 (1981)

[210] G. Rowe, M. Salomon, and R. H. Landau *Phys. Rev. C* **18** 584 (1978)

[211] H. W. Bertini, *Phys. Rev. C* **6** 631 (1972)

[212] S. J. Lindenbaum and R. M. Sternheimer, *Phys. Rev.* **105** 1874 (1957)

[213] A. A. Aguilar-Arevalo *et al.* (MiniBooNE Collaboration), *Phys.Rev. D* **81** 092005 (2010)

[214] A. A. Aguilar-Arevalo *et al.* (MiniBooNE Collaboration), *Phys.Rev. D* **83** 052009 (2011)

[215] A. A. Aguilar-Arevalo *et al.* (MiniBooNE Collaboration), *Phys.Rev. D* **83** 052007 (2011)

[216] A. A. Aguilar-Arevalo *et al.* (MiniBooNE Collaboration), *Phys.Rev. D* **81** 013005 (2010)

[217] E. J. Moniz *et al.*, *Phys. Rev. Lett.*, **26** 445 (1971)

[218] O. Benhar, A. Fabrocini, S. Fantoni, I. Sick, *Nucl. Phys. A* **579** 493 (1994)

[219] O. Benhar, N. Farina, H. Nakamura, M. Sakuda, R. Seki, *Phys. Rev. D* **72** 053005 (2005)

[220] H. Nakamura, T. Nasu, M. Sakuda, O. Benhar, *Phys. Rev. C* **76** 065208 (2007)

[221] A. A. Aguilar-Arevalo *et al.* (MiniBooNE Collaboration), *Phys. Rev. D* **81**, 092005 (2010)

[222] V. Lyubushkin *et al.* (NOMAD Collaboration), *Eur. Phys. J. C* **63** 355 (2009)

[223] M. Hasegawa *et al.* (K2K Collaboration), *Phys. Rev. Lett.* **95** 252301 (2005)

[224] K. Hiraide *et al.* (SciBooNE Collaboration), *Phys. Rev. D* **78** 112004 (2008)

[225] Y. Kurimoto *et al.* (SciBooNE Collaboration), *Phys. Rev. D* **81** 111102 (2010)

[226] P. Adamson *et al.* (MINOS Collaboration), *Phys. Rev. D* **81**, 072002 (2010)

[227] M. Day, K. S. McFarland *Phys. Rev. D* **86** 053003 (2012)

[228] D. Ashery *et al.*, *Phys. Rev. C* **23** 2173 (1981)

[229] I. Navon *et al.*, *Phys. Rev., C* **28** 2548 (1983)

[230] E. Bellotti *et al.*, *Nuovo Cim. A* **18** 75 (1973)

[231] E. Bellotti *et al.*, *Nuovo Cim. A* **14** 567 (1973)

[232] D. Ashery *et al.*, *Phys. Rev. C* **30** 946 (1984)

[233] I. Navon *et al.*, *Phys. Rev. Lett.* **42** 1465 (1979)

[234] M. K. Jones *et al.*, *Phys. Rev. C* **48** 2800 (1993)

[235] F. Binon *et al.*, *Nucl. Phys. B* **17** 168 (1970)

[236] A. Saunders *et al.*, *Phys. Rev. C* **53** 1745 (1996)

[237] S. M. Levenson *et al.*, *Phys. Rev. C* **28** 326 (1983)

[238] H. Hilscher *et al. Nucl. Phys. A* **158** 602 (1970)

[239] R. H. Miller *et al. Nuovo Cim. V* **1** 882 (1957)

[240] K. V. Alanakian *et al.*, *Phys. Atom. Nucl.* **61** 207 (1998)

[241] S. Agostinelli *et al.* (GEANT4 Collaboration), *Nucl. Instrum. Meth. B* **506**, 250 (2003)

[242] J. Apostolakis *et al.*, *J. Phys. Conf. Ser.* **160** 012073 (2009)

[243] J. Birks, *Proc. Phys. Soc. A* **64** 874 (1951)

[244] J. Birks, *Theory and Practice of Scintillation Counting*, Pergamon Press (1964).

[245] C. Giganti, Ph.D. thesis, L'Universite Paris-Sud (2010).

[246] I. Thormahlen, J. Straub, and U. Grigull, *J. Phys. Chem. Ref. Data* **14** 933 (1985)

[247] K. Abe *et al.* (Super-Kamiokande Collaboration), *Nucl. Instrum. Meth. A* **737** 253 (2014)

[248] S. Wolfram, *Rev. Mod. Phys.* **55** 601 (1983)

[249] S. Wolfram, *A New Kind of Science* (2002)

[250] H. Maesaka, Ph.D. thesis, Kyoto University (2005)

[251] S. J. Barish *et al.*, *Phys. Rev. D* **19** 2521 (1979)

[252] C. Baltay *et al.*, *Phys. Rev. Lett.* **44** 916 (1980)

[253] N. J. Baker *et al.*, *Phys. Rev. D* **25** 617 (1982)

[254] A. Benvenuti *et al.*, *Phys. Rev. Lett.* **32** 1457 (1974)

[255] B. C. Barish *et al.*, *Phys. Rev. Lett.* **2** 1595 (1977)

[256] D. MacFarlane *et al.*, *Zeit. Phys. C* **26** 1 (1984)

[257] P. S. Auchincloss *et al.*, *Zeit. Phys. C* **48** 411 (1990)

[258] T. Kitagaki *et al.*, *Phys. Rev. Lett.* **49** 98 (1982)

[259] G. Taylor *et al.*, *Phys. Rev. Lett.* **51** 739 (1983)

[260] N. Baker *et al.*, *Phys. Rev. Lett.* **51** 735 (1983)

[261] W. Seligman, Thesis NEVIS-292 (1997)

[262] D. Naples *et al.* (NuTeV Collaboration), *Nucl. Phys. Proc. Suppl.* **118** 164 (2003)

[263] D. Colley *et al.* (BEBC WA59 Collaboration), *Zeit. Phys. C* **2** 187 (1979)

[264] P. Bosetti *et al.* (BEBC WA59 Collaboration), *Phys. Lett. B* **110** 167 (1982)

[265] D. Allasia *et al.* (BEBC WA59 Collaboration), *Nucl. Phys. B* **343** 285 (1990)

[266] I. Budagov *et al.*, *Phys. Lett. 29 B* **524** (1969)

[267] T. Eichten *et al.*, *Phys. Lett. B* **46** 274 (1973)

[268] S. Ciampolillo *et al.*, *Phys. Lett. B* **84** 281 (1979)

[269] O. Erriquez *et al.*, *Phys. Lett. B* **80** 309 (1979)

[270] J. Morfin *et al.*, *Phys. Lett. B* **104** 235 (1981)

[271] J. P. Berge *et al.*, *Zeit. Phys. C* **35** 443 (1987)

[272] M. Jonker *et al.*, *Phys. Lett. B* **99** 265 (1981)

[273] J. Allaby *et al.*, *Zeit. Phys. C* **38** 403 (1988)

[274] A. Asratian *et al.*, *Phys. Lett. B* **76** 239 (1978)

[275] D. Baranov *et al.* (SKAT Collaboration), *Phys. Lett. B* **81** 255 (1979)

[276] A. Vovenko *et al.*, *Sov. J. Nucl. Phys.* **30** 528 (1979)

[277] V. B. Anikeev *et al.*, *Zeit. Phys. C* **70** 39 (1996)

[278] Q. Wu *et al.* (NOMAD Collaboration), *Phys. Lett. B* **660**, 19 (2008)

[279] Y. Nakajima *et al.* (SciBooNE Collaboration), *Phys. Rev. D* **83** 012005 (2011)

[280] K. Abe *et al.* (T2K Collaboration), *Phys. Rev. D* **87**, 092003 (2013)

[281] W. Feller, *An Introduction to Probability Theory and Its Applications* **1** (1968)

[282] W. Feller, *An Introduction to Probability Theory and Its Applications* **2** (1971)

[283] K. Abe *et al.* (T2K Collaboration), *Phys. Rev. D* **90** 052010 (2014)

[284] B. G. Tice *et al.* (MINERνA Collaboration), *Phys. Rev. Lett.* **112** 231801 (2014)

[285] J. L. Alcaraz-Aunion and J. Walding (SciBooNE Collaboration), *AIP Conf.Proc.* **1189** 145 (2009)

[286] L. B. Auerbach *et al.* (LSND Collaboration), *Phys. Rev. C* **66** 015501 (2002)

[287] M. Martini, M. Ericson, G. Chanfray, and J. Marteau, *Phys. Rev. C* **80** 065501 (2009)

[288] M. Martini, M. Ericson, and G. Chanfray, *Phys. Rev. C* **84** 055502 (2011).

[289] J. Nieves, I. Ruiz Simo, and M. J. Vicente Vacas, *Phys. Rev. C* **83** 045501 (2011)

[290] J. Nieves, I. Ruiz Simo, and M. J. Vicente Vacas, *Phys. Lett. B* **707** 72 (2012)

[291] A. Bodek, H. S. Budd, M. E. Christy *Eur. Phys. J. C* **71** 1726 (2011)

[292] O. Lalakulich, K. Gallmeister, and U. Mosel, *Phys. Rev. C* **86** 014614 (2012)

[293] J. E. Amaro, M. B. Barbaro, J. A. Caballero, and T. W. Donnelly, *Phys. Rev. Lett.* **108** 152501 (2012)

[294] A. V. Butkevich, *Phys. Rev. C* **82** 055501 (2010)

[295] A. V. Butkevich and D. Perevalov, *Phys. Rev. C* **84** 015501 (2011)

[296] A. Meucci and C. Giusti, *Phys. Rev. D* **85** 093002 (2012)

[297] A. M. Ankowski, *Phys. Rev. C* **86** 024616 (2012)

[298] J. E. Amaro *et al.*, *Phys. Lett. B* **725** 170 (2013)

[299] O. Benhar, D. day, and I. Sick, *Rev. Mod. Phys.* **80** 189 (2008)

[300] A. Gil, J. Nieves, and E. Oset, *Nucl. Phys. A* **627** 543 (1997)

[301] T. Kikawa, *J. Phys. Conf. Ser.* **408** 012082 (2013)

[302] G. A. Fiorentini *et al.* (MINERνA Collaboration), *Phys. Rev. Lett.* **111** 022502 (2013)

[303] T. Golan, C. Juszczak, J. T. Sobczyk, *Phys. Rev. C* **86** 015505 (2012)

[304] R. Gran, J. Nieves, F. Sanchez, M. J. Vicente Vacas, *Phys. Rev. D* **88** 113007 (2013)

[305] H. Faissner *et al.*, *Phys. Lett. B* **125**, 230 (1983)

[306] E. Isiksal, D. Rein and J. G. Morfin, *Phys. Rev. Lett.* **52**, 1096 (1984)

[307] H. J. Grabosch *et al.* (SKAT Collaboration), *Zeit. Phys. C* **31**, 203 (1986)

[308] F. Bergsma *et al.* (CHARM Collaboration), *Phys. Lett. B* **157**, 469 (1985)

[309] P. Vilain *et al.* (CHARM-II Collaboration), *Phys. Lett. B* **313**, 267 (1993)

[310] P. Marage *et al.* (BEBC WA59 Collaboration), *Zeit. Phys. C* **31**, 191 (1986)

[311] P. P. Allport *et al.* (BEBC WA59 Collaboration), *Zeit. Phys. C* **43**, 523 (1989)

[312] M. Aderholz *et al.* (E632 Collaboration), *Phys. Rev. Lett.* **63**, 2349 (1989)

[313] S. Willocq *et al.* (E632 Collaboration), *Phys. Rev. D4* **7**, 2661 (1993)

[314] A. A. Aguilar-Arevalo *et al.* (MiniBooNE Collaboration), *Phys. Lett. B* **664**, 41 (2008)

[315] C. T. Kullenberg *et al.* (NOMAD Collaboration), *Phys. Lett. B* **682** 177 (2009)

[316] A. Kartavtsev, E. A. Paschos and G. J. Gounaris, *Phys. Rev. D* **74** 054007 (2006)

[317] S. K. Singh, M. Sajjad Athar and S. Ahmad, *Phys. Rev. Lett.* **96** 241801 (2006)

[318] C. H. Berger and L. M. Sehgal, *Phys. Rev. D* **79** 053003 (2009)

[319] E. A. Paschos and D. Schalla, *Phys. Rev. D* **80** 033005 (2009)

[320] L. Alvarez-Ruso, L. S. Geng and M. J. Vicente Vacas, *Phys. Rev. C* **76** 068501 (2007)

[321] L. Alvarez-Ruso, L. S. Geng, S. Hirenzaki and M. J. Vicente Vacas, *Phys. Rev. C* **75** 055501 (2007)

[322] L. Alvarez-Ruso, L. S. Geng, S. Hirenzaki and M. J. Vicente Vacas, *Phys. Rev. C* **80** 019906 (2009)

[323] E. Hernandez *et al.*, *Phys. Rev. D* **76** 033005 (2007)

[324] S. X. Nakamura *et al.*, arXiv:0901.2366 (2009)

[325] T. Kikawa, 9th International Workshop on Neutrino-Nucleus Interaction in the Few-GeV Region (2014)

[326] K. Hiraide *et al.* (SciBooNE Collaboration), *AIP Conf. Proc.* **1189** 249 (2009)

[327] A. Higuera, E. A. Paschos, *Eur. Phys. J. Plus* **129** 43 (2014)

[328] D. I. Scully, Ph.D. thesis, University of Warwick (2013)

[329] L. Aliaga *et al.* (MINERνA Collaboration), *Nucl. Inst. and Meth. A* **743** 130 (2014)

[330] H. Gallagher, D. Harris, *AIP Conf. Proc.* **967** 158 (2007)

[331] A. Mislivec, 9th International Workshop on Neutrino-Nucleus Interaction in the Few-GeV Region (2014)

[332] C. Rubbia, CERN-EP-INT-77-08 (1977)

[333] C. Anderson *et al.*, *Journal of Instrum.* **7** 10019 (2012)

[334] E. Santos, 9th International Workshop on Neutrino-Nucleus Interaction in the Few-GeV Region (2014)

[335] H. Chen, *et al.*, FERMILAB-PROPOSAL-0974 (2007)

[336] B. Rebel *et al.*, *J. Conf. Ser.* **308** 012023 (2011)

[337] H. Berns *et al.*, arXiv:1309.1740 (2013)

[338] A. M. Szelc *et al.*, *Journal of Instrum.* **8** 09011 (2013)

[339] G. Fogli *et al.*, *Phys. Rev. D* **84** 053007 (2011)

[340] K. Hagiwara, N. Okamura, K. Senda, arXiv:1107.5857

[341] Y. Ashie *et al.* (Super-Kamiokande Collaboration), *Phys. Rev. D* **71** 112005 (2005)

[342] F. James, M. Roos, *Comput. Phys. Commun.* **10** 343 (1975)

[343] R. Brun and F. Rademakers, *Nucl. Instrum. Meth. A* **389** 81 (1997)

[344] R. Wendell, http://www.phy.duke.edu/~raw22/public/Prob3++/ (2012)

[345] C. Barger *et al.*, *Phys. Rev. D* **22** 2718 (1980)

[346] M. Friend, T. Kikawa and M. Ikeda, XXVI International Conference on Neutrino Physics and Astrophysics (2014)

[347] K. Abe *et al.* (Super-Kamiokande Collaboration), *Phys. Rev. Lett.* **110** 181802 (2013)

[348] N. Agafonova *et al.* (OPERA Collaboration), *Phys. Rev. D* **89** 051102 (2014)

[349] A. Himmel (Super-Kamiokande Collaboration), arXiv:1310.6677 (2013)

[350] P. Adamson *et al.* (MINOS Collaboration), arXiv:1403.0867 (2014)

[351] G. J. Feldman and R. D. Cousins, *Phys.Rev. D* **57**, 3873 (1998)

[352] P. Adamson *et al.*, *Phys. Rev. Lett.* **110** 171801 (2013)

[353] S. Pascoli, S. T. Petcov and A. Riotto, *Phys. Rev. D* **75**, 083511 (2007)

[354] S. Pascoli, S. T. Petcov and A. Riotto, *Nucl. Phys. B* **774**, 1 (2007)

[355] K. Abe *et al.*, arXiv:1109.3262 (2011)

[356] I. Chemakin *et al.*, *Phys. Rev. C* **77** 015209 (2008)

[357] R. J. Abrams *et al.*, *Phys. Rev. D* **1** 1917 (1970)

[358] J. V. Allaby *et al.*, *Yad. Fiz.* **12** 538 (1970)

[359] B. W. Allardyce *et al.*, *Nucl. Phys. A* **209** 1 (1973)

[360] G. Bellettini *et al.*, *Nucl. Phys.* **79** 609 (1966)

[361] B. M. Bobchenko *et al.*, *Sov. J. Nucl. Phys.* **30** 805 (1979)

[362] A. S. Carroll *et al.*, *Phys. Lett. B* **80** 319 (1979)

[363] J. W. Cronin *et al.*, *Phys. Rev.* **107** 1121 (1957)

[364] F. F. Chen *et al.*, *Phys. Rev.* **99** 857 (1955)

[365] S. P. Denisov *et al.*, *Nucl. Phys. B* **61** 62 (1973)

[366] M. J. Longo and B. J. Moyer, *Phys. Rev.* **125** 701 (1962)

[367] A. V. Vlasov *et al.*, *Sov. J. Nucl. Phys.* **27** 222 (1978)

[368] L. Demortier and L. Lyons, CDF note 5776 (2002)